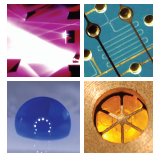


SCHRIFTEN DES INSTITUTS FÜR MIKROSTRUKTURTECHNIK  
AM KARLSRUHER INSTITUT FÜR TECHNOLOGIE (KIT)



Band 43

FLORIAN BRÜDERLIN

## Advanced Elastocaloric Cooling Devices Based on Shape Memory Alloy Films



Florian Brüderlin

**Advanced Elastocaloric Cooling Devices Based on  
Shape Memory Alloy Films**

Schriften des Instituts für Mikrostrukturtechnik  
am Karlsruher Institut für Technologie (KIT)  
Band 43

Hrsg. Institut für Mikrostrukturtechnik

Eine Übersicht aller bisher in dieser Schriftenreihe  
erschienenen Bände finden Sie am Ende des Buchs.

# **Advanced Elastocaloric Cooling Devices Based on Shape Memory Alloy Films**

by

Florian Brüderlin

Karlsruher Institut für Technologie  
Institut für Mikrostrukturtechnik

Advanced Elastocaloric Cooling Devices Based on  
Shape Memory Alloy Films

Zur Erlangung des akademischen Grades eines Doktor-Ingenieurs  
von der KIT-Fakultät für Maschinenbau des Karlsruher Instituts für  
Technologie (KIT) genehmigte Dissertation

von Florian Brüderlin, M.Sc.

Tag der mündlichen Prüfung: 27. Juli 2020

Referent: Prof. Dr. rer. nat. Manfred Kohl

Korreferent: Prof. Dr. -Ing. Stefan Seelecke

**Impressum**



Karlsruher Institut für Technologie (KIT)

KIT Scientific Publishing

Straße am Forum 2

D-76131 Karlsruhe

KIT Scientific Publishing is a registered trademark  
of Karlsruhe Institute of Technology.

Reprint using the book cover is not allowed.

[www.ksp.kit.edu](http://www.ksp.kit.edu)



*This document – excluding parts marked otherwise, the cover, pictures and graphs –  
is licensed under a Creative Commons Attribution-Share Alike 4.0 International License  
(CC BY-SA 4.0): <https://creativecommons.org/licenses/by-sa/4.0/deed.en>*



*The cover page is licensed under a Creative Commons  
Attribution-No Derivatives 4.0 International License (CC BY-ND 4.0):  
<https://creativecommons.org/licenses/by-nd/4.0/deed.en>*

Print on Demand 2022 – Gedruckt auf FSC-zertifiziertem Papier

ISSN 1869-5183

ISBN 978-3-7315-1065-9

DOI 10.5445/KSP/1000125495





# Abstract

Our modern society and technology are virtually unthinkable without cooling. On the large-scale, entire industries like the food or medical sector depend on the reliable availability of cold. On the small-scale, the increasing power density in miniaturized electronics and appliances raises the need for active temperature control and cooling. The cooling technologies utilized today depend on critical substances or are bound to low efficiencies. Thus, there is a tremendous need for innovative cooling technologies that are both environmentally friendly and efficient.

Elastocaloric cooling is a new emerging solid-state cooling technology with the potential to provide environmentally friendly efficient cooling. Currently, superelastic shape memory alloys (SMA) are the most promising elastocaloric materials. Superelastic SMA films respond with heating and cooling to a stress application and removal, respectively. This effect occurs due to a reversible solid-to-solid phase transformation in the material between two phases referred to as austenite and martensite. SMA films are especially promising for elastocaloric cooling, since they combine a high elastocaloric effect size with highly efficient heat transfer due to the high surface-to-volume ratio of film geometries. In previous work, SMA film-based elastocaloric cooling has shown potential for small-scale applications. In this work, the limits of SMA film-based elastocaloric cooling are investigated and new concepts are developed to overcome limitations in cooling capacity and device temperature span.

Cold-rolled NiTiFe and sputtered TiNiCuCo films with a thickness of 30  $\mu\text{m}$  are used as active materials. The NiTiFe films reach an adiabatic temperature change  $\Delta T_{ad}$  due to the elastocaloric effect of +20 and -16°C upon loading and unloading, respectively. Three TiNiCuCo alloys with slightly altered cobalt content are used. The slight composition change is designed to shift the austenite finish temperature, in this case from 1.7 °C to 13.3 °C. In this way the

## Abstract

---

temperature range of operation of the films is increased. The films reach a maximum  $\Delta T_{ad}$  of 12.2 and -14.5 °C. TiNiCuCo films are especially promising for elastocaloric cooling due to their ultra-low fatigue properties. They have been reported to withstand more than  $10^7$  load cycles based on their tailored microstructure and high compatibility of austenite and martensite lattices.

The potential of SMA film-based elastocaloric cooling is demonstrated in single film-based devices. A device temperature span up to 14 °C is reached in combination with a high specific cooling capacity of up to 19 W/g. In addition, the device operates efficiently with a device coefficient of performance of up to 6. However, absolute cooling capacities in the small-scale device are limited to 220 mW and the device temperature span already is close to its theoretical limit given by  $\Delta T_{ad}$  of the used SMA film.

To overcome the limitations of single film elastocaloric cooling devices in terms of cooling capacity and device temperature span, two different advanced device architectures are developed and investigated. A parallelized cooling device is engineered to increase the absolute cooling capacity. The parallelized device combines the elastocaloric effect of five SMA films. It preserves the high specific cooling capacity unique to SMA film-based cooling devices, but increases the absolute cooling capacity to 900 mW. Thus, the parallelized device shows how to successfully upscale SMA film-based elastocaloric cooling devices in order to meet the demands of large-scale cooling applications like e.g., air conditioning in buildings.

In order to overcome the limitation of the device temperature span, a cascaded elastocaloric cooling device is developed. In the cascaded device, the elastocaloric effect of three SMA films is combined in a serial manner. The effect of the first two films is used to precool the next SMA film, and only the last film directly absorbs heat from the heat source. In this way, the device temperature span of the cascaded device is increased to 27.3 °C. Thus, the cascaded device overcomes the  $\Delta T_{ad}$  of a single film. However, the combined  $\Delta T_{ad}$  for heating and cooling has not been overcome so far. Nevertheless, the cascaded device has proven to largely increase the device temperature span

of SMA film-based elastocaloric cooling devices. This allows to address applications that require high temperature spans, such as refrigeration.

The results of this work form the basis to provide a variety of cooling applications with efficient and environmentally friendly SMA film-based elastocaloric cooling. Advanced devices based on parallelization and cascading offer high cooling capacities and broad device temperature spans.



# Kurzfassung

Unsere moderne Gesellschaft ebenso wie die zunehmend technologisierte Wirtschaft sind ohne Kühlung praktisch undenkbar. Ganze Industriezweige, wie beispielsweise die Lebensmittel- oder Medizinbranche, sind auf die zuverlässige Verfügbarkeit von Kälte im großen Maßstab angewiesen. Zusätzlich erfordert die zunehmende Leistungsdichte in miniaturisierter Elektronik vermehrt aktive Temperaturregelung und Kühlung im kleinen Maßstab. Dabei basieren heutige Kühltechnologien entweder auf kritischen Substanzen oder haben niedrige Wirkungsgrade. Es besteht daher ein zunehmender Bedarf an innovativen Kühltechnologien, die sowohl umweltfreundlich als auch effizient sind.

Der elastokalorische Effekt bietet die Grundlage für eine neuartige, festkörperbasierte Kühltechnologie, mit dem Potenzial effizient und umweltfreundlich Kühlleistung bereitzustellen. Die derzeit vielversprechendsten elastokalorischen Materialien sind superelastische Formgedächtnislegierungen (FGL). Diese reagieren auf das Anlegen einer mechanischen Spannung und anschließendes Entlasten mit Erwärmung bzw. Abkühlung. Der elastokalorische Effekt in superelastischer FGL basiert auf einer reversiblen Festkörper-Phasenumwandlung zwischen der Austenit- und Martensitphase. FGL-Dünnsschichten sind aufgrund ihres hohen Oberfläche-zu-Volumen-Verhältnisses besonders für die elastokalorische Kühlung geeignet, da sie hohe elastokalorische Effektgrößen mit effizienter Wärmeübertragung vereinen. Bereits in Vorgängerarbeiten hat sich das große Potenzial elastokalorischer Kühlung mit FGL-Dünnsschichten für Anwendungen im Miniaturbereich gezeigt. In dieser Arbeit werden die Leistungsgrenzen der FGL-Dünnsschicht-basierten elastokalorischen Kühlung untersucht. Darüber hinaus werden neue Konzepte entwickelt, um die bisherigen Grenzen der Kühlleistung und der Temperaturspanne im Kühlelement zur überwinden.

Kaltgewalzte NiTiFe- und gesputterte TiNiCuCo-Dünnsschichten mit einer Dicke von 30 µm werden als aktive Materialien verwendet. In NiTiFe-Dünnsschichten führt der elastokalorische Effekt beim mechanischen Be- und Entlasten zu einer adiabatischen Temperaturänderung  $\Delta T_{ad}$  von +20, bzw. -16 °C. Zusätzlich werden drei TiNiCuCo-Legierungen mit leicht verändertem Kobaltgehalt verwendet. Der unterschiedliche Kobaltgehalt wurde so eingestellt, dass die Austenit-Endtemperatur im Bereich von 1,7 bis 13,3 °C verschoben wird. Dies ermöglicht einen erweiterten Betriebsbereich der TiNiCuCo-Dünnsschichten, in welchen der elastokalorische Effekt eine maximale adiabate Temperaturänderung von 12,2 bzw. -14,5 °C hervorruft. TiNiCuCo-Dünnsschichten sind aufgrund ihrer einzigartigen Ermüdungsfreiheit besonders vielversprechend für elastokalorische Kühlanwendungen. Durch ihre angepasste feinkörnige Mikrostruktur in Kombination mit herausragender Kompatibilität der Austenit- und Martensitgitter können TiNiCuCo-Dünnsschichten mehr als  $10^7$  Lastzyklen standhalten.

In elastokalorischen Kühleinheiten, die auf einer einzelnen FGL-Dünnsschicht basieren, wurden hohen spezifischen Kühlleistung von bis zu 19 W/g und eine Temperaturspanne von bis zu 14 °C erreicht. Darüber hinaus arbeitet das Gerät effizient mit einer maximalen Leistungszahl von bis zu 6. Allerdings ist die absolute Kühlleistung der Kühleinheit auf 220 mW begrenzt. Gleichzeitig liegt die Temperaturspanne bereits nahe an der theoretischen Grenze, die durch die Temperaturänderung der FGL im adiabatischen Grenzfall gegeben ist.

Um die Limitierung der beschriebenen elastokalorischen Kühleinheit hinsichtlich Kühlleistung und der Temperaturspanne zu überwinden, werden parallelisierte und kaskadierte Gerätearchitekturen entwickelt und untersucht. Ziel der parallelisierten Kühleinheit ist es die absolute Kühlleistung zu erhöhen. Diese parallelisierte Einheit kombiniert den elastokalorischen Effekt von fünf FGL-Dünnsschichten. Sie vereint die hohe spezifische Kühlleistung von auf einzelnen FGL-Dünnsschichten basierenden Kühleinheiten mit einer erhöhten absoluten Kühlleistung. So erreicht die parallelisierte Einheit 900 mW Kühlleistung und zeigt, wie FGL-dünnsschichtbasierte, elastokalorische Kühlgeräte

erfolgreich erweitert werden können. Neue Anwendungsbereiche werden dadurch in Zukunft ermöglicht, wie beispielsweise die Raumklimatisierung.

Zusätzlich wird eine kaskadierte elastokalorische Kühleinheit entwickelt, um die Begrenzung der Temperaturspanne hin zu größeren Werten zu verschieben. In der kaskadierten Einheit wird der elastokalorische Effekt von drei FGL-Dünnsschichten kombiniert und in Reihe geschaltet. Der Effekt der ersten beiden Dünnsschichten wird genutzt, um die jeweils nächste FGL-Dünnsschicht vorzukühlen. Nur die dritte Dünnsschicht absorbiert Wärme direkt von der Wärmequelle, welche somit gekühlt wird. Auf diese Weise wird der Temperaturunterschied innerhalb der kaskadierten Einheit auf 27,3 °C erhöht. Damit überwindet die kaskadierte Kühleinheit die Begrenzung durch die adiabate Temperaturänderung  $\Delta T_{ad}$ . Die Summe der adiabaten Temperaturänderungen beim Be- und Entlasten konnte jedoch nicht überwunden werden. Dennoch hat sich gezeigt, dass die kaskadierte Gerätearchitektur die Temperaturspanne der elastokalorischen Kühleinheit beträchtlich erhöht und somit neue Anwendungen ermöglicht, beispielsweise die Kühlung auf Temperaturniveaus unterhalb der Umgebungstemperatur.

Die Ergebnisse dieser Arbeit bilden die Grundlage einer umweltfreundlichen und effizienten elastokalorischen Kühltechnologie basierend auf FGL-Dünnsschichten. Parallelisierte und kaskadierte Gerätearchitekturen erlauben es in Zukunft Anwendungen zu adressieren, welche große Kühlleistungen oder auch große Temperaturunterschiede benötigen.



# Acknowledgements

Over the past years I have received a lot of support which has contributed significantly to the success of this work. Therefore, I would like to thank all those who accompanied and helped me professionally as well as personally.

First and foremost, I would like to thank my supervisor Prof. Dr. Manfred Kohl for the trust he has placed in me, the open and constructive atmosphere, and constant professional support. His willingness to make his time available so generously has been very much appreciated.

I thank Prof. Dr. Stefan Seelecke for taking the effort of being my co-referee and for the collegial and constructive relationship throughout the whole project.

I would like to express my appreciation to Prof Dr. Eckhard Quandt and Lars Bumke from Kiel University for the beneficial collaboration. They supported me with superior TiNiCuCo speci-mens that have been the basis for large portions of this work. It was a great pleasure to work and discuss with Lars.

I would like to extend my thanks to my predecessor Hinnerk Oßmer. Not only did his work create the foundations for the present work, but he also remained a valuable advisor and discussion partner throughout the entire project and contributed in many ways to the success of this work.

I also welcomed the friendly and constructive working environment among the PhD students at IMT and especially among my work group. In particular I would like to mention and thank Frank Wendler, Randy Fechner, Sanaz Rastjoo, Kiran Jacob, Shahab Ahmadi, Joel Joseph, Lena Seigner, Xi Chen, Tim Finkbeiner, Ruben Garschagen, Daniela Sánchez and Helena Melzer.

Furthermore, I appreciated the cooperation with my former colleagues from Memetis GmbH for their support and the generous opportunity to rely on

their machinery and equipment. Marcel Gültig, Christoph Megnin and Hinrich Oßmer were a great help to me.

With his experience and patience, Marvin Schmidt from the University of the Saarland helped me a lot implementing my experimental test setup.

I would like to thank Giulia Ulpiani for her dedicated and motivated cooperation, her valuable work and her enthusiastic nature.

Special thanks are due to my students without whom this project would not have been possible in this form. I thank Amir Ghiami, Jan Wachter, Raphael Weidemann, Daniel Schall, Romain Buda and Carina Ludwig for their dedicated work.

I want to acknowledge the supportive colleagues at IMT that helped me in the most diverse concerns and projects. Especially Nina Giraud was always a great help to me.

I am grateful for my dear friends, who supported me a lot, not only through the years of my Phd project, but at any other time. I can always count on them.

Finally, I would like to deeply thank Johanna and my family Ursula, Klaus, Gerda and Jonas. With their love and constant support, they made it possible for me to be who I am today. Thank you so much.

Karlsruhe, July 2020

Florian Brüderlin

# Contents

<b>Abstract</b> .....	i
<b>Kurzfassung</b> .....	v
<b>Acknowledgements</b> .....	ix
<b>Abbreviations</b> .....	xv
<b>Parameters and Indices</b> .....	xvii
<b>1 Introduction</b> .....	1
1.1 Motivation .....	1
1.2 Objectives .....	5
1.3 Outline .....	6
<b>2 Background and State of the Art</b> .....	7
2.1 Caloric Cooling .....	7
2.1.1 Magnetocaloric Effect .....	10
2.1.2 Electrocaloric Effect.....	12
2.1.3 Elastocaloric Effect .....	14
2.1.4 Barocaloric Effect .....	14
2.1.5 Multicaloric Effects.....	16
2.2 Shape Memory Alloys and the Elastocaloric Effect .....	17
2.2.1 Martensitic Transformation .....	17
2.2.2 Shape Memory Effect .....	21
2.2.3 Superelasticity .....	23
2.2.4 Fatigue in Superelastic SMAs.....	25
2.2.5 Elastocaloric Material Properties and Figures of Merit.....	28
2.2.6 Elastocaloric Materials .....	31
2.3 Engineering of Elastocaloric Cooling Devices .....	34

2.3.1	Mechanical Loading States of SMAs for Elastocaloric Cooling.....	35
2.3.2	Heat Transfer and Separation of Heat Flows in Caloric Systems.....	37
2.3.3	Work Recovery .....	42
2.3.4	Heat Recovery .....	47
2.3.5	The Elastocaloric Cooling Cycle in SMA Film-Based Devices .....	49
2.3.6	Figures of Merit of Elastocaloric Refrigerators.....	51
2.4	State of the Art in Elastocaloric Cooling Devices .....	54
2.4.1	Classification of Elastocaloric Cooling Devices .....	54
2.4.2	Overview on Elastocaloric Cooling Prototypes.....	58
2.4.3	Previous work on SMA Film-Based Elastocaloric Cooling Devices .....	72
<b>3</b>	<b>Material Characterization.....</b>	<b>79</b>
3.1	Methods .....	79
3.1.1	SMA Film and Foil Fabrication .....	79
3.1.2	Mechanical Characterization .....	82
3.1.3	Thermal Characterization .....	85
3.2	NiTiFe .....	87
3.3	TiNiCuCo .....	94
<b>4</b>	<b>Concept and Operation of SMA Film-Based Elastocaloric Cooling Devices .....</b>	<b>101</b>
4.1	General Concepts .....	101
4.1.1	Compliant Structures in SMA Film-Based Cooling Devices .....	101
4.1.2	Scaling Laws of Elastocaloric Refrigerators .....	104
4.1.3	Cascaded System Architecture for Increased Temperature Span.....	109
4.1.4	Parallelized System Architecture for Increased Cooling Capacity .....	110
4.2	Device Simulation .....	111

4.3	Fabrication of Elastocaloric Cooling Devices .....	116
4.3.1	Fabrication of Copper Heat Sink and Source Elements .....	116
4.3.2	Fabrication of Polymer Support Structures: Additive Manufacturing .....	118
4.4	Experimental Test Setup.....	121
4.5	Experimental Operation of SMA Film-Based Elastocaloric Cooling Devices.....	125
<b>5</b>	<b>Single SMA Film Devices .....</b>	<b>127</b>
5.1	Single Film Device .....	127
5.1.1	Concept .....	127
5.1.2	Experimental Device and Operation .....	127
5.1.3	Results .....	128
5.1.4	Discussion .....	130
5.2	Single Film Device with Thermal Load .....	132
5.2.1	Concept .....	132
5.2.2	Experimental Device and Operation .....	133
5.2.3	Results .....	134
5.2.4	Discussion .....	136
5.3	Miniature Single Film Device .....	140
5.3.1	Concept .....	140
5.3.2	Experimental Device and Operation .....	140
5.3.3	Results .....	141
5.3.4	Discussion .....	143
5.4	Coupled Device .....	144
5.4.1	Concept .....	144
5.4.2	Experimental Device and Operation .....	145
5.4.3	Results .....	146
5.4.4	Discussion .....	151
<b>6</b>	<b>Advanced SMA Film Devices .....</b>	<b>153</b>
6.1	Parallelized Device .....	153
6.1.1	Concept .....	153

6.1.2 Experimental Device and Operation .....	154
6.1.3 Results .....	156
6.1.4 Discussion .....	158
6.2 Cascaded Device with In-plane Loading .....	161
6.2.1 Concept .....	161
6.2.2 Experimental Device and Operation .....	162
6.2.3 Results .....	165
6.2.4 Discussion .....	170
6.3 Cascaded Device with Out-of-plane Loading.....	173
6.3.1 Concept .....	173
6.3.2 Experimental Device and Operation .....	174
6.3.3 Results .....	176
6.3.4 Discussion .....	179
<b>7 Discussion of Elastocaloric Cooling Devices .....</b>	<b>181</b>
<b>8 Conclusion and Outlook.....</b>	<b>199</b>
8.1 Conclusion .....	199
8.2 Outlook .....	206
<b>Publications .....</b>	<b>209</b>
<b>Figures .....</b>	<b>211</b>
<b>Tables .....</b>	<b>227</b>
<b>References .....</b>	<b>229</b>

# Abbreviations

ABS	acrylonitrile butadiene styrene
AMR	active magnetic regeneration
BCC	body-centered cubic
BTO	barium titanate
CAU	Kiel University
CFCs	chlorofluorocarbons
CHEX	cold heat exchanger
CNT	carbon nano tubes
COP	coefficient of performance
DIC	digital image correlation
DLP	digital light processing
DOE	U.S. Department of Energy
DSC	differential scanning calorimetry
eCM	elastocaloric material element
EDM	electrical discharge machining
FDM	fused deposition modeling
FGL	Formgedächtnislegierung
HCFC	hydrochlorofluorocarbons
HFC	hydrofluorocarbons
HHEX	hot heat exchanger
HR	heat recovery
HTF	heat transfer fluid

HVAC	heating, ventilation, and air conditioning
IMT	Institute of Microstructure Technology
IOT	internet of things
IR	infrared
KIT	Karlsruhe Institute of Technology
LEM	lumped element model
NBT	sodium-bismuth titanate
PDMS	polydimethylsiloxan
PEEK	polyether ether ketone
PLA	polylactic acid
PMMA	polymethylmethacrylat
PMN	magnesium niobate
PSN	lead scandium niobate
PST	lead scandium tantalate
PVDF	polyvinylidene fluoride
PZT	lead zirconium titanate
RT	room temperature
RTA	rapid thermal annealing
SL	stereolithography
SMA	shape memory alloy
WR	work recovery

# Parameters and Indices

## Parameters

$A$	area
$A_f$	austenite finish temperature
$A_s$	austenite start temperature
$Bi$	Biot number
$COP_{device}$	device coefficient of performance
$COP_{mat}$	material coefficient of performance
$c_p$	specific heat capacity
$d\varepsilon/dt$	strain rate
$E_A$	Young's modulus of austenite
$E_M$	Young's modulus of martensite
$\varepsilon$	strain
$\varepsilon_T$	transformation strain
$f$	frequency
$F$	force
$h$	surface heat transfer coefficient
$G$	Gibbs free energy
$\Delta H$	enthalpy change
$k$	thermal conductivity
$l$	length, displacement
$m$	mass
$M_f$	martensite finish temperature

$M_s$	martensite start temperature
$\dot{q}_0^{cool}$	specific cooling capacity
$\dot{Q}_0^{cool}$	absolute cooling capacity
$Q_{lat}$	latent heat of transformation
$R$	thermal resistance
$\Delta S$	entropy change
$\Delta S_{iso}$	isothermal entropy change
$\sigma$	stress
$\sigma^{crit}$	critical stress of transformation
$T$	temperature
$\Delta T_{ad}$	adiabatic temperature change
$T_c$	Curie temperature
$\Delta T_{device}$	maximum temperature span of an elastocaloric refrigerator
$\Delta T_{device}^{cool}$	maximum device temperature span available for cooling
$U$	internal energy
$W$	work
$\Delta W_{device}$	mechanical work input per cycle of operation
$\Delta W_{mat}$	hysteresis work
$x_{M_+}$	martensite phase fraction
$\lambda_2$	middle eigenvalue of the transformation stretch matrix

**Indices**

<i>A</i>	austenite
<i>ad</i>	adiabatic
<i>AM</i>	from austenite to martensite
<i>cond</i>	conduction
<i>cont</i>	contact
<i>conv</i>	convection
<i>cool</i>	cooling
<i>device</i>	device related
<i>el</i>	elastic
<i>f</i>	finish
<i>in</i>	input
<i>iso</i>	isothermal
<i>load</i>	loading related
<i>M</i>	martensite
<i>MA</i>	from martensite to austenite
<i>mat</i>	material
<i>max</i>	maximum
<i>out</i>	output
<i>s</i>	start
<i>sink</i>	heat sink related
<i>SMA</i>	SMA related
<i>source</i>	heat source related
<i>t</i>	transformation



# **1      Introduction**

## **1.1    Motivation**

Our modern society is unimaginable without cooling. Food storage, supply and even production completely depend on reliably available cooling. Even more health care and the complete medical sector would break down without refrigeration available around the clock. The technological world surrounding us requires cooling on all scales from computer chips that need temperature control to large-scale nuclear power plants, which can often be recognized already from large distance by their distinctive cooling tower. Even to preserve the diversity of life on earth, humanity relies on cooling and creates cryogenic repositories [1].

The cooling capacity needed for all these different purposes adds up to a tremendous energy consumption. It is estimated that the use of air conditioners and electric fans already accounts for about 20 % of the world's whole electricity demand in buildings [2]. Especially the energy needed for cooling in/of residential buildings is predicted to further increase up to 750 % by 2050 compared to 2010, mainly due to population increase, growth of income and global warming [3]. As an example, the future cooling demand of a single city like Mumbai might compare to 24 % of the entire demand of the USA [4].

As the effects of climate change become more pronounced in the future, demand for cooling will increase. However, cooling contributes to global warming itself in several ways. Cooling technology not only promotes the greenhouse effect through its massive energy demand, but in addition the use of refrigerants in vapor compression cycle-based cooling is critical. Since chlorofluorocarbons (CFCs) and hydrochlorofluorocarbons (HCFCs) are phased out by the Montreal protocol due to their ozone depleting properties, mostly hydrofluorocarbons (HFCs) have been used as refrigerants in the last decade. Due

to the high global warming potential of HFCs (up to 14000) the phase down of HFCs was established in the Kigali Amendment [5]. Accordingly, there is a tremendous need for new refrigerants or even more preferable, for new efficient and environmentally friendly cooling technologies for macroscale cooling applications.

Besides the challenges in large-scale refrigeration applications, active cooling plays an increasingly important role in miniaturized devices [6]. At the small-scale miniaturization has paved the way for today's major technological trends such as the internet of things (IoT) and industries 4.0. This was only made possible by the enormous progress in microtechnology, enabling the cost-effective production of highly potential miniaturized computer chips, sensors and communication modules [7, p. 3 ff]. This ongoing trend of miniaturization enabled also completely new fields like e.g. microfluidics and lab-on-a-chip systems [8]. One common phenomenon related to miniaturization is that with increased functional density also the power density and heat flux generation increases in miniaturized devices. Therefore, temperature control and active cooling play an important role. Often passive cooling technologies like ventilation and heat pipes are considered sufficient, but conventional methods come to their limits with continued miniaturization. Today this need for active cooling in the small scales is mainly addressed by Peltier cooling. However, Peltier cooling has one major disadvantage, a limited efficiency [9]. So not only in the macroscale world, but also in miniaturized systems, there is an urgent need for new cooling technologies combining efficiency with environmental compatibility.

One especially innovative approach to provide cooling in an efficient and environmentally friendly way is elastocaloric cooling [10]. The elastocaloric effect is based on special solid materials that respond to changing stress fields with the release and absorption of heat. The elastocaloric effect size can reach impressively high values, for example in NiTi-based shape memory alloys elastocaloric temperature changes reach up to 40 °C [11] and latent heats reach up to 35 J/g [12]. In addition it has been shown that the NiTi-based

shape memory alloys can withstand millions of load cycles required for elastocaloric cooling applications [13]. Especially shape memory alloy films are promising for elastocaloric cooling due to their high surface-to-volume ratio needed for efficient heat transfer and high specific cooling capacity [14]. Elastocaloric cooling technology demonstrates a more favorable scaling behavior than other conventional technologies and consequently can provide cooling to miniaturized systems as well as in the macroscopic world [15;16]. Figure 1 schematically shows an elastocaloric cooling cycle that is the basis of elastocaloric cooling. The elastocaloric element is cyclically loaded (0-1) and unloaded (2-3) mechanically, and responds to the changing mechanical load by an increase (0-1) and decrease (2-3) in temperature. Therefore, the elastocaloric element can absorb (3-0) and release (1-2) heat from and to its surrounding. The absorbed and released heat can be used in elastocaloric devices for cooling and heat pumping.

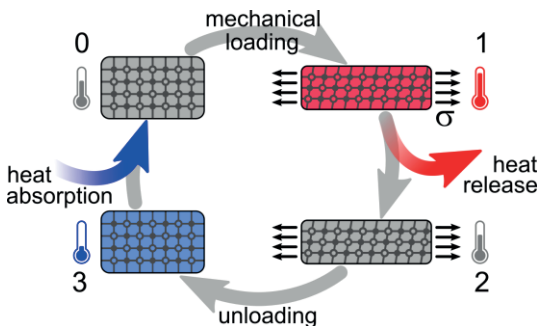


Figure 1 General schematic elastocaloric cooling cycle with four steps: mechanical loading of the elastocaloric element (0-1) that responds to application of the stress field with a rise in temperature; heat release to the environment (1-2); release of the mechanical load and temperature drop of the element (2-3); heat absorption from the environment (3-0). The absorbed heat in (3-0) can be used for cooling.

The elastocaloric effect was already discovered in the 19<sup>th</sup> century by Gough in natural rubber [17] and by Joule in wood and metals [18]. The effect has

also been discovered in single crystal shape memory alloys (SMA) in the 1980s [19–21], and in FeRh alloy and NiTi alloy in the 1990s [22–25]. However, the research field of elastocaloric cooling did not evolve until 2008, when an adiabatic temperature change based on the elastocaloric effect of 15 °C was estimated for copper based shape memory alloys [26] and the elastocaloric effect was proposed for mechanical refrigeration [27;28]. The field has experienced a huge boost since 2014, when a report prepared for the U.S. Department of Energy (DOE) found elastocaloric cooling to be the most promising alternative to vapor-compression technology for heating, ventilation, and air conditioning (HVAC) systems of commercial and residential buildings [10]. Since 2014 the number of publications in the field of elastocaloric cooling has increased largely from 9 to 66 publications in the year 2019<sup>a</sup>.

At the current state, the field of elastocaloric cooling revealed the potential to provide efficient cooling on various scales without the use of refrigerants and hazardous or environmentally harmful substances. Few elastocaloric cooling demonstration devices have been built at this early stage of the research field [15;16;30;30;31]. Hence, the technology has to demonstrate that it can solve and exploit its specific issues and opportunities and it can make the step from scientific interest to successful industrial application.

The goal of this work is to develop advanced cooling demonstrators dedicated to miniature-scale systems, which make use of the specific advantages of elastocaloric SMA in film geometry. In this way, the present work aims to demonstrate the potential, to reveal and address criticalities of the elastocaloric cooling technology, and thus, make a contribution to the field of elastocaloric cooling on its path to application.

---

<sup>a</sup> 89 % of the publications in the field have been published since 2014. Meta-analysis based on publication database Scopus [29], analysis was performed on 10 March 2020. The search was performed with the keyword “elastocaloric” for search fields title, abstract and keywords in all source types.

This work is in the fortunate position of not having to start from scratch but being able to rely on the detailed previous work carried out at the Karlsruhe Institute of Technology (KIT)<sup>b</sup>. In addition, it is embedded in cooperation with the research group of Prof. Quandt at the Kiel University (CAU) who developed first ultra-low fatigue SMA films [13]. In this cooperation, research at CAU focuses on material synthesis and fundamental material science of SMAs for elastocaloric applications. The focus of this work based at KIT is on material characterization and especially the engineering of elastocaloric cooling units and devices based on the SMA films prepared in Kiel.

## 1.2 Objectives

The main objective of this work is to develop and investigate new advanced SMA film-based elastocaloric cooling devices with enhanced temperature span and cooling capacity. Therefore, limits of existing single SMA film-based have to be explored to overcome these limitations in advanced SMA film-based elastocaloric cooling devices.

For the understanding and engineering of elastocaloric cooling devices, the precise knowledge of material properties and the understanding of the elastocaloric effect on the material level is crucial. Thus, one part of this work is focused on the characterization and understanding of the different SMA films used as active material. To examine the performance limits of existing SMA film-based cooling devices, the development of a new advanced experimental test platform is necessary. The new experimental test setup allows to vary operation parameters in a wide range. Based on the material understanding and the new experimental test platform, the performance limits of existing cooling designs will be explored. Subsequently, this work focuses on

---

<sup>b</sup> Previous work on elastocaloric cooling at KIT was mainly covered by Hinnerk Ossmer [32]. He worked on this field before this work started. His prior work can be considered the foundation of the present work.

new advanced cooling devices to overcome the limitations found for existing designs: Cascaded devices are developed to increase temperature span and parallelized devices to increase cooling capacity.

### 1.3 Outline

The following chapter 2 provides the reader with the most relevant background information to understand and classify the results gained in this work. The fundamentals of calorific cooling technologies are discussed, a special focus lies on elastocaloric cooling by shape memory alloys. The basic principles of elastocaloric refrigerators are introduced, followed by the state of the art in elastocaloric refrigerators. In chapter 3, the material properties of SMA films used in this work are investigated and discussed. Chapter 4 introduces the reader into the concepts and operation of SMA film-based elastocaloric cooling devices. Elastocaloric cooling devices based on a single SMA film are presented in the following chapter 5, and experimental results are discussed in detail. To overcome the performance limitations found in Single SMA film devices, advanced devices with parallelized and cascaded device architecture are developed and presented the following chapter 6. The experimental results of all cooling devices investigated and developed in this work is discussed and compared in chapter 7. In the last chapter, the results of this work are reviewed, a conclusion and a brief outlook are given.

## 2 Background and State of the Art

### 2.1 Caloric Cooling

Innovative cooling technologies have attracted a lot of interest lately and among them, technologies based on caloric effects belong to the most promising [10;33–35]. In caloric materials the application and removal of a specific driving field triggers a reversible change of entropy that gives rise to the related caloric effect [36]. Magnetocaloric, electrocaloric, elastocaloric and barocaloric effect are each named after their triggering field. Depending on how the field is applied, the change of the materials entropy is directly connected to the isothermal release / absorption of heat or will involve a change in the materials temperature [35]. In Figure 2 a) a typical caloric cooling cycle is displayed schematically. The cycle is comparable to the so-called reverse Brayton cycle depicted in Figure 2 b). The reverse Brayton cycle includes adiabatic heating and cooling process steps and heat release and absorption under constant pressure [37,pp. 226–227]. In the special case of caloric cooling, the driving field is constant instead of the pressure. We start our detailed consideration of the caloric cooling cycle in the state 0 in which the element is at room temperature and no field is present. In step (0-1) an external field is applied adiabatically and due to the caloric effect, the temperature of the caloric element increases and reaches its maximum in state 1. For the application of the field, an energy input  $W_{in}$  is required. In the next step (1-2), the element releases heat to a heat sink under constant field. From there on, the field is removed adiabatically again (step 2-3) and the temperature of the caloric element drops. In the subsequent step (3-4), the caloric element can absorb heat from a heat source under constant field. It reaches the initial state 0 and the cycle can start again. The released and absorbed heat in steps ii and iv can be utilized for heat pumping and cooling by separating the two heat flows accordingly. In this schematic showcase the reverse Brayton cycle

is used. However, also other thermodynamic processes can be used in caloric cooling [38;39].

The external driving fields, which the different caloric effects are named after, are also referred to as order parameter. Magnetic and electric fields are the external fields in the magnetocaloric and electrocaloric effect [40;41]. In case of stress fields, it is distinguished between an uniaxial stress field with the related elastocaloric effect and a hydrostatic pressure field that triggers the barocaloric effect [26;42]. Elastocaloric and barocaloric effects are often classified together as mechanocaloric effect [43].

The most prominent caloric effects can be found in ferroic materials [35;36]. Ferroic materials are generally characterized by a disordered high temperature phase and a more ordered low temperature phase in which domains are formed. The domains of the low temperature phase may be aligned by an external field. The phase transformation between high and low temperature phase is associated with a change in the lattice structure of the material. It involves a large change of physical properties within a small temperature window [36;44]. Ferromagnetism is probably the best known ferroic effect. Ferromagnetic materials change between para- and ferromagnetic at a transition temperature, called Curie temperature  $T_c$ . If the ferromagnetic domains in the low temperature phase are aligned, a specimen behaves as a permanent magnet, given the coercivity is high enough [45,pp. 52–57]. Similarly, in ferroelectric materials ferroelectric domains of aligned electric dipoles are formed below  $T_c$ , which can be arranged by an external electric field. Ferroelectric materials are widely used in capacitors and piezoelectric actuators [44]. A third group are ferroelastic materials that undergo a reversible diffusionless martensitic transformation between a high temperature phase and a low temperature phase. In general, ferroelastic materials are known as shape memory alloys (SMAs) and the martensitic transformation is the basis of the shape memory effect and superelasticity in SMAs [46]. SMAs are discussed in chapter 2.2 in detail.

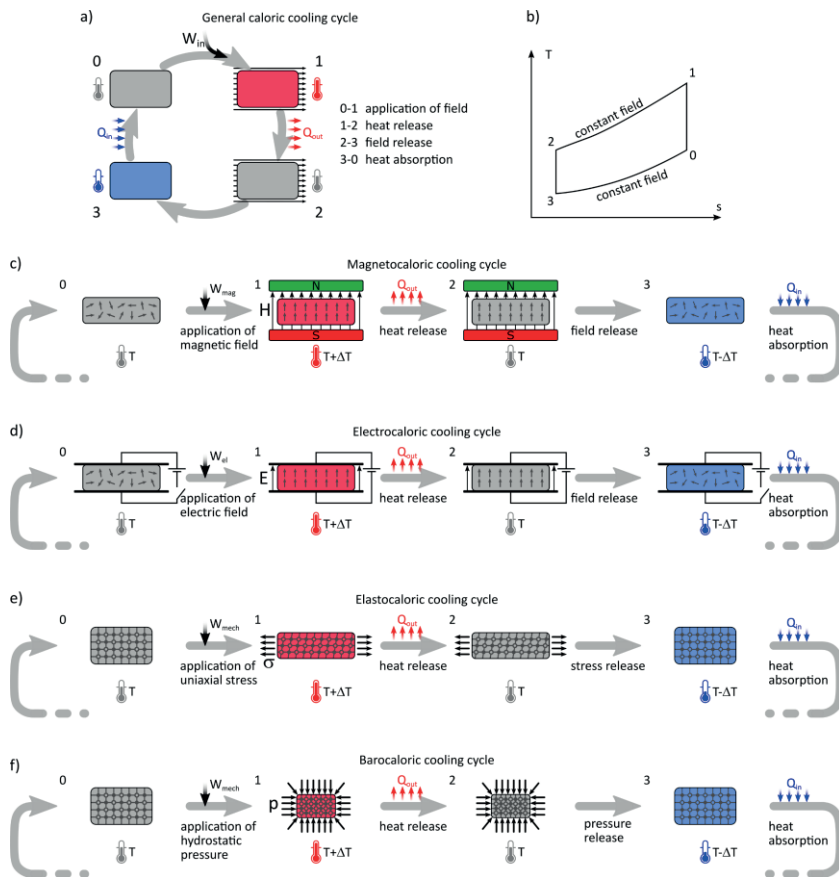


Figure 2 (a) Generalized caloric cooling cycle. A caloric cooling cycle can be subdivided into four process steps: field application and heating (0-1), heat release to a heat sink (1-2), field release and cooling (2-3) and heat absorption from a heat source (3-0). (b) Temperature-entropy diagram of the reverse Brayton cycle that is used as reference for the caloric process. Magnet-, electro-, elasto- and barocaloric cooling cycles are illustrated in c), d), e) and f), respectively.

In ferromagnetic, ferroelectric and ferroelastic materials besides temperature also the associated magnetic, electric or stress field can be used to drive

the material through the ferroic phase transition. The release and absorption of the phase transition's latent heat gives rise to the magnetocaloric, electrocaloric and elastocaloric effect [36]. Thus ferromagnetism, ferroelectricity, ferroelasticity and the magnetocaloric, electrocaloric, elastocaloric effect are based on the same physical principles. Depending on the mode of field application, the caloric effect is observed as isothermal entropy change  $\Delta s_{iso}$ , adiabatic temperature change  $\Delta T_{ad}$  or intermediate process [35]. If the application of the field leads to heating of the materials, it is referred to as conventional caloric effect; if the application of field leads to cooling it is called an inverse caloric effect [47].

Certain materials respond to more than one external field, which is referred to as multicalorics [48]. For a general overview on the fundamentals of caloric cooling the reader may refer to [36;44;49]. Thermodynamic fundamentals and material overviews on ferroic materials for caloric applications can be found in [35;50;51]. In the following, the caloric effects are discussed individually and the most important material systems transferring near room temperature (RT) are introduced in combination with a comment on caloric cooling demonstrators.

### 2.1.1 Magnetocaloric Effect

Among the different caloric cooling technologies, magnetocaloric cooling is considered to be the most mature. In magnetocaloric cooling a change of an external magnetic field  $H$  drives the magnetocaloric effect [40;45,p. 3]. A schematic magnetocaloric cooling cycle is illustrated in Figure 2 c).

Two types of magnetocaloric materials can be classified: materials with first and second order transition [52]. In materials that exhibit a first order transition, the order parameter - in this case the magnetization  $M$  of the material - changes discontinuously with temperature and thus also a discontinuous change in the material's entropy can be found. This discontinuous change in entropy is related to a phase transition between two different phases of diffe-

rent magnetization. Between the two phases either a change in lattice structure occurs or the lattice structure persists but lattice parameters are subjected to an abrupt change. As it is common for first order phase transitions, the transformation takes place through a nucleation-and-growth process and shows hysteretic properties. Magnetocaloric materials with first order transition often have a narrow operation temperature window around the material's phase transition temperature [53]. In materials with second order transitions, magnetization and entropy of the material change continuously with temperature [52]. Second order materials mostly utilize the magnetic transition between ferro- and paramagnetic state around the Curie temperature  $T_c$ . Thus, highest effects are found around  $T_c$ . Generally, the temperature window for operation is broader than in materials with first order transition [53].

The benchmark magnetocaloric material is Gadolinium (Gd). Gadolinium exhibits a second order transition near  $T_c$  in the room temperature regime. The maximum adiabatic temperature change  $\Delta T_{ad}$  and isothermal entropy change  $\Delta s_{iso}$  of gadolinium are 5.8 K and 5.2 J/kgK, respectively at a field change of 2 T. At a field change of 1 T it is 2.9 K and 2.8 J/kgK, respectively [53;54]. Further prominent groups of magnetocaloric materials for refrigeration near room temperature are La(FeSi)<sub>13</sub>-based alloys [55], binary Fe<sub>49</sub>Rh<sub>51</sub> [56], MnFe(P,X) based alloys [57] and NiMnX based alloys [58]. Detailed overviews on magnetocaloric materials can be found in [53;59–62].

Generally, the magnitude of the magnetocaloric effect depends on the magnitude of the applied magnetic field. Although in laboratory conditions high magnetic fields of around 5 T can be generated, the magnetic field that can be applied efficiently in a magnetocaloric cooling device is limited to about 1 T [63]. Under this prerequisite, gadolinium still shows the best performance in terms of  $\Delta T_{ad}$  near room temperature [53]. Due to the limitation of the material's  $\Delta T_{ad}$  to a few Kelvin, magnetocaloric refrigerators need to incorporate a concept to increase the device temperature span above  $\Delta T_{ad}$ . Concepts to utilize the magnetocaloric effect in a refrigerator are summarized in

[64;65]. The concept of active magnetic regeneration (AMR) is used in most cases [66]. Main engineering challenges in AMR are related to efficient switching between low and high magnetic field and the engineering of a regenerator that combines efficient heat transfer with an efficient hydraulic system. For efficient operation a low hydraulic pressure drop is needed, when the heat transfer fluid (HTF) is pumped through the regenerator [65]. Detailed overviews on magnetocaloric refrigeration demonstrators can be found in [67–70]. To highlight few experimental works, Jacobs et al. presented a magnetocaloric cooling system for naval applications. It provide a cooling capacity of 2502 W over a temperature range of 11 K [71]. Engelbrecht et al. developed a rotary active magnetic refrigerator that can provide a cooling capacity of 100 W under a temperature span of 20.5 K [72]. Johra et al. reported a magnetocaloric heat pump for domestic applications. It could reach a seasonal coefficient of performance (COP) of 3.51 [73]. First companies work on the commercialization of the magnetocaloric cooling technology<sup>c</sup>.

### 2.1.2 Electrocaloric Effect

In electrocaloric materials, the electrocaloric response of the material is triggered by a change of externally applied electric field  $E$  [41]. A schematic of an electrocaloric cooling cycle is illustrated in Figure 2 d). In electrocaloric materials, the change of electric field  $E$  induces a large change in the polarization. The change in polarization is related to a change in entropy giving rise to the electrocaloric effect. Similar to other caloric systems, high entropy changes can be found at the ferroelectric to paraelectric transition in ferroelectric materials around  $T_c$  [41;77;78].

Electrocaloric materials can be roughly divided into three categories: bulk samples from monocrystals; ceramics in form of bulk samples, thick films, thin films and multilayers; polymer thick films, thin films and multilayers [79;80].

---

<sup>c</sup> Ubiblue, Strasbourg, France (former “Cooltech Applications”) [74]; MagnoTherm Solutions, Darmstadt, Germany [75]; BASF, Ludwigshafen, Germany [76]

In electrocaloric materials, the sample geometry plays a major role for the application of the electric field and the dielectric strength. Sample geometry in electrocaloric films is also very important for the measurement of the electrocaloric effect. Electrocaloric materials fail due to electrochemical breakdown, if the applied field is too high. However, high fields are advantageous for the magnitude of electrocaloric effect. Thus, improving the dielectric strength in electrocaloric materials is of major importance. Dielectric strength might be improved by chemical composition, decreased thickness, homogenous material composition, and improved contact to electrodes [79].

Among the electrocaloric material systems, lead-based ceramic perovskite oxides play a major role. Decent electrocaloric effects can be found in lead zirconium titanate (PZT) based ceramics, lead scandium tantalate (PST) based ceramics, lead scandium niobate (PSN) based ceramics, lead magnesium niobate (PMN) based ceramics and PMN-PT based ceramics. In order to avoid the potential health hazards of lead, in recent years the interest in lead-free ceramic perovskite oxides increases. Potential candidates are barium titanate (BTO) and sodium-bismuth titanate (NBT) based ceramics [81]. Electrocaloric polymers, mainly polyvinylidene fluoride (PVDF) based polymers, show conventional ferroic or also relaxor ferroic properties [82]. Relaxor-type behavior can occur in both, polymer and ceramic materials. In relaxor type materials the long-range ferroelectric order is disturbed and a transition between polar-glass states and polar-state with high polarization occurs, which gives rise to high electrocaloric effect sizes [83]. Comprehensive compilations of electrocaloric materials can be found in [79;80;82;84]. In bulk ceramic samples, the  $\Delta T_{ad}$  of current materials is limited to few Kelvin, e.g. in BZT ceramics  $\Delta T_{ad}$  of 4.5 K and  $\Delta s_{iso}$  of 7.8 J/kgK has been reached [85]. In ceramic thin films, much higher values have been reported, e.g.  $Pb_{0.8}Ba_{0.2}ZrO_3$  reaches  $\Delta T_{ad}=45.3$  K. Similar high values could be found in polymer thin films with, e.g. in irradiated P(VDF-TrFE) copolymers with  $\Delta T_{ad}=35$  K [86]. Thin films allow extremely high electric field changes. However, measurement techniques become very challenging due to substrate effects. In addition, efficiency is assumed to be reduced in thin films due to Joule heating [79]. Furthermore, the high values for

$\Delta T_{ad}$  found in certain thin film materials so far could not be transferred to the device level. The  $\Delta T_{ad}$  of the electrocaloric materials that could be incorporated in the few existing electrocaloric cooling demonstrators are limited to 2 K [87]. Therefore, a device architecture like in magnetocaloric cooling is needed to increase the device temperature span above  $\Delta T_{ad}$ . Active regeneration and cascades have been proposed to do so. An overview of electrocaloric system architectures can be found in [88]. Recent electrocaloric devices are limited to device temperature spans of 3.3 K [87] and specific cooling capacity of 2.8 W/g [89]. Much higher values have been predicted in simulation though [87;90,p. 36].

### 2.1.3 Elastocaloric Effect

In elastocaloric materials, the elastocaloric effect is triggered by a change of an externally applied uniaxial stress field [26]. Showcase elastocaloric materials are superelastic shape memory alloys (SMAs) that undergo a reversible phase transformation between two crystallographic phases referred to as austenite and martensite under the application and removal of a stress field [43]. In analogy to ferromagnetic and electromagnetic materials SMAs are referred to as ferroelastic materials. The reversible stress-induced phase transformation in the material is related to a change of the entropy and thus heat is released and absorbed upon stress cycling. A schematic elastocaloric cooling cycle is illustrated in Figure 2 e). The fundamentals of the elastocaloric effect and the different elastocaloric materials are discussed in detail in chapter 2.2, corresponding cooling devices in chapter 2.4.

### 2.1.4 Barocaloric Effect

The barocaloric effect occurs under changing isostatic pressure. The pressure change induces a change of volume in the barocaloric material that is related to a change of entropy [42]. A schematic barocaloric cooling cycle is illustrated in Figure 2 f). In general, the barocaloric effect occurs in all material systems,

since the free energy of a system is directly related to pressure [91]. Therefore, the barocaloric effect can be found in very different material systems, including non-ferroic materials. Nevertheless, among the known groups of barocaloric materials, ferroic materials already introduced in the above chapters play a prominent role. The ferromagnetic, ferroelectric and ferroelastic transitions in ferroic material systems presented above can often - besides through temperature and the corresponding field - be triggered by a change in isostatic pressure. Thus, the entropy change of ferroic transitions can also be accessed by pressure changes and can be utilized in barocaloric cooling cycles [43]. Attractive barocaloric effects can be found in magnetocaloric materials like gadolinium-based alloys [92], Heusler alloys [93], LaFeSi-based alloys [94], FeRh [95] as well as in electrocaloric materials like BaTi<sub>3</sub> ceramics [96], in ammonium sulfate ((NH<sub>4</sub>)<sub>2</sub>SO<sub>4</sub>) [97] or in oxyfluorides ((NH<sub>4</sub>)<sub>2</sub>MoO<sub>2</sub>F<sub>4</sub>) [98]. Furthermore, barocaloric effects can be found in different materials systems like in the superionic conductor AgI [99], in rubbers [100–102] and in plastic crystals [103;104]. Compilations of barocaloric materials can be found in [43;105]. High isothermal entropy changes  $\Delta S_{iso}$  have been reported for the barocaloric effect, especially in plastic crystals with up to 687 J/kgK [104]. In natural rubber, direct measured adiabatic temperature changes  $\Delta T_{ad}$  of 25 K have been found [102]. The reported numbers of the barocaloric effect in various materials are very promising. However, only few values obtained by direct measurement techniques have been reported due to experimental issues [43]. The mechanisms that make a direct measurement of the barocaloric effect very difficult hinder also the engineering of barocaloric cooling devices. It is very challenging to apply isostatic pressure under adiabatic conditions and even if this issue would be managed, the barocaloric specimen is hard to access for temperature measurement. Similarly, it is especially hard to apply the isostatic pressure changes in a possible barocaloric demonstrator device, ensure efficient heat transfer with the barocaloric material, and separate the hot from cold heat flows simultaneously [106]. The barocaloric effect is promising, but the effect so far could not be transferred to the device level.

### 2.1.5 Multicaloric Effects

Multicaloric materials respond to more than one stimulating field [36;48] with a caloric effect. For example, often the magnetocaloric effect and the barocaloric effect are coupled in a materials system as described above in section 2.1.4. Two different sorts of multicaloric material systems can be distinguished: either a single material responds to different external fields [107], or different materials with different caloric effects are coupled into one composite [108]. The multicaloric effect can be used in different ways in caloric cooling systems. It can be used to achieve larger caloric effect size with smaller field changes in one domain. The temperature range of operation can be increased. Hysteresis can be eliminated in one domain by shifting it to another [109]. Furthermore, the multicaloric effect enables even new modes of operation utilizing the hysteretic behavior of the multicaloric material [110]. Theoretical investigations have predicted that multicaloric approaches can also increase the efficiency of caloric cooling cycles [111].

Multicaloric effects in multiferroic materials have been studied in various material systems. For example, the coupling of magnetocaloric and elastocaloric effects have been studied in magnetic SMAs [112;113], coupling of electrocaloric effect with elasto- and barocaloric effect has been found in ferroic perovskites [81;114]. In  $(La_{0.7}Pb_{0.3}MnO_3)_x - (PbTiO_3)_{1-x}$  even a coupling of magneto-, electro-, and elastocaloric effect can be found [115]. Due to the high potential of multicaloric approaches, first multicaloric cooling devices have been proposed, however no multicaloric cooling device has been realized to date [110;113]. Besides for caloric cooling, multiferroic materials are also of high interest for research fields as diverse as energy harvesting [107], development of a new generation of memories [116] and ultra-low power electronics [117].

## 2.2 Shape Memory Alloys and the Elastocaloric Effect

The elastocaloric effect in shape memory alloys (SMAs) and superelasticity of SMAs are directly connected. In consequence, the fundamentals of SMAs are highly important for elastocaloric cooling and are thus discussed in the following chapters in detail.

### 2.2.1 Martensitic Transformation

The unique properties of SMAs are based on a reversible martensitic transformation between a high temperature phase and a low temperature phase. The high temperature phase, referred to as austenite, has a high symmetry lattice structure. The low temperature phase, referred to as martensite, has a structure of lower symmetry. In the SMAs that are most relevant to this work, the austenite parent phase has BCC (body-centered cubic) structure, referred to as B2-type, whereas the martensite phase has a monoclinic structure called B19' in case of NiTi and also NiTiFe. The TiNiCu(Co) alloys used later in this work have a orthorhombic martensite structure (B19) [13;119]. A unit cell of both crystal structures is illustrated in Figure 3.

The transformation between the two phases takes place diffusionless by the cooperative displacive movement of atoms that transform the austenitic into the martensitic structure or vice versa. Due to the lower symmetry of the martensite structure, one austenite cell can transfer into 24 variants of martensite. They all have the same crystal structure, but different orientations. The martensitic transformation in SMAs is a first order transformation and thus undergoes a process of nucleation and growth. The interface between the austenite and martensite lattice is referred to as habit plane. The transformation takes place by movement of the habit plane. Depending on the lattice mismatch between the two crystal structures, high stresses can arise at the interface. If the internal stress is too high, lattice invariant shear occurs

either by slip or twinning. In SMAs, twinning is the dominant process for stress relaxation [120, pp. 11–12].

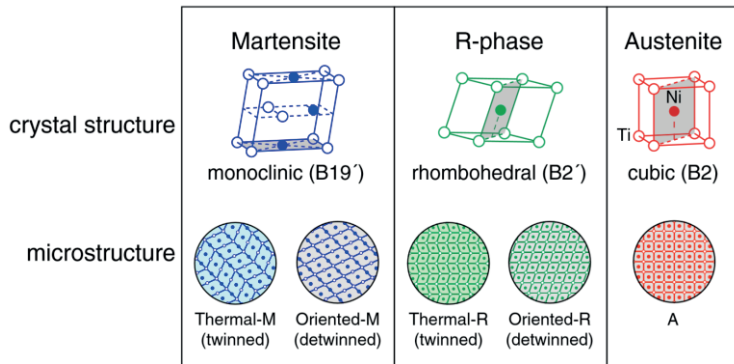


Figure 3 Unit cell of the crystal structure and according schematic microstructure of the high temperature austenite phase, the intermediate R-phase and the low temperature martensite phase. Martensite and R-phase can both be present in self accommodated twinned state or oriented detwinned state. © 2008, Society for Experimental Mechanics, reprinted from [118] with permission.

In binary NiTi-based SMAs the martensitic transformation can take place via an intermediate phase, which is referred to as R-phase [121]. The transformation properties of SMA are often investigated by differential scanning calorimetry (DSC) measurements [118]. In DSC-measurements, the transformation occurs as peak, as illustrated in the schematic DSC curve in Figure 4 a). For detailed information on DSC measurements refer to chapter 3.1.3. The onset and end of the peaks mark the start and end of the transformation, the area under the peak is a measure for the latent heat of the transformation  $Q_{lat}$ . When cooling down from the austenitic phase, the martensitic transformation starts at the so-called martensite start temperature  $M_s$  and completes at the martensite finish temperature  $M_f$ . Similarly, upon heating the transformation to austenite starts at the austenite start temperature  $A_s$  and

completes at the austenite finish temperature  $A_f$ . A thermal hysteresis  $\Delta T_{th}$  exists between the forward and reverse transformation.

Which crystal structure is preferred at a given temperature, is a question of the free energy of the system. The Gibbs free energy of the martensite and austenite phases writes as:

$$G^{A,M} = U^{A,M} - S^{A,M}T - \varepsilon^{A,M}\sigma \quad (\text{I})$$

With the internal energy  $U$ , the entropy  $S$ , temperature  $T$  and stress and strain tensors  $\sigma$  and  $\varepsilon$ . Austenite and martensite are denoted by  $A$  and  $M$ , respectively. For a given temperature, the phase with the lower free energy is stable. The Gibbs free energy of austenite and martensite is illustrated in a simplified schematic in Figure 5 b). Zero stress is assumed. At low temperatures the free energy of martensite is lower, and thus martensite is stable in this temperature regime. The same is the case for austenite at high temperatures. The two phases are in equilibrium at  $T_0$ . A certain driving force  $\Delta G_{AM}$  and  $\Delta G_{MA}$  is needed for nucleation and to start the transformation thereby. Thus, supercooling (superheating) is needed to start the transformation and the thermal hysteresis  $\Delta T_{th}$  forms. Within the temperature range between  $M_f$  and  $A_f$  the lattice structure of the SMA is therefore not defined clearly. It depends not only on the temperature, but also on the history of the SMA specimen [120,pp. 21–25].

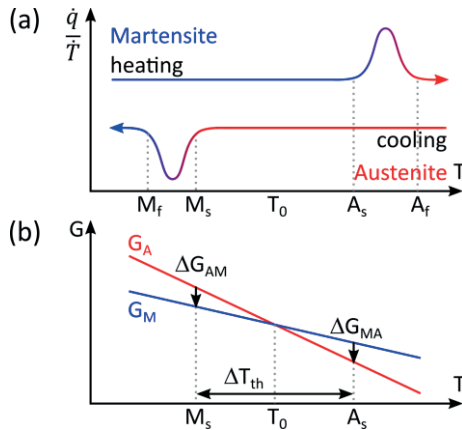


Figure 4 (a) Schematic differential scanning calorimetry (DSC) measurement of a SMA. The temperature induced phase transition is indicated by the peaks in the DSC curve. DSC measurements are often used to determine the transformation temperatures  $M_s$ ,  $M_f$ ,  $A_s$ , and  $A_f$  of the martensitic transformation. (b) Gibbs free energy of the austenite and martensite phase. The phase with the lower free energy is stable. To start the phase transformation, a driving potential  $\Delta G$  is needed. For b) compare [120,p. 23]

As already indicated in equation (I), the Gibbs free energies not only depend on the temperature, but also on the stress state. Thus, the reversible martensitic transformation in SMAs is not only triggered by temperature but also by stress. The temperature and stress driven martensitic transformation is the base of the shape memory effect and superelasticity in SMAs. Both effects are included in the overview of SMA material's behavior at different temperature regimes in Figure 5, and are discussed in the following chapters.

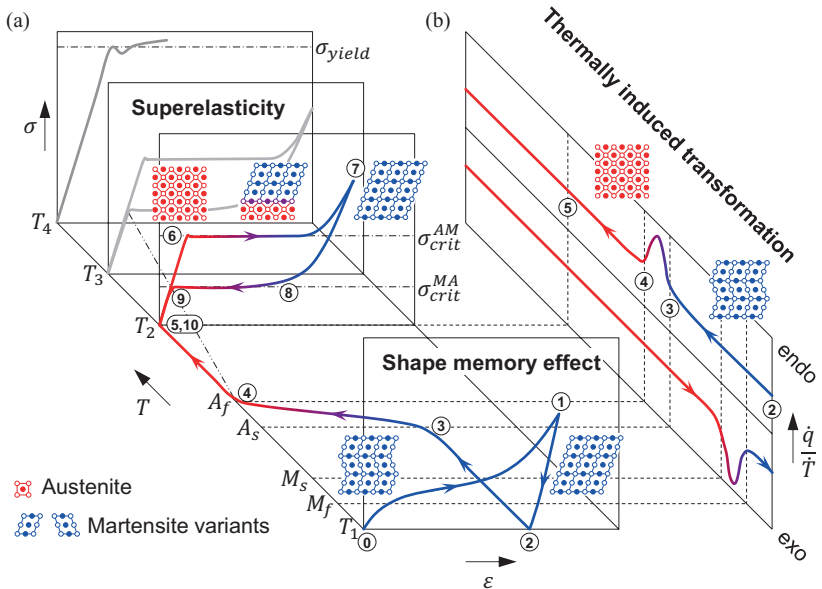


Figure 5 Effects in SMAs at different temperature regimes. (a) Superelasticity and the shape memory effect in a stress-strain-temperature space. (b) Thermally induced transformation is illustrated as DSC-curve and indicates the transformation temperatures in stress free state. Lattice structure and simplified microstructure are indicated. Figure adapted from [32,p. 18], © Ossmer, used under Creative Commons License (CC BY-SA 3.0 DE), legend modified.

## 2.2.2 Shape Memory Effect

The shape memory effect (SME) gives SMAs their name. It describes the ability to recover a predefined shape after a quasi-plastic deformation. A simplified model based on a single crystal specimen of the SME is illustrated in Figure 6 a). The consideration is started with the specimen in austenitic state above  $A_f$  (1). If the specimen is cooled below  $M_f$ , self-accommodated martensite is formed (2). Many different martensite variants coexist (for simplicity only two are illustrated) and the macroscopic shape of the specimen is unchanged. If now mechanical load is applied to the specimen, it is quasi-

plastically deformed. Martensite variants in the load direction will grow at the expense of variants with less favored orientation (3). Eventually, the martensite is completely oriented (4). When the deformed martensite is now heated again above  $A_f$ , it transforms back to austenite. Since all the possible martensite variants have only one parent austenite variant, the specimen recovers its original shape (1). In polycrystalline SMAs, the process is much more complex, but works in a similar way [120,pp. 36–40]. Generally, the SME can be used at working temperatures below  $M_f$ , but also in the transformation regime between  $M_f$  and  $A_f$  the SME can occur, as indicated by Figure 6 b). The stress levels must not be too high to prevent permanent defects in the crystal structure that hinder the full shape recovery upon heating [46].

The SME is mainly used for actuation. SMA based actuators allow for high strains up to 8 % and reach enormous power densities up to  $2.5 \cdot 10^7 \text{ J/m}^3$  [122;123]. SMA based actuators are used in aerospace applications, automotive applications and also in the biomedical field [123]. The high power densities also make SMA actuation highly interesting for microscale applications. For example SMA actuation has been used in microtechnology for grippers [124], microvalves [125], and damping [126].

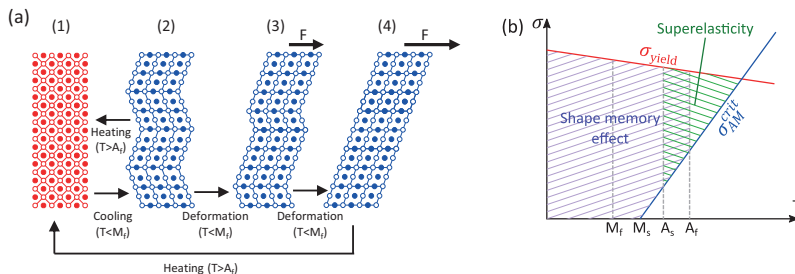


Figure 6 (a) Simplified schematic model of the shape memory effect (SME) in a single crystal SMA. Austenite is indicated in red, martensite in blue. (b) Regions of the SME and superelasticity in stress-temperature space. For a) compare [120,p. 37], for b) compare [46].

### 2.2.3 Superelasticity

A uniaxial stress field shifts the equilibrium between the free energy of austenite and martensite to lower temperatures and stabilizes the martensite phase. At temperatures above  $A_f$ , the application of a uniaxial load can thus lead to the formation of stress-induced martensite that transforms back to austenite, when the load is released. This gives rise to the superelastic effect in SMAs.

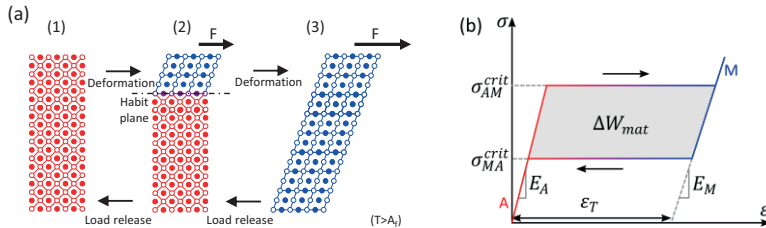


Figure 7 (a) Simplified schematic model of superelasticity in a single crystal SMAs. Austenite is indicated in red, martensite in blue. (b) Schematic superelastic stress-strain curve with the most important superelastic material parameters indicated. For (a) compare [120,p. 17].

In literature, the superelastic effect is also referred to as pseudoelastic effect [46;120,pp. 27–30]. The superelastic effect is illustrated by a simplified model of a single crystal specimen in Figure 7 a). The consideration starts from the stress-free specimen in austenitic state (1). The whole process takes place at temperatures above  $A_f$ . If the specimen is mechanically loaded, at a critical stress, martensite nucleates. Oriented martensite forms according to the direction of the external stress field (2). The transformation proceeds through the propagation of the habit plane between the two phases through the specimen, until the complete specimen is transformed to martensite (3). Upon load removal, in a similar process, austenite nucleates at a second critic stress

and grows as the load is released until the complete sample transformed back to austenite [120,pp. 27–30].

A schematic stress-strain characteristic of a superelastic SMA is illustrated in Figure 7 b). The transformation occurs at critical stresses  $\sigma_{AM}^{crit}$  and  $\sigma_{MA}^{crit}$  for the forward and reverse transformation. The phase transformation takes place at constant stress until the complete specimen is transformed and the martensite is strained elastically. The Youngs modulus of austenite  $E_A$  and martensite  $E_M$  and the transformation strain  $\varepsilon_T$  can also be deduced from stress-strain characteristics of superelastic SMAs to characterize the material behavior.

As indicated in Figure 6 b) the superelastic effect might not only occurs above  $A_f$ , but also in the intermediate temperature range between  $A_s$  and  $A_f$ . The applied stress has to be higher than  $\sigma_{AM}^{crit}$ , however must not surpass the yield stress of austenite to avoid irreversible damage to the SMA. The critical stresses themselves depend on the temperature. The critical stresses of the forward and reverse superelastic transformation increase linearly with the temperature. This can be described by the Clausius Clapeyron relation:

$$\frac{d\sigma}{dT} = -\frac{\Delta S}{\varepsilon_T} = -\frac{\Delta H}{\varepsilon_T T} \quad (\text{II})$$

Here,  $\Delta S$  denotes the entropy change of the transformation and  $\Delta H$  the change in enthalpy [120,p. 25].

In NiTi alloys the recoverable superelastic strain can reach up to 8 % [127]. Today, the main application field of superelastic SMA are biomedical systems as for example self-expandable stents for vascular treatments [123].

Superelasticity is also the physical base of the pronounced elastocaloric effect in SMAs. The phase transformation between austenite and martensite is associated with a change in latent heat. Thus, the latent heat of the phase transformation is released upon forward transformation from austenite to

martensite, and is absorbed upon reverse transformation. If the phase transformation takes place under isothermal conditions, the elastocaloric effect occurs as isothermal entropy change. If the superelastic phase transformation however takes place under adiabatic conditions, the elastocaloric effect manifest as adiabatic temperature change [35;43].

#### 2.2.4 Fatigue in Superelastic SMAs

Elastocaloric cooling puts high demands on the fatigue resistance of the SMAs used as active material. For successful application in an elastocaloric refrigeration device, the SMA has to withstand at least millions of load cycles.

Two sorts of fatigue are distinguished in SMAs, structural and functional fatigue. Structural fatigue describes changes in the SMA's physical integrity. It often proceeds through surface roughening, initiation and propagation of cracks that eventually results in the final fracture of the SMA specimen. Functional fatigue describes the change of functional properties of the SMA with the number of load cycles [128].

Like known from fatigue in structural materials, structural fatigue in SMAs is closely linked to the formation of surface cracks and gradual crack growth [128]. To achieve good structural fatigue, it is important to avoid sites for crack initiation in SMA specimen. Thus, carbides and voids within the SMA specimen and sharp edges as well as roughness at the surface of the specimen have to be avoided [16]. Improved surface roughness can be achieved by mechanical polishing and electropolishing [16;129].

Functional and structural fatigue are connected in SMAs. Functional fatigue leads to surface roughening and in turn allows for crack initiation and structural fatigue [130]. Functional fatigue in superelastic SMA manifests typically in degradation of the superelastic plateau stresses, accumulation of remanent strain and decrease of the latent heat of transformation [128;131]. Accumulation of defects is the reason for fatigue in SMAs. In superelastic SMAs,

the formation of defects is closely related to possibly high mismatch stresses at the interface between austenitic parent phase and the martensite phase that might favor the formation of dislocations. One way to reduce the formation of defects is a suitable microstructure with small grain size and fine coherent precipitates [132–134]. However, in recent years it has been found that a suitable microstructure alone is not sufficient, but in addition the crystallographic mismatch between the two phases has to be reduced to achieve ultra-low fatigue in SMAs. High crystallographic compatibility can be reached if besides volume conservation the middle eigenvalue  $\lambda_2$  of the transformation stretch matrix equals one and the so-called cofactor conditions are met. This is referred to as supercompatibility between phases [135;136]. The meaning of the cofactor condition is illustrated in Figure 8.  $f$  denotes the volume fraction between the two martensite variants illustrated in green and blue. The parent austenite phase is marked in red.  $\det(G_f - I)$  is a measure for the bulk energy in the elastic transition layer between phases and thus for the mismatch stress at the interfaces between the different lattices. In cases b), which is the case for most NiTi SMAs, there are four illustrated possible configurations per twin system that can exist with vanishingly small mismatch stress. If the cofactor conditions are met, there is an infinite number of possible stress-free lattice configurations [136]. This allows for the phase transformation to take place without high mismatch stresses at the interface, and therefore, the main driving force for the formation of defects is eliminated. For detailed information on supercompatibility refer to [135;136].

So far, supercompatibility has been found in two material systems, AuCuZn and TiNiCu(Co) [13;137]. However, in the TiNiCuCo system solely supercompatibility is not sufficient to avoid fatigue under stress-induced superelastic cycling. Upon the stress-induced transformation, defects might not only arise from the mismatch stress at the interface between phases, but also from the externally applied stress field. Thus, additional measures have to be taken. In TiNiCuCo, a suitable microstructure is needed besides supercompatibility for ultra-low fatigue properties [13;138;139]. Both small grain sizes and fine coherent precipitates are beneficial for the fatigue life of TiNiCuCo. Fine  $Ti_2Cu$

precipitates are found to be coherent to the austenite and martensite lattice, and functions as sentinels that ensure complete forward and reverse transformation. If a suitable microstructure and supercompatibility are combined, TiNiCu(Co) can withstand more than  $10^7$  load cycles without signs of degradation [13;136].

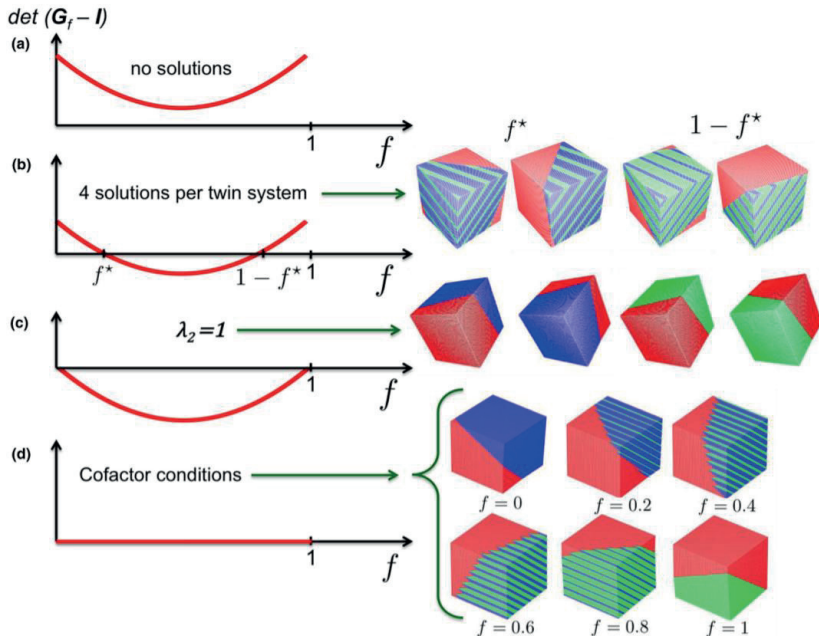


Figure 8 Implications of the cofactor conditions. If the cofactor conditions are met, an infinite number of combinations between the austenite lattice (red) and the two martensite variants (green and blue) exists that have vanishingly small mismatch stress. Figure reprinted from [136], © 2017 Elsevier, use permitted under Creative Commons License (CC BY NC ND).

Besides the very successful application of the theory of supercompatibility to NiTi-based SMAs described above, also other strategies have been pursued

to increase fatigue life of NiTi-based alloys for elastocaloric cooling applications. Reducing the strain amplitude considerably improves the fatigue life in SMAs [128;140]. A similar effect is well known from so called Wöhler curves for structural materials. However, reducing the strain amplitude also decreases the elastocaloric effect [140]. Thus, this approach is of limited use for elastocaloric cooling. A second approach is to utilize compression instead of tension to reach good fatigue performance [141–143]. Structural fatigue resistance is largely increased under compression compared to tension since it delays crack growth. Up to  $7 \cdot 10^7$  load cycles have been reported for NiTi cylinders loaded under compression [142]. Although compression is favorable in terms of fatigue life, it requires bulky sample-geometries to avoid buckling, which in turn is unfavorable for elastocaloric cooling (see chapter 2.3.1 and 4.1.2).

Fatigue resistance of SMA materials is one of the most crucial issues and has to be solved on the way of elastocaloric cooling to successful commercialization. The promising advances in recent years based on the supercompatibility of phases and tailored microstructure in TiNiCu(Co), and also based on compressive loading of NiTi, encouraging that the problem of fatigue in SMA can be solved in future.

### 2.2.5 Elastocaloric Material Properties and Figures of Merit

The most interesting elastocaloric materials known today are superelastic SMAs. The mechanical properties of SMAs are essentially characterized by the critical stresses  $\sigma_{AM}^{crit}$ ,  $\sigma_{MA}^{crit}$  and the transformation strain  $\varepsilon_t$ , which have been introduced in chapter 2.2.3. Another mechanical parameter that is important for all elastocaloric materials is the hysteresis work  $\Delta W_{mat}$ . It is the amount of work needed to drive the elastocaloric cooling cycle once.  $\Delta W_{mat}$  is represented by the area enclosed by the stress-strain curve of the material during a load cycle.

$$\Delta W_{mat} = \oint \sigma d\varepsilon \quad (\text{III})$$

The stress-strain characteristic of SMA is influenced by the strain rate due to the effect of self-heating and cooling. Thus  $\Delta W_{mat}$  is influenced by the strain rate and the thermal connection of the SMA specimen to the environment.

In general, the manifestation of the elastocaloric effect highly depends on the thermal boundary conditions of the elastocaloric specimen during mechanical loading and unloading. Under isothermal conditions, the elastocaloric effect manifests as the isothermal entropy change  $\Delta S_{iso}$ . Quasi-isothermal conditions are obtained at slow strain rates, where time is sufficient for the elastocaloric specimen to exchange heat with the environment fast enough to stay at constant temperature. The isothermal entropy change cannot be measured directly, but so-called indirect or quasi-direct methods can be used to determine it. Indirect methods calculate  $\Delta S_{iso}$  based on Maxwell relations or the Clausius-Clapeyron relation [35]. Quasi-direct methods determine the entropy change based on the temperature-dependent change of heat capacity and heat flux in a DSC measurement [35;43].

However, the adiabatic temperature change  $\Delta T_{ad}$  occurs under adiabatic loading conditions. Quasi-adiabatic conditions are reached for very fast strain rates. In this case, the heat release and absorption are sufficiently fast to suppress relevant heat transfer to the environment and thus the thermal power mainly results in a temperature change of the elastocaloric material itself. The adiabatic temperature change can be measured directly. To do so the temperature of the elastocaloric specimen has to be measured while it is loaded and unloaded mechanically under quasi-adiabatic conditions. Depending on the specimen dimensions adiabatic conditions are hard to achieve, since the velocity of loading / unloading is limited due to experimental restrictions and heat exchange cannot be avoided completely. Thus, the temperature measurement needs to be considered with special attention. Contactless measurement techniques are favorable since they do not alter the thermal boundary conditions of the specimen. If quasi-adiabatic condi-

ons cannot be achieved, the adiabatic limits can also be extrapolated from measurements at medium strain rate [144]. The measurement of temperature changes upon adiabatic load cycling is referred to as direct measurement technique [35].

The adiabatic temperature change, isothermal entropy change and the latent heat of the transformation  $Q_{lat}$  are related through the following simplified equation [35]:

$$\Delta T_{ad} = -\frac{Q_{lat}}{c_p} = -\frac{T \Delta S_{iso}}{c_p} \quad (\text{IV})$$

The specific heat capacity of the elastocaloric material is denoted by  $c_p$ . The latent heat of phase transformation is determined either by using the above equation or is deduced by DSC measurements. However, the phase transformation in the DSC-based measurement technique is thermally induced, whereas the transformation in an elastocaloric cycle is stress-induced. The  $Q_{lat}$  of the stress-induced transformation might only represent a fraction of the  $Q_{lat}$  of the thermally induced transformation. At the end of the stress plateau the stress-induced transformation might appear to be complete, but still austenite exists that does not contribute to latent heat of the transformation [145;146]. Therefore, values of  $Q_{lat}$  calculated from direct measurements tend to be lower compared to DSC-based values. To improve the measurement technique of the elastocaloric effect and to bridge this gap in future, recently a new measurement technique has been developed. The new technique calculates the latent heat based on Joule heating that results in a similar temperature evolution of the elastocaloric specimen during loading or that cancels the elastocaloric cooling effect during unloading [147].

To describe the efficiency of the elastocaloric effect in a material, the material coefficient of performance  $COP_{mat}$  is defined:

$$COP_{mat} = \frac{Q_{lat}}{\Delta W_{mat}} \quad (\text{V})$$

It relates the heat absorbed by the elastocaloric material during a load cycle to the hysteresis work applied. An ideal elastocaloric material absorbs a high amount of heat and at the same time does not require much mechanical work. A COP normally relates to a thermodynamic process cycle. However, the above definition is not always used in this way. Therefore, it was suggested to refer to it as “materials efficiency” rather than COP [35], or, to define the COP based on a reverse Sterling or reverse Brayton cycle [30;148]. Although the above definition is under discussion, none of the alternative approaches has been accepted and the above definition still is widely used in the field of elastocaloric cooling and also in this work. Nevertheless, different  $COP_{mat}$  values from literature should be compared with caution. A direct comparison can only be recommended for values obtained under similar conditions.

### 2.2.6 Elastocaloric Materials

In the 19<sup>th</sup> century, Gough and Joule discovered temperature changes in rubber, metals and wood upon mechanical load cycling at room temperature [17;18]. Binary NiTi SMA, the benchmark elastocaloric material today [30], was already reported in 1963 [149]. Although the physical background of the elastocaloric effect in SMAs was known for a long time, it was not until the 21<sup>st</sup> century that the use of the elastocaloric effect for heat pumping and refrigeration has been proposed [26;28].

Elastocaloric cooling puts high demands on the used elastocaloric materials (eCM). The eCM needs to combine high elastocaloric effect size ( $\Delta T_{ad}$ ,  $\Delta S_{iso}$ ,  $Q_{lat}$ ) with a low mechanical work input  $\Delta W_{mat}$  to achieve a high elastocaloric materials efficiency  $COP_{mat}$ . In addition, eCMs need superior fatigue properties to withstand millions of load cycles without functional or structural degradation [16]. Furthermore, high thermal conductivity is desirable and the elastocaloric properties need to persist over a large temperature range [43].

Today, SMAs are the most promising group of elastocaloric materials. Suitable SMAs for elastocaloric applications can be divided into NiTi-based, Cu-based, Fe-based alloys, as well as magnetic SMAs [43;105]. To give a brief overview, elastocaloric materials are listed in Table 1 with their most relevant properties. For a more detailed review, refer to [43;105;150]

Table 1 Elastocaloric properties of selected materials suitable for elastocaloric cooling near room temperature. Only polycrystalline materials have been considered. The measurement technique the values are based on is indicated. Numbers in brackets have not been stated in the original work, but have been approximated with the help of equation (IV). Temperature of the investigation  $T$ ; adiabatic temperature span  $\Delta T_{ad}$ ; iso-thermal entropy change  $\Delta S_{iso}$ ; latent heat of transformation  $Q_{lat}$ .

Material composition	specimen geometry	$T / \text{K}$	$\Delta T_{ad} / \text{K}$	$\Delta S_{iso} / \text{Jkg}^{-1}\text{K}^{-1}$	$Q_{lat} / \text{Jg}^{-1}$	Reference
Cu <sub>68</sub> Zn <sub>16</sub> Al <sub>16</sub>	ribbon	300	6 <sup>d</sup>	18 <sup>i</sup>	(5.4 <sup>j</sup> )	[151]
Ni <sub>50</sub> Ti <sub>50</sub>	wire	295	+25/-17 <sup>d</sup>	(41 <sup>q</sup> )	12 <sup>q</sup>	[152]
Ni <sub>50</sub> Ti <sub>50</sub>	film	295	+17/-16 <sup>d</sup>	(68 <sup>q</sup> , 24 <sup>d</sup> )	20 <sup>q</sup> , 7.2 <sup>d</sup>	[153]
Ni <sub>45</sub> Ti <sub>47.25</sub> Cu <sub>5</sub> V <sub>2.75</sub>	ribbon	295	21 <sup>d</sup>	(31 <sup>q</sup> )	9.2 <sup>q</sup>	[154]
Ti <sub>54.7</sub> Ni <sub>30.7</sub> Cu <sub>12.3</sub> Co <sub>2.3</sub>	film	293	+7.5/-10.2 <sup>d</sup>	39 <sup>i</sup>	7.9 <sup>q</sup> , 8.2 <sup>i</sup>	[155]
Fe <sub>49</sub> Rh <sub>51</sub>	ribbon	311	5 <sup>d</sup>	13 <sup>d</sup>	4.1 <sup>d</sup>	[22]
Ni <sub>45</sub> Mn <sub>44</sub> Sn <sub>11</sub>	rod	292	6 <sup>d</sup>	31 <sup>q</sup>	8.4 <sup>q</sup>	[156]
Ni <sub>50</sub> Mn <sub>31.5</sub> Ti <sub>18.5</sub>	rod	295	31.5 <sup>d</sup>	45 <sup>i</sup>	(13.3 <sup>j</sup> )	[157]
Natural Rubber	sheet	283	12 <sup>d</sup>	44 <sup>i</sup>	13 <sup>i</sup>	[158]

<sup>i</sup> indirect measurement technique;

<sup>d</sup> direct measurement technique;

<sup>q</sup> quasi-direct measurement technique

(or calculated from measurements performed with the indicated measurement technique)

NiTi-based SMAs are the most widespread in elastocaloric cooling devices, due to their high elastocaloric effect size and their brought availability. Binary NiTi alloys reach high adiabatic temperature changes of 25 K and reach large latent heat of transformation up to 30 J/g [12;152]. Alloying of binary NiTi with Cu, Co, Fe, Cr, V is used to tailor transformation temperatures and material properties [12;154;155]. Two recent research trends in NiTi-based SMAs are very promising for elastocaloric cooling applications. NiTi-based SMA films alloyed with Cu and Co have been developed that show ultra-low fatigue properties, and withstand more than 10 million load cycles without degradation. In addition, they show good elastocaloric performance [13;155]. The ultra-low fatigue properties in these alloys are reached by highly compatible phases of austenite and martensite and a tailored microstructure [136]. The fabrication technique allows the precise tuning of chemical composition and allows even to fabricate gradients of the transformation temperature within one single specimen [159]. As these results show, the high demands on the fatigue properties of elastocaloric materials can be met by SMAs. The second recent trend in SMA materials science and production engineering highly relevant to elastocaloric cooling is additive manufacturing. The new fabrication technology has been successfully applied to NiTi-based SMAs [143;160;161]. This will allow to fabricate completely new specimen geometries in future that might combine highly efficient heat transfer with an easy application of a uniform stress profile not only in tension but also in compression.

Cu-based SMAs generally have a lower critical stress than NiTi-based alloys and show a high thermal conductivity. In single crystal CuZnAl adiabatic temperature changes up to 15 K have been reported [26], however, in polycrystal specimen  $\Delta T_{ad}$  is found to be around 6 K [151].

Fe-based SMAs like FeRh reach adiabatic temperature changes of 5 K and show not only a elastocaloric but also a magnetocaloric effect. Thus, they might be of interest to multicaloric cooling cycles [22]. The need for highly expensive components like Pt and Rh prevent a wide spread application.

Magnetic SMAs, so called Heusler alloys, combine elastocaloric and magnetocaloric properties as well. Heusler alloys like  $\text{Ni}_{45}\text{Mn}_{44}\text{Sn}_{11}$  reach adiabatic temperature changes of 6 K [156]. Recently a  $\text{Ni}_{50}\text{Mn}_{31.5}\text{Ti}_{18.5}$  alloy has been reported that reaches a adiabatic temperature as high as 31.5 K [157]. Nevertheless, the brittleness of magnetic SMA has hindered their use in an elastocaloric cooling device so far.

Apart from SMA-based systems, the elastocaloric effect was found in a wide range of material systems, as e.g. in ferroelectric ceramics [81;162], CNTs and graphene [163;164], in liquid crystals [165], and rubbers [100;101;106]. However, of all these alternative material systems, only rubber appears to be a viable option for elastocaloric applications in the near future due to its promising elastocaloric performance, broad availability and low cost. Natural rubber shows adiabatic temperature changes of up to 12 K [158]. Recently a first elastocaloric cooling device based on rubber has been reported [166].

## 2.3 Engineering of Elastocaloric Cooling Devices

In order to provide useful cooling capacity, elastocaloric cooling devices have to fulfill several tasks. The device has to apply an oscillating stress field to the elastocaloric element to repeatedly trigger the elastocaloric effect. In addition, the heat released in the material during loading has to be transferred out of the elastocaloric element (hot heat flow) and the heat absorbed during unloading has to be transferred back into the element (cold heat flow). Furthermore, the resulting hot and cold heat flow have to be separated outside the elastocaloric element. This is very important to avoid that the elastocaloric heating equals the cooling. The cold heat flow can then be used to provide useful cooling capacity based on the elastocaloric effect. In the following chapter the different possible mechanical loading states and mechanisms for heat transfer and separation of hot and cold heat flow in elastocaloric cooling devices are discussed. In addition, the two concepts of work and heat recovery are discussed. The basic concept of SMA film-based elastocalo-

ric cooling is presented. Figures of merit of elastocaloric cooling devices are introduced.

### 2.3.1 Mechanical Loading States of SMAs for Elastocaloric Cooling

The reversible application and release of a uniaxial stress field above  $\sigma_{AM}^{crit}$  and below  $\sigma_{MA}^{crit}$  in SMAs triggers the elastocaloric effect and thus is the basis for the elastocaloric cooling cycle. Different mechanical load cases are suitable to achieve the required stress levels. In general, tensile and compressive forces can be used as well as bending and torsion. Hydrostatic pressure triggers the barocaloric effect, which is closely related to the elastocaloric effect, but not the focus of this work (see chapter 2.1.4). In case of bending and torsion, a non-uniform stress profile arises in the SMA element with maximum stress at the outer surface and a line of zero stress in the element. As a result, the SMA element undergoes phase transition only partly under bending and torsional load. The elastocaloric effect per total volume of SMA is reduced. In case of pure compressive or tensile loading, the stress level in the whole SMA element is uniform. The complete element contributes to the elastocaloric effect. In consequence compressive and tensile loading is favored. Whether compressive or tensile loading are better suited for elastocaloric cooling is under ongoing discussion in research.

The main advantages of compressive stress is that the hysteresis work can be reduced compared to tensile stress, and a higher  $COP_{mat}$  can be reached therefore [142;152]. In addition, compressive loading is favorable over tensile loading in terms of fatigue life [141;142]. The main disadvantage of compressive stress is the need for bulky SMA geometries to prevent buckling. In consequence, geometries suited for loading with compressive stress are mostly bulky with a low surface-to-volume ratio. This restricts the heat transfer from the SMA to the surroundings that is of major importance in elastocaloric cooling (see also chapters 2.3.2 and 4.1.2). A geometry suitable for compressive loading that also provides a good heat transfer and surface-to-

volume ratio will always be a compromise [167]. This leads directly to the main advantage of tensile loading of SMA elements for elastocaloric cooling. In case of SMA elements loaded under tensile stress, less restrictions apply to the geometry. Thin films and wires with high surface-to-volume ratio can be used, which enables fast heat transfer being crucial for elastocaloric cooling [16].

In case of a thin film geometry, there is a second mode of load application possible besides the known loading in direction of the geometrical long axis. This is referred to as in-plane loading in this work (see Figure 9). The second mode describes loading in perpendicular direction to the film surface in out-of-plane direction with the two ends of the film fixed. In this case, bending stress would be dominant for bulky geometries, whereas in film samples forces are predominantly tensile. Due to the small thickness, bending stress can be neglected and almost pure tension occurs in the film. The geometrical relations between the angle  $\alpha$ , the deflection height  $\Delta h$ , the initial length of the film  $l_0$  and the strain  $\varepsilon$  are as follows:

$$\Delta h = 1/2 l_0 \sqrt{(1 + \varepsilon)^2 - 1} \quad (\text{VI})$$

$$\varepsilon = \sqrt{1 + (\Delta h/l_0)^2} - 1 \quad (\text{VII})$$

$$\cos \alpha = \frac{1}{1 + \varepsilon} \quad (\text{VIII})$$

Figure 9 shows the force-displacement characteristics that follow from the same schematic material behavior in case of in-plane loading and out-of-plane deflection.

Clearly, the deflection or displacement is higher and the maximum force is lower in case of out-of-plane deflection. Out-of-plane deflection reduces the maximum forces needed to load a SMA element in a simple manner and thus reduces the requirements on the actuation unit. A similar concept for the mechanical loading of bulk samples can be found in [168]. Out-of-plane deflect-

ion allows to combine the loading of a SMA film with heat switching, reducing the complexity of film-based elastocaloric cooling devices considerably.

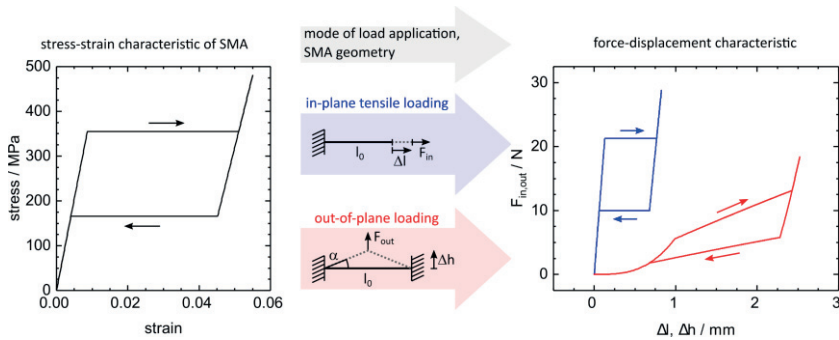


Figure 9 The force-displacement characteristic of a SMA originates from its stress-strain characteristic, its geometry and also the mode of load application. Here, a schematic stress-strain characteristic is shown in combination with the resulting force-displacement characteristics for loading in-plane and out-of-plane.<sup>d</sup>

### 2.3.2 Heat Transfer and Separation of Heat Flows in Caloric Systems

In a vapor compression cycle, the fluidic refrigerant releases heat in the condenser and absorbs heat in the evaporator. Heat absorption and release take place at two physically separate sites. Therefore, hot and cold heat flows can easily be separated in a vapor compression cycle-based refrigerator. In caloric cooling systems, heating and cooling take place at the same position in the solid caloric material element. The heat release and absorption are separated in time, not in space. Heat release in the caloric element gives rise to a hot

<sup>d</sup> Material properties are based on NiTiFe presented in chapter 3.2. For clarity, a simplified, schematic stress-strain characteristic is used here. Following geometry is assumed:  $l_0$ : 15 mm, thickness: 30  $\mu\text{m}$ , width: 2 mm.

heat flow out of it. Heat absorption in the caloric materials results in a cold heat flow into it. To utilize the cold heat flow for refrigeration, two things have to be achieved. First, the heat generated during the field application has to be transferred out of the material and the heat absorbed during the field removal has to be transferred back into the caloric material. Otherwise, the heating and cooling effect would cancel. Secondly, the generated hot and cold heat flows must be separated from each other outside the caloric material. The hot heat flow can be transferred to environment and the cold heat flow can be utilized for refrigeration. Concepts for efficient heat transfer and the separation of the cold and hot heat flow form the heart of every caloric cooling system. In Table 2 possible modes of heat transfer and mechanisms to separate the hot and cold heat flows are summarized.

Heat conduction within the caloric material and the thermal resistance at the surface of the caloric specimen are the two dominant effects that determine the heat transfer out of the material. The heat conduction within the specimen depends mainly on the thermal conductivity of the caloric material and the geometry, especially thickness and surface-to-volume ratio. The resistance at the surface depends on the surface area and the surface heat transfer coefficient and in turn depends on the selected mode of heat transfer. For the heat transfer at the surface of the caloric specimen different processes can be used. In the following each mode of heat transfer will be assigned a short code b1 to b4, an overview is given in Table 2 and in chapter 2.4.1. The mechanical contact between two solid surfaces can be used for heat transfer (b1) [14;32;39;89;169;170]. Furthermore, convective heat transfer to a liquid heat transfer fluid (HTF) (b2), or a gas phase HTF (b3) can be used [31;39;171–173]. In cases b2 and b3 heat transfer changes the temperature of the HTF, thus, the sensible heat of the HTF is changed. However, heat transfer between the SMA and the HTF might also evaporate or condensate the HTF under special conditions (b4). In this case, the latent heat of the HTF changes instead of the sensible heat. In such a system, heat is transported via the material-bound transport of latent heat of the working fluid. For the operation the working fluid has to be kept under conditions similar to the ones in a

heat pipe. The working fluid must coexist in liquid and gaseous state at a pressure near to its saturation pressure [174;175].

If heat transfer is accomplished through one of the concepts described above, the hot and cold heat flow have to be separated. Following concepts might be used to achieve this:

- Changing contact conditions of the caloric material and additional elements (c1) [14;32;39;89;169].
- Relative motion between the caloric element and additional solid elements or an HTF (c2) [31;39;171–173;175;176].
- Thermal diode elements that allow only heat flows in one direction (c3) [49;65;177]. Thermal diodes allow a heat flow in one direction but function as a thermal insulator in the opposite direction [178].

In Table 2 concepts are illustrated that combine a heat transfer mode with a mechanism for the separation of hot and cold heat flows. Only concepts that have been used or proposed in the field of caloric refrigeration are presented.

In the first concept (b1-c1) heat is transferred through conductive heat transfer between solid elements and the hot and cold heat flow is separated by changing contact conditions between the caloric material and a separated heat sink and heat source. A heat sink is brought in contact when heat is released and absorbs the hot heat flow. The contact is then broken subsequently and contact is made with a heat source, from which the cold heat flow is absorbed [14;16;32;39;89;169].

The concept (b1-c2) works similar. However, no mechanical contacts are cyclically interrupted or re-established, but the contact is maintained and the caloric material is moved relative to an element known as a regenerator, in which a temperature gradient is established in this way [176].

Thermal diode elements that are inserted between the caloric element and the heat sink and source direct the heat flows through their inherent

properties (b1-c3) [49;65;177]. The concept itself is simple. The caloric material is coupled to two thermal diode elements on two sides of the caloric material that ensure a directed heat flow from the heat source to the caloric element and from there to the heat sink. The main challenge in this concept is the acquisition or development of efficient thermal diodes [178].

The separation can also be accomplished by relative motion between the caloric material and an HTF in combination with convective heat transfer. Heated HTF is pumped to one side in the direction of a hot heat exchanger (HHEX) or heat sink and cooled HTF is pumped to the opposite side to a cold heat exchanger (CHEX) or heat source. Liquid phase HTFs (b2-c2) [39;171] or gas phase HTFs (b3-c2) [31;172;173] can be used.

Concept (b4-c2) works similar, however, the heat is not transferred to the sensible heat of the HTF, but is transferred to the latent heat of the HTF and forces a phase transition in the HTF. When the temperature in the caloric material decreases due to the caloric effect, gaseous HTF condensates on the surface of the caloric material and thus the condensation heat is transferred to the caloric material. When the caloric material heats up due to the caloric effect, the liquid HTF on the surface of the caloric material evaporates and the heat of evaporation is absorbed. In such a system, the heat transfer is coupled to the latent heat of the gaseous HTF. Heat transport from a heat source to a heat sink is achieved through a mass flow of gaseous HTF. Therefore, the mass flow of HTF has to be directed from the heat source, where the HTF evaporates, to the heat sink, where the HTF condensates [175]. If the reader intends to deepen the subject, he is referred to [178;179].

Table 2 Categorization of possible modes of heat transfer and separation of hot and cold heat flows in a caloric refrigeration device with associated illustration. Five schematic concepts to achieve the separation of heat flows in caloric devices that have been demonstrated or proposed in literature are presented. HTF denotes heat transfer fluid. Naming b1 to b4 and c1 to c3 is chosen with reference to Figure 13.

Concept for heat transfer	Concept for separation of heat flows	Absorbing heat from heat source (cold heat flow)	Illustration	Reference
solid to solid (b1)	changing contact conditions (c1)			[14;16;32;39;89;169], this work
solid to solid (b1)	relative movement (c2)			[176]
solid to solid (b1)	thermal diodes (c3)			[49;65; 177]
solid to sensible heat of liquid phase (b2), or gas phase (b3) HTF	relative movement (c2)			[31;39;171–173]
solid to latent heat of HTF (b4)	relative movement (c2)			[175]

### 2.3.3 Work Recovery

When a SMA element is mechanically loaded and unloaded, it can be considered as a nonlinear, hysteretic spring. This comparison suggests that the SMA can perform work when unloaded. The loading work ( $W_{load}$ ) partly is dissipated by the SMA ( $\Delta W_{mat}$ ) and partly is stored elastically ( $W_{el}$ ,  $W_{load} = \Delta W_{mat} + W_{el}$ ). The introduced works are illustrated as areas in Figure 10 a) and b for better understanding. The dissipated work  $\Delta W_{mat}$  is referred to as hysteresis work. Upon unloading, the SMA element can perform the elastically stored work  $W_{el}$ . However, a suitable mechanism must be in place to recover this work. For the efficient operation of an elastocaloric refrigerator, the recovery of  $W_{el}$  is essential [148;169]. To recover the released mechanical work, it either has to be used directly, or it has to be stored. The storage of the mechanical work could be achieved by transferring it to a mechanical energy storage device such as a mass flywheel or a spring. Furthermore, it could be transferred to electrical energy by using the mechanical work to drive an electrical generator. The released work can also directly be used to help loading a second SMA element [15;148;169]. This is referred to as antagonistic coupling [32,pp. 157–160;169]. The concept benefits from its simplicity and effectiveness and avoids additional energy conversions that again are subjected to losses. Thus, in this work, work recovery (WR) based on the antagonistic coupling of two SMA elements has been selected. In consequence this chapter also focuses on antagonistic coupling.

To achieve WR through antagonistic coupling two SMA samples have to be connected and the point of force application has to be at the connection (see schematics in Figure 10). In addition, the two samples have to be pre-strained with respect to each other. Four different cases of antagonistic WR are illustrated in Figure 10. They differ in the mode of load application and the pre-strain conditions. Sample geometry and SMA properties are the same for all

cases<sup>e</sup>. Firstly, the force-displacement curves without WR are illustrated for in-plane loading (a) and out-of-plane loading (b). This allows for later comparison and evaluation between the cases with and without WR. In WR-cases (c) and (e) load is applied to the antagonistic pair in-plane direction. WR-cases (d) and (f) load is applied out-of-plane. Two different pre-straining conditions are used. In (c) and (d) pre-straining is performed in a way that if one specimen is loaded completely, the second is unloaded completely. The two matched strains are highlighted by circles. In cases (e) and (f) the SMA elements are cycled between the end points of the superelastic plateaus in forward and reverse direction (highlighted by stars). In this case, both SMA elements stay within the SMA superelastic plateau region, and are never fully released.

In Figure 10, for all four discussed WR-cases, the force-displacement curves are shown for the single SMA elements and the coupled characteristic. Like for the single element in (a) and (b), for the coupled characteristics the loading work  $W_{load}$ , the hysteresis work  $\Delta W_{mat}$ , and elastically stored work  $W_{el}$  are illustrated. In the coupled characteristics the equilibrium position, where the system rests without applied force, is not clearly defined. Comparing the single force-displacement characteristic in (a) and (b) to the coupled ones in (c)-(f), one has to keep in mind that the single ones are for one SMA element and the coupled ones are for two SMA elements of the same size. In Table 3 numbers are given for  $W_{load}$ ,  $\Delta W_{mat}$ ,  $W_{el}$  in the cases (a) to (f). In addition, fractions  $f_{load}$  and  $f_{el}$  are given that report how much of the loading work without WR ( $W_{load}^{w/o}$ ) is saved by WR, and how much of the elastically stored work in the case without WR ( $W_{el}^{w/o}$ ) is saved by WR, respectively.

---

<sup>e</sup> Material properties are based on NiTiFe presented in chapter 3.2. For clarity, a simplified, schematic stress-strain characteristic is used here. Following geometry is assumed:  $l_0$ : 15 mm, thickness: 30  $\mu\text{m}$ , width: 2 mm.

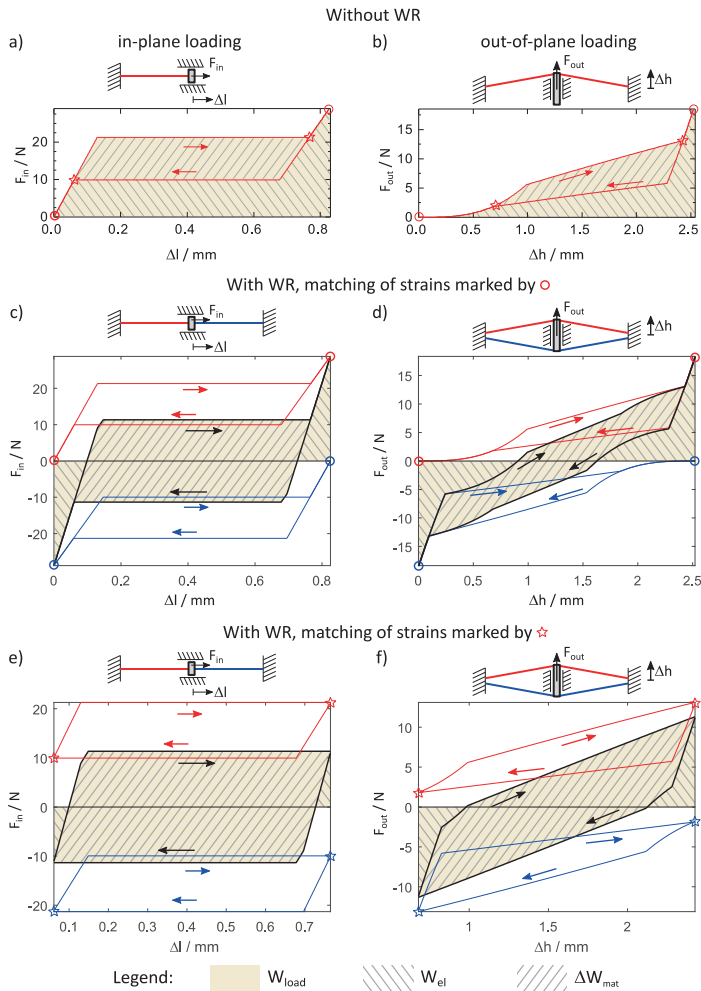


Figure 10 Force-displacement characteristics of a single SMA element (a,b) and antagonistic coupled SMA elements (c-f). Antagonistic coupling is used for work recovery (WR). Each characteristic (c) - (f) represents a different WR case. The force-displacement characteristic of each single SMA element (blue, red) is given in combination with the coupled characteristic (black). The in-plane and out-of-plane loading conditions are indicated by schematics. Strains in the two coupled elements that are matched by pre-straining are indicated by circles and stars. For each characteristic, loading work  $W_{load}$ , hysteresis work  $\Delta W_{mat}$  and elastically stored work  $W_{el}$  are indicated.

The schematics and numbers show that  $W_{load}$  is influenced by the antagonistic coupling and also the pre-strain conditions. Generally, WR reduces  $W_{load}$ . This is also represented in the numbers of  $f_{load}$  that report a reduction of  $W_{load}$  by 25 % or even by 50 % in case (d) and (e), respectively. However,  $\Delta W_{mat}$  is constant, since the work dissipated within the SMA's full superelastic hysteresis is an intrinsic material property, and does not depend on external loading conditions.  $\Delta W_{mat}$  is the least amount of work needed for load cycling.  $W_{el}$  is largely reduced by the antagonistic coupling. This proves the effectiveness of the introduced WR cases. Under ideal WR conditions, the complete  $W_{el}^{w/o}$  would be recovered, and thus  $f_{el} = 1$  would apply. In the presented WR-case (e), almost the complete  $W_{el}^{w/o}$  is recovered with  $f_{el} = 0.97$ , which is near to ideal case. However, in case (d) only  $f_{el} = 0.44$  could be achieved, which means that 56 %  $W_{el}^{w/o}$  are not recovered.

The presented numbers show that WR by antagonist coupling can be a highly efficient mechanism, but its efficient depends on the exact implementation. WR is more efficient in the case of in-plane loading compared to out-of-plane loading. In addition, it becomes obvious that the amount of pre-straining has a high influence on the effectiveness of the concept. E.g., in out-of-plane loading,  $f_{el}$  increases from 0.44 (case d) to 0.84 (case f) simply by changing the pre-strain conditions. It is beneficial to pre-strain the antagonistically coupled system in a way that both SMA elements are never fully unloaded, and both are cycled within the range of the superelastic plateau, as done in cases (e) and (f). In addition, maximum forces are reduced by WR in this case of pre-straining.

Table 3 Overview on the work needed to load two SMA elements ( $\mathbf{W}_{load}$ ) in the loading cases (a) to (f). In addition, hysteresis work ( $\Delta\mathbf{W}_{mat}$ ) and the elastically stored work  $\mathbf{W}_{el}$  are given.  $f_{load}$  states the fraction of  $\mathbf{W}_{load}$  that is recovered by WR. The fraction  $f_{el}$  shows, how much of  $\mathbf{W}_{el}$  is recovered for the different WR cases. The cases (a) to (f) are illustrated in Figure 10.

Case (see Figure 10)	$\mathbf{W}_{load}$ / mJ	$\Delta\mathbf{W}_{mat}$ / mJ	$\mathbf{W}_{el}$ / mJ	$f_{load} =$ $\frac{\mathbf{W}_{load}^{w/o} - \mathbf{W}_{load}^{WR}}{\mathbf{W}_{load}^{w/o}}$	$f_{el} =$ $\frac{\mathbf{W}_{el}^{w/o} - \mathbf{W}_{el}^{WR}}{\mathbf{W}_{el}^{w/o}}$
(a), without WR, in-plane loading	32.82	14.22	18.6	-	-
(b), without WR, out-of- plane load- ing	32.82	14.22	18.6	-	-
(c), with WR, in-plane loading	17.06	14.22	2.84	0.48	0.85
(d), with WR, out-of-plane loading	24.62	14.22	10.4	0.25	0.44
(e), with WR, in-plane loading	14.63	14.22	0.41	0.55	0.97
(f), with WR, out-of-plane loading	16.61	14.22	2.39	0.49	0.87

To sum up, in this showcase, WR by antagonistic coupling can reduce the required work input by up to 50 %. The precise numbers depend on the direction of load application and on how pre-straining is performed. Besides that, the material parameters have an influence, what is not further investigated here. The presented numbers show the significant influence of WR on the efficiency of a complete cooling system. The efficiency of a refrigerator normally is given by its coefficient of performance COP (see chapter 2.3.6). If the work input can be cut by 50 % as shown above, the COP would double as an

effect of the WR. However, one has to note that at the current state of research, the work input for the COP calculation is often directly calculated from force-displacement characteristics by integration (compare equations (XIII) to (XV)). By this method, full work recovery is automatically assumed, and therefore, the integration of WR in elastocaloric cooling devices does not influence COP values derived by the described method.

### 2.3.4 Heat Recovery

Besides WR, heat recovery (HR) is another general concept that can increase efficiency of elastocaloric refrigerators. Furthermore, HR can also increase the maximum temperature span of a refrigerator. The concept of active regeneration, known from magnetocaloric refrigeration and also from first elastocaloric refrigerators [172;180], is a special case of HR. To understand the concept of HR one has to take a closer look at a reverse Brayton cycle that is applied to the caloric material in a caloric refrigerator (Figure 11 a). In steps (1-2) and (3-0), heat is transferred to a thermal heat sink and from a thermal heat source, respectively. The device temperature difference  $\Delta T_{device}$  is the difference between the sink and source temperatures. Assuming a temperature difference larger than zero, not the complete heat released in the caloric material can be used, since heat can only be transferred as long as the temperature of the caloric material is higher than the temperature of the heat sink (red area in Figure 11 a). Therefore, the heat marked by the grey area cannot be transferred to the heat sink. The same applies during heat absorption. Heat can only be absorbed by the caloric material as long as the temperature is lower than the temperature of the heat source. The rest of the released and absorbed heat cannot be used. HR uses heat that cannot be used to heat and cool the heat sink and source (grey) to pre-cool and pre-heat the caloric material in an intermediate HR-step. Before heat release and absorption due to the caloric effect takes place in steps (0-1) and (2-3), the caloric element is pre-heated and pre-cooled in the HR-step (see Figure 11 c). In this way a portion of the lost heat marked in grey is recovered, what gives the concept its name. For better understanding the temperature evolution of

the caloric element during an idealized cycle is shown in Figure 11 b) without and in Figure 11 c) with a heat recovery step. In general, heat recovery may be used to either increase the efficiency of a system or to increase the temperature span of the device on the cost of efficiency.

HR can be incorporated in systems in different ways. For HR a portion of the heat released during step (1-2) for pre-heating before the temperature change in step (0-1) and a portion of the heat absorbed during step (3-0) for pre-cooling of the caloric element before step (2-3). To do so, heat must be stored temporarily in an additional element, called regenerator. A solid element might be used as regenerator [176], or a heat transfer fluid (HTF) might cover this function. Two different concepts to accomplish HR based on an HTF can be found in literature. An additional fluidic cycle can be designed [181] or the concept of active regeneration can be used [172]. In active regeneration, the separation of heating and cooling heat flows and the pre-heating and -cooling of the caloric element and thus HR are closely linked and cannot be clearly separated.

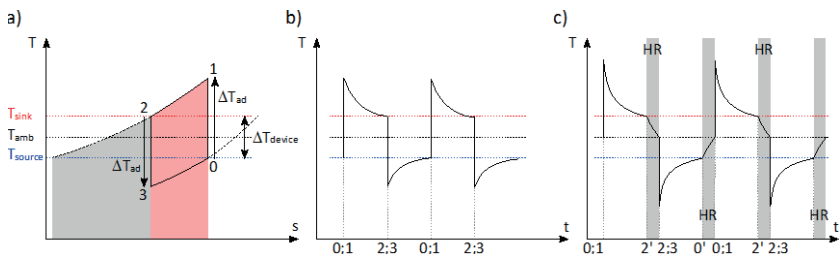


Figure 11 The concept of heat recovery (HR) uses a portion of the heat that is released and absorbed due to the elastocaloric effect internally to pre-heat and pre-cool the caloric element. (a) In the reverse Brayton cycle of a system without HR, not all the heat released during the field application (0-1) can be released to the heat sink, but only the heat represented by the red area. The heat marked as grey area cannot be transferred, since the temperature of the element is lower than the temperature of the heat sink. HR uses a portion of the otherwise unused heat (grey) to pre-heat the caloric element before the next field application occurs (0-1). In case of heat absorption from the heat source (3-0), the concept works similar and the caloric element is pre-cooled before field removal (2-3). (b) Temperature evolution of the caloric element without HR, and with HR (c).

### 2.3.5 The Elastocaloric Cooling Cycle in SMA Film-Based Devices

In this chapter the operation principle of SMA film-based elastocaloric cooling devices is presented in detail based on the concepts introduced previously. The concept relies on out-of-plane loading of SMA films (see chapter 2.3.1), solid-to-solid heat transfer and separation of the hot and cold heat flow by changing contact conditions (concept b1, chapter 2.3.2). In Figure 12 a schematic elastocaloric cooling cycle is shown in combination with its implementation in a simple SMA film-based device. The setup consists of four main components: most important the elastocaloric element (in this case a SMA film) a solid heat sink, a solid heat source, and an actuation unit, here indicated by the arrows. The SMA film is fixed at both ends and fixed the actuation unit in a way that keeps the ends of the film at constant distance. This allows for actuation by out-of-plane loading. The heat sink and source elements

alternately are brought in contact with the SMA film during operation. Direct solid-to-solid contact allows for efficient heat transfer. The heat sink has a triangular shaped surface that loads the SMA film by out-of-plane loading when both are pressed onto each other. The heat source has a flat surface, to which the SMA film is brought in contact in a low stress state to absorb heat from. The concept described here is based on previous work at KIT (compare chapter 2.4.3) [14;32;169].

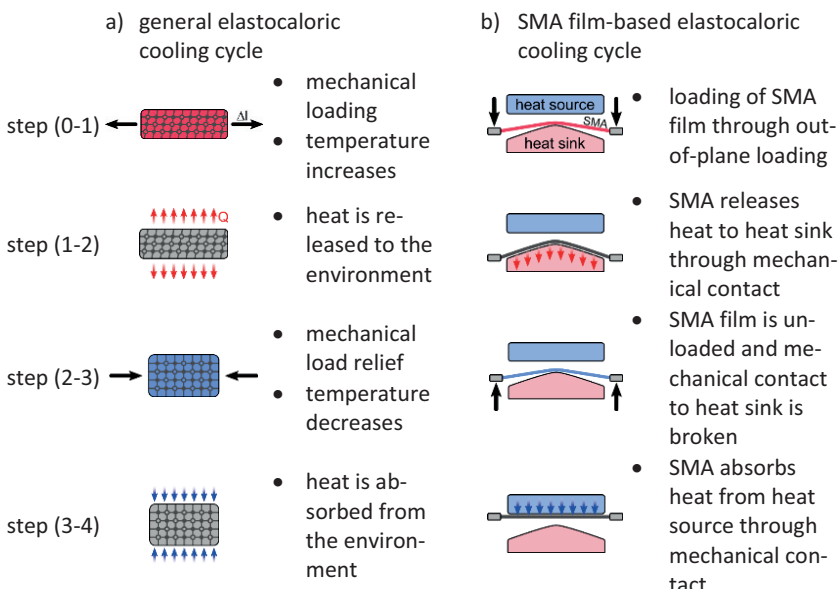


Figure 12 General elastocaloric cooling cycle with four steps (a) and implementation of the steps in the particular case of a SMA film-based elastocaloric cooling device (b).

To operate the setup, the SMA film first is moved in the direction of the heat sink and pressed onto its surface (step 0-1). In this way the SMA film is loaded and simultaneously brought in contact with the heat sink. The latent heat of the transformation is released, and heats up the SMA film. Heat is transferred via the mechanical contact to the heat sink (step 1-2), as long as the contact

is maintained. With increasing holding time, the system moves towards a thermodynamic equilibrium state. Hereafter, the SMA film is moved to the opposite direction (step 2-3). The load is released, and the reverse transformation takes place. The latent heat of the transformation is absorbed within the SMA film, cooling it. This allows the SMA film to absorb heat from the heat source, it is brought in contact with (step 3-4). The process can be compared to the reverse Brayton cycle (see Figure 2 b).

The film geometry features a high surface-to-volume ratio of the SMA and thus results in an efficient heat transfer compared to bulk geometries. The separation of the hot and cold heat flow is accomplished by the changing contact conditions of the film and the sink and source surfaces. In this configuration, only one actuator is needed for both, alternating the contact conditions and the cyclic loading of the SMA. The simple system configuration is favorable for application and miniaturization. This concept is the base of SMA film-based elastocaloric cooling in this work.

### 2.3.6 Figures of Merit of Elastocaloric Refrigerators

The main parameters needed to characterize the performance of an elastocaloric refrigerator are the temperature span the refrigerator can achieve, the cooling capacity, and its efficiency. However, all these figures depend on each other. E.g., a typical device will have a much higher cooling capacity, when operated at a low temperature span, compared to the cooling capacity at a higher device temperature span. For this reason, limit values of the introduced main parameters will be used as figures of merit. These limit values are not able to describe the refrigeration performance at all operating points. Nevertheless, they are well suited to highlight potentials and limits of an elastocaloric refrigerator. In the following, these figures of merit are introduced one by one.

The maximum temperature span of an elastocaloric refrigerator  $\Delta T_{device}$  can be determined as the difference between the temperatures of the heat sink

$T_{sink}$  and heat source  $T_{source}$  under steady-state conditions (i.e., when the device reaches saturation) with no thermal load applied. If saturation cannot be reached the maximum values can be used instead.

$$\Delta T_{device} = T_{sink} - T_{source} \quad (\text{IX})$$

$$\Delta T_{device}^{cool} = T_o - T_{source} \quad (\text{X})$$

$\Delta T_{device}$  cannot fully be used for cooling, thus the maximum device temperature span available for cooling  $\Delta T_{device}^{cool}$  is important as well. For  $\Delta T_{device}^{cool}$  the difference of  $T_{source}$  and the temperature of the reservoir that absorbs the waste heat of the system  $T_o$  is used. For refrigerators operating at room temperature, as the devices developed in this work,  $T_o$  can be considered equal to room temperature. If the heat sink and source do not have a uniform temperature distribution, the values obtained by this method might be influenced by the placement of the temperature sensors in a real experiment. Especially if a heat transfer fluid (HTF) is considered to act as heat sink and source, temperature measurement requires special care.

The upper limit of the cooling capacity of an elastocaloric refrigerator can be determined with zero thermal load applied and at zero temperature span. For most elastocaloric refrigerators, this maximum cooling capacity  $\dot{Q}_0^{cool}$  is determined at the very beginning of the device operation. The initial temperature change rate of the heat source  $\dot{T}_{source}$  in combination with the thermal mass of the heat source  $m_{source}c_p$  allow a conclusion on the magnitude of the elastocaloric cooling capacity at this operating point.

$$\dot{Q}_0^{cool} = m_{source}c_p\dot{T}_{source} \quad (\text{XI})$$

For some investigations, not the absolute cooling capacity is of particular interest but rather the specific cooling capacity. To obtain the specific cooling capacity  $\dot{q}_0^{cool}$  the absolute cooling capacity is divided by the mass of elastocaloric material needed.

$$\dot{q}_0^{cool} = \dot{Q}_0^{cool} / m_{SMA} \quad (\text{XII})$$

The specific cooling capacity gives insights how efficiently the elastocaloric material is used and is of particular interest for applications with strict weight or space restrictions.

The mechanical power input of the elastocaloric refrigerator is needed for the determination of the device efficiency. The mechanical work input per cycle of operation  $\Delta W_{device}$  is calculated by integration of the applied force over the displacement.

$$\Delta W_{device} = \oint F \, dx \quad (\text{XIII})$$

The mechanical power input then writes:

$$\dot{W}_{device} = f \Delta W_{device} \quad (\text{XIV})$$

This approach takes into account only the irreversible work input. It mainly consists of the elastocaloric material's hysteresis work, but also losses in the setup due to friction contribute. The approach already assumes work recovery (WR) automatically, since the elastically stored energy portion of the loading work is not included in  $\Delta W_{device}$  (compare chapter 2.3.3). Therefore, the presented approach assumes WR, and in addition, does not account for the actuator efficiency. As the technology will approach specific applications in future, further losses and efficiencies of e.g. driving motors have to be taken into account in order to obtain a realistic total efficiency measure. Though, at this stage, this procedure helps to get a clear view on the elastocaloric performance of the cooling structure without overestimating the influence of experimental test setups.

The efficiency of a refrigerator is characterized by its coefficient of performance (COP) that sets the cooling capacity of the refrigerator into relation to the input power needed for operation.

$$COP_{device} = \frac{\dot{Q}_0^{cool}}{\dot{W}_{device}} \quad (XV)$$

The  $COP_{device}$  introduced here includes all the assumptions that went into the calculation of  $\dot{Q}_0^{cool}$  und  $\dot{W}_{device}$ . For this reason,  $COP_{device}$  represents an upper limit of the device COP.

Upon operation, the available device temperature span, cooling capacity and the achieved COP depend on each other and on the operation point of the cooling device. This is not represented by the figures of merit  $\Delta T_{device}$ ,  $\Delta T_{device}^{cool}$ ,  $\dot{Q}_0^{cool}$ ,  $\dot{q}_0^{cool}$ ,  $COP_{device}$  introduced in this chapter. These are limiting values and are not achieved at the very same point of operation. Please keep in mind that these figures of merit are suited well for comparison, however, do not represent the entire device performance under load.

## 2.4 State of the Art in Elastocaloric Cooling Devices

### 2.4.1 Classification of Elastocaloric Cooling Devices

During recent years, various elastocaloric refrigerator prototypes have been engineered and investigated. The basic concepts of these refrigerators vary a lot. In this chapter, a general classification for elastocaloric refrigerators is developed based on the general concepts introduced in the previous chapter 2.3. This classification will help to identify similarities and main differences between different prototypes and thus will help to draw comparisons and to identify new promising refrigerator concepts. Similar classifications have been done before for magnetocaloric [64;70], and electrocaloric [88] refrigerator prototypes. The classification categories are developed to precisely classify the elastocaloric core cooling unit. More general aspects as for example the future field of application or the source of mechanical power are not taken into account, in order to focus on the core elastocaloric cooling technolo-

logy rather than more general aspects. Here the classification is introduced and in the next chapter 2.4.2 different prototypes presented in literature will be discussed and classified.

Elastocaloric refrigerator prototypes are classified under four main categories that are device concept, heat transfer and separation of hot and cold heat flow, mechanical actuation and active material. A graphical representation of the classification is presented in Figure 13. The main categories include sub-categories (a to i), each with different possible device characteristics (1 to 5). Elastocaloric refrigerator prototypes can be classified based on their characteristics in each subcategory. The presented classification approach covers all the characteristics found in prototypes known today and also includes further possibilities. However, as the field progresses the classification can easily be extended by further categories and characteristics that cannot be foreseen today.

Different **device concepts** are discriminated based on the caloric amplification of the device (a). Caloric amplification allows an elastocaloric refrigeration device to reach temperature spans  $\Delta T_{device}^{cool}$  that exceed the materials adiabatic temperature span  $\Delta T_{ad}$ . Elastocaloric refrigerators can operate without caloric amplification, or might include caloric amplification either by the well-known concept of active regeneration, or by a cascaded device architecture. Furthermore, heat recovery might be used to increase  $\Delta T_{device}^{cool}$ . The **heat transfer** between the active material and its direct surrounding (b) and the separation of the hot and cold heat flow generated in the active material (c) is critical to every elastocaloric refrigerator. The heat transfer (b) can be a contact heat transfer between the solid active material and a solid heat sink and source, but can also be transferred through convective heat transfer to a heat transfer fluid (HTF) in liquid phase or in gas phase. Mostly, the transferred heat changes the temperature, and thus sensible heat, of the HTF. However, under special conditions it is also possible to utilize latent heat transfer and evaporate or condensate the HTF. Basic principles of separating the hot and cold heat flow (c) are either based on changing thermal and mechanical

contact conditions between the active material and the heat sink and source, relative motion between the active material and an HTF, a solid element or thermal diodes. Different types of elastocaloric refrigerators can also be characterized based on their **mechanical actuation**. First of all, refrigerators can be characterized based on the relative motion between active material and the heat sink and source or the HTF (d). Configurations are possible with no movement between the two, with a moving elastocaloric material element (eCM) and static heat source and sink, a static eCM and moving heat source and sink or both eCM and heat source and sink moving. The configuration without relative movement can only work in combination with thermal diodes. In addition, a discrimination can be made based on the main actuation movement (e). Linear oscillatory, rotational oscillatory and rotational continuous actuation movements are possible. Refrigerators can also be classified based on the stress state applied to the eCM (f). Most prominent are pure tensile or compressive stress states but also bending or torsion could be applied to the eCM and tensile stresses can also be applied by out-of-plane deflection in thin geometries. Furthermore, the mechanical actuation could include a mechanism for work recovery (g), e.g., through antagonistic coupling. Finally, a classification of elastocaloric refrigerators can be made based on the eCM that is used as **active material** in the device. Both, the material of the active cooling element (h) and the geometry of the active element are important (i). To date, mostly NiTi-based SMAs are used for the eCM. However, in future also SMAs based on other material systems, e.g. Cu-based SMAs, might be used. Even elastocaloric materials that do not belong to the group of SMA materials, like elastomers, have attracted recent interest and might be a future alternative [106;166]. Most common geometries of the eCM are film / foil-based geometries, wires, plate or tube-based geometries, but also more complex bulk-based geometries are possible.

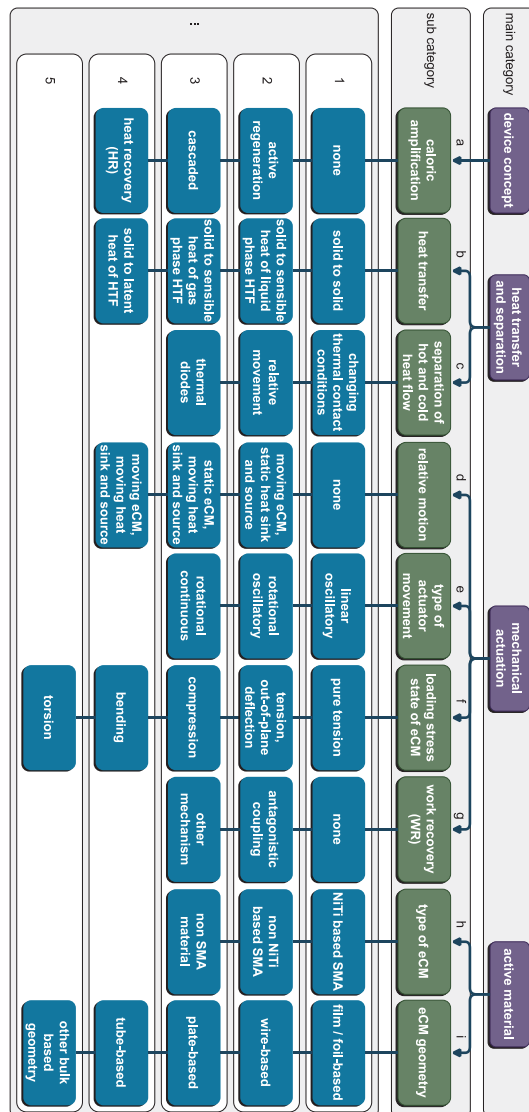


Figure 13 Classification of elastocaloric cooling devices. Devices are classified based on their most important engineering properties (a to i). Possible characteristic values of the properties are included (1 to 5). eCM denotes elastocaloric material element.

### 2.4.2 Overview on Elastocaloric Cooling Prototypes

The classification developed in 2.4.1 is applied in the following to elastocaloric refrigerators found in literature and summarized in Table 4. In addition, these refrigerators are presented in detail to provide an overview on the state-of-the-art of elastocaloric cooling devices. Purely theoretical studies are not included in the following overview. SMA film-based elastocaloric cooling devices developed prior to this work are not presented here, but in the following chapter 2.4.3. In Table 5, key performance results of the presented devices are summarized to give a comprehensive overview.

Schmidt et al. developed a scientific test setup for the investigation of elastocaloric cooling processes [182]. The device is developed to investigate the fundamentals and control parameters of a SMA-based elastocaloric cooling cycle. The scientific test setup combines the experimental control and the monitoring of the experiment in one unit. The setup allows for both, the investigation of the elastocaloric properties of the pure SMA material [182–184], and the refrigerator configuration [39;182]. In the setup, a ribbon of SMA is strained and unstrained under tensile load by a first linear actuator. A second set of linear actuators is used to alternately bring the SMA in directly mechanical contact to a solid heat sink and a solid heat source, depending on the loading state. In this way the hot and cold heat flow caused by the elastocaloric effect are separated. The scientific test setup is illustrated in Figure 14. To focus on the investigation of the basic elastocaloric cooling cycle, no calorific amplification or mechanism for WR is included. Conventional NiTi alloys as well as NiTiCuV alloys are investigated in the setup [182–184]. Different operation parameters like the strain rate, the maximum applied strain, and contact time are investigated. Higher maximum strains increase the temperature span of the device, however decrease the efficiency. A maximum  $\Delta T_{device}$  of 7 °C has been achieved [182].  $\dot{q}_0^{cool}$  reaches a maximum value of 0.35 W/g, the  $COP_{device}$  reaches 4.56 [39]. A detailed analysis of thermodynamic process cycles reveals that the combination of a non-adiabatic loading process and an adiabatic unloading process increases the efficiency by 15 %

compared to the pure adiabatic process cycle. A process cycle based on non-adiabatic loading and combined adiabatic and isothermal unloading can additionally increase the cycle efficiency [39].

Table 4 Classification of elastocaloric refrigerators found in literature. Each elastocaloric cooling device is classified according to the approach introduced in chapter 2.4.1. The single characteristics are coded by numbers according to Figure 13. The overview allows to quickly identify similarities and key differences between elastocaloric cooling devices. If no information is available on a specific detail, the corresponding entry is left empty.

Author, reference	short unique feature	description /	classification categories according to chapter 2.4.1								
			a	b	c	d	e	f	g	h	i
Schmidt, [182]	scientific test setup		1	1	1	3	1	1	1	1	3
Qian, [185]	large scale, HR cycle		4	2	2	3	1	3	2	1	4
Tušek, [172]	elastocaloric regenerator		2	2	2	3	1	1	1	1	3
IPM [186;187]	latent heat transfer			4	2 / 3	3		3		1	4
Sharar, [188]	bending mode		1	1	2	2	3	4	3	1	2
Kirsch, [189]	direct air cooler		1	3	2	4	3	1	3	1	2
Snodgras, [31]	multistage device architecture		3	2	2	3	1	1	1	1	2
Sebald, [166]	rubber		2	2	2	3	1	1	1	3	4
Ossmer, [190]	single SMA film devices		1	1	1	2	1	2	1	1	1
Ossmer, [169]	coupled SMA film devices		1	1	1	2	1	2	2	1	1

#### Legend:

- a) caloric amplification: 1 none; 2 active regeneration; 3 cascaded; 4 heat recovery (HR);
- b) heat transfer: 1 solid-to-solid; 2 solid to sensible heat of liquid phase HTF; 3 solid to sensible heat of gas phase HTF; 4 solid to latent heat of HTF;
- c) separation of hot and cold heat flow: 1 changing thermal contact conditions; 2 relative movement; 3 thermal diodes;

- 
- d) relative motion: 1 none; 2 moving eCM, static heat sink and source; 3 static eCM, moving heat sink and source; 4 moving eCM, moving heat sink and source;
  - e) type of actuator movement: 1 linear oscillatory; 2 rotational oscillatory; 3 rotational continuous;
  - f) loading stress state of eCM: 1 pure tension; 2 tension, out-of-plane deflection; 3 compression; 4 bending; 5 torsion;
  - g) work recovery: 1 none; 2 antagonistic coupling; 3 other mechanism;
  - h) type of elastocaloric material: 1 NiTi-based SMA; 2 non NiTi based SMA; 3 non SMA material;
  - i) geometry of elastocaloric material: 1 film / foil-based; 2 wire-based; 3 plate-based; 4 tube-based; 5 other bulk-based geometry;
- 

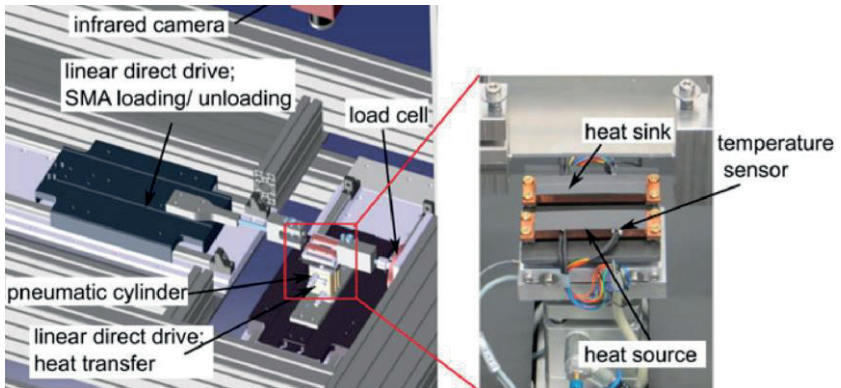


Figure 14 CAD visualization of the complete scientific test setup for SMA-based elastocaloric cooling developed by Schmidt et al., including a section of the heat sink and source unit. © 2016 Taylor & Francis, figure reprinted from [39].

Qian et al. developed a compression-based elastocaloric cooling device with a fluidic circuit for separation of hot and cold heat flows including heat recovery [173;185;191]. The system is based on NiTi tubes that are loaded under compression by a linear actuator. A heat transfer fluid (HTF), water in this case, is pumped through the NiTi tubes, absorbing and transferring heat from and to the SMA tubes. Heated and cooled HTF are pumped in different directions and thus the hot is separated from the cold heat flow. The fluidic

system includes an additional circuit for heat recovery in the system. WR is included in the system by coupling two bundles of NiTi tubes in an antagonistic way. Before operation, the two beds are pre-strained with respect to each other. An operation cycle comprises three phases: (1) loading and unloading of the NiTi beds, (2) pumping of the heated HTF in direction of the hot heat exchanger (HHEX) and the cooled HTF in direction of the cold heat exchanger (CHEX), (3) internal heat recovery cycle to pre-heat and pre-cool the SMA tubes.

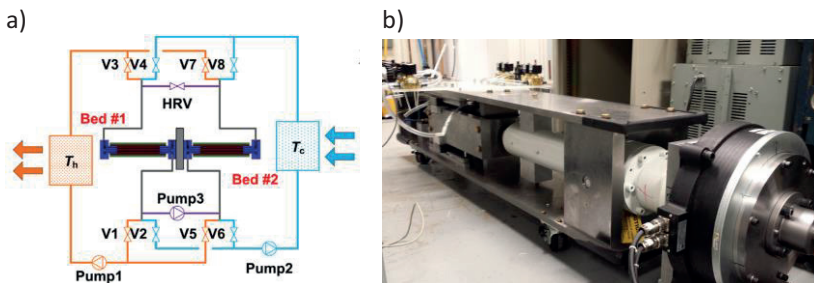


Figure 15 (a) Schematic setup of the compression-based elastocaloric refrigerator including the two SMA beds and the fluidic system with the heat recovery cycle. © 2015 Elsevier Ltd and IIR, reprinted with permission from [192]. (b) Experimental setup. The image was kindly provided by Suxin Qian, © Suxin Qian.

A schematic of the cooling system is illustrated in Figure 15. The system was subject to extensive theoretical studies to create a deeper understanding of the system and to uncover the potential for improvement [148;181;192]. NiTi tubes with an outer diameter of 5 mm and a wall thickness of 0.5 mm have been used, having a length of 25.54 cm [191]. The best performance has been achieved in a device configuration that includes Polyether ether ketone (PEEK) insulation at the end of the tubes and polymer insertions to reduce the HTF volume in the tubes. Ten NiTi tubes per bed are used. A maximum temperature span of 4.7 °C and a maximum cooling capacity of 65 W is reached [185]. The main issues in the device have been heat generation from pumps, fluid mixing in the fluidic system, convective heat losses to the ambient and

high dead volumes of the HTF [185]. Based on the findings in the presented cooling device, a second generation is developed [173].

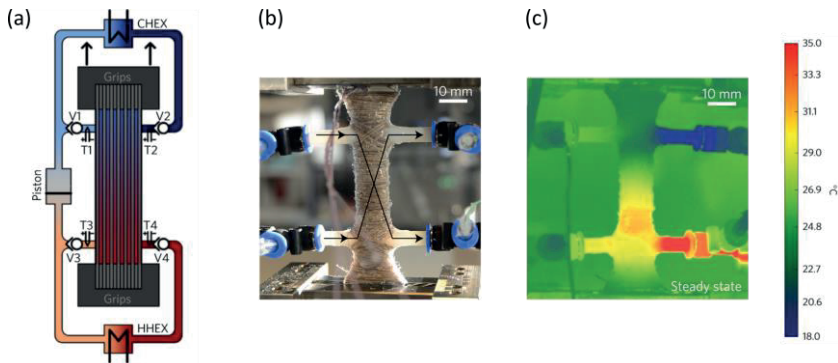


Figure 16 (a) Schematic of the elastocaloric heat pump based on active regeneration developed by Tušek et al. (b) Core of the experimental setup including the regenerator with fluidic connections. (c) IR thermograph of the regenerator and the fluidic connection under steady state operation. © 2016 Macmillan Publishers Limited, part of Springer Nature, figure reprinted with permission from [172].

Tušek et al. developed an elastocaloric heat pump based on the concept of active regeneration [172]. The concept is well known from the field of magnetocaloric refrigeration [180] and allows to increase the temperature span of the cooling setup. In the presented work, a stack of NiTi plates is cyclically loaded under tension by a linear actuator while an HTF, here water, is pumped back and forth along the plates and in between. The moving HTF separates the hot and cold heat flow, as heated HTF is transported to one side of the regenerator and to the HHEX, whereas cooled HTF is transported to the opposite side to the CHEX. Upon operation, a temperature gradient forms along the SMA plates, the hot end is pre-heated, the cold end pre-cooled. Nine Ni<sub>0.55</sub>Ti<sub>0.44</sub><sub>2</sub> plates with a thickness of 200 µm are combined into one stack to form the regenerator. A schematic of the setup and the experimental implementation of the concept are illustrated in Figure 16 a) and b). Device

performance is investigated in detail for different maximum strains. At operation with a maximum strain of 3.4 % the device reaches a maximum temperature span  $\Delta T_{device}$  of 15.3 K, a heating capacity of 0.782 W/g or 4536 mW and a COP for heating of 3.5. At lower maximum strains, the device reaches a higher COP of 5.5, temperature span and heating capacity decrease to 6.5 °C and 0.355 W/g [172]. In a second series of experiments with a slightly improved device configuration the influence of the cycle time, regenerator configuration and the fluidic cycle on the device performance is investigated. An increased maximum temperature span of 19.9 °C has been reached [193].

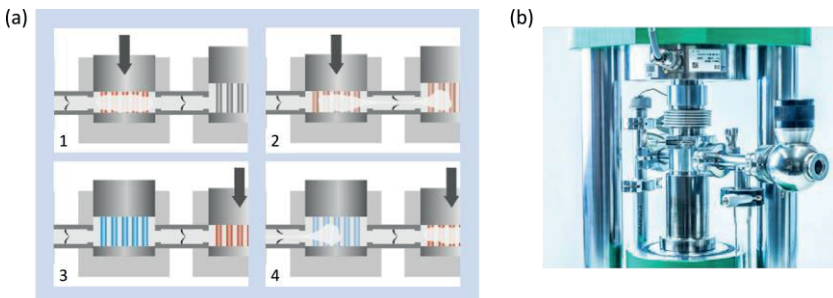


Figure 17 (a) Schematic operation principle of the elastocaloric refrigerator developed at Fraunhofer IPM based on latent heat transfer. In 1) the SMA rods are loaded under compression, heat up, and evaporate HTF. 2) Heat is transferred to the next chamber by the mass flow of gas phase HTF. 3) SMA rods are released and cool down, HTF condenses on the cold rods. 4) Heat is absorbed from the previous chamber by a mass flow of gas phase HTF. (b) Experimental setup of the refrigerator. ©2019 Fraunhofer IPM, reprinted from [186] with permission.

At the Fraunhofer IPM, Freiburg, Germany a new concept for caloric refrigerators based on latent heat transfer is developed [186;187]. A unique feature is that the heat transfer from the SMA to the HTF does not change the temperature of the HTF, but instead condenses or evaporates the HTF similar to the heat transfer in heat pipes and thermosiphons [175]. The latent heat of the HTF is changed instead of the sensible heat. To achieve this, the system

of elastocaloric material and the HTF is sealed hermetically and all non-condensing gas are removed from the system. In the enclosed system, the pressure has to be adapted so that the HTF is existent in liquid and gaseous form simultaneously. Here, pure water is used. Elastocaloric heating and cooling then is transferred to the HTF and forces it to evaporate or condensate [175;187]. In such a system, heat and mass transfer are directly connected (see chapter 2.3.2 and Figure 17 a). The concept of latent heat transfer is motivated by the high heat transfer coefficients that allow for high operation frequencies of the elastocaloric system [175]. The elastocaloric cooling prototype is based on latent heat transfer loads NiTi rods of 11 mm length and 2.5 mm in diameter under compression within the hermetically sealed system. Hot and cold heat flow are separated controlling the flow of gaseous HTF in the system by check valves. Several elastocaloric cooling chambers easily can be connected into a cascaded system to increase the device temperature span [186]. To the present date, no experimental data of the elastocaloric refrigerators based on latent heat transfer is published.

Sharar et al. developed an elastocaloric refrigerator based on the bending of a NiTi wire [188]. A wire loop is placed over a drive wheel on one side and bends over a copper tube at the second side. The experimental setup is illustrated in Figure 18. The drive wheel is actuated by a stepper motor. Its diameter is large enough to prevent phase transition in the wire when both are in contact. Other than that, the radius of the copper tube is small enough to induce a phase transformation in the material. Thus, the material heats up when it is bent around the tube that functions as heat sink. When the wire straightens again after the tube, it cools down and a copper heat source is brought in contact to the wire to harvest this cooling power. The system can run continuously at a maximum strain rate of  $0.025 \text{ s}^{-1}$ . This corresponds to rotational frequency of 0.71 Hz. The device reaches a cooling temperature span of  $1.85 \text{ }^{\circ}\text{C}$  after 20 min of operation at the maximum frequency. A cooling capacity of 50 mW is applied to the copper heat source in this case [188].

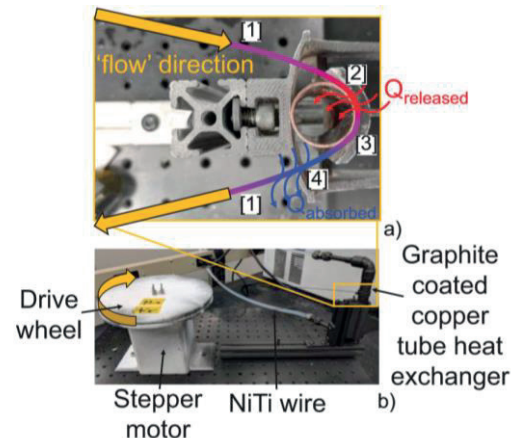


Figure 18 Elastocaloric refrigerator using a NiTi wire loop that is loaded in bending-mode by a continuous rotational actuation. Heat transfer is accomplished through mechanical contacts of the wire with a copper tube functioning as heat sink and a separate copper element that is cooled and utilized as heat source. © 2018 IEEE, figure reprinted from [188] with permission.

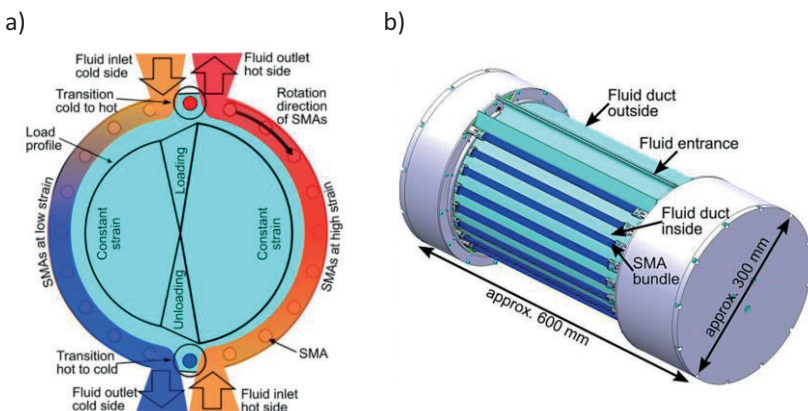


Figure 19 (a) Schematic of the operating principle of the elastocaloric air cooler developed by Kirsch et. al. (b) CAD visualization of the device, including the SMA wire bundles illustrated in blue and the flow duct. © 2018 Wiley-VCH Verlag GmbH & Co. KGaA, figure reprinted from [15] with permission.

Kirsch et al. developed an elastocaloric air cooler [189], based on the findings and the understanding of their previously developed scientific test setup [15;39;171]. In the direct air cooler, NiTi wire bundles are moved by a rotational motor in a hollow cylindrical air gap. The ends of the bundles are guided on a camshaft and thus the bundles are subjected to a defined tension stress profile. In addition, fans move two opposing air streams through the air gap. The air streams leave the setup at opposite sides, where one air stream is heated and the opposite one is cooled down. An illustration of the working principle and the direct air cooler is presented in Figure 19 a). The setup works without caloric amplification and uses forced convection between the air flow and the wires to absorb and transfer heat from and to the SMA wires. The two air flows separate the hot from the cold heat flow in the device. Since several wire bundles are loaded and released on the same camshaft, the setup automatically includes antagonistic work recovery. The device development has been aided by materials characterization and experimental parameter analysis [147;194;195], and SMA materials and device simulation [15;196;197]. For operation, TiNiCo wires arranged in 24 bundles of 30 wires each are used. The wires have a diameter of 200 µm and a length of 300 mm. Upon experimental operation, the device reaches a  $\Delta T_{device}$  between the heated and cooled air flow of 6 °C at an air flowrate of 46 m<sup>3</sup>/h. If the air flowrate is increased to 133 m<sup>3</sup>/h,  $\Delta T_{device}$  decreases only slightly to 5.1 °C [189]. Device simulation predicts that also a higher  $\Delta T_{device}$  of 20 °C with a cooling capacity  $\dot{Q}_0^{cool}$  of 25 W and  $COP_{device}$  of 9.5 is possible [15].

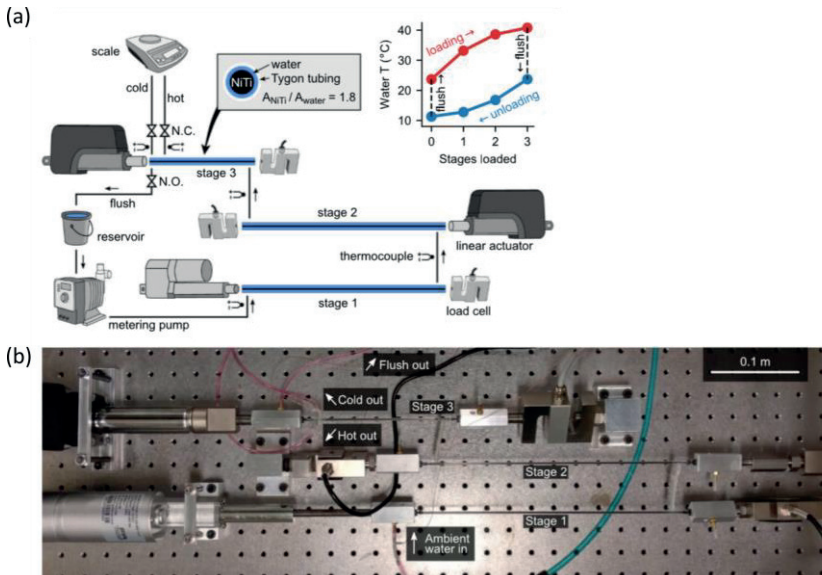


Figure 20 (a) Schematic setup of the cascaded elastocaloric refrigerator developed by Snodgras and Erickson. (b) Experimental setup comprising the three linear actuators that load a SMA wire based elastocaloric cooling stage each. The stages are connected by a fluidic system. Figure reprinted from [31], © Snodgrass & Erickson, use permitted under Creative Commons License (CC BY).

Snodgras and Erickson developed a cascaded elastocaloric refrigerator that utilizes the combined effect of three NiTi wires [31]. Each wire is surrounded by a tubing that allows to pump a liquid HTF along the wire. The three wires are mechanically loaded in tensile-mode by three individual linear actuators. Loading (unloading) of the NiTi wires triggers the elastocaloric effect, and heat is released (absorbed) to (from) the HTF. By moving the heated and cooled HTF, hot and cold heat flows are separated in the device. The heated or cooled HTF is used to preheat or precool the next wire, or the cooling capacity is used directly. If the cooled HTF is used to pre-cool the next NiTi wire, the cooling effect of the single wires add up and a high  $\Delta T_{device}$  is possible. In the presented work, the pumping direction is always the same, so the hot end

of the device is also the cold end, but at different times of the cooling cycle. The schematic and experimental setup of the cascaded elastocaloric refrigerator are illustrated in Figure 20. A detailed parameter study was performed to find the optimum device performance. The influence of the HTF cycle, the maximum strain, the timing between the three cycles, and the system configuration is investigated. In particular, the effect of the three cascaded stages in comparison with two stages or a single stage is examined. To quantify the cooling performance, the device temperature span, the temperature span available for cooling, heating and cooling capacity, and the COP for heat pumping and cooling are determined. A maximum device temperature span of 28.3 °C, and a maximum temperature span for cooling of 12.3 °C are reported, both for three cascaded stages (see Table 5). The device reaches its best  $COP_{device}$  of 6 and  $\dot{q}_0^{cool}$  of 0.777 W/g with a single stage configuration. The highest  $\dot{Q}_0^{cool}$  of 1323 mW is reached with two stages. The promising results underline the potential of a cascaded device architecture of elastocaloric refrigerators. Increasing the number of cascaded cooling stages not only increases the device temperature span by 50 % in the given device, but also increases the  $COP_{device}$  for a given temperature span [31].

Sebald et al. developed an active regeneration based elastocaloric cooling device with rubber as active material [166]. The main objective of the experimental setup is to validate a simulation model. A single rubber tube is used that is made from purified polyisoprene rubber and has a length and outer diameter of 25 mm and 5 mm, respectively. The rubber tube is connected to a linear actuator at one end, and is fixed in position at the second end. Two additional linear actuators are connected at both ends of the tube to pump an HTF through the rubber tube. The schematic and experimental setup is presented in Figure 21. Upon operation, the rubber tube is loaded by 600 % in a sinusoidal movement. The HTF is pumped in phase with the rubber elongation. An operation frequency of 0.3 Hz is applied. Under such operation, the regeneration base device reaches a device temperature span at saturation of 1.2 °C. Compared to the SMA based devices presented above, the

value seems low. However, the  $\Delta T_{device}$  still exceeds the materials  $\Delta T_{ad}$  that is 1 °C in this case.

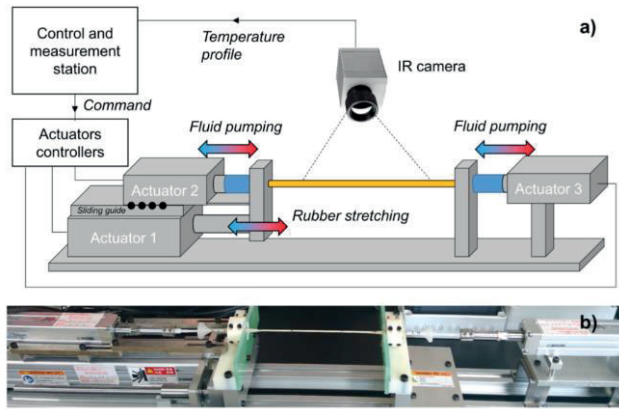


Figure 21 (a) Schematic of the active regeneration based elastocaloric cooling device developed by Sebald et al. The device uses the elastocaloric effect of a rubber tube. (b) Experimental implementation of the device. © 2020 Sebald, reprinted with permission from [166].

Table 5 Key experimental results of the elastocaloric cooling devices presented in this chapter. If known, the following parameters are given: operation frequency  $f$ , device temperature span  $\Delta T_{device}$ , cooling temperature span  $\Delta T_{device}^{cool}$ , absolute cooling capacity  $\dot{Q}_0^{cool}$ , specific cooling capacity  $\dot{q}_0^{cool}$ , efficiency of the device expressed as  $COP_{device}$ .

Author	comment	$f / \text{Hz}$	$\Delta T_{device} / ^\circ\text{C}$	$\Delta T_{device}^{cool} / ^\circ\text{C}$	$\dot{Q}_0^{cool} / \text{mW}$	$\dot{q}_0^{cool} / \text{Wg}^{-1}$	$COP_{device} / -$	Reference
Schmidt	NiTi	0.28	7	3.3				[182]
	TiNiCuV	0.114	2		0.35	4.56	[39]	
	TiNiCuV	0.114	5		0.15	2.44	[39]	
Qian		< 0.1	4.7**		65000**	0.6**		[185]
Tušek	$\varepsilon_{max} = 3.4\%$	0.25	15.3		4536*	0.782*	3.5*	[172]
	$\varepsilon_{max} = 1.7\%$	0.25	6.5		2059*	0.355*	5.5*	[172]
	, $\varepsilon_{max} = 3.5\%$	< 0.33	19.9					[193]
Sharar		0.71		1.85**	50**			[188]
Kirsch	air flow 46 m <sup>3</sup> /h	0.6	6	2.3				[189]
	air flow 133 m <sup>3</sup> /h	0.6	5.1	2.1				[189]
Snodgras	highest $\Delta T_{device}$ , 3 stages	0.0625	28.3	11.4	228	0.042	0.5	[31]
	highest $COP_{device}$ , one stage	0.125	5.2	2.3	713	0.648	6	[31]
	highest $\dot{q}_0^{cool}$ , one stage	0.125	6.9	2.8	847	0.777	4.9	[31]
	highest $\dot{Q}_0^{cool}$ , two stages	0.91	15.3	6.4	1323	0.241	2	[31]
Sebald	rubber	0.3	1.2					[166]

\* value given for heating, not cooling

\*\* maximum values are given in each category, values are not measured at the same point of operation

### 2.4.3 Previous work on SMA Film-Based Elastocaloric Cooling Devices

The present work builds on previous work on SMA film-based elastocaloric cooling devices at KIT [14;32;169;190,pp. 153–192]. Therefore, the previous work is discussed in detail in this chapter.

First-of-its-kind SMA film-based elastocaloric cooling devices, which are all characterized by a common operation principle, have been developed [14]. SMA film stripes are installed in so-called bridges that fix the ends of the films and keep the distance of the two ends constant. These SMA film bridges are cyclically loaded and unloaded in the cooling device by out-of-plane deflection (for more information see chapter 2.3.1). In the deflected state, the films are brought into contact with a solid heat sink, to which they transfer heat, and in the unloaded state they are brought into contact with a solid heat source, from which they absorb heat. The concept is explained in detail in chapter 2.3.5. Based on the described concept two groups of demonstrator devices have been developed and investigated, single film-based elastocaloric cooling devices and coupled devices that utilize two coupled SMA films to achieve work recovery (see chapter 2.3.3). The fabrication of all elastocaloric demonstrators is based on similar technologies, namely precision machining of copper and brass elements that function as heat sink and source and 3D printing of polymer support structures. Cold-rolled NiTiFe foil stripes and magnetron sputtered TiNiCu-based films with a thickness of 30 µm have been used as active material. A tensile testing machine has been utilized for operation and characterization of the various elastocaloric cooling devices that shall be introduced in the following. In Figure 22 schematics of the various elastocaloric cooling devices developed in previous work are given. Key results gained with these demonstrators are summarized in Table 6.

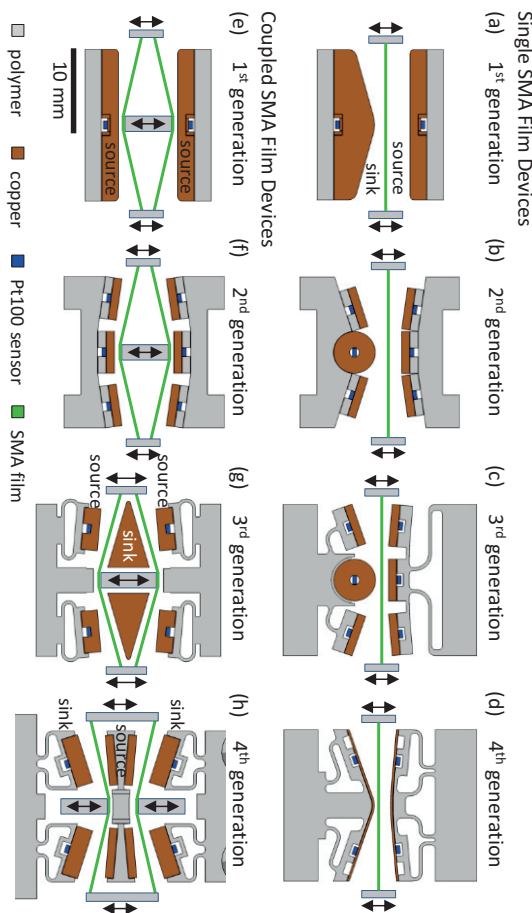


Figure 22 Schematics of miniature elastocaloric cooling demonstrators developed in previous work at KIT. Four device generations are presented for single SMA film devices and coupled double SMA film devices. Figure adapted from [32,pp. 164, 173, 176], © Ossmer, used under Creative Commons License (CC BY-SA 3.0 DE), figure reorganized.

The first single film demonstrator generation illustrated in Figure 22 a) incorporates the basic concept described above. The device is engineered from two monolithic brass blocks, the heat sink with a triangular shaped surface to

apply the out-of-plane deflection and the heat source with a completely flat surface. The characterization of the first generation device unveiled that in this first demonstrator the thermal mass of the sink and source element is too high compared to the mass of the SMA film to allow a considerable effect. In addition, it was found that accumulation of plastic strains in the SMA film lead to buckling of the unloaded SMA when it should be in contact with the flat heat source and thus no efficient heat transfer could be established between the SMA film and the heat source. In the second device generation (Figure 22 b) sink and source elements have been subdivided into several elements to allow for better adaption between the SMA film and the sink and source elements and to decrease the total thermal mass. In addition, a slight angle has been introduced in the surface of the heat source to compensate for slight length changes in the SMA film. It turned out that small inaccuracies in the ridged suspension of the single copper elements introduced load peaks on the SMA film that in turn lead to fracture and inhomogeneous heat transfer. To address this issue, spring-like compliant structures have been introduced in the third device generation (Figure 22 c). The benefits of the compliant structures proved to be threefold. The compliant structures allow an individual adaption of the copper elements to the SMA film and improve the heat transfer in this way. In addition, load peaks are omitted and the insulation of the copper element is improved (see chapter 4.1.1). Therefore, device temperature spans of up to 7.9 K could be reached in the third single film device generation and an efficiency of the device characterized by the  $COP_{device}$  of 2.9 is achieved. In the fourth device generation (Figure 22 d) a continuous copper sheet is used as heat sink and source. This increases the contact area between film and sink / source. It turned out that not only the heat transfer was increased, but also parasitic heat losses. The performance in terms of device temperature span was comparable to the one reached in the third device generation, but cooling capacity and efficiency was lower. In Figure 23 a) the temperature evolution of the sink and source elements of the fourth single film device generation is shown as a showcase for two operation frequencies [32,pp. 161–172].

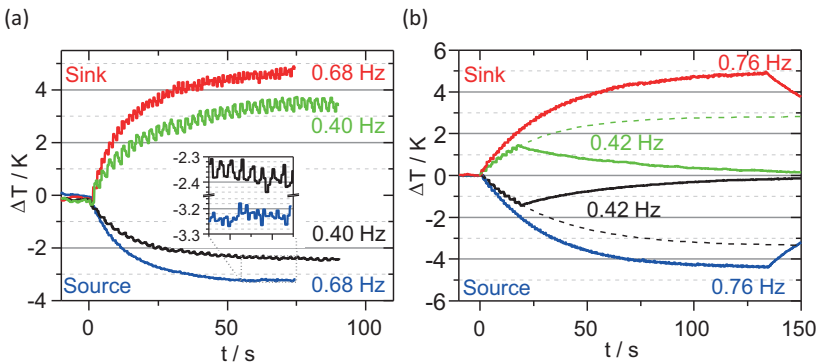


Figure 23 Temperature evolution of the sink and source elements in SMA film-based cooling devices for different operation frequencies. (a) Characteristic of the single film 4<sup>th</sup> generation device. (b) Results from the coupled 4<sup>th</sup> generation device. Figure adapted and from [32, pp. 167, 177], © Ossmer, used under Creative Commons License (CC BY-SA 3.0 DE), figure reorganized.

In the 4<sup>th</sup> generation of single film device, sputtered TiNi and TiNiCuCo have been utilized. Due to experimental issues, the achieved performance did not meet the results gained with cold-rolled NiTiFe films [190].

Table 6 Key results and performances of the previous SMA film bases elastocaloric cooling devices. For each device the best performance is reported. For detailed information references are given.

Device	$f / \text{Hz}$	$\Delta T_{\text{device}} / \text{K}$	$\Delta T_{\text{device}}^{\text{cool}}$ / K	$\dot{Q}_{\text{cool}}^{\text{max}} / \text{mW}$	$\dot{q}_0^{\text{cool}} / \text{Wg}^{-1}$	$COP_{\text{device}}$ /	Reference
<b>single SMA film device, NiTiFe</b>							
1 <sup>st</sup> generation	0.68	3	1.7	16.6	2.1	5.5	[32,p. 168]
2 <sup>nd</sup> generation	0.66	7	3	50	6.4	2.8	[14]
2 <sup>nd</sup> generation	0.72	4.2	1.7	23.1	2.6	2.9	[32,p. 168]
3 <sup>rd</sup> generation	0.75	7.9	3.1	24	3.1	2.9	[169]
4 <sup>th</sup> generation	0.68	8.2	3.3	12	3.1	1.3	[32,p. 168]
<b>single SMA film device, TiNiCuCo</b>							
4 <sup>th</sup> generation	0.75	3.5	2	14.4	1.6	2.9	[190]
<b>coupled SMA film devices, NiTiFe</b>							
2 <sup>nd</sup> generation	0.84		1.2	20	1.3	2.4	[14]
3 <sup>rd</sup> generation	0.76	5.5	5	51	3.3	3.2	[169]
4 <sup>th</sup> generation	0.71	9.4	4.4	45	2.9	3.1	[169]

The development of coupled SMA film devices shows a similar learning curve as the single film devices. In the first generation of coupled devices (Figure 22 e), two flat monolithic heat sources are used and the surrounding air is used as heat sink. Like in the single film device, it turned out that buckling of the SMA film in contact with the flat heat source impeded efficient heat transfer. Thus, in the second generation (Figure 22 f) the heat source was divided into segments and a slight angle with respect to the SMA bridge was introduced. This helped to improve the thermal contact between the SMA film and the heat sources, but it was found that pure convective heat transfer with the surrounding air is too slow to cool down the SMA film efficiently. Therefore, in the third device generation (Figure 22 g) a brass heat sink is incorporated in the middle between the two heat sources to absorb the heat released by the SMA film. The mass of the heat sink was chosen 17 times higher than the mass of the heat source and thus the achieved temperature change of the heat sink with 0.5 K is considerably lower than the change of the heat source,

which cools down by 5 K. In the fourth generation (Figure 22 h), a single heat source is placed in the middle of the setup and two heat sinks are placed above and below. In Figure 23 b) the temperature evolution of the sink and source elements is presented for two different operation frequencies. A maximum device temperature span of 9.4 K could be reached with a corresponding  $COP_{device}$  of 3.1.

This comprehensive compilation of previous work on SMA film-based cooling devices will allow the reader to better classify and differentiate the concepts and results of this work presented in chapter 4 to 6. In previous work operation parameters could hardly be investigated due to limitations of the experimental setup. Load could only be applied with a constant velocity and the operation frequency was limited to 0.84 Hz. Thus, a new experimental test setup is developed in this work and reported in chapter 4.4. This new experimental test setup allows to extend the characterization of existing device designs. New advanced SMA film-based elastocaloric cooling devices are developed and characterized. The new advanced devices are developed to increase the systems temperature span or cooling capacity compared to the previous devices.



# 3 Material Characterization

Today the most promising elastocaloric materials are NiTi-based shape memory alloys (SMAs) [43]. They can combine high elastocaloric effect size with a good elastocaloric efficiency and sufficient fatigue life. Therefore, NiTi-based SMA films and foils are used as active materials in the present work. Film and foil geometries have a high surface to volume ratio that allows highly efficient heat transfer, which is of highest importance for elastocaloric cooling. In this chapter, first the used methods of fabrication, mechanical and thermal materials characterization are discussed. Secondly, the material properties of the SMAs are presented in detail.

## 3.1 Methods

### 3.1.1 SMA Film and Foil Fabrication

There are two fundamentally different fabrication routes for SMA films and foils. In the first process, a SMA foil is manufactured from a metallurgically produced ingot by a forming process. Different technologies are available for the bulk metallurgical melting of the ingot. Vacuum arc melting or vacuum induction melting might be used. The purity of base materials and the metallurgical process are of highest importance [198]. Subsequently, the SMA ingot is shaped by forming processes to the desired geometry. In case of the present work hot-forging followed by **cold rolling** is used to form SMA foils [199]. A final rolling reduction of 40 % is used to fabricate SMA foil sheets with a thickness of 30 µm. Cold rolling forms the already crystallized ingot and thus has a direct influence on the microstructure of the SMA foil. The fabrication process directly influences the materials properties in cold rolled foils [127;199;200]. In this work, cold rolled NiTiFe foils are used. After the fabrication of the SMA foil sheets they are subjected to an additional heat

treatment and lateral dimensions are structured.<sup>f</sup> Heat treatment is carried out to remove residual strains present from the fabrication process without recrystallization. In this way the fine deformation texture of the cold rolled SMA is preserved [127]. The annealing is performed in an evacuated oven to prevent oxidation. The SMA is annealed for 30 min at a temperature of 500 °C. The lateral structuring of cold rolled SMA foils is carried out by two processes, either simple mechanical cutting or laser cutting. In the present work samples are cut in rolling direction, since this has been found to be beneficial for elastocaloric cooling [169].

The second fabrication process is **magnetron sputter deposition** of SMA films. In this case, freestanding SMA film specimens are directly fabricated in the desired lateral dimensions by combining magnetron sputtering with UV-lithography and wet chemical etching of a sacrificial layer. The process is presented in [201] in detail. First a Si-wafer is prepared with a sacrificial layer of copper and a thin 1.5 µm film of TiNi. The thin TiNi film later functions as a seed layer for the deposition of the desired SMA film with higher thickness. The seed layer TiNi film is structured by UV-lithography and wet chemical etching to the desired lateral structure of the SMA specimen. Then the Cu-sacrificial layer is wet chemical etched with the structured TiNi seed layer as etch-mask. The etching process is stopped, when uncovered copper layer is removed without releasing the structured TiNi seed layer. After this step, the desired SMA film is deposited to the prepared substrate by magnetron sputtering. Films with a thickness of up to 80 µm are possible [16]. After deposition, the remaining copper sacrificial layer is removed by chemical wet etching and the SMA film specimen with structured lateral dimensions is released from the substrate. In the as-deposited state, the SMA has an amorphous structure. The microstructure is adjusted in a rapid thermal annealing (RTA) process. A typical treatment is the annealing at 700 °C for 15 min. Additionally, the

---

<sup>f</sup> The SMA foil sheets used within this work are fabricated by the University of Tsukuba, Japan [199]. Subsequent heat treatment and lateral structuring and are carried out at KIT.

surface quality of the sputtered SMA specimen is increased and edges are rounded off by electropolishing.

This fabrication procedure allows for complex specimen geometries like e.g. perforated membranes or also tube geometries and small lateral feature sizes in the range of a few microns [201;202]. Since the microstructure is formed starting from the amorphous phase, a high variety of possible microstructures can be adjusted. Grain size can be tailored in a wide range, formation and structure of precipitates can be controlled. Variations in the chemical composition easily can be applied, even composition gradients within one specimen are possible [155;159].

Table 7 Fabrication parameters of the three TiNiCuCo SMA films used in this work.

material	layer 1, Ti <sub>55.5</sub> NiCu, (1050 layers)		layer 2, Co, (1050 layers)		annealing temperature / °C	annealing duration /min
	sputter parameter	duration / s	sputter parameter	duration / s		
TiNiCuCo-1	600W, 20sscm Ar, 2·10 <sup>-3</sup> mBar	22	20W, 20sscm Ar, 2·10 <sup>-3</sup> mBar	15	720	15
TiNiCuCo-2	600W, 20sscm Ar, 2·10 <sup>-3</sup> mBar	23	20W, 20sscm Ar, 2·10 <sup>-3</sup> mBar	16	720	15
TiNiCuCo-3	600W, 20sscm Ar, 2·10 <sup>-3</sup> mBar	22	20W, 20sscm Ar, 2·10 <sup>-3</sup> mBar	17	750	15

In this work sputtered TiNiCuCo specimens are used mainly in the form of stripes with 3 mm of width and 32 mm in length and a thickness of 30 µm.<sup>g</sup> Three different TiNiCuCo films are used with a slightly different cobalt content. Thus, the austenite finish temperature of the three alloys is slightly shifted. The Co-content in the alloy is adjusted by sequential sputtering of TiNiCu and Co-layers with defined thicknesses. In the subsequent rapid thermal

<sup>g</sup> Sputtered SMA film specimens used within this work are fabricated by collaboration partners at Kiel University, Germany [159].

annealing step, the material composition homogenizes. The fabrication parameters of the three TiNiCuCo films are summarized in Table 7. Before use, the surfaces and edges of the TiNiCuCo films are smoothed by electropolishing with an applied voltage of 14 V.

### 3.1.2 Mechanical Characterization

The superelastic SMAs are characterized mechanically with a tensile testing machine. Tensile testing is a well-established process for the mechanical characterization of structural materials. In tensile testing the specimen is subjected to a one-dimensional stress state, i.e., it is elongated along its long axis by an externally applied force. In most cases, the specimen is loaded until failure. While the sample is elongated, the elongation and the applied force are tracked. These parameters can easily be converted into engineering stress  $\sigma = F/A_0$  and engineering strain  $\varepsilon = \Delta l/l_0$ . The initial cross-sectional area is denoted as  $A_0$ , the initial length of the specimen as  $l_0$ , the applied force as  $F$ , and the specimen elongation as  $\Delta l$ . Engineering stress is often depicted as a function of engineering strain to receive a stress-strain curve, which is characteristic to the investigated material. In structural materials, among the most important materials parameters deduced from stress-strain curves are the Youngs modulus, Yield strength and ultimate tensile strength [203,pp. 16–27].

In the present work tensile testing is utilized to characterize the superelastic material properties of SMA films and foils. In contrast to classical tensile testing, specimens are not loaded until fracture, but are subjected to load cycles. Besides that, procedures are similar, but sample geometries and fixations are different and depend on the available SMA films and foils.

In Figure 24 a schematic illustration of the test setup used within this work is shown. A tensile testing machine (ZwickRoell, Z0.5) is used in combination with the measurement and control software (testControl II). The specimen is fixed by two clamps. The lower one is fixed in position, the upper one is connected to the traverse of the tensile testing machine. The traverse loads

the specimen by moving upwards and elongating the specimen. The traverse is equipped with a position sensor that determines the displacement with a resolution of 25  $\mu\text{m}$ . A load cell measures the applied force.

SMA foil specimen for tensile testing are cut from the cold rolled 30  $\mu\text{m}$  thick sheets to have a rectangular shape with a width of 2 mm and a length of about 25 mm. Clamping length used for the NiTiFe foil specimen is 15 mm. The sputtered film specimens are already fabricated in a rectangular shape with a width of 3 mm and length of 32 mm. SMA film and foil specimen are fixed at both ends to the tensile testing machine by clamping between two polished steel surfaces. Specimen are carefully aligned to avoid any tilting or misalignment. A defined starting point of the tensile testing experiment is ensured by starting from a pre-force of 0.2 N. Load is applied strain controlled with a defined strain rate. Strain rates  $d\varepsilon/dt$  report how much strain is applied within a certain time step, in case of this work per second. The specimen is loaded until a defined maximum strain that depends on the investigated material. At maximum strain the position is kept for a holding time of 10 s to allow the specimen to achieve thermal equilibrium with ambient. After that, strain is reduced with the same strain rate as during loading until the starting position of the experiment is reached. If several load cycles are applied within one experiment, again a holding time of 10 s is included before the next load cycle starts. All tensile tests presented within this work are conducted at room temperature. Strain rate can be varied between  $10^{-4} \text{ s}^{-1}$  and  $1 \text{ s}^{-1}$  for the used specimen geometry and test setup. Prior to materials characterization, training is applied to the SMA specimen to ensure constant materials behavior. In case of NiTiFe foils, 20 load cycles at a strain rate of  $0.01 \text{ s}^{-1}$  are applied as training. As it turns out, no training is needed for TiNiCuCo films. The strain measurement is subject to an error due to the mechanical compliance of the load cell, traverse and specimen holder. For example, the described measurement setup equipped with a 50 N load cell has to be corrected by 5.3  $\mu\text{m}/\text{N}$ . In all the presented results this error is subsequently eliminated by an algorithm implemented in MATLAB.

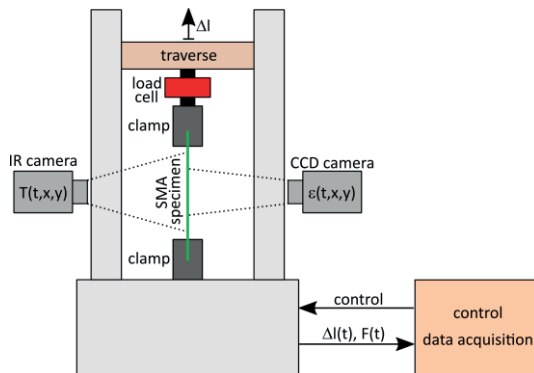


Figure 24 Schematic illustration of a tensile testing test setup. The tensile testing machine is combined with an IR-camera and a CCD-camera.

Additional insights on the SMA materials behavior are gained by capturing the specimen surface during tensile testing with an infrared (IR) camera and a CCD-camera. The arrangement of tensile testing machine, CCD-camera and IR-camera is shown in Figure 24. Surface temperature profiles are captured with the IR-camera (see chapter 3.1.3 below).

The images gained by the CCD camera<sup>h</sup> are used as the basis for digital image correlation (DIC). An area of  $2 \times 3 \text{ mm}^2$  in the middle of the specimen is investigated with the CCD camera. DIC allows to generate information on the spatial distribution of the strain during load cycling. For DIC, fine black sprinkles of carbon black spray coat are applied to the specimen surface. This generates reliable features for tracking. The DIC algorithm tracks the relative motion between surface features over subsequently captured images. The images are taken with a frame rate of 10 fps. The DIC algorithm used within this work is coded in MATLAB.<sup>i</sup> The DIC algorithm can reveal the strain at the specimen

<sup>h</sup> myBluefox 124G, Matrix Vision, resolution of 1200 x 1600 pixels, equipped with a macro lens

<sup>i</sup> The DIC code used within this work was developed by Christoph Eberl et al., and is available to public under [204].

surface in a spatially resolved manner. Thus, DIC reveals local transformation behavior in SMA specimens during load cycling.

### 3.1.3 Thermal Characterization

Two different thermal measurement techniques are used in this work to investigate the properties of elastocaloric superelastic SMAs: direct temperature measurements by infrared-thermography and differential scanning calorimetry measurements.

Contactless temperature measurement of the SMA specimens surface temperature upon load cycling is performed by means of **infrared- (IR-) thermography**. IR-thermography measures the heat radiation emitted by the specimen and calculates back on the specimens surface temperature based on its emission coefficient [205,p. 15 ff]. Spatially resolved temperature profiles help to understand the nature of phase transformation in SMA films. In addition, IR-thermography is used to measure the materials adiabatic temperature change  $\Delta T_{ad}$ . Measurements of the elastocaloric  $\Delta T_{ad}$  by temperature measurement upon adiabatic load cycling are referred to as “direct measurement technique” in literature [35;206].

Measurements are conducted with an IR-camera (FLIR A655sc) equipped with a macro lens. The resolution of the camera is 640 x 480 pixels with a pixel size of 25  $\mu\text{m}$ . The frame rate is up to 200 fps. The accuracy of the absolute temperate measurement is 2 K. The software “FLIR research IR” is used for control of the camera, data acquisition and basic evaluation. The surface of the SMA specimen is covered with a thin layer of carbon spray to adjust the specimen emissivity to 0.95. IR-measurements are taken parallel to tensile testing as indicated in Figure 24. Surface temperature profiles are taken of the complete specimen width and a length of 15 mm. In addition, the temperature average over an area of 1 x 1  $\text{mm}^2$  in the middle of the sample is used to evaluate the temperature trend and  $\Delta T_{ad}$ .

**Differential scanning calorimetry (DSC)** is used to determine phase change properties of SMAs used in this work. The basic concept of DSC measurements is to heat or cool a certain amount of the specimen material and a reference specimen under a constant heating or cooling-rate and measure the applied heat flux. If material properties are not subjected to changes and heat capacity is constant, the heat flux to maintain the heating or cooling-rate is constant. However, if in the materials an endothermic or exothermic phase transition occurs, heat flux will change. Hence, changes in heat flux allow to determine phase transitions in SMAs. To increase the accuracy of the method, not the absolute heat flux is evaluated but the difference between the heat flux to the SMA specimen and the reference specimen [207,p. 21 ff]. In DSC measurements of SMAs, phase transitions are represented by peaks in the DSC curve. Therefore, DSC measurements are well suited to determine phase transformation temperature like austenite finish temperature  $A_f$  or martensite start temperature  $M_s$ . The latent heat of phase transformations is determined by the area below the peaks [118].

In the present work, a Netzsch Phoenix DSC 204 is used for measurements. Aluminum pans are used as reference specimen and specimen container. Cold nitrogen gas from evaporation liquid nitrogen is used for cooling. In addition, nitrogen gas at room temperature is used as purge gas and inert gas to prevent the specimen or also the measurement setup from oxidation. At least 7 mg of specimen material is used. Specimen mass is determined precisely with a precision scale. The temperature range from -100 to 150 °C is investigated. A heating and cooling rate of 10 K/min is used in accordance with standard ASTM F2004-17 [208]. Between heating and cooling a holding time of 2 min is included. DSC measurements are started from -100 °C and include heating the specimen to 150 °C, cooling back to -100 °C and heating again to 150 °C. The cooling step and the second heating step are used for evaluation. Evaluation of experimental results is conducted with Netsch analysis software. Transformation temperatures are determined using the tangent rule. Latent heats of transformation are determined to be the area between peak and the flat baseline.

## 3.2 NiTiFe

NiTiFe foils used in this work are fabricated by cold rolling. The alloys chemical composition is  $\text{Ni}_{50.5}\text{Ti}_{49.1}\text{Fe}_{0.4}$ . For sample fabrication and treatment, see above chapter 3.1. The iron content in the alloy reduces the austenite finish temperature  $A_f$  below room temperature to achieve a superelastic material behavior [209]. Mostly foils with a thickness of 30  $\mu\text{m}$  are used.<sup>j</sup>

The DSC measurement of the SMA is presented in Figure 25. Clearly a two-step transformation can be found upon heating and cooling. The transformation peak temperatures are 1 and 92 °C for the exothermic phase transition during cooling. Peak temperatures of the endothermic transition upon heating are -14 and 5 °C. The two-step transformation found in the DSC measurement indicates that the lattice structure does not directly transfer between austenite and martensite, but over an intermediate phase. This intermediate phase is referred to as rhombohedral (R-) phase [211]. The latent heat  $Q_{lat}$  represented by the areas of the two peaks sums up to 15 J/g. This  $Q_{lat}$  represents an upper limit for the latent heat accessible for stress-induced phase transformation.

---

<sup>j</sup> The content of chapter 3.2 was previously published by the author in similar form in [210].

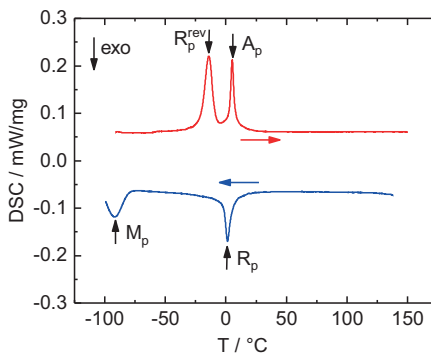


Figure 25 DSC measurement of the NiTiFe SMA foil material. Phase transitions are represented by peaks. The DSC measurement reveals a two-step transformation via an intermediate R-phase for both, the endothermic heating curve (red) and the exothermic cooling curve (blue). © 2017 IOP Publishing Ltd, figure reprinted from [210] with permission.

An engineering stress-strain characteristic of the NiTiFe SMA is displayed in Figure 26 a) for strain rates of 0.001, 0.01 and  $0.1 \text{ s}^{-1}$ . The measurement is conducted at RT. For details on the experimental procedure, see chapter 3.1. In the mechanical characterization of the material, the two-stage transformation cannot be identified. A direct conversion seems to take place. This is in line with literature that reports direct stress-induced transformation between austenite and martensite in SMA materials that show a two-step transformation upon stress-free temperature induced transition [121;212]. Critical stresses of phase transformation are determined to be  $\sigma_{AM}^{\text{crit}} = 355 \text{ MPa}$  for the forward transformation and  $\sigma_{MA}^{\text{crit}} = 166 \text{ MPa}$  for the reverse transformation. Under the low strain rate of  $0.001 \text{ s}^{-1}$ , the temperature changes due to the phase transformation are low. Thus, this condition can be considered as quasi-isothermal. Here, the stress-induced transformation from austenite to martensite takes place under constant stress within the stress plateau. This holds also true for the reverse transformation at a lower stress level. The hysteresis work  $\Delta W_{\text{mat}}$  that is dissipated by the material upon one load cycle is

represented by the area enclosed by the loading and unloading curve and is in the isothermal case  $7.5 \text{ MJ/m}^3$  or  $1.1 \text{ J/g}$ .

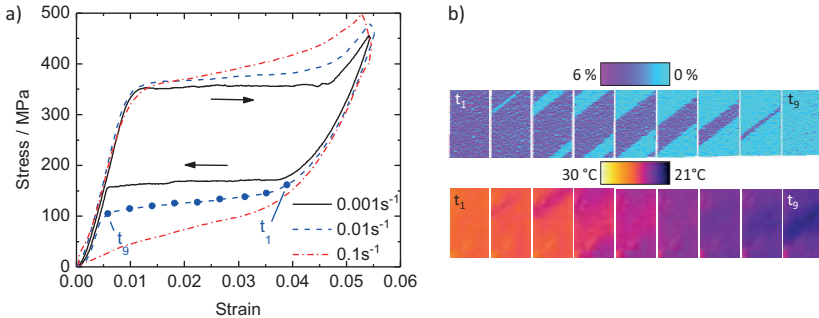


Figure 26 (a) Stress-strain curve of the superelastic NiTiFe SMA foil at three different strain rates. With increasing strain rate, the stress plateaus tilt due to self-heating and self-cooling. (b) Local strain and surface temperature profiles of the NiTiFe foil during unloading at a strain rate of  $0.01 \text{ s}^{-1}$ . Strain and temperature changes occur localized at propagating strain bands. Strain and temperature evolution are correlated. © 2017 IOP Publishing Ltd, figure reprinted from [210] with permission.

The presented characteristic is obtained after an initial training routine. Why this is needed can be understood in Figure 27. Here the stress-strain characteristic of the material is shown for the first 100 cycles. Especially between the very first cycles the material response changes largely. Critical stresses decrease and remanent strain accumulates. The critical stress of the forward transformation decreases faster compared to the critical stress of the reverse transformations and hence the hysteresis work decreases. Nevertheless, the material behavior stabilizes after about 20 cycles and only minor changes occur. All other measurements presented here are taken under an initial training to ensure constant material behavior. Increasing strain rates lead to an inclination of the stress plateaus and thus also to an increase of the hysteresis work to  $1.6$  and  $2 \text{ J/g}$  for  $0.01 \text{ s}^{-1}$  and  $0.1 \text{ s}^{-1}$ , respectively. The tilting of the stress plateaus at higher strain rates can only be understood with the thermo-

mechanical behavior of the material in mind. When the critical stress of transformation is reached, phase transformation starts and propagates through the whole stress plateau. Transformation is related to the release (loading) and absorption (unloading) of the latent heat of the phase transformation. The SMA specimen self-heats during loading and self-cools during unloading. The critical stress of transformation depends on the specimen temperature as described by the Clausius-Clapeyron relation (see equation (II), chapter 2.2.3). Thus, the critical stress increases due to increase of specimen temperature during loading and decreases during unloading. In consequence, the stress plateaus tilt increasingly with increasing strain rate.

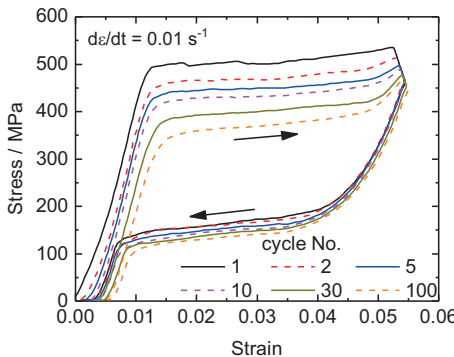


Figure 27 Stress-strain curve of the initial training of the NiTiFe foil. Especially during the first load cycles the material behavior is subjected to changes. Critical stresses decrease and remanent strain accumulates. The material behavior stabilizes after about 20 load cycles.

The local transformation behavior is also investigated in this work. Local strain maps are generated by digital image correlation (DIC), and the spatial distribution of the SMA foil's surface temperature is tracked by infrared (IR) thermography during load cycling. In Figure 26 b) the strain maps and surface temperature distributions during the reverse transformation are shown for a strain rate of  $0.01 \text{ s}^{-1}$ . The pictures are taken at indicated times (see Figure

26 a). The temperature and strain profiles suggest two conclusions. First of all, the transformation does not propagate homogenously, but strain bands with high local strain nucleate and propagate through the specimen. These strain bands are referred to as Lueders-like strain bands [146;213]. The Lueders-like strain bands orientate with an angle of  $55^\circ$  with reference to the sample edge. It has been found that the angle of  $55^\circ$  results from an equally distributed lateral transformation strain tensor [146]. Furthermore, the comparison of temperature and strain profiles shows that they are correlated. Heat is absorbed and thus the surface temperature is reduced whenever a strain band nucleates or propagates. The two propagating fronts of one strain band result in two temperature bands. Heat conduction however smears out the sharp strain band in the temperature profiles. In Figure 28 four surface temperature profiles are given for loading and unloading at strain rates from  $0.001\text{ s}^{-1}$  to  $1\text{ s}^{-1}$ . Here images 1 and 4 show the temperature profile before and after forward transformation (images 5 and 8 before and after reverse transformation). The intermediate images are taken during the transformation evenly distributed in time. The comparison of the temperature profiles taken at different strain rates shows that with increasing strain rate the temperature changes clearly increase. At high strain rates the number of strain bands increases considerably. The high number of bands leads to more uniform temperature profiles. At low strain rates mostly one temperature band forms at the specimen fixation and propagate through the whole sample. At high strain rates however, a fine net of temperature bands form. This can be understood again by the thermo-mechanical behavior of the material during transformation. At high strain rates temperature increases considerably at the propagating strain bands and therefore the critical stress of transformation is increased (see above), and the further propagation is hindered. Thus, at high strain rates the nucleation of a new strain band in an untransformed region of the sample becomes more favorable compared to further propagation of existing strain bands.

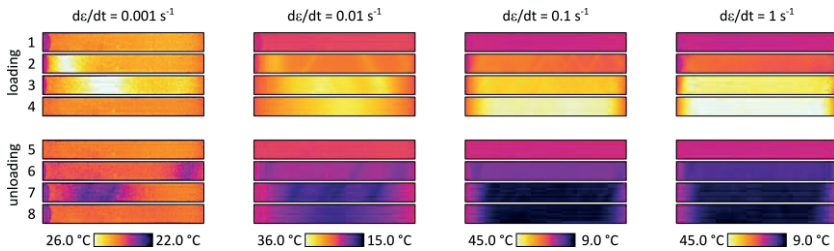


Figure 28 Local surface temperature profiles of the NiTiFe foil during load cycling at four different strain rates between  $0.001\text{ s}^{-1}$  and  $1\text{ s}^{-1}$ . In each case, one image depicts the temperature profile before the transformation occurs (1, 5), after the transformation (4, 8) and two images taken during the transformation. With increasing strain rate, the number of temperature bands increases and temperature profiles become increasingly homogenous.

Besides the surface temperature profiles at distinct times, IR-measurements reveal the temperature evolution of the SMA foils during load cycling. In Figure 29 a) the temperature evolution versus time is depicted for different strain rates. In Figure 29 b) the maximum temperature changes during loading and unloading are displayed as a function of the strain rate. For low strain rates the temperature changes vanish as isothermal conditions are approached. On the other side, temperature changes saturate above  $0.1\text{ s}^{-1}$ , as quasi-adiabatic conditions are reached. Under quasi-adiabatic loading conditions, the adiabatic temperature change  $\Delta T_{ad}$  of the material, an important elastocaloric figure of merit, can be determined. The given material shows a  $\Delta T_{ad}$  of  $20\text{ }^{\circ}\text{C}$  during loading and  $-16\text{ }^{\circ}\text{C}$  during unloading.

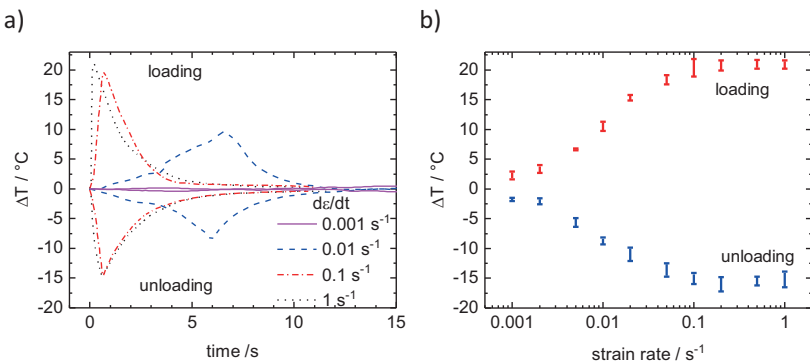


Figure 29 (a) Time-dependent temperature evolution of a NiTiFe foil specimen during mechanical loading and unloading at three different strain rates. (b) Temperature changes of a NiTiFe foil specimen upon load cycling as a function of the applied strain rate. At low strain rates, the isothermal case is approached. Released and absorbed heat is directly transferred to the surrounding and does hardly change the specimen temperature. At high strain rates, the adiabatic limit is approached. Heat transfer to the surrounding is hindered. Under quasi adiabatic conditions, the adiabatic temperature change  $\Delta T_{ad}$  of the material is defined to be  $20^\circ C$  during loading and  $-16^\circ C$  during unloading. © 2017 IOP Publishing Ltd, figure reprinted from [210] with permission.

From the adiabatic temperature changes also the latent heat of the transformation can be accessed. This is referred to as direct measurement method in literature (see chapters 2.2.5, 3.1.3) [35]. For the given material, the latent heat of transformation derived by the direct method is  $9 \text{ J/g}$  (loading) and  $7.2 \text{ J/g}$  (unloading). These values are lower compared to the value determined by DSC measurements presented above. Most likely, this is the case since the stress-induced phase transformation can only partly access the latent heat of the thermal transformation [145;146]. Thus, values determined by the direct measurement technique are reduced.

With latent heat of transformation and hysteresis work of the material both at hand, one can determine the  $COP_{mat}$  of the material as a measure for its elastocaloric efficiency. Unsurprisingly, the different values for  $Q_{lat}$  obtained

by different measurement techniques lead to different values of  $COP_{mat}$ . Maximum values are obtained comparing quasi-direct measured  $Q_{lat}^{quasi}$  from DSC measurements with the isothermal hysteresis work  $\Delta W_{mat}^{iso}$ . For the calculation of  $\Delta W_{mat}$  complete work recovery is assumed. This approach leads to an upper limit of  $COP_{mat}$ , which is 13 for the given material. Another approach is dedicated to the thermodynamic cycle the material undergoes in quasi-adiabatic tensile testing. Here, the direct measured  $Q_{lat}^{direct}$  and the  $\Delta W_{mat}^{ad}$  under adiabatic conditions are used for the calculation of  $COP_{mat}$ . In this case  $COP_{mat}$  is determined to be 3.6.

To avoid confusion, NiTiFe foils are also referred to as films in the context of SMA film-based elastocaloric cooling devices in the chapters below.

### 3.3 TiNiCuCo

Sputtered TiNiCuCo films are used as elastocaloric materials within this work. The outstanding advantage of TiNiCuCo films is their ultra-low fatigue behavior [13;155]. The TiNiCuCo films used in this work are fabricated at Kiel University according to the process described above in chapter 3.1.1. The ultra-low fatigue properties in Ti-rich TiNiCu-based films can be maintained over a broad compositional window. Transformation temperatures of these film can either be lowered by reducing the annealing temperatures and thereby forming Guinier-Preston-Zones, or by adding Cobalt in small amounts (< 4 at.%) [159;214]. It was shown that tailoring  $A_f$  by the Co-content maintains larger latent heat of transformation [155;159;215]. The cobalt content in the alloy is known to shift  $A_f$  by 22.3 K/at.% [155]. Here, films with three slightly different alloy compositions are presented. The three SMAs are denoted as TiNi-CuCo<sub>1</sub>, TiNiCuCo<sub>2</sub> and TiNiCuCo<sub>3</sub> and have a chemical composition of  $(\text{Ti}_{55}\text{Ni}_{33}\text{Cu}_{12})_{100-x}\text{Co}_x$  with a slight change in the cobalt content around 2.4 at.%. The cobalt content increases from TiNiCuCo<sub>1</sub> to TiNiCuCo<sub>3</sub> to tune  $A_f$  in the three materials (compare Table 7).

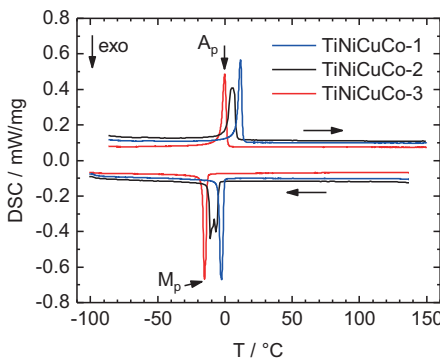


Figure 30 DSC measurement of three TiNiCuCo based alloy compositions with increasing Co-content from TiNiCuCo-1 to TiNiCuCo-3. The increase of the Co-content reduces  $A_f$ . In the TiNiCuCo SMAs the forward and reverse phase transformation occurs in one-step indicated by a single sharp peak in the DSC curve.

In the DSC-measurement of the three materials depicted in Figure 30 a clear shift of the transformation temperatures can be found. The austenite finish temperature  $A_f$  of the materials TiNiCuCo-1, TiNiCuCo-2 and TiNiCuCo-3 is 13.3, 8.5 and 1.7 °C, respectively. The decrease of  $A_f$  is attributed to the increased Co-content. The TiNiCuCo alloy shows a sharp direct transition for both, endothermic heating and exothermic cooling. In TiNiCuCo-2, the transformation peak during cooling is split into two peaks close to each other, for which improper sample preparation has been identified as the most likely cause. In samples prepared by sputter deposition a slight composition gradient can occur along the sputtered specimen, especially for large dimensions. Most likely, the peak split originates from the DSC specimen that was combined from several film pieces. The quasi-direct measured latent heat of the phase transition that is represented by the peak area in the DSC measurement, can be determined to be 10.4 J/g for TiNiCuCo-1 and -3. For above reasons, the numbers for TiNiCuCo-2 have not been evaluated.

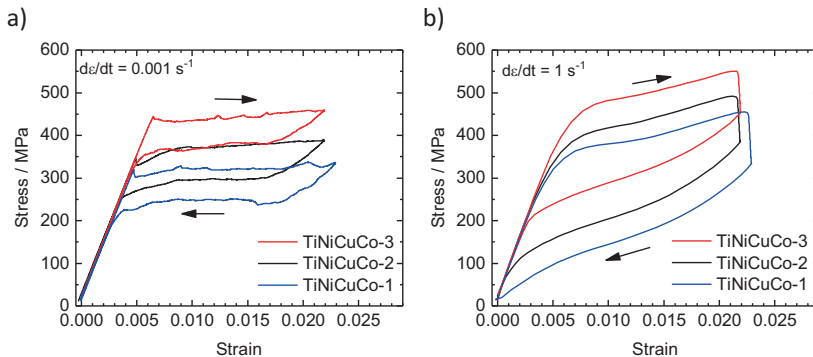


Figure 31 Stress-strain curves of TiNiCuCo-1, -2 and -3 specimen under isothermal loading conditions at a strain rate of  $0.001\text{ s}^{-1}$  (a) and under adiabatic loading conditions at  $1\text{ s}^{-1}$  (b).

The superelastic stress-strain characteristics of the materials under isothermal conditions is depicted in Figure 31 a). All three materials show a narrow stress hysteresis. The main difference is the change of critical stress. The end of the stress plateau under isothermal loading conditions is chosen as the maximum applied strain for all three TiNiCuCo alloys. The critical stress of the forward transformation  $\sigma_{AM}^{crit}$  increases from 320 MPa in TiNiCuCo-1 to 370 MPa in TiNiCuCo-2 and 440 MPa in TiNiCuCo-3. Critical stresses of reverse transformation are 240, 290, 370 MPa for TiNiCuCo-1, -2, -3, respectively. The Clausius Clapeyron coefficient of the forward transition in the materials system is known to be 10.4 MPa/K [155]. Thus, the change in  $A_f$  and the change in critical stresses found in the three alloy compositions are in balance with each other. The Young's modulus of austenite is 65 GPa and the same for all investigated TiNiCuCo alloys. The hysteresis work of the three materials is measured to be 0.2 J/g (TiNiCuCo-1), 0.18 J/g (TiNiCuCo-2), 0.14 J/g (TiNiCuCo-3) for the isothermal case at a strain rate of  $0.001\text{ s}^{-1}$ . High strain rates change the shape of the superelastic stress-strain characteristics. In Figure 31 b) the stress-strain characteristics of the materials in the adiabatic limit ( $d\varepsilon/dt = 1\text{ s}^{-1}$ ) is presented. The loading and unloading stress plateaus tilt due

to the self-heating and cooling of the SMA film during load cycling. As the transformation starts, the released (for the reverse transformation during unloading: absorbed) latent heat of the transformation causes an increase (decrease) of the SMA film temperature. Due to the Clausius Clapeyron relation the critical stresses of transformation increase (decrease) with temperature. This effect leads to an increase (decrease) of the plateau stress as the transformation proceeds under conditions where the released (absorbed) heat cannot be transferred directly to the environment. Although the stress-strain curves of all TiNiCuCo films change under high strain rates, the shift of stress in between the materials remains. A closer look at the stress-strain curve of TiNiCuCo-1 under adiabatic conditions shows that its  $A_f$  represents a limit case for the given materials system at room temperature. If  $A_f$  would only be slightly higher and thus the critical stresses slightly lower, the material would not transform back directly upon unloading. The stress would come back to zero at a strain larger than zero. In this case, additional time would be needed to absorb heat from the environment and heat up, before the complete backward transformation could occur. This is not acceptable for elastocaloric cooling applications.

Other than the NiTiFe SMA foils discussed above in chapter 3.2, the TiNiCuCo SMA films do not need a mechanical training prior to material characterization. TiNiCuCo SMA films show very constant material behavior from the first loading cycle. In Figure 32 a) the stress-strain curve of the first 1000 mechanical load cycles of a TiNiCuCo-1 film is shown. Only slight deviations can be found. The stress-strain curve has a slightly different shape compared to the ones presented above, since in this experiment no holding times are included between loading and unloading. This alters the thermal conditions of the SMA during load cycling.

Surface temperature profiles depicted in Figure 33 give additional insights how temperature changes and how phase transformation occurs in the TiNi-CuCo films. As before in Figure 28 for NiTiFe foils, at each strain rate one picture is taken before and after forward (1, 4) and reverse (5, 8) transformation.

Two images are taken during transformation (2, 3; 6, 7). Clearly the non-homogenous nature of temperature evolution can be understood. The comparison of surface temperature distributions with local strain maps in the previous chapter reveals that both are closely correlated in superelastic SMAs. Therefore, the surface temperature plots in Figure 28 do not only show the non-homogenous temperature profiles but also the non-homogenous transformation behavior of the TiNiCuCo films. The transformation takes place by nucleation and growth of Lueders-like strain bands. The moving interfaces of the strain bands are represented by bands of higher temperature during loading and lower temperature during unloading. Thus, each strain band is represented by two temperature bands in the presented surface temperature profiles. At low strain rate of  $0.001\text{ s}^{-1}$ , few bands nucleate at the film fixations and propagate through the sample. At increasing strain rates, more bands nucleate as the nucleation of new bands in untransformed and thermally unaffected regions is favored compared to the growth of bands. In the adiabatic limit the net of bands becomes increasingly dense. The temperature distribution becomes almost uniform.

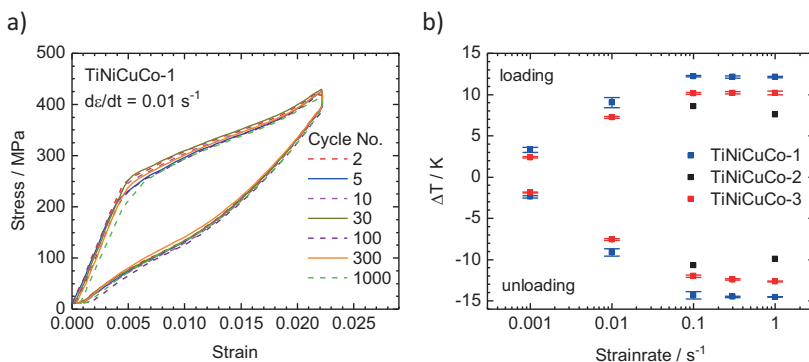


Figure 32 (a) Stress-strain curves of selected load cycles from the second to 1000<sup>th</sup> load cycles. The SMA shows very stable mechanical properties without degradation. (b) Temperature changes of TiNiCuCo-1, -2, -3 specimen upon load cycling as a function of the applied strain rate. Loading conditions range from quasi-isothermal conditions ( $0.001\text{ s}^{-1}$ ) to quasi-adiabatic conditions ( $>0.1\text{ s}^{-1}$ ).

The maximum temperature lift and decrease that occurs during loading and unloading is plotted versus strain rate in Figure 32 b) for the TiNiCuCo materials. The adiabatic limit is reached above  $0.1\text{ s}^{-1}$ . The adiabatic temperature changes  $\Delta T_{ad}$  differ between the three alloys. Upon heating  $\Delta T_{ad}$  of materials TiNiCuCo-1, TiNiCuCo-2, TiNiCuCo-3 is 12.2 K, 8.1 K, 10.2 K, respectively. Upon cooling  $\Delta T_{ad}$  is -14.5 K, -10.3 K, -12.4 K, respectively. TiNiCuCo-1 reaches the highest  $\Delta T_{ad}$ , TiNiCuCo-2 the lowest. The finding that TiNiCuCo-1 reaches the highest  $\Delta T_{ad}$  is in line with expectations, as it is known that the latent heat of transformation increases in SMAs with higher  $A_f$  [12;155]. Accordingly, TiNiCuCo-3 should have the lowest  $\Delta T_{ad}$ , not TiNiCuCo-2. The increased  $\Delta T_{ad}$  of TiNiCuCo-3 compared to TiNiCuCo-2 might be explained by the combination of two effects. A lower maximum strain has been applied to TiNiCuCo-2. Thus, a lower percentage of the TiNiCuCo-2 film did undergo the transformation under high strain rates. In addition, the increased annealing temperature in TiNiCuCo-3 is known to increase the latent heat of the transformation in TiNiCu-alloys [215]. The latent heat of the transformation  $Q_{lat}$  deduced from the direct measurement of  $\Delta T_{ad}$  is 6.5 J/g, 4.6 J/g, 5.6 J/g for the three materials 1, 2, 3, respectively. These are about half of the value measured by DSC measurements. As discussed before in chapter 3.2 the elastocaloric efficiency  $COP_{mat}$  of the materials can be calculated based on different numbers. An upper limit of  $COP_{mat}$  is obtained setting quasi-direct measurements of  $Q_{lat}^{quasi}$  from DSC measurements into relation with the iso-thermal hysteresis work  $\Delta W_{mat}^{iso}$ . In this case  $COP_{mat}$  of TiNiCuCo-1, TiNiCuCo-2, TiNiCuCo-3 is 52, 60, 72, respectively. If  $COP_{mat}$  is calculated based on the directly measured  $Q_{lat}^{direct}$  and the  $\Delta W_{mat}^{ad}$  that were measured in exactly the same load cycle values for the three materials 1, 2, 3 are 9.7, 8.4, 12.1, respectively. These values are directly related to the thermodynamic cycles that the SMA films undergo upon adiabatic load cycling in air with holding times after loading and unloading and represent a much more realistic value with reference to application.

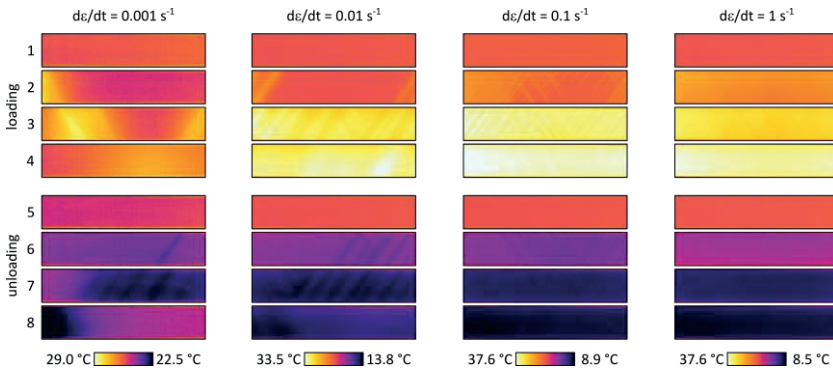


Figure 33 Surface temperature profiles before (1), during (2, 3), and after (4) mechanical loading and unloading (5-8) at different strain rates. Images are taken from IR-measurements with TiNiCuCo-1. Temperature changes occur where strain bands nucleate or propagate. The higher the strain rate, the more bands form and the more uniform the temperature profiles occurs.

A comparison between the NiTiFe foils and the TiNiCuCo films reveals that the elastocaloric effect size in terms of  $Q_{lat}$  and  $\Delta T_{ad}$  is higher in the NiTiFe foils. For an elastocaloric demonstration device, the use of NiTiFe might be favorable, since slightly higher device temperature spans and cooling capacities are expected with NiTiFe. The more the development goes towards application, the more important become the advantages of TiNiCuCo films. TiNiCuCo films have a higher efficiency  $COP_{mat}$  and especially promising ultra-low fatigue properties. In addition, transformation temperatures can easily be tailored in TiNiCuCo films according to the application.

# **4 Concept and Operation of SMA Film-Based Elastocaloric Cooling Devices**

## **4.1 General Concepts**

In chapters 5 and 6, all elastocaloric cooling demonstrators developed within this work are presented and discussed. Although the demonstrators have different scopes and functional principles, the main underlying concept remains similar for most of them: cyclic mechanical deflection and release of SMA films, and separation of hot and cold heat flows by changing mechanical contacts of the SMA film with additional solid heat sink and source elements. This common approach is discussed in chapter 2.3.5 in detail. In the following chapters basic concepts unique to the SMA film-based elastocaloric cooling devices developed in this work are discussed. So, a basis is provided for the understanding of the designs and concepts of the different cooling devices.

### **4.1.1 Compliant Structures in SMA Film-Based Cooling Devices**

For the performance of all SMA film-based elastocaloric cooling devices, the quality of the mechanical contact between the film and the solid heat source and sink elements is of tremendous importance. The contact can be considered appropriate with a low thermal contact resistance, if both metal parts have a smooth and flat contact surface, a sufficient contact pressure is applied, and no misalignment between the surfaces exists [16;169]. Here, compliant spring-like structures are proposed to achieve the desired contact pressure, and to avoid the negative consequences of misalignment [169;210].

In Figure 34 the example of the contact between SMA film and heat source demonstrate how compliant structures help to achieve good thermal contacts. Even though in practice dimensions are subject to inaccuracies and tolerances. As a result, the question is not whether there is an angular misalignment between the SMA film and the heat source, but only how large the inaccuracy is. An angular misalignment is very critical for a good surface contact, and should therefore be minimized as it leads to an unfavorable line contact instead (see Figure 34 a). To avoid this issue, fabrication precision has to be very high, or the misalignment must be compensated for with a compliant suspension of the heat source (see Figure 34 a). Especially in miniaturized systems the effort to achieve the necessary fabrication accuracy is often extremely high. Accordingly, inaccuracies cannot be avoided but need to be compensated.

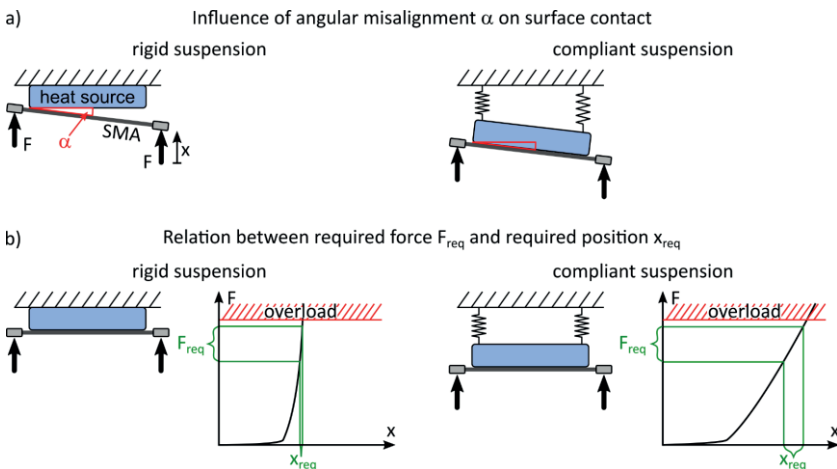


Figure 34 (a) Influence of an angular misalignment  $\alpha$  on the surface contact in devices with rigid (left) and compliant (right) suspension of the solid heat source. The compliant suspension compensates for the misalignment and thus ensures a flat contact over the whole surface. (b) The required contact force  $F_{req}$  needs to be high enough to ensure efficient heat transfer, and at the same time must be limited to avoid damage to the setup. In case of a compliant suspension this requirement can be easily met, since the required accuracy of the position  $x_{req}$  is poor.

As illustrated in Figure 34 b), compliant support structures are beneficial in a second way. A low and reproducible thermal contact resistance between the two solid surfaces is only achieved if the contact pressure between the surfaces is high enough [216]. At the same time, there is also an upper limit, too high contact forces can damage the setup. In addition, the critical stress of the phase transformation of the SMA must not be reached at the heat source. Thus, there is a limited range of forces  $F_{req}$  suitable for the contact force. As a general rule, the actuation unit of an elastocaloric device is operated via a position control. The suitable positions  $x_{req}$  to reach  $F_{req}$  depends on the force-displacement characteristic of the combined system of actuator unit, SMA film, heat source and support structure. A system with a rigid support structure generally is characterized by a steep force-displacement characteristic and therefore the position control of the actuator has to be very precise to reach the desired contact forces. At the same time any deviations in the setup involve serious consequences. A system including compliant structures in contrast shows a gradual increase of the force with the displacement. Hence, a lower position accuracy of the actuator unit is sufficient to ensure the desired force range and the system reacts more forgivingly to inaccuracies. The advantages of a compliant system apply to both, the contact to the heat source and to the heat sink. As an example, the compliant structures in the coupled device have a spring constant of 16 and 3 N/mm at the heat sink and source, respectively. If the motor position varies by 0.2 mm due to overshooting at high frequencies, the resulting change of the contact force is only 0.6 N in case of the contact with the heat source. This is uncritical to the device. If the source would be fixed with a more rigid suspicion (i.e., with a spring constant of 150 N/mm) the very same deviation of the position would result in an additional force of 30 N. This would most likely damage the SMA film.

### 4.1.2 Scaling Laws of Elastocaloric Refrigerators

The performance of an elastocaloric refrigerator is highly influenced by the size and geometry of the elastocaloric material used. Especially in case of miniaturized cooling systems, scaling laws become highly important. The subsequent investigation focuses on the scaling laws in elastocaloric refrigerators and reveals how the performance of an elastocaloric refrigerator is influenced by miniaturization of the elastocaloric materials geometry and its surface-to-volume ratio<sup>k</sup>. The aim is not a precise calculation, but to reveal general trends valid for scaling. Not included in the following investigation is the influence of insulation that is discussed later.

From a thermal point of view, there are two dominant physical processes in elastocaloric refrigerators: first, the heat release and absorption in an elastocaloric material due to the elastocaloric effect, and second, the heat transfer between the elastocaloric material and heat sink and source. The release and absorption of the latent heat of phase transformation  $Q_{lat}$  in the elastocaloric material is a volumetric effect. It scales with the volume of the elastocaloric material  $Q_{lat} \sim V \sim r^3$ . In other words, the amount of heat is proportional to the volume  $V$  of the material.  $r$  represents a generalized spatial length dimension. The heat exchange of the elastocaloric material with the heat sink and source elements must pass through the surface area of the elastocaloric material. Therefore, it scales in first approximation with the surface area  $A$  ( $\dot{Q} \sim A \sim r^2$ ). As the two processes follow different scaling laws, the surface-to-volume ratio of the elastocaloric material geometry is particularly important.

In the following simplified study, it is assumed that the mechanical loading and unloading takes place under adiabatic condition independent of the geometry. Furthermore, the elastocaloric element is assumed to be thermally thin. In this case, it can be modeled as a single concentrated thermal element with a single uniform temperature  $T_{SMA}$ . The heat sink is assumed infinite and

---

<sup>k</sup> The content of chapter 4.1.2 was previously published by the author in similar form in [23].

thus its temperature stays at constant  $T_0$ . The SMA element and the heat sink are coupled to each other via the heat resistance  $R = 1/hA$ . A schematic of the model is illustrated in Figure 35 a,i). The thermal energy balance of the system writes as:

$$\rho V c_p \dot{T}_{SMA}(t) = hA(T_{SMA}(t) - T_0) \quad (\text{XVI})$$

$\rho$  represents the mass density,  $c_p$  the specific heat capacity and  $h$  the heat transfer coefficient to the heat sink. Assuming, the observation starts with the moment the elastocaloric material has just been adiabatically loaded ( $T_{SMA}(t = 0) = T_0 + \Delta T_{ad}$ ), the analytical solution for the temperature evolution is as follows:

$$T_{SMA}(t) = T_0 + \Delta T_{ad} e^{-\frac{t}{\tau}}, \quad \tau = \frac{\rho c_p V}{hA} \quad (\text{XVII})$$

with the time constant of heat transfer  $\tau$ .

Based on the assumptions and the resulting simple equation, various scaling trends of an elastocaloric refrigerator can be deduced. The heat transfer coefficient  $h$  is considered independent of the size. The minimum period  $T_{period}$  of operation is mainly defined by the time needed for heat transfer after mechanical loading and unloading, so  $T_{period} \sim \tau \sim V/A \sim r$ . Thus, the maximum operation frequency scales as  $f = T_{period}^{-1} \sim r^{-1}$ . The maximum cooling capacity that can be provided by an elastocaloric material is proportional to the latent heat that is absorbed each operation cycle and is directly proportional to the operation frequency as well. Accordingly, the provable absolute cooling capacity scales with  $\dot{Q}^{cool} \sim f Q_{lat} \sim r^{-1} r^3 = r^2$ , cooling capacity per surface area with  $\dot{q}_A^{cool} = \dot{Q}^{cool} A^{-1} \sim r^0$ , and the volumetric cooling capacity  $\dot{q}_V^{cool} = \dot{Q}^{cool} V^{-1} \sim r^{-1}$ .

The assumptions needed for the analytical, single concentrated mass model might not be valid for all possible scenarios, in particular thicker samples. Therefore, a second model is set up. The second model assumes the elasto-

caloric material to have a flat film or sheet like geometry. An infinite plate of elastocaloric material is assumed that is in direct contact to a second infinite plate from copper, that represents the heat sink. In this case, the elastocaloric material is assumed to be a NiTi SMA. Both infinite plates are discretized along the axis perpendicular to the plate surface. Temperature profiles within the elastocaloric material and the heat sink are possible in this way. The one dimensional lumped element model (LEM) is illustrated in Figure 35 a,ii). The elastocaloric material is modeled by 5 elements, the sink by 15 elements. The contact heat resistance between the SMA and the copper plate is taken to be  $h_{cont} = 1000 \text{ W/m}^2\text{K}$ . The second side of the heat sink is coupled to the environment with  $h_{cont}$  as well. In this showcase the thickness of the copper plate is assumed to be 5 mm, the thickness of the SMA is varied between 10  $\mu\text{m}$  and 3 mm. As in the simple analytic model, adiabatic loading is assumed, with  $\Delta T_{ad} = 10^\circ\text{C}$ . So in the simulation the initial temperature of the SMA is  $T_{SMA}(t = 0) = T_0 + \Delta T_{ad}$  and the initial temperature of the copper heat sink is  $T_{SMA}(t = 0) = T_0$ . The model is implemented and solved numerically in the MATLAB addon Simscape. In analogy to the simplified analytic model, the time constant of heat transfer is determined at the time at which the average temperature of the SMA reaches  $T_0 + \frac{1}{e} \Delta T_{ad}$ . The calculation of the maximum possible frequency assumes the heat transfer to be completed when 80 % of the heat is transferred from the SMA to the heat sink. Based on the absolute latent heat released in the SMA and the maximum possible operation frequency the cooling capacity per contact area is calculated. The results of this investigation are plotted in Figure 35 b) over the thickness of the SMA and presented with the analytical solution in the same plot. For small thicknesses of the SMA below 100  $\mu\text{m}$  the results of the LEM model and the simplified analytical model are consistent. With increasing SMA thickness, a deviation between analytical and numerical results arises. Increasing thickness leads to a non-uniform temperature profiles in both, the SMA and the copper plates, and thus, additional internal heat resistance comes into play. In other words, the assumptions of the analytical model lose their validity for thick samples. In the given showcase the critical thickness is 100  $\mu\text{m}$ . For

thicker samples, the cooling capacity per contact area drops and the SMA cannot be used efficiently. The scaling laws derived above clearly overestimate the performance of thicker samples.

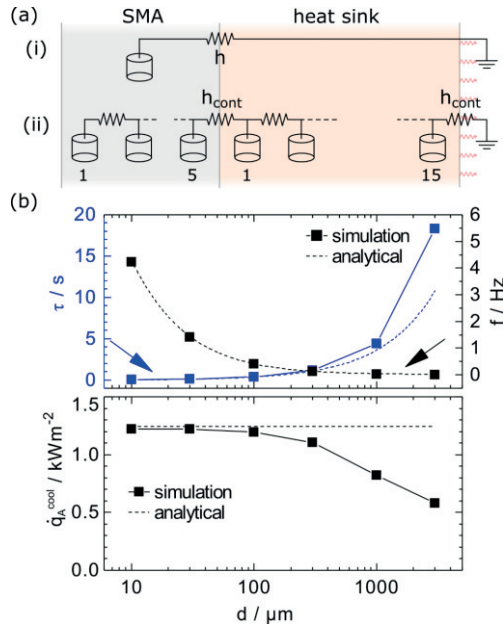


Figure 35 Graphical illustration of thermal equivalent circuits used in the simplified analytical model (a,i), and the 1D discretized lumped element model (LEM) (a,ii). Both models represent a SMA film or plate in contact to a copper heat sink that is coupled to ambient. The models are used to estimate the influence of the SMA thickness on the operation frequency and the cooling capacity of an elastocaloric cooling device (b). © 2018 Wiley-VCHVerlag GmbH&Co. KGaA , figure reprinted from [16] with permission.

Both models are simplified and closely related to the SMA film-based setups developed in this work. The key detail of all elastocaloric refrigerators are covered: the heat transfer from the elastocaloric material to the heat sink. Hence, overall trends derived above remain valid for other elastocaloric

devices, although numbers will change. Decreasing the geometry size of the elastocaloric system will improve the specific cooling capacity. Therefore, miniaturization has a huge potential in the field of elastocaloric cooling. Investigations by Qian et al. on the optimization of a elastocaloric cooling system that is based on an entirely different concept with an HTF agree with the general trends found here [30;192]. The surface-to-volume ratio of the SMA geometry is of highest importance for efficient elastocaloric systems. The scaling laws derived above show that miniaturization is especially beneficial for elastocaloric cooling devices in terms of volumetric or specific cooling capacity.

Other challenges arise upon miniaturization of elastocaloric devices. In miniaturized systems, efficient insulation is increasingly challenging with decreasing feature sizes. Temperature gradients increase and at the same time the volume available for insulation decreases. Thus, it becomes increasingly challenging to obtain high device temperature spans in miniaturized systems. In addition, fabrication and assembly requires completely different technologies when it comes to microscale systems. Miniaturized elastocaloric cooling systems need simplified designs that fit the needs of available fabrication, actuation and insulation technologies. This gives a limit to the miniaturization of elastocaloric systems despite the advantageous scaling laws.

The derived scaling laws highlight the importance of the surface-to-volume ratio of the elastocaloric material geometries. In future, new fabrication technologies, like Additive manufacturing of SMAs, possibly have the potential to provide high surface-to-volume SMA geometries on a larger scale [143;160]. For example, honeycomb SMA structures might be an future alternative [143]. Nevertheless, currently thin films and thin wires are most promising due to their availability and technologically mature fabrication processes.

### 4.1.3 Cascaded System Architecture for Increased Temperature Span

The fundamentals of the elastocaloric cooling cycle are explained in chapter 2.3.5. Thermodynamic cycles that can be applied to a single uniform element of elastocaloric material have a limited temperature span. This limit originates from the adiabatic temperature span of the material  $\Delta T_{ad}$ . In the reverse Brayton cycle illustrated in Figure 36 a) the temperature increase (0-1) and decrease (2-3) are represented by the adiabatic temperature change of the material  $\Delta T_{ad}$ , and thus are limited. Assuming that the SMA element can exchange heat exclusively with the heat sink and source, the device temperature span is represented by  $\Delta T_{device} = T_2 - T_0$ . The larger  $\Delta T_{device}$  is, the less heat can be transferred between the SMA element and the heat sink and source in step (1-2) and step (3-0). When  $\Delta T_{device}$  approaches  $\Delta T_{ad}$ ,  $T_2$  approaches  $T_1$ , and  $T_3$  approaches  $T_0$ . Hence, no heat can be transferred anymore. In consequence,  $\Delta T_{ad}$  is the ultimate limit of  $\Delta T_{device}$  for an elastocaloric cycle based on the reverse Brayton cycle. However, in a real device the SMA element might also exchange heat with ambient, which complicates the above consideration. In best case, the heat exchange with ambient could have an effect similar to heat recovery explained in chapter 2.3.4. Nevertheless, the device temperature span of a single SMA element is ultimately limited. One way to overcome this limitation is a cascaded system architecture [177;218]. In a cascaded system, the cooling and heating capacity of one caloric element is used to precool or preheat the neighboring caloric element in a series connection. In this way, the temperature span of each single element is still limited as discussed before, but complete system is not, as the limits add up. The operation temperature of each cascaded element differs, and thus the overall temperature span of the system increases. In Figure 36 b) the Brayton cycles of three cascaded elements and their interactions are shown in a schematic way. The cooling capacity of the complete system is provided by last element that is directly connected to the external heat sink. Similar, heat is only released to the environment through the first unit. All the other heat flows of the single units are used internally in the system to

precool the next unit. Elastocaloric cooling devices based on a cascaded system architecture are presented and characterized in chapter 6.2 and 6.3.

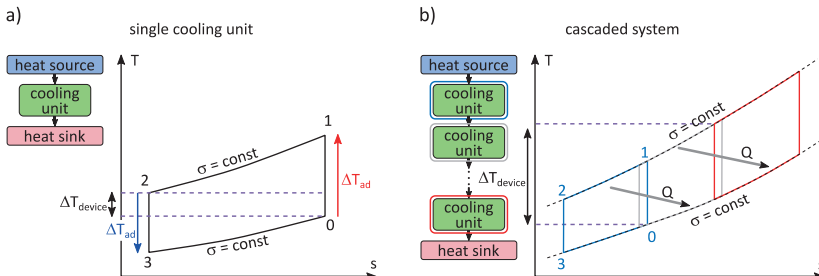


Figure 36 Schematic temperature-entropy diagram of a reverse Brayton cycle. (a) Cycle of a single unit is shown. (b) Cycles of three cascaded units. The cascaded architecture enables increased device temperature spans. Figure adapted from [217] with permission from VDE VERLAG GMBH.

#### 4.1.4 Parallelized System Architecture for Increased Cooling Capacity

The first idea to increase the cooling capacity of a system is often to simply enlarge the system. This only works to a limited extent in elastocaloric systems, as discussed in chapter 4.1.2. If the system, including the elastocaloric material, is simply enlarged, the surface-to-volume ratio of the elastocaloric material geometry decreases. Although the absolute amount of latent heat absorbed within the elastocaloric material per operation cycle increases with the volume, the heat transfer between the active material and its surrounding is hindered. Therefore, the surface-to-volume ratio of the elastocaloric materials geometry has to be preserved in enlarged systems.

One promising concept to do so in SMA film-based elastocaloric refrigerators is the parallel interconnection of single SMA film-based refrigerators into a larger system (see Figure 37 b). In this way the performance of the single

refrigeration unit can be preserved but the cooling capacity of the parallelized system is increased with the number of parallelized units. In particular, the cooling capacities of the parallelized units add up, while the active material in all units follows the same thermodynamic cycle. This approach also allows new actuator concepts with either numerous distributed actuators or a single motor with a force distribution mechanism operating a number of cooling devices simultaneously.

Series connection and parallel connection can also be combined in a modular approach, which is not considered in this thesis. This would allow to fit the system characteristic to a specific application. The series connection of cooling units into cascades would enable the desired system temperatures span, and in the same system, parallel connected modules set the desired cooling capacity. Therefore, this modular approach would allow customized system characteristics based on the interconnection of modular standardized cooling units.

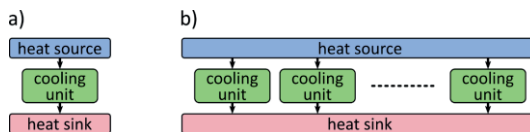


Figure 37 Schematic of a single cooling unit (a) and a parallelized system (b) in which the cooling capacities of the single units add up to the system cooling capacity.

## 4.2 Device Simulation

The performance of SMA film-based cooling devices is the outcome of the complex interplay of:

- Mechanical loading and unloading of the SMA
- Heat absorption and release in the SMA film due to the elastocaloric effect

- Changing contact conditions between SMA film and heat sink and source elements
- Heat flows between the elements of the device and the environment.

Sudden changes in conditions and many cross dependencies prevent an analytical assessment of the system. Numerical simulation is well suited to improve the understanding of the device performance. Here, a lumped element model (LEM) approach is used<sup>1</sup>. In LEM approaches a specially distributed physical system is represented by discrete components with concentrated properties. The concept is well known from the modelling of electrical systems by electrical equivalent circuits, but can also be applied to other areas, in this case thermal systems [178;210].

In thermal LEMs, physical elements are discretized into discrete thermal masses or capacities with a single uniform temperature. These discrete thermal masses are interconnected by thermal resistances to allow for heat transfer between them [219,pp. 256–270]. In thermal LEM, the Biot number can be used to estimate, if modeling an element as one single thermal mass with uniform temperature is appropriate or not. The Biot number relates the internal heat resistance in an element to the surface heat resistance ( $Bi = R_{internal}/R_{surface} = hL_0/k$ , characteristic length:  $L_0$ , surface heat transfer coefficient:  $h$ , thermal conductivity:  $k$ ) [219,p. 260]. If the surface heat resistance dominates ( $Bi \leq 0.1$ ) the assumption is considered valid. If not, further discretization is indicated [219,p. 261].

The LEM approach is discussed here on the basis of the coupled device (see chapter 5.4). Due to the symmetry in two dimensions, only one fourth of the system is considered in the model. A graphical illustration of the thermal equivalent circuit is presented in Figure 38. The model is based on three thermal capacities representing the heat source ( $C_2$ ), the SMA film ( $C_1$ ) and the heat

---

<sup>1</sup> The content of chapter 4.2 was previously published by the author in similar form in [210].

sink ( $C_3$ ), or more precisely one quarter of each. All three thermal masses are coupled to the environment via conductive and convective heat transfer represented by  $R_{1,2,3}^{cond}$  and  $R_{1,2,3}^{conv}$  with  $R^{cond} = \frac{1}{A L_0} k$  (surface area  $A$ ). The thermal masses are interconnected via the resistances  $R_{12}^{cont}, R_{13}^{cont}$  that represent the contact heat resistance between the SMA film and the sink and source element. These resistances are changed in an on-off manner, based on the changing contact condition within the elastocaloric cooling cycle. Convective and contact heat resistances are calculated as  $R^{cont,conv} = \frac{1}{Ah}$ , heaviside functions are used to turn the contact heat resistance on and off based on the SMA elements position. The values for the heat transfer coefficients  $h_{12}^{cont}$ ,  $h_{13}^{cont}$  and  $h_{1,2,3}^{conv}$  are 800, 3700, 6 W/m<sup>2</sup>K, respectively. In addition, a heat release and absorption term  $\dot{Q}_L$  is introduced and directly connected to the SMA element to simulate the elastocaloric effect. The underlying material model is discussed below.

In general, the internal energy balance of an elastocaloric material can be expressed as follows:

$$\rho c_p \dot{T} = \nabla(k(x_M) \nabla T) + \dot{q}_L(\dot{x}_M) \quad (\text{XVIII})$$

The materials volumetric mass density is represented by  $\rho$ , the specific heat capacity by  $c_p$ . The thermal conductivity  $k$  is dependent on the martensitic phase fraction  $x_M$ . The volumetric heat release and absorption within the material due to the elastocaloric effect is described by  $\dot{q}_L$ .

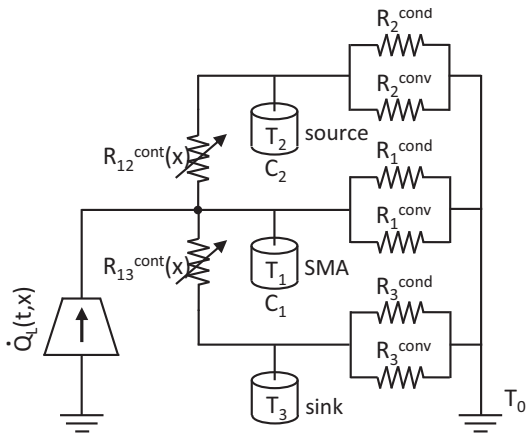


Figure 38 Lumped element model (LEM) thermal equivalent circuit representing the coupled device discussed in chapter 5.4. The model of the cooling device is based on three interconnected concentrated thermal masses representing the SMA film and the heat source and sink. The elastocaloric effect is modelled by the source term  $\dot{Q}_L$ . © 2017 IOP Publishing Ltd, figure reprinted from [210] with permission.

In the special case of the device model illustrated in Figure 38 the thermal energy balances for the lumped SMA film element is given in the following equation:

$$C_1 \dot{T}_1 = - \left( \frac{1}{R_1^{cond}(x)} + \frac{1}{R_1^{conv}(x)} \right) (T_1 - T_0) - \frac{1}{R_{12}^{cont}(x)} (T_2 - T_1) - \frac{1}{R_{13}^{cont}(x)} (T_1 - T_3) + \dot{Q}_L \quad (\text{XIX})$$

The thermal capacity of the SMA element is  $C_1 = \rho c_p V_1$ , the heat source term is  $\dot{Q}_L = V_1 \dot{q}_L$ . The temperatures  $T_1, T_2, T_3$  denote the temperatures of the three lumped elements of the model. Similar to equation XIX thermal energy balances can be stated for the heat source element ( $C_2$ ) and the heat sink element ( $C_3$ ):

$$C_2 \dot{T}_2 = -\left(\frac{1}{R_2^{cond}(x)} + \frac{1}{R_2^{conv}(x)}\right)(T_2 - T_0) - \frac{1}{R_{12}^{cont}(x)}(T_2 - T_1) \quad (\text{XX})$$

$$C_3 \dot{T}_3 = -\left(\frac{1}{R_3^{cond}(x)} + \frac{1}{R_3^{conv}(x)}\right)(T_3 - T_0) - \frac{1}{R_{13}^{cont}(x)}(T_3 - T_1) \quad (\text{XXI})$$

Modelling the release and uptake of latent heat during the phase transformation in the SMA is done with a simplified kinetic model. It is assumed that the transformation starts above the critical stress  $\sigma_{AM}^{crit}$  during loading and below  $\sigma_{MA}^{crit}$  during unloading. The martensite phase fraction is assumed to propagate linearly with the stress within the superelastic stress plateau. At the end of the stress plateau a complete transformation is assumed ( $x_{M+} = 1$ ). Therefore, the martensite fraction can be expressed as

$$x_{M+} = \begin{cases} 0, & \varepsilon < \varepsilon_{el} \\ \frac{\varepsilon - \varepsilon_{el}}{\varepsilon_t}, & \varepsilon_{el} < \varepsilon < \varepsilon_{el} + \varepsilon_t \\ 1, & \varepsilon > \varepsilon_{el} + \varepsilon_t \end{cases} \quad (\text{XXII})$$

with the elastic strain  $\varepsilon_{el} = \sigma^{crit}/E$  and the transformation strain  $\varepsilon_t$ . The release and uptake of latent heat due to phase transition, or in other words lattice transformation, can then be written as

$$\dot{q}_L = Q_{lat}^{AM} \dot{x}_{M+} = \begin{cases} \frac{Q_{lat}^{AM}}{\varepsilon_t} \dot{\varepsilon}, & \varepsilon_{el} < \varepsilon < \varepsilon_{el} + \varepsilon_t \\ 0, & \text{else} \end{cases} \quad (\text{XXIII})$$

with the complete latent heat of the stress-induced phase transformation  $Q_{lat}^{AM}$  and the strain rate  $\dot{\varepsilon}$ . The model is implemented in the add-on Simscape to the MATLAB extension Simulink.

The presented model is set up to simulate the system performance of the coupled device based on three lumped elements. However, this generic model can be adjusted to other SMA film-based elastocaloric cooling devices with only little changes.

Simulative results on the elastocaloric device performance are presented in later chapters 5.4 and 6.3 side by side with the experimental results. Nevertheless, it already can be stated here that the presented LEM is well suited to reproduce experimental results. The LEM simulations help to understand the functionality of SMA film-based elastocaloric cooling devices, and provide valuable information on possible optimization strategies.

## 4.3 Fabrication of Elastocaloric Cooling Devices

The fabrication of the elastocaloric cooling devices developed within this work rely on few fabrication technologies that will be discussed in this chapter to allow a better understanding of the devices.

### 4.3.1 Fabrication of Copper Heat Sink and Source Elements

All elastocaloric cooling devices in this work comprise copper elements that function as heat sink and source. Two different fabrication technologies have been used to shape the copper elements: precision milling and wire electrical discharge machining.

A CNC controlled milling machine has been used for structuring of the copper element's surface geometry. The process of milling is well known [220]. To ensure that the machining forces and clamping forces do not cause plastic deformation in the soft copper, a low depth of cut was selected.

Wire electrical discharge machining (EDM) was also used to shape the Cu-parts. In EDM, a voltage is applied between the workpiece and a wire-shaped electrical electrode. During this process, the workpiece and electrode are in a dielectric fluid. When the electrical field between the workpiece and the wire increases, either due to reduced distance or increased voltage, and the breakdown voltage is reached, a current flows in form of a spark jump. This causes the material of the workpiece to melt or even vaporize locally. In this way

repeated discharges causes the electrode wire to “cut” through the work-piece without mechanical contact. Removed material is flushed away by the dielectric fluid. In addition to the workpiece-electrode material combination, the voltage, frequency and shape of the applied voltage pulse, the polarity and the gap width are of major importance for the machining result [221]. One important benefit of the EDM technology are the low processing forces that allow to structure thin geometries as e.g. sheets without deforming them.

After structuring the copper elements by either milling or EDM, the surfaces that will be in contact with the SMA during operation need to be smoothened. This is achieved by mechanical grinding with increasingly fine abrasive papers up to a grit size of P2500. A final polishing step was done with a fine fabric and a diamond polishing dispersion with particle size of 9 µm. In Figure 39 a) a copper part fabricated by EDM (i) is shown next to a part with mechanically polished surfaces (ii).

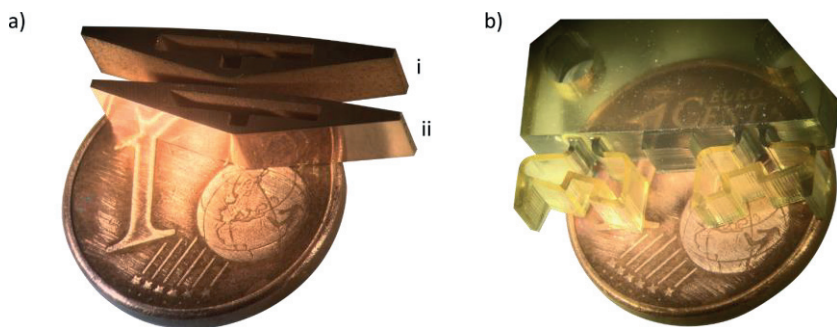


Figure 39 (a) Copper elements that function as combined heat sink and source in the cascaded device with out-of-plane loading after structuring by EDM (i) and after mechanical polishing (ii). (b) 3D printed support structure used in the coupled device. The part is fabricated by stereolithographic 3D printing. All parts are placed on a one euro-cent coin to illustrate the size.

### **4.3.2 Fabrication of Polymer Support Structures: Additive Manufacturing**

Additive manufacturing, also referred to as 3D printing or rapid prototyping, is on the way to revolutionize the production of prototypes in the development process and in some cases even the production of end products [222,p. 3]. In this work, additive manufacturing technologies proved to be extremely useful in the fabrication of support structures used in elastocaloric cooling devices and to fabricate a variety of auxiliary structures. Additive manufacturing allows to fabricate complex 3D designs with only little process planning and a largely decreased role of production-oriented design compared to conventional fabrication technologies [222,p. 7].

As a general rule, additive manufacturing technologies fabricate 3D geometries based on 2D layers. Therefore, the 3D geometry is approximated by 2D cross-sections with a defined layer thickness that are added onto each other during the additive manufacturing process. In this way complex geometries can be fabricated in one fabrication step with no needs for different fabrication technologies and complex fabrication process planning. However, after the additive manufacturing process few post processing steps might be necessary depending on the used technology [222,p. 44 ff].

A variety of additive manufacturing technologies are available. In this work, additive manufacturing based on fused deposition modeling (FDM) and stereolithography (SL) is used and thus these two technologies will be shortly discussed in the following.

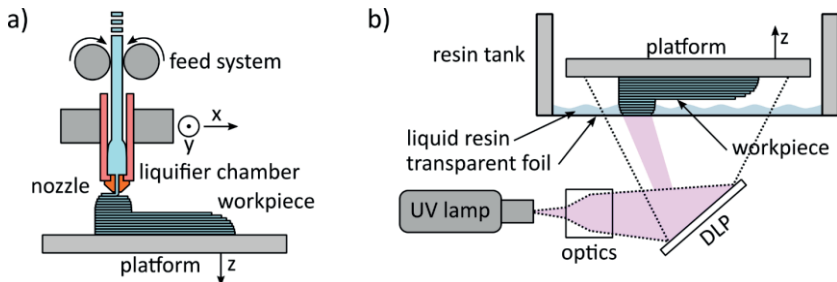


Figure 40 Schematic illustrations of the structure and main components of a fused deposition modeling (FDM) (a) and a stereolithography (SL) (b) based additive manufacturing system. The schematic representations are oriented to the systems used in this work. a) adapted from [46, S. 150], b) adapted from [222,p. 65]).

Figure 40 a) shows the schematic structure of a FDM based 3D printer. Commonly thermoplastic polymers are used in FDM printers in the form of filaments. The filament is pressed by a feeder system into a liquefier chamber. In the liquefier chamber the thermoplastic polymer is heated to a temperature above the glass transformation temperature and melds up. The molten filament is then pressed out of a nozzle of defined diameter and is added in lines to the platform of the printer or the underlying layer of the print. The printed lines follow predefined paths to form the desired geometry. After the molten filament leaves the nozzle it bonds to the underlying layers and the neighboring lines and solidifies (cools down) to preserve the desired geometry [222,p. 147 ff]. The most commonly used materials in non-industrial FDM printers are acrylonitrile butadiene styrene (ABS) and polylactic acid (PLA). For PLA the printing temperature is around 210 °C. In this work, one Ultimaker 2+ and one Ultimaker 3 by the company Ultimaker are used. The resolution of the printers is mainly defined by the nozzle size that varies in this case from 0.25 to 0.8 mm. FDM-based 3D printing is used to fabricate various auxiliary structures, but was hardly used as a process for the device manufacturing itself.

Stereolithographic (SL) additive manufacturing is based on radiation-curable resins [222,p. 63 ff]. In Figure 40 b) a schematic setup of a SL manufacturing system is shown. The liquid radiation-curable resins undergo a chemical reaction (polymerization) if exposed to radiation, and solidify. Different types of radiations might be used, like for example visible light, X-rays, electron beams or UV light [222,p. 64]. However, UV is used most commonly. The radiation wave length has to fit the sensitivity of the used resin. For the selective exposure of the resin with radiation according to the desired geometry, different optical systems are used. Structuring of the resin layers can be achieved by mask-less direct-writing e.g. by vector scans. Layer wise mask projection with the help of digital light processing (DLP) chipsets is also used frequently. This process allows the exposure of a complete printing layer at one time. Furthermore, structuring can also be achieved by two-photon lithography [223]. In an SL additive manufacturing system layers of defined height of liquid resin are structured and solidified in series onto each other. Complex structures are fabricated layer by layer. Since radiation and polymerization does not apply forces to the work piece this technology allows to manufacture delicate and highly complex structures. After printing, the work piece has to be cleaned from liquid resin and in general a post curing step is applied [222,p. 63 ff].

In this work a “Miicraft +” printer from the company Miicraft is used. The highest resolution of the printer in x-, y- direction is 56 µm, in z- direction it is 5 µm. The main components of the optical system are a UV-A lamp and DLP chip. The resin “Model 2.0” from NextDent is mostly used. It is developed originally for dental models and its main component are monomers based on acrylic esters [224].

Figure 39 b) shows a polymer support structure used in the coupled device presented in chapter 5.4. The structure was fabricated by SL 3D printing with the system introduced above. This fabrication technology allows to print free-standing spring-like structures that are important for operation (compare chapter 4.1.1). These freestanding spring structures could hardly be fabricated in this way by any non-additive fabrication technology. In addition, the

use of polymeric support structures is beneficial due to their low heat conductivity. Few support structures in this work like in the cascaded device with in-plane loading are CNC milled, however most are 3D printed due to the described advantages.

All in all, additive manufacturing is particularly suitable for low quantities with highly complex geometry. It allows the free design of geometric shapes and short iteration cycles in the development process. These features make the additive manufacturing technology extremely helpful in the development of new elastocaloric cooling devices.

## 4.4 Experimental Test Setup

The task of an elastocaloric refrigerator is the same as for any other refrigerator, in fact to provide cooling capacity. To do so a refrigerator uses an input power ( $P_{in}$ ) to force a heat flow from a low temperature heat source that is cooled ( $\dot{Q}_{in}$ ) to a high temperature heat sink ( $\dot{Q}_{out}$ ). A stand alone, market-ready elastocaloric refrigerator would comprise all the necessary components that are the elastocaloric material element(s), a control unit, a sensor unit, the actuation unit and a heat unit for separating and providing heat flows to the exterior of the machine (compare Figure 41). Given the early stage of development of the elastocaloric research field, it makes sense to divide all these functions into two devices, namely an experimental test setup and the elastocaloric cooling device itself. As indicated in Figure 41 in this work the experimental test setup includes the actuation, control and monitoring of the device as well as the data acquisition. The elastocaloric cooling device includes the elastocaloric material and the heat unit, so to speak, the heart of the elastocaloric refrigerator. This separation of functions largely reduces the development activities for a new elastocaloric cooling prototype and is thus of major importance for this work. Both, the experimental test setup and the elastocaloric cooling devices, which are presented in following chapters, have been developed within this work. In the following, the experimental test

setup that is later used for the characterization of all different elastocaloric cooling devices is presented in detail.

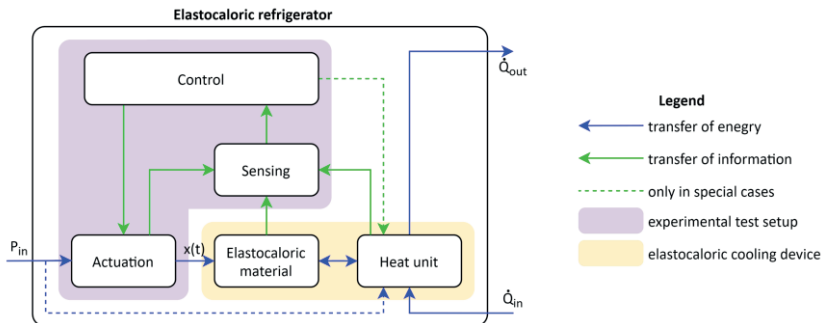


Figure 41 Schematic of the main components of an elastocaloric refrigerator and interconnecting flows of energy and information between the components. In this work the functions and components needed in the complete elastocaloric refrigerator are split between an experimental test setup and the elastocaloric cooling devices.

An overview of the experimental test setup is given in Figure 42. As in the previous figure, information flows are indicated by green, energy flows by blue arrows. The experimental test setup is operated by a controller that positions two actuators and allows simultaneous measurements of temperatures and forces. For this controller a real time capable cRIO-9067 from National Instruments is used. The cRIO is programmed via LabVIEW. The programs are started and programmed on a connected lab PC, but run directly on the cRIO. Five additional modules are used in the experimental test setup with the cRIO: module NI 9212 can read up to eight different thermocouples simultaneously; module NI 9217 can read four pt100 temperature sensors; module 9237 is used to take force readings from load cells, in addition, there is an analog input (NI 9215) and output module (NI 9263) each. All the modules are plugged directly to the cRIO. The motor controllers are connected to the cRIO via one EtherCAT Bus. Via EtherCAT the cRIO dictates the operating states of

the motors and sends target positions to the motor controllers<sup>m</sup>. Simultaneously, the motor controllers report the current operating state together with the motor-position and motor-velocity back to the cRIO. The motor controllers control the motor current internally, based on the actual position of the motor and the target position received from cRIO. Both actuators are ironless synchronous linear motors from the company “ESR Pollmeier GmbH”. The two motors differ in their size and nominal force. The larger one named ML 1612 can apply a permanent force of 116 N and a peak force of 400 N. The force limits of ML 1606 are half the ones from ML 1612. Based on the described control the linear motors apply a defined, position-controlled displacement to the elastocaloric cooling device and thereby operate it.

While the elastocaloric cooling devices is operated, its performance is monitored by the experimental test setup. Temperature in the elastocaloric cooling setup is measured by thermoelements and pt100 sensors. Mostly class A pt100 sensors with dimensions of  $1 \times 3 \text{ mm}^2$ , type K thermocouples with a wire diameter of 0.076 mm, and type T thermocouples with a wire diameter of 0.2 mm and tolerance according to ANSI MC96.1 Class 1, from RS electronics are used in this work. In case of pt100 sensors, three wire measurement is used to exclude the wire resistances. The force applied by the actuator is measured by a loadcell. Two loadcells from the company HBM of type U9C are used, one with the nominal force of 100 N, one with 500 N. The sensors are read by the modules described above and the data acquisition again is done by the cRIO. The analog input and output modules increase the flexibility of the test setup. They are used to apply the thermal load on the single film device with thermal load. At the side, surface temperature profiles of the elastocaloric cooling device can be taken by an IR camera from the company FLIR of type A655s equipped with a macro lens. Sensors need to be in direct contact with the elastocaloric cooling device and thus are located at the interface between the experimental test setup and the elastocaloric cooling

---

<sup>m</sup> The author would like to thank Marvin Schmidt from Saarland University for the support setting up the EtherCAT communication.

device. The different elastocaloric cooling devices presented in chapters 5 and 6 impose different demands on the test setup. Not all components are used for all elastocaloric cooling setups. E.g. in most cases only the larger linear motor (ML 1612) is used. However, the described experimental test setup is used for the characterization of all elastocaloric cooling devices presented in this work. Special adaptations of the test setup to the individual elastocaloric cooling devices are highlighted in the according chapters.

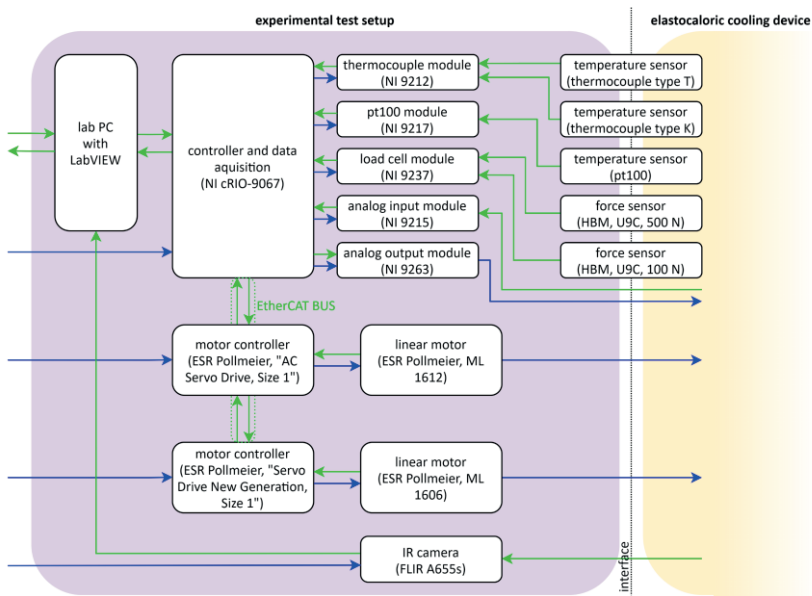


Figure 42 Detailed visualization of the components of the experimental test setup and the integration of the components.

## 4.5 Experimental Operation of SMA Film-Based Elastocaloric Cooling Devices

The linear motor applies a defined displacement  $\Delta l$  to the elastocaloric cooling device during operation. Although the experimental test setup allows arbitrary displacement profiles, the applied profile is kept similar in order to maintain comparability between experiments and devices. This profile is described in the following in detail. The position of the motor, and thus the displacement  $\Delta l$  in the elastocaloric cooling device, follow a sinusoidal movement. At the turning points of the movement the position is kept constant for a certain holding time. The holding time allows the heat transfer to take place. The holding times are equal with the times for movement to the next holding position in the operation cycle. In Figure 43  $\Delta l$  is plotted versus the time for one cycle of operation. The stroke (-a to a) the linear motor does during operation is individually adapted to each elastocaloric cooling device. In combination with the geometry of the cooling device and the chosen zero point of movement, the stroke defines the strain applied to the elastocaloric material. The period  $T_{period}$  of the operation cycle and thereby the frequency of operation  $f = 1/T_{period}$  are varied in most devices between 0.5 and 4 Hz. If the operation cycles of a certain device deviates from this showcase, it will be noted in the associated chapter.

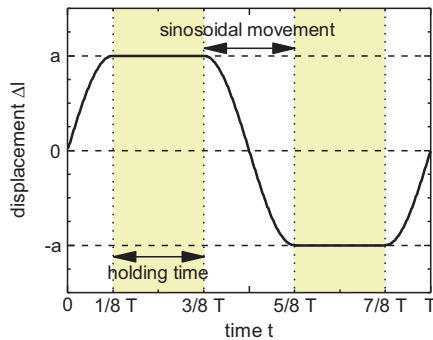


Figure 43 General operating cycle used in this work. The displacement induced by the actuator  $\Delta l$  follows a sinusoidal movement, holding times are inserted at the turning points. The time for movement equals the holding time in each cycle.

# 5 Single SMA Film Devices

## 5.1 Single Film Device

### 5.1.1 Concept

The single film device based on out-of-plane loading of a single SMA film is the most simple configuration of a SMA film-based elastocaloric cooling device. The simple configuration comprises only the SMA film, a heat sink and a heat source. Therefore, it allows a clear view on the basic mechanisms and trends in SMA film-based elastocaloric cooling devices. Thus, the single film device is considered as a reference for most of the other devices developed in this work and presented in following chapters.<sup>a</sup>

### 5.1.2 Experimental Device and Operation

The single film device presented in this chapter is reduced to the core of needed elements. In Figure 44 a) the schematic setup comprising the SMA film, heat sink and source is presented. The device is operated by oscillatory movement of the SMA film. In this way the SMA film is loaded out-of-plane at the triangular shaped heat sink and releases heat to it. The triangular shape of the heat sink has an angle of 12.7° to apply a strain of 2.5 % to the SMA film in full contact. In the unloaded state, the SMA film is brought in contact with the heat source from which it absorbs heat. The heat source also comprises a small angle to ensure a good and even mechanical and thermal contact. The masses of the sink and source elements are 0.36, and 0.33 g, respectively. A detailed description of the operation concept can be found in chapter 2.3.5. The device is operated by the experimental test setup (see

---

<sup>a</sup> The content of chapter 5.1 was previously published by the author in similar form in [16].

chapter 4.4) according to the sinusoidal operation cycle described in chapter 4.5. A TiNiCuCo film with a thickness of 30  $\mu\text{m}$  is used as active material. Material properties are presented in detail in chapter 3.3. The experimental device (see Figure 44 b) is fabricated by precision machining of copper elements and stereolithographic 3D printing of the support structure as discussed in chapter 4.3. Compliant spring-like structures are included in the support structures to ensure a good adaption and contact between the SMA film and the sink and source elements without overloading the SMA film (see chapter 4.1.1).

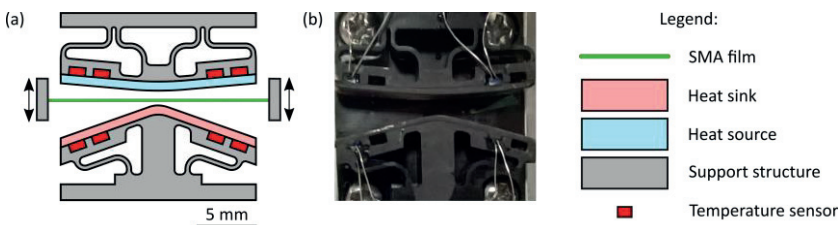


Figure 44 (a) Schematic setup of the single film device. Main components are the TiNiCuCo SMA film, the copper heat sink and source elements and the polymer support structure that includes spring-like elements. Actuation is indicated by arrows. (b) Experimental setup. © 2018 Wiley-VCHVerlag GmbH&Co. KGaA , figure adapted and reprinted from [16] with permission.

### 5.1.3 Results

When the operation of the single film device is started, immediately the temperature of the heat sink and source elements increases and decreases, respectively. In Figure 45 a) the temperature evolution of the sink and source elements with time is shown. The temperature difference  $\Delta T$  of the sink and source temperature and ambient temperature is plotted. A series of experiments with different operation frequencies  $f$  between 0.5 and 4 Hz is presented. All experiments are conducted at room temperature.

Temperature changes in a stepwise manner that represents the changing contact conditions between SMA film and the sink and source elements. This holds true for all operation frequencies, but can be seen best at low frequencies. In the presented experimental series, the device is operated for 100 s. After the start of operation, temperature changes fast for the first 20-30 s, and saturates subsequently. At higher operation frequencies  $f$ , the device reaches saturation faster and higher temperature changes are observed than at low  $f$ . At  $f$  up to 1 Hz, heating and cooling is equally distributed. At frequencies above 1 Hz a drift to higher temperatures is observed. Therefore,  $\Delta T_{sink}$  exceeds  $\Delta T_{source}$  in this case. For the operation frequency of 4 Hz, surface temperature profiles of the device before operation, after 5 s and after 100 s of operation are presented in Figure 45 b). The temperature profiles are obtained by IR-thermography. Along the copper heat source and sink, temperature evolves evenly. Clearly, not only the copper heat sink and source elements, but also the polymer support structure is subjected to temperature changes.

The temperature span between the sink and source element under saturation  $\Delta T_{device}$  is presented in Figure 45 c) with the specific cooling capacity  $\dot{q}_0^{cool}$  and  $COP_{device}$  as a function of  $f$ . The device temperature span  $\Delta T_{device}$  rises with  $f$ , however reaches saturation, and only increases slightly above 2 Hz. A maximum  $\Delta T_{device}$  of 14 °C is reached at 4 Hz. The cooling capacity of the device shows a similar trend and increases with the operation frequency. The maximum specific cooling capacity  $\dot{q}_0^{cool}$  of 19 W/g is reached at 4 Hz. This corresponds to the absolute value of  $\dot{Q}_0^{cool} = 220$  mW. The efficiency of the device measured by the  $COP_{device}$  reaches the highest value of 6.7 at the lowest operation frequency of 0.5 Hz and decreases considerably with increasing  $f$ .

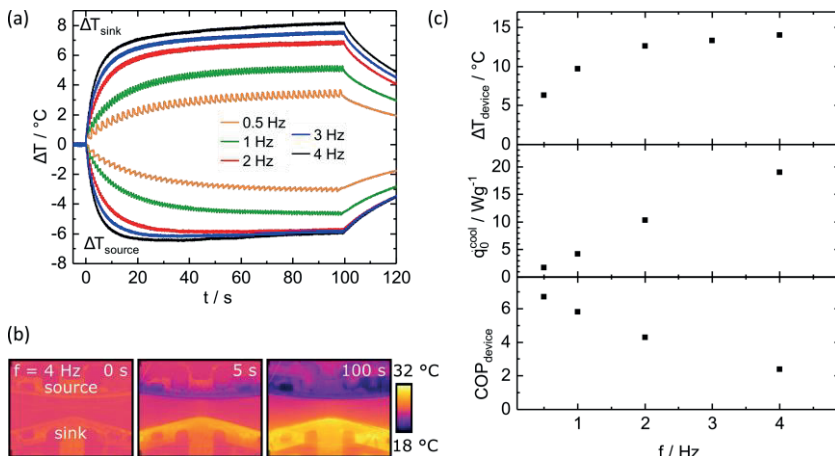


Figure 45 (a) Temperature evolution of heat sink and source elements of the single SMA film elastocaloric cooling device. A series of experiments with operations frequencies from 0.5 to 4 Hz is depicted. (b) Surface temperature profiles of the device at different indicated times during operation at 4 Hz. (c) Frequency dependence of device temperature span  $\Delta T_{device}$ , specific cooling capacity  $\dot{q}_0^{cool}$  and  $COP_{device}$ . Figure a) and b) are adapted from [16], © 2018 Wiley-VCHVerlag GmbH&Co. KGaA , figure reprinted with permission.

### 5.1.4 Discussion

The presented results of the single film device demonstrate the potential of SMA film-based cooling and also reveal general performance trends. It comprises all elements needed for the successful operation of SMA film-based elastocaloric cooling devices: the SMA film, a triangular shaped solid heat sink, a flat heat source and actuation provided by a single actuator of the experimental test setup. Additional concepts like e.g. work recovery are not included here, but will follow in the devices presented in subsequent chapters.

The comparison with previous work with rigid support structure highlights the importance of the spring-like compliant support structures [16]. The compliant structures reduce requirements for accuracy in fabrication, alignment and

operation. In addition, they help to achieve a uniform and reproducible mechanical and thermal contact between the SMA film and the copper elements. The single film device benefits from the compliant structures by improved heat transfer and improved reliability.

The temperature evolution of the sink and source elements saturates during device operation. Saturation is reached, when there is a balance between the cooling and heating effect of the elastocaloric SMA film on the one hand and the parasitic heat losses on the other. With increasing operation frequency, the mechanical power input and the cooling capacity increase, and therefore the thermal equilibrium is shifted to higher temperature differences. The device temperature span  $\Delta T_{device}$  increases. The increase of  $\Delta T_{device}$  with  $f$  saturates for frequencies above 2 Hz. The high frequencies allow only for a very short contact time, which becomes increasingly too short for sufficient heat transfer. In addition, the temperature differences between the SMA film and the sink and source elements become small when the device is operated at high  $f$  and reaches high  $\Delta T_{device}$ . Furthermore, the temperature drift at high operation frequencies points to the increasing influence of dissipative, frictional effects. The hindered heat transfer and increasing losses lead to the saturation of  $\Delta T_{device}$ . Nevertheless, the maximum  $\Delta T_{device}$  of 14 °C is reached at the highest operation frequency of 4 Hz, where also the maximum cooling capacity  $\dot{q}_0^{cool}$  of 19 W/g is reached. The mechanical power input increases over proportional with the operation frequency, since the number of load cycles scale with  $f$  and in addition the hysteresis work per cycle increases with increasing strain rate (compare chapter 3.3). Therefore, the device efficiency decreases with increasing  $f$ , even though the cooling capacity increases. For the given device in combination with a TiNiCuCo film,  $COP_{device}$  decreases from 6.7 at 0.5 Hz to 2.4 at 4 Hz. The opposing trends in  $\Delta T_{device}$ ,  $\dot{q}_0^{cool}$  and  $COP_{device}$  demand a compromise. A high  $f$  is desirable if an application requires high  $\Delta T_{device}$  and  $\dot{q}_0^{cool}$ . Though,  $f$  should be limited to low values if the efficiency is of high importance.

The results exceed the experimental performance reached with a similar design in previous work by far.  $\Delta T_{device}$  is increased by 300 % compared to previous work based on TiNiCuCo and by 70 % compared to operation with NiTiFe [32,p. 168;190]. The performance enhancement is attributed to improvements in the experimental device, like polished copper surfaces, and an improved experimental test platform that enables operation at high operation frequency as high as 4 Hz.

Compared to results from elastocaloric cooling devices found in literature, the high specific cooling capacity is particularly striking. The highest values found in literature are with 0.8 W/g more than one order of magnitude lower [31;172]. However, the absolute values of cooling power are rather low due to the small size of the single film device. Still, the highest temperature span can compete with most devices found in literature. Only two devices have been reported with higher device temperature spans [31;193].

The single film device is considered a benchmark and basis for the other devices developed in this work. In further work it has also been shown that the same principle, slightly modified, can also be implemented with a rotary motor [a], or even with rubber as active material [c].

## 5.2 Single Film Device with Thermal Load

### 5.2.1 Concept

Concept, operation and fabrication of the single film device with thermal load presented in this chapter are similar to the single film device presented in the previous chapter 5.1. The device is modified in two ways to address two different research questions.

The mass of the heat sink in the single film device with thermal load is increased largely. The aim is to investigate the influence of the sink's mass and a highly unbalanced ratio of sink and source mass on the temperature evolution

of the heat sink and source. Additionally, a resistance heater is included in the device and directly connected to the heat source. This allows to apply a thermal load to the cooling device upon operation. Hence, the cooling performance of the SMA film-based elastocaloric cooling device can be investigated under thermal load. This is of high importance for the application of elastocaloric cooling devices.

### 5.2.2 Experimental Device and Operation

The special features of this elastocaloric cooling device are the large heat sink and the resistance heater connected to the heat source element. Both is illustrated in the schematic setup in Figure 46 a). The rest of the setup, including fabrication and experimental operation are comparable to the single film device. However, a different SMA material is used as active material, i.e., NiTi-Fe film material (refer to chapter 3.2 for detailed information on material properties). The increased heat sink comprises lamellar structures at the backside to promote convective heat transfer to ambient. The mass of the heat sink is 3.65 g, which is about 12 times the mass of the heat source (0.31 g). The flat resistance heater is glued to the backside of the copper heat source element. A SMD-type  $100\ \Omega$  resistor is used. The resistor is in direct contact to the heat source, but not to the polymer support structure. During device operation, different constant voltages are applied to the resistor. Heat is generated in the resistor according to  $P_{load} = U^2/R$  with the voltage  $U$  and the resistance  $R$ . The generated heat is transferred directly to the heat source as thermal load  $P_{load}$ . Although  $P_{load}$  is applied only through the area of contact between the resistor and the heat source, IR thermography reveals that the temperature distributes evenly within the heated copper sheet. The temperature is found to vary only by 1 °C along its length. In a series of experiments, different thermal loads are applied to the device to investigate the change of device performance under load. In each case, a constant thermal load is applied from the start of operation until its end.

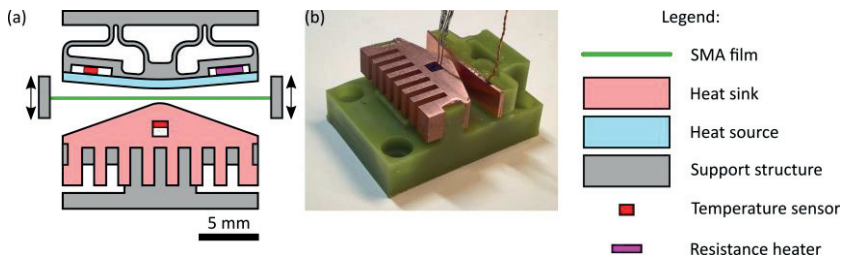


Figure 46 (a) Schematic device setup of the single film device with thermal load. Besides the large heat source and the resistance heater, the device is comparable to the single film device presented in previous chapter 5.1. (b) Experimental device.

### 5.2.3 Results

The temperature evolutions of the heat sink and source elements are presented in Figure 47. A series of experiments is displayed with different applied thermal loads from 0 mW to 170 mW at two operation frequencies of 1 and 2 Hz. The temperatures are plotted as temperature difference between the absolute temperature and the initial starting temperature. The curves without thermal load (black in Figure 47) allow a clear view on the influence of the heat sink's high mass on the device performance. The temperature decrease of the heat source is comparable to the single film device. It changes stepwise with the operation cycles. First, the temperature changes rapidly, and then levels off approaching saturation. Here, saturation is not completely reached, since the device is only operated for 30 s. Temperature evolution of the large heat sink behaves differently. No clear stepwise evolution can be seen, temperature changes almost steadily. At the same time, the temperature changes with almost constant rate within the time of operation. In general, the temperature change of the large heat sink is very low compared to the heat source. Without thermal load, the device reaches a device temperature span  $\Delta T_{device}$  of 10.5 °C at 2 Hz, of which 8.5 °C are available for cooling. An absolute cooling capacity  $\dot{Q}_0^{cool}$  of 107 mW is achieved.

A clear influence of the applied thermal load  $P_{load}$  on the temperature evolution of the heat source can be found at both investigated operation frequencies. The applied thermal load directly leads to a decreased temperature change. The higher the thermal load, the lower is the temperature change. In addition, saturation is reached faster under an applied thermal load.

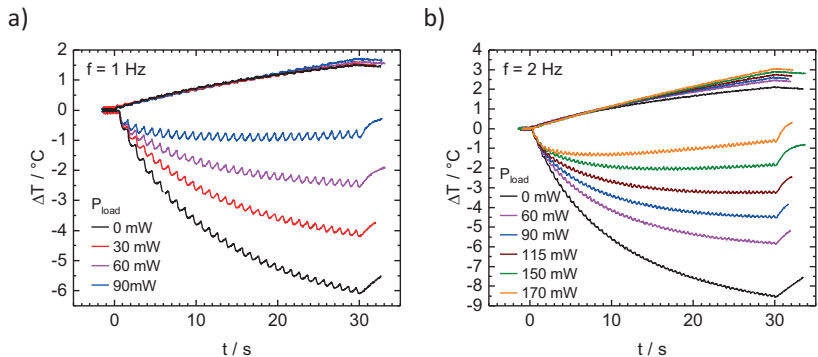


Figure 47 Temperature evolution of heat sink and source elements at the operations frequencies of 1 Hz (a), and 2 Hz (b). Temperature curves are presented for different thermal loads applied to the heat source of the cooling device.

In Figure 48 device temperature span available for cooling  $\Delta T_{device}^{cool}$  is plotted versus  $P_{load}$  and thereby a device characteristic under load is obtained.  $\Delta T_{device}^{cool}$  is deduced from the curves presented in Figure 47. The device shows a linear decrease of the accessible temperature span  $\Delta T_{device}^{cool}$  for increasing  $P_{load}$  at both investigated operation frequencies. In case of the higher operation frequency of 2 Hz, the characteristic curve is shifted to higher temperature spans compared to the 1 Hz curve. In addition, the zero-load cooling capacity  $\dot{Q}_0^{cool}$  of the device is indicated in Figure 48 as round dots.

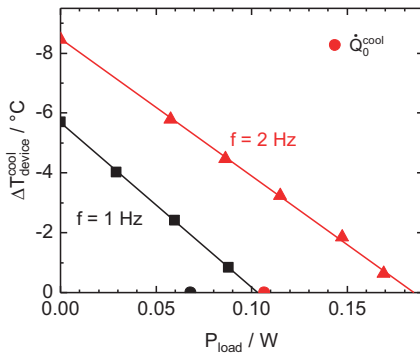


Figure 48 Device temperature span available for cooling  $\Delta T_{device}^{cool}$  as a function of the applied thermal load  $P_{load}$  for operation frequencies of 1 and 2 Hz. The device shows a linear decrease of  $\Delta T_{device}^{cool}$  with the applied thermal load. The absolute cooling capacity  $Q_0^{cool}$  is indicated as dots on the x-axis.

### 5.2.4 Discussion

Due to the unbalanced mass ratio of the heat sink and source,  $\Delta T_{device}^{cool}$  accounts for about 80 % of  $\Delta T_{device}$  in the present device. In SMA film-based elastocaloric cooling devices with a balanced mass ratio, 50 % or less are common [16]. In addition, the large heat sink approaches saturation much slower, compared to a smaller one. The observations lead to several conclusions with regards to the increased thermal mass:

- Small thermal masses lead to a fast thermal respond and high temperature spans within a small time frame. High thermal masses of sink and source elements lead to a slow thermal device respond. Thermal saturation is reached much slower.
- An unbalanced mass ratio of the heat sink and source leads to an increased contribution of the element with smaller thermal mass to  $\Delta T_{device}$ .

Tailoring the masses of the heat sink and source elements thus might be one way to modify the temperature span and the temporal response behavior of the elastocaloric cooling device.

The application of the thermal load on the cooled heat source during operation reveals the cooling performance of the device under load. This is of major importance for application. Figure 48 reveals a linear decrease of the device temperature span available for cooling  $\Delta T_{device}^{cool}$  under thermal load for both investigated operation frequencies. The linear characteristic proves that the device function persists under thermal load even if the accessible temperature span  $\Delta T_{device}^{cool}$  decreases. From application point of view, it is important to know that the device performance and function does not break down at a certain thermal load.

The investigated device performance under thermal load also lays the foundation for a deeper understanding of the cooling performance of SMA film-based elastocaloric cooling devices. The figures of merit of elastocaloric cooling devices introduced in chapter 2.3.6 reveal the device temperature span  $\Delta T_{device}$ , cooling capacity  $\dot{Q}_0^{cool}$ , and the  $COP_{device}$ . Single values are determined for  $\Delta T_{device}$  under zero thermal load, the cooling capacity  $\dot{Q}_0^{cool}$  and  $COP_{device}$  are determined for zero temperature span. These limit values are important to know and of high value for the comparison of different elastocaloric cooling devices. Nevertheless, under operation, temperature span, cooling capacity and COP depend on each other and on the point of operation. These complex cross dependencies are not captured by the figures of merit. Fortunately, the nature of these cross dependencies is revealed by the investigated cooling device performance under load.

Under steady state conditions, the thermal load  $P_{load}$  applied to the system can be considered the cooling capacity of the system at the temperature span that occurs. Therefore, the thermal power that can be applied when the saturation temperature span is zero, should equal  $\dot{Q}_0^{cool}$ . Figure 48 reveals that the values do not coincide in the given investigation.  $\dot{Q}_0^{cool}$  obtained by the

linear fit of the results under thermal load exceeds  $\dot{Q}_0^{cool}$  obtained by the procedure explained in chapter 2.3.6 by about 50 %. This deviation is likely to be attributed to experimental shortcomings in the experiments presented above. Two main issues are identified. Although, only direct contact exists between the heat resistor and the copper element, the generated heat might partly be transferred directly to the ambient or the polymer support structure. Thus, the numbers of the thermal load stated above might overestimate the actual thermal load on the heat source. Secondly, saturation is only reached for high thermal loads, but not for low loads.

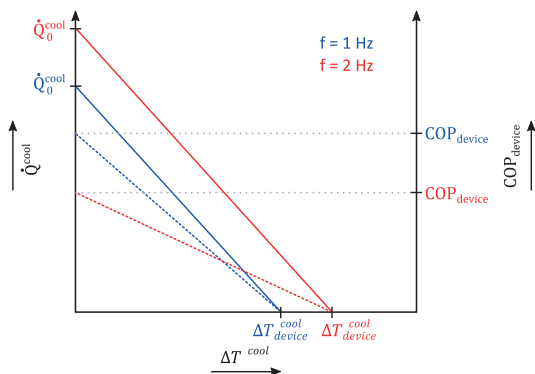


Figure 49 Schematic characteristic of  $\dot{Q}^{cool}$  and  $COP_{device}$  as a function of  $\Delta T^{cool}$ . The dependencies are approximated by a simplified model to include the cross dependencies of the device temperature span, cooling capacity and the  $COP_{device}$  under different points of operation. A complete cooling device characteristic can be interpolated from the figures of merit introduced in chapter 2.3.6. Linear relations are chosen according to the findings on the device performance under thermal load presented in this chapter.

Keeping the experimental shortcomings in mind, the linear characteristic revealed in Figure 48 still paves the way to a simplified model for the cross dependencies between the three figures of merit. If the cooling capacity  $\dot{Q}^{cool}$  is plotted as a function of the device temperature span available for cooling,

the values of  $\Delta T_{device}^{cool}$  and  $\dot{Q}_0^{cool}$  determined according to chapter 2.3.6 represent the x- and y-intercept of the device characteristic, respectively. The experimental results presented above reveal a linear curve in between the two values. Therefore,  $\Delta T^{cool}$  as a function of the cooling capacity  $\Delta T_{device}^{cool}(\dot{Q}^{cool})$ , or vice versa, the cooling capacity as a function of the temperature span  $\dot{Q}^{cool}(\Delta T^{cool})$  can be approximated by a linear connection of the two y- and x-intercepts, as done in Figure 49. Furthermore,  $COP_{device}$  that is related to  $\dot{Q}^{cool}$  is known and can be included in the figure on a second y-axis. In addition,  $COP_{device}$  becomes zero according to its definition, when  $\dot{Q}^{cool}$  approaches zero. A second point of  $COP_{device}(\dot{Q}^{cool})$  is known. Assuming that the mechanical power input in first approximation is only influenced by the operation frequency, but not by the applied thermal load, the  $COP_{device}(\dot{Q}^{cool})$  characteristic is approximated by linear connection of the two known COPs. Thus,  $COP_{device}(\dot{Q}^{cool})$  can be included in Figure 49. The approach is illustrated in Figure 49 for two different operation frequencies. With this approach based on the linear relation between cooling device temperature span and the cooling capacity, it is now possible to approximate the device performance of an SMA film-based elastocaloric cooling device under operation at different operation points and applications. High  $COP_{device}$  can only be achieved at low temperature spans. At high temperature spans only low cooling capacities are available. If high cooling capacities are required, only low temperature spans are possible. At the same time, this approach also shows how important it is to improve the maximum values of  $\Delta T_{device}$ ,  $\dot{Q}_0^{cool}$ , and  $COP_{device}$ , to broaden the scope of possible applications and to increase the device efficiency under operation.

## 5.3 Miniature Single Film Device

### 5.3.1 Concept

The idea of the miniaturized experimental setup is to investigate the benefits and challenges of further miniaturization in SMA film-based elastocaloric cooling devices. In addition, a miniature dog-bone shaped sample geometry of the SMA can be used in this setup that is used as a standard geometry in the research group of Prof. Quandt at University Kiel [201]. A simple single SMA film configuration is used in the present investigation, similar to the single film device presented in chapter 5.1. The concept is retained, while the size of the cooling device is reduced roughly by a factor of four. The simplicity of the setup is the base for further miniaturization.

### 5.3.2 Experimental Device and Operation

The fabrication and design of the miniaturized cooling device presented in this chapter and shown in Figure 50 does not vary fundamentally from a larger single film device. The main difference is the size of the setup and its simpler design, i.e., compliant support structures are not included here. The monolithic polymer support structure is fabricated by stereolithographic 3D printing. Copper elements that function as the heat sink and source are fabricated by precision machining and mechanical polishing. The heat sink and source elements have a mass of 0.021 g. The dimensions of the core device shown in Figure 50 b) are 6.5 mm x 6 mm and 4 mm in height. The length of the TiNiCuCo dog bone specimen used as active material in the setup is 7 mm of which 5 mm have a uniform width of 0.4 mm. The thickness is 30  $\mu\text{m}$ . The TiNiCuCo alloy used in this device shows a similar mechanical performance as TiNiCuCo-2 (see chapter 3.3). However, the alloy has a slightly altered composition with an increased copper content ( $\text{Ti}_{53}\text{Ni}_{24}\text{Cu}_{20.9}\text{Co}_{2.1}$ ). The adiabatic temperature span of the specific SMA is 10 °C upon loading and -13 °C upon unloading. Two miniature T-type thermocouples with a tip size of 0.4 mm are

used to measure the temperature of the copper elements during operation. Actuation and control are provided by the experimental test setup described in chapter 4.4. The operation is performed as described in chapter 4.5.

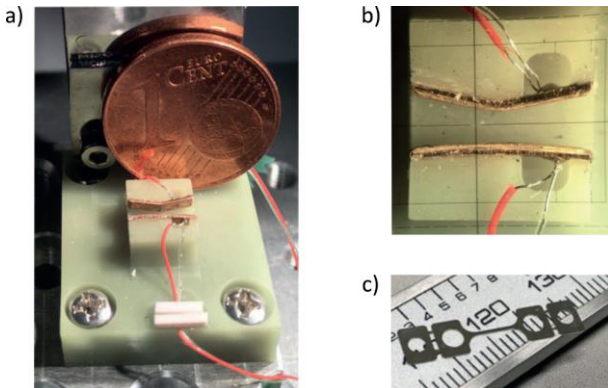


Figure 50 (a) Experimental setup of the miniature single film device with a 1 cent coin for scale. Like a larger setup the device consists of a 3D printed support structure, heat sink and source element from copper and the SMA film. Temperature is investigated via miniature scale thermocouples. (b) The core cooling device. (c) Dog-bone shaped TiNiCuCo SMA sample geometry used as active material.

### 5.3.3 Results

Similar to the single film device, here, the device is operated by oscillating movement of the SMA film that is pressed alternately onto the heat sink and source elements. The device is operated at frequencies  $f$  of 0.5, 1, 2, 3 and 4 Hz. The oscillatory mechanical loading and unloading of the SMA film triggers the elastocaloric release and absorption of heat within the SMA film and thereby the stepwise heating of the heat sink and cooling of the heat source. In Figure 51 a) the evolution of the sink and source temperatures and ambient temperature are presented. The temperatures are plotted as temperature difference between the absolute temperature and the initial starting

temperature of 23.2 °C. At first, heat sink and source change their temperature quickly, and after about 20 s the temperatures saturate. In the presented showcase operated at 4 Hz, the temperature span for cooling saturates at 1.5 °C, the device temperature span  $\Delta T_{device}$  reaches 3.5 °C. Figure 51 a) also shows a clear drift of the saturated temperature of about 0.2 °C in 950 s. However, having a look at the evolution of the ambient temperature, this drift simply follows the ambient temperature that heats up. Similar experiments to the one presented in Figure 51 a) are conducted at different operation frequencies. The results of  $\Delta T_{device}$ ,  $\Delta T_{device}^{cool}$ , and  $\dot{q}_0^{cool}$  are compiled in Figure 51 b). Results gained from various experiments are averaged and the averaged results are presented in combination with the standard deviation (at 3 Hz only one result is available and thus no standard deviation could be given).

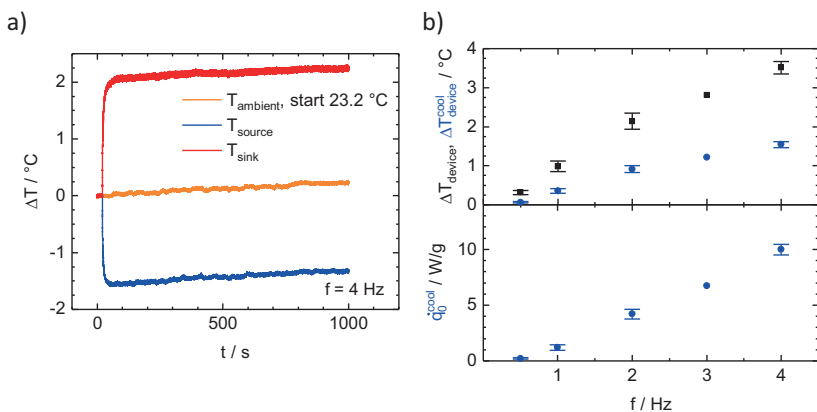


Figure 51 (a) Evolution of the temperature difference of the sink and source elements and the initial temperature during operation at a frequency of 4 Hz. Operation is maintained over a time period of 1000 s or 4000 load cycles. (b) Device temperature span, cooling device temperature span, and specific cooling capacity versus the operation frequency of the miniaturized elastocaloric cooling device. Average values in combination with the standard deviation are given for results gained in a series of experiments.

The results show a clear dependence of the device performance on the operation frequency.  $\Delta T_{device}$ ,  $\Delta T_{device}^{cool}$  and  $\dot{q}_0^{cool}$  display a clear, almost linear increase with the operation frequency within the investigated frequency range. Maximum values of  $\Delta T_{device}^{cool} = 1.5 \text{ }^{\circ}\text{C}$ ,  $\Delta T_{device} = 3.5 \text{ }^{\circ}\text{C}$ , and  $\dot{q}_0^{cool} = 10 \text{ W/g}$  and  $\dot{Q}_0^{cool} = 4 \text{ mW}$  are gained at 4 Hz.

### 5.3.4 Discussion

The general cooling behavior of the miniature single film device follows similar trends compared to the larger version presented in chapter 5.1. Temperature of sink and source elements change rapidly right after the start of operation and after about 20 s the temperatures saturate and a thermal equilibrium is reached. The main difference is that in the miniaturized device the equilibrium is reached at much lower device temperature spans.  $\Delta T_{device}$  reaches only 3.5 °C compared to 14 °C in the larger version, although both results are based on similar TiNiCuCo alloys. The device temperature span is reduced, since in the miniaturized device the role of parasitic heat losses becomes more dominant. Upon miniaturization, the effective separation, control and insulation of heat and heat flows becomes increasingly challenging. This effect manifests in the reduced temperature span  $\Delta T_{device}$ . The relatively long continuous operation for 1000 s at 4 Hz reveals a stable device performance over time. Sink and source temperatures are subjected to a temperature drift, however, this drift is attributed to a drift in the ambient temperature.  $\Delta T_{device}$  is stable during operation.

Similar to the larger single SMA film device,  $\Delta T_{device}$ ,  $\Delta T_{device}^{cool}$ , and  $\dot{q}_0^{cool}$  increase with the operation frequency  $f$  within the investigated range from 0.5 to 4 Hz. The specific cooling capacity  $\dot{q}_0^{cool}$  reaches similar, slightly lower values compared to the larger setup. Most likely, the reduction is related to the missing compliant structures, and related reduction of the surface contact quality between the SMA film and the sink and source elements. The increase of  $\Delta T_{device}$  and  $\Delta T_{device}^{cool}$  with  $f$  does not saturate within the investigated range of  $f$ . This effect is related to the low absolute numbers of  $\Delta T_{device}$  that

lead to an increased temperature gradient between SMA film and copper elements. This enables an increased heat transfer under operation, even if the thermal contact might be slightly worse. The lower absolute values of  $\Delta T_{device}$  shift the saturation of  $\Delta T_{device}$  to a higher  $f$ , which could not be investigated due to experimental restrictions.

The TiNiCuCo sample that lasted the longest in this setup withstood 10460 load cycles of operation. This is considered about one order of magnitude higher cycle live time compared to the larger experimental setups. However, the four used samples withstood an average lifetime of 4930 cycles with a high standard deviation of 4090 cycles. The scattering is high and the number of tested samples is too low to draw a general, robust conclusion. Nevertheless, miniaturization seems to have a beneficial effect on the device lifetime.

To sum up, the miniature single film device with base area as low as 6.5 mm x 6 mm shows a reliable cooling performance, and represents the general cooling performance trends known from larger SMA film-based elastocaloric cooling devices. No fundamental obstacles are found that hinder further miniaturization. The downscaling is enabled by the simple device configuration with few components and only one actuator needed. Nevertheless, insulation and separation of cold and hot heat flow becomes increasingly challenging.

## 5.4 Coupled Device

### 5.4.1 Concept

The coupled device presented in this chapter is designed to integrate work recovery (WR) in SMA film-based elastocaloric cooling devices. WR is introduced by antagonistic coupling of two SMA films in one device. For detailed information on antagonistic coupling and WR, refer to chapter 2.3.3. In addition, this coupled device is used as an example for device simulation of SMA

film-based elastocaloric cooling devices. A simulation model based on lumped element modelling (LEM) is set up according to chapter 4.2.<sup>b</sup>

### 5.4.2 Experimental Device and Operation

The coupled device is illustrated in Figure 52. The two SMA films are loaded in out-of-plane direction. They are antagonistically coupled and pre-strained with respect to each other. The SMA films in the antagonistic pair counteract each other, and thereby WR is included in the device. Cold-rolled NiTiFe films are used in this setup. A detailed discussion of material properties can be found in chapter 3.2. The coupled device has two heat sinks and one heat source. The two heat sinks, placed at the top and bottom part of the device, are each cooled by one of the SMA films (top and bottom with reference to Figure 52). The heat source is placed in the middle between the two SMA films, and is cooled by both of them. The heat sources and sinks are split in the middle to leave room for the element that couples and pre-strains the two SMA films against each other. The angles of the sink and source surface are matched to a maximum and minimum strain of 4.5 % and 0.5 %, respectively. Polymer support structures are fabricated by stereolithographic 3D printing. The heat source and sink elements are fabricated from copper with mechanically polished surfaces. The mass of the sink and source elements is 350 mg and 180 mg, respectively. Fabrication is explained in detail in chapter 4.3. Compliant spring-like structures are included in the support structures. The compliant structures compensate for misalignments and ensure a good thermal contact between the SMA films and the copper elements (see chapter 4.1.1). In the particular case of the coupled setup, the compliant structures at the sink have a spring constant of 16 N/mm, and at the source of 3 N/mm. This leads to contact forces of 12 N and 9 N between the SMA film and the sink and source, respectively.

---

<sup>b</sup> The content of chapter 5.4 was previously published by the author in similar form in [210].

For the operation, the experimental test setup presented in chapter 4.4 is used. Due to the coupling of the two SMA films, one actuator is sufficient to operate both. The operation cycle is performed as described in chapter 4.5. In the coupled device the two SMA films both are unloaded and loaded within one cycle of operation. When the actuator moves the coupled SMA films upwards, the upper SMA film is loaded, whereas the lower SMA film is unloaded. Simultaneously, the actuator movement brings the upper SMA film in contact to the upper heat sink and the lower SMA film in contact to the heat source. When moved in downward direction, the upper SMA film is unloaded and brought in contact with the heat source, and the lower film is loaded and brought in contact with the lower heat sink. Therefore, the heat source is cooled twice in each cycle of operation, whereas each heat sink is only cooled once.

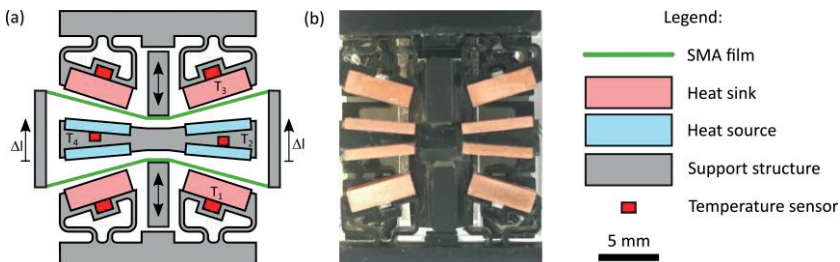


Figure 52 (a) Schematic of the coupled device. The actuation is indicated by arrows, the components of the setup by color. (b) Image of the experimental device without SMA films. Figure adapted from [16], © 2018 Wiley-VCHVerlag GmbH&Co. KGaA, figure reprinted with permission.

### 5.4.3 Results

The temperature evolution within the first two cycles of operation in combination with the displacement  $\Delta l$  induced by the linear actuator helps to understand the operation and function of the coupled SMA film-based elastocaloric cooling device. Both are plotted in Figure 53 for the operation

frequency  $f = 0.5$  Hz. The temperature difference  $\Delta T$  represents the temperature difference between the absolute temperature and the initial (i.e. ambient) temperature. The experiments are conducted at room temperature. As described in chapter 4.5. and illustrated in Figure 53 a),  $\Delta l$  follows a sinusoidal motion with holding times included at the turning points. Operation starts from the middle position ( $\Delta l = 0$  mm). The initial downward movement unloads the upper SMA film and loads the lower SMA film, and brings them in contact with the upper side of the heat source and the lower heat sink, respectively. Consequently,  $\Delta T_1$  increases,  $\Delta T_2$  decreases, and  $\Delta T_3$ ,  $\Delta T_4$  are unaffected at first (compare Figure 52 a) for the position and allocation of the sensors). When the coupled SMA films are moved to the opposite direction, loading and unloading reverse, and also the contacts change. So  $\Delta T_3$  increases,  $\Delta T_4$  decreases, and  $\Delta T_1$ ,  $\Delta T_2$  are not affected. Each copper element is subjected to a stepwise change in temperature once per cycle, when they are brought in contact to the SMA films during the holding time. Afterwards, the temperatures change slowly towards the initial temperatures due to parasitic heat losses, until the next contact event occurs in the following cycle of operation. Although the device has only one heat source, the temperatures  $\Delta T_2$  and  $\Delta T_4$  show different trends here. This is the case, because the different copper elements of the heat source are separated by a polymer support structure. Over time, the support structure and the copper elements adopt a uniform temperature, as can be seen in the IR image of the device during operation in Figure 55 c).

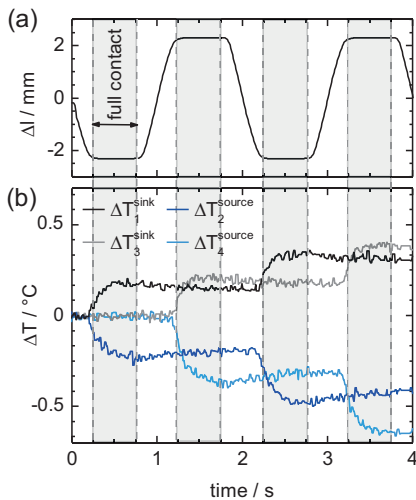


Figure 53 Displacement  $\Delta l$  induced to the elastocaloric cooling device for operation (a), and the evolution of the temperature differences  $\Delta T_1$  to  $\Delta T_4$  (b) with time in the first two cycles of operation. Holding time periods with full contact between the SMA and the sink and source elements are highlighted. The operation frequency is 0.5 Hz. Clearly the stepwise evolution of temperatures in the elastocaloric cooling device can be understood. © 2017 IOP Publishing Ltd, figure reprinted from [210] with permission.

For the other operation frequencies, the operation works in the same manner. The temperature evolution of the sink and source elements is displayed in Figure 54 a) for operation frequencies between 0.5 and 4 Hz for a longer operation of 100 s. An excerpt of the initial temperature evolution in the first 10 s is shown in Figure 54 b). The temperatures are plotted as temperature difference between the absolute temperature and the initial starting temperature. Experimental and simulation results are shown side by side. Simulation results are discussed below. Especially within the first 20-30 s, the temperature span between the sink and source elements rises rapidly. Afterwards, the temperature increase (decrease) reduces and finally saturates. The higher the operation frequency, the faster the temperature changes initially, and the faster the system approaches equilibrium.

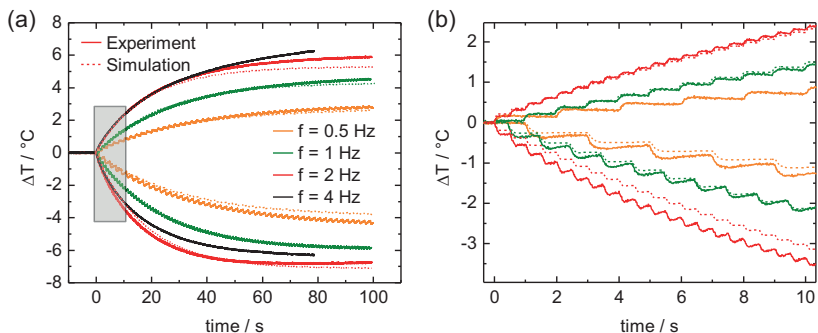


Figure 54 Temperature difference of heat sink and source elements as a function of time during operation at different frequencies. Temperature differences are displayed for 100 s of operation (a) and the first 10 s (b). Experimental and simulated results are given. © 2017 IOP Publishing Ltd, figure reprinted from [210] with permission.

The device temperature spans  $\Delta T_{device}$  reached in the device for the different operation frequencies are presented in Figure 55 a). The highest experimental  $\Delta T_{device}$  of 13 °C is reach at 3 Hz. Then,  $\Delta T_{device}$  saturates, and does not rise anymore for increasing frequencies. At 4 Hz, it even slightly decreases since the temperature drop of the heat source decreases slightly after 70 s of operation. For operation frequencies of 3 Hz and lower, heating and cooling contribute almost equally to  $\Delta T_{device}$ . The cooling capacity  $\dot{Q}_0^{cool}$  shows a similar trend. At 0.5 Hz,  $\dot{Q}_0^{cool}$  is 30 mW.  $\dot{Q}_0^{cool}$  rises with the frequency to 120 mW at 2 Hz and then saturates. Normalized by the mass of active SMA films, the specific cooling capacity  $\dot{q}_0^{cool}$  reaches 7.7 W/g. The surface temperature distribution of the device before and after operation is shown for the case of 2 Hz in Figure 55 c).  $\Delta T_{device}$  shows a strong increase with the operation frequency, especially below 2 Hz. The mechanical work input per cycle of operation  $\Delta W_{device}$  is determined at low operation frequencies to be 20 mJ. The  $COP_{device}$  is calculated based on cooling capacity and the work input as a measure for the device efficiency. Values for  $COP_{device}$  are given in Figure 55 b) for all investigated operation frequencies. A maximum  $COP_{device}$  of 3.2

is obtained at 1 Hz. The  $COP_{device}$  drops especially for frequencies above 2 Hz.

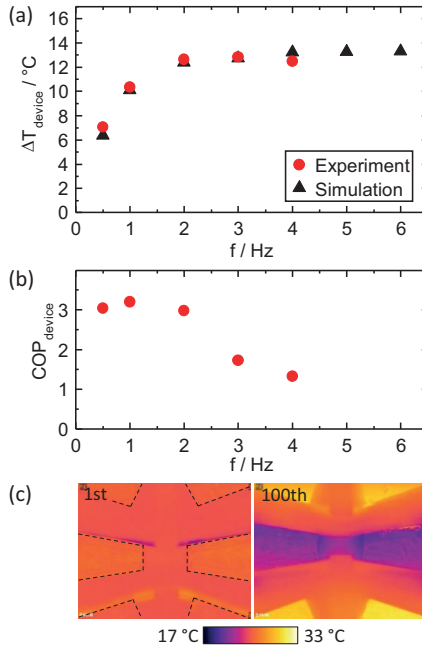


Figure 55 Experimental and simulated device temperature span  $\Delta T_{device}$  (a) and  $COP_{device}$  (b) as a function of operation frequency.  $\Delta T_{device}$  saturates above 2 Hz, the maximum experimental value of 13 °C is reached at 3 Hz. The maximum  $COP_{device}$  of 3.2 is reached at 1 Hz. The  $COP_{device}$  decreases for frequencies above 2 Hz. (c) IR image showing the surface temperature profile of the cooling device before and after operation at 2 Hz for 100 s. © 2017 IOP Publishing Ltd, figure reprinted from [210] with permission.

The experimental and simulative results are in good agreement. The model is explained in detail in chapter 4.2. Especially the stepwise temperature evolution of the heat sink and source (Figure 54 b) are well represented. The LEM

reproduce the influence of the operation frequency on the temperature evolution well. The model allows to investigate higher operation frequencies that could not be covered in the experimental work due to experimental restrictions. However, in Figure 55 a) it can be understood that also higher operation frequencies up to 6 Hz are not expected to improve  $\Delta T_{device}$ .  $\Delta T_{device}$  saturation for high frequencies, as already indicated by the experimental results.

#### 5.4.4 Discussion

One of the major requirements on elastocaloric cooling devices is a low work input per cycle of operation. On the materials side, elastocaloric materials with low critical stresses and low hysteresis work are beneficial. However, efficient operation of elastocaloric devices is only possible with appropriate measures on the device level. The coupled device presented in this chapter shows, how to implement WR successfully in SMA film-based elastocaloric cooling devices. In addition, the coupled device uses the concept of out-of-plane loading. The concept allows for a simple device architecture with a single actuator for mechanical load cycling and separation of the hot and cold heat flow within the elastocaloric device. The use of two SMA films within one setup puts high demands on the manufacturing and assembly accuracy. Both SMA films need to be precisely pre-strained and positioned with respect to each other. This challenge is met by compliant support structures of the heat sink and source elements.

The device temperature span reaches up to 13 °C. Furthermore, the device reaches a maximum cooling capacity of 7.7 W/g and a  $COP_{device}$  of 3.2. The results in the present investigation especially highlight the major influence of the operation frequency in the investigated range of 0.5 to 4 Hz.  $\Delta T_{device}$  and  $\dot{Q}_0^{cool}$  show similar trends with  $f$ . Both increase significantly until 2 Hz and saturate afterwards. This behavior is supported by the simulation model also for higher operation frequencies up to 6 Hz. The COP shows high values for low  $f$  and decreases considerably above 2 Hz. The conflicting trends require a compromise between reaching high  $\Delta T_{device}$ ,  $\dot{Q}_0^{cool}$  and  $COP_{device}$ . For this

specific setup, the operation frequency of 2 Hz gives good values for all figures of merit.

Compared to previous work on a similar coupled SMA film-based elastocaloric cooling system the maximum  $\dot{q}_0^{cool}$  has been largely improved by roughly 165 %, but also  $\Delta T_{device}$  could be improved by 38 % [169]. The improvement is mainly attributed to enhanced operation parameters, especially the frequency, but also improvements in fabrication and alignment play a role.

The LEM simulation of the device performance confirms the major importance of the operation frequency. For high operation frequencies the time for heat transfer becomes too short, and heat cannot be transferred efficiently between the SMA films and the sink and source elements. Therefore,  $\Delta T_{device}$  and  $\dot{Q}_0^{cool}$  saturate and  $COP_{device}$  decreases. This points out the importance of the heat transfer coefficient between the SMA and the sink and source elements. Higher operation frequencies can only be used efficiently, if heat transfer can be improved. A second improvement strategy revealed by LEM is to reduce parasitic heat losses through conduction in the support structures. Conduction has been found to be the dominant loss compared to convection.

# **6 Advanced SMA Film Devices**

The single SMA film devices presented in the last chapter reach good performance values, especially high specific cooling capacities. Yet device temperature span and absolute cooling capacity have found to be bound by limits due to the active material's adiabatic temperature span and the limited mass of SMA. Advanced SMA film devices are developed to shift these limits and combine the high specific cooling capacity with increased absolute cooling capacity and also high device temperature spans. Therefore, parallelized and cascaded system architectures are developed (compare chapters 4.1.3 and 4.1.4). Devices based on these concepts are presented and characterized in the following chapters.

## **6.1 Parallelized Device**

### **6.1.1 Concept**

The concept of SMA film-based elastocaloric cooling has proven its potential to provide efficient elastocaloric cooling performance in the previous chapters 5.1 to 5.4. Especially high specific cooling capacities up to 19 W/g are reached. However, absolute cooling capacity is limited below 220 mW. To broaden the scope of possible applications of SMA film-based elastocaloric cooling devices, the absolute cooling capacity has to be increased. An upscaling approach is developed to achieve this aim based on the gained knowledge on SMA film-based elastocaloric cooling devices. The investigation on the scaling behaviour of elastocaloric devices in chapter 4.1.2 has revealed the surface-to-volume ratio of the SMA element as the key to high cooling performance. Thus, the high surface-to-volume ratio of SMA films has to be maintained in the upscaled device. A parallelized device architecture, as introduced in chapter 4.1.4, has been found to be well suited. The parallelized

device presented in the following is developed to combine and add up the cooling capacity of five SMA films.<sup>a</sup>

### 6.1.2 Experimental Device and Operation

A schematic of parallelized device is presented in Figure 56 a). Like in the single film device, the device concept is based on out-of-plane loading of the SMA films, and changing mechanical contact conditions separate the cold and hot heat flows. The SMA films are coupled antagonistically to include work recovery (WR) in the device and increase the efficiency thereby (compare chapter 2.3.3 for detailed information on WR). The parallelized device comprises one heat source element and one heat sink element. Both elements are precision milled from one monolithic copper element. The heat sink has three extrusions A, C, E, with a total of five triangular shaped surfaces that load the SMA films by out-of-plane deflection upon operation. The contact surfaces are mechanically polished to achieve good heat transfer between the copper surfaces and the SMA films. The angles of the triangular surfaces are adjusted to apply a maximum strain of 4.7 % to the SMA films. The heat source has three extrusions B, D, F with five surfaces for contact with the SMA films as well. The surfaces of the heat source are slightly barreled for good contact to the unloaded SMA film. Since the contact surfaces for all five SMA films belong to one monolithic element, the heating and cooling power applied to the sink and source during each cycle of operation by the five SMA films add up. The heat sink and source have a mass of 79.8 g and 62.09 g, respectively. These values, which are high in comparison with the other devices, are the result of the extrusions and the demand for the simplest possible geometry. To reduce parasitic heat flows between the heat sink and source elements, a PMMA layer with honeycomb-structured surfaces is included in between. Fiber reinforced polyamide screws with low heat

---

<sup>a</sup> The content of chapter 6.1 is based on the master thesis of R. Weidemann, which was co-supervised by the author [d]. The results of R. Weidemann's master thesis are used with his permission.

conductivity are used for fixation. The experimental setup is presented in Figure 56 b).

In the parallelized device NiTiFe films are used as active material. Material properties are discussed in chapter 3.2. The films are cut into lateral dimensions of 56 mm x 4 mm. The ends of each film are glued to 3D-printed fixations that are then screwed to a single rigid frame. The frame is connected to a single linear actuator of the experimental test setup that is used for operation. When the rigid frame is moved in x-direction the SMA films 1, 3, 5 are loaded, since they are pressed onto extrusions A, C and E. At the same time, the films 2 and 3 are unloaded and brought in contact with extrusions B and D. Films 1, 3, 5 transfer heat to the heat sink, whereas films 2 and 3 absorb heat from the heat source. When the frame is subsequently moved to the opposite direction, films 1, 3, 5 are released and brought in contact with extrusions B, D, F from where they absorb heat. Simultaneously, films 2 and 3 are pressed onto extrusions C, E, and release heat to the heat sink. This operation is cyclically repeated. In this way a heat flow is generated by all SMA films from the heat source to the heat sink. The heat source is enabled to provide cooling capacity. The actuation of the operation and monitoring of the performance is done by the experimental test platform presented in chapter 4.4. Sinusoidal load cycles with holding times are applied as described in chapter 4.5.

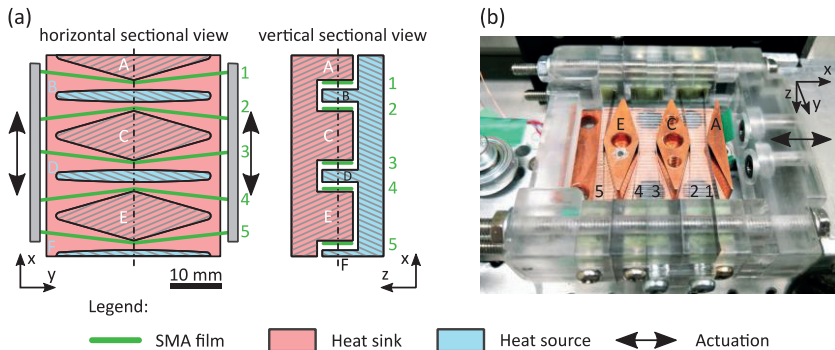


Figure 56 (a) Schematic setup of the parallelized elastocaloric cooling device. Two sectional views are presented for better understanding. The SMA films 1 to 5 are loaded by the triangular surfaces of extrusions A, C, E in out-of-plane deflection and are brought in contact with the surfaces of extrusions B, D, F in the unloaded state. Cyclic operation generates a heat flow from the cooled heat source to the heated heat sink. (b) The experimental device with the five SMA films, the frame they are fixed to, and the heat sink. The heat source is not included to enable the view of the SMA films.

### 6.1.3 Results

When the parallelized device is operated by cyclic movement of the frame with the SMA films, the temperatures of the heat sink and source start to change gradually. Temperature evolution of the heat sink and source are presented in Figure 57 a) for operation under frequencies  $f$  of 0.1, 0.5 and 1 Hz. Temperatures are presented as temperature difference between the absolute temperature and the initial starting temperature. The temperature slope reduces as the temperature difference between the sink and source elements increases. However, the temperatures do not saturate within the 100 s of operation. In Figure 57 c) device temperature spans  $\Delta T_{device}$  after 100 s of operation at operation frequencies between 0.05 and 1 Hz are summarized. A linear increase of  $\Delta T_{device}$  with  $f$  can be found. A maximum  $\Delta T_{device}$  of 4.4 °C is reached at 1 Hz. For all frequencies the heating and cooling contributes evenly to the device temperature span.

The force-displacement curve of the five antagonistically coupled SMA films in the device is presented in Figure 57 b) for different operation frequencies. Due to the uneven number of SMA films, the characteristic is not symmetric. The work dissipated per load cycle  $\Delta W_{device}$  is 130 mJ, 197 mJ and 280 mJ for the operation frequencies of 0.05 Hz, 0.25 Hz and 1 Hz, respectively. As expected from the superelastic material behavior, the dissipated work increases with the velocity of the cyclic movement.

The specific cooling capacity of the device also shows a linear increase with the operation frequency, as depicted in Figure 57 c). A maximum of  $\dot{q}_0^{cool} = 4.67 \text{ W/g}$  is reached at 1 Hz. This compares to an absolute cooling capacity of  $\dot{Q}_0^{cool}$  of 0.9 W. The absolute cooling capacity of the device utilizes the combined elastocaloric effect of all five SMA films.

Based on  $\Delta W_{device}$  and  $\dot{Q}_0^{cool}$  presented above, the  $COP_{device}$  is calculated as a metric for the efficiency of the device operation. The values of  $COP_{device}$  are plotted against the operation frequency in Figure 57 c).  $COP_{device}$  shows a maximum of 4.5 at the operation frequency of 0.25 Hz. At lower frequencies the operation is too slow to generate considerable cooling performance, thus  $COP_{device}$  is low as well. For higher operation frequencies,  $\Delta W_{device}$  increases faster than  $\dot{Q}_0^{cool}$  with  $f$ , and therefore  $COP_{device}$  reduces again. At 1 Hz  $COP_{device}$  is 3.2.

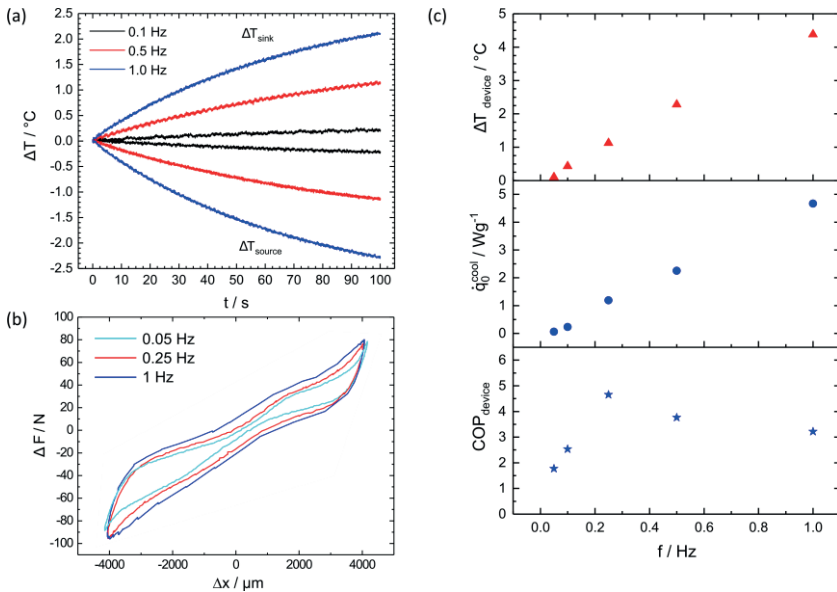


Figure 57 (a) Temperature evolution of heat sink and source elements as a function of time during operation at 0.1, 0.5 and 1 Hz. The parallelized device is operated for 100 s. (b) Force-displacement characteristic of the five coupled SMA films incorporated in the parallelized device at operation frequencies of 0.05, 0.25 and 1 Hz. (c) Device temperature span  $\Delta T_{device}$ , specific cooling capacity  $\dot{q}_0^{cool}$  and  $COP_{device}$  as a function of operation frequency  $f$ .  $\Delta T_{device}$  and  $\dot{q}_0^{cool}$  increase linearly with  $f$ . The maximum  $\dot{q}_0^{cool}$  is 4.67 W/g and corresponds to an absolute cooling capacity  $\dot{Q}_0^{cool}$ .

### 6.1.4 Discussion

The main goal of the parallelized device is to upscale the absolute cooling capacity, while maintaining the high specific cooling capacity of SMA film-based elastocaloric cooling devices. To obtain high specific cooling capacity, the high surface-to-volume ratio of the SMA films has to be maintained (compare chapter 4.1.2).

In the parallelized device, the film geometry with high surface-to-volume ratio is maintained, and the elastocaloric effect of five SMA films is added up in a parallelized device architecture.

The parallelized device reaches an absolute cooling capacity of 900 mW and specific cooling capacity of 4.67 W/g, both at 1 Hz. To evaluate the parallelized device performance, a comparison is drawn to the single film device presented in chapter 5.1. The single film device reaches maximum values of 220 mW and 19 W/g at 4 Hz, at 1 Hz it reaches 50 mW and 4.2 W/g. If performance is compared at the same operation frequency, specific cooling capacity is almost equal for both devices. Absolute cooling capacity is increased largely by a factor of 18 from 50 mW to 900 mW. This proves the function of the parallelized device architecture. However, the linear increase of  $\Delta T_{device}$ ,  $\dot{Q}_0^{cool}$  and  $\dot{q}_0^{cool}$  with the operation frequency in the investigated range and the comparison to the high value of  $\dot{q}_0^{cool}$  achieved in the single film device at high frequencies (19 W/g at 4 Hz in case of single film device) point out the potential of high operation frequencies also in the parallelized cooling device. Unfortunately, high operation frequencies were not possible due to experiment restrictions. Improvements in the experimental device and test platform are needed to reveal the full potential of the parallelized elastocaloric cooling setup.

The  $\Delta T_{device}$  in the parallelized device is limited to comparably low values of 4.4 °C. This is attributed to the high mass of the sink and source elements. Compared to the single film device, sink and source mass are increased roughly by a factor of 200. If higher  $\Delta T_{device}$  and faster device response is required, the thermal mass of the sink and source elements needs to be decreased considerably in the parallelized device. In addition, measures should be taken to achieve a more uniform and thus improved heat transfer between the SMA films and the sink and source element. The use of insulation could decrease parasitic heat losses and would contribute to an increased device temperature span in this way. The values for  $COP_{device}$  are comparable to the single film device, so no influence of parallelization on the device efficiency can be

found. WR is successfully implemented in the parallelized elastocaloric cooling setup.

The main challenge in the parallelized device is the accurate and repeatable loading of all the SMA films. This restricts the lifetime of SMA films and prevents higher operation frequencies in the given setup, since the demands on the actuator precision are increased. In single film devices, sufficient precision and repeatability is achieved by manual alignment and the use of compliant structures. The recurring arrangement of the five SMA films and the arrangement of heat sink and source below and above the films significantly restrict the available construction space in the parallelized device. This prevents the usage of beneficial compliant structures and leads to increased demands on the fabrication and alignment precision. However, precise alignment on the individual film level is hardly possible in the device. Furthermore, the statistical probability of a film failure is increased in the parallelized device solely due to higher number of films. In order to address this issue, fabrication and alignment precision have to be increased and at the same time the demands on the precision should be decreased by compliant structures (see chapter 4.1.1). A promising approach to include compliant structures is the space-saving use of soft materials, like done in the cascaded device with in-plane loading in the following chapter. In addition, a modular system approach could increase fabrication precision and ease alignment in the next generation of parallelized devices.

To conclude, the parallelized device architecture has proven its potential for upscaling of the absolute cooling capacity in SMA film-based elastocaloric cooling devices. However, in the given setup, device temperature spans are low compared to the other SMA film-based elastocaloric cooling devices developed in this work. In addition, reliable operation is challenging in the given device. Thus, in a next device generation, the mass of sink and source elements in comparison to the amount of active material should be reduced, fabrication and alignment precision has to be increased, possibly in a modular approach, and compliant structures should reduce the demands on the

precision. In this way, massive parallelization based on the introduced concept might pave the way for future planar cooling panels that allow for easy integration in the built environment. Hence, innovative environmentally friendly elastocaloric cooling can be integrated into standardized building components and a completely new field of application can be addressed [225].

## 6.2 Cascaded Device with In-plane Loading

### 6.2.1 Concept

The cascaded system architecture introduced in chapter 4.1.3 is implemented in the experimental elastocaloric cooling device presented in this chapter. The aim of cascaded elastocaloric cooling devices is mainly to increase the device temperature span. Three SMA films transport heat in a series connection with intermediate copper elements. In the cascade, only the first (1 with reference to Figure 58) and last SMA film (3) release and absorb heat directly to the heat sink (A) and from the heat source (D), respectively. The intermediate copper elements (B, C) interconnect their neighboring films thermally and function as heat sink for one of them and heat source for the other. In this way, each film operates at different temperature levels and the device temperature span increases.

Unlike the other elastocaloric cooling demonstrators presented in this work, here the SMA films are not loaded in out-of-plane, but are loaded in-plane (compare chapter 2.3.1). In-plane loaded devices with changing mechanical contacts require two actuators for operation, one to load the SMA and one to change the thermal contacts [182]. The increased complexity owed to the two actuators increases the flexibility of the in-plane loaded device. In-plane loading allows to vary operation parameters in a simple way with a single experimental setup. The maximum applied strain is not defined by the device geometry like in devices operated by out-of-plane loading, but can be easily

varied. This allows to investigate different materials with different transformation strains within the very same device. The timing between the loading cycle and the cycle for heat transfer can also be varied and investigated. In the following investigation, the influence of operation parameters, which cannot be investigated in devices loaded out-of-plane, is revealed. Even more important, the influence of the cascaded device architecture on the cooling performance and in particular on the device temperature span is investigated to evaluate the concept of cascaded elastocaloric cooling devices.

### 6.2.2 Experimental Device and Operation

The cascaded experimental setup consists mainly of four copper elements A to D that function as heat sink / source and three SMA films, which are all aligned in parallel. The schematic setup is displayed in Figure 58. All copper elements are connected to a common support structure that is connected to a linear bearing that allows movement perpendicular to the SMA film surface in  $x_1$ -direction. This support structure is coupled to actuator 1. The ends of the SMA films are connected together at defined distance. One of their ends is fixed in position, the second end is connected to actuator 2 that moves in-plane direction of the SMA film ( $x_2$ ). So, the SMA is basically loaded like in a tensile testing machine by actuator 2, while actuator 1 changes the contact conditions between the SMA films and the copper elements.

The experimental implementation of the concept is shown in Figure 59. The complete experimental test setup is shown in Figure 59 a), including the two linear actuators and a load cell that measures the load applied in  $x_2$ -direction to the SMA films. The single elements of the device can be found in Figure 59 c). The experimental test setup introduced in chapter 4.4 is used for operation and monitoring of the elastocaloric cooling device. Main difference to the experimental operation of the other SMA film-based elastocaloric cooling devices presented in this work is that two linear motors are used at once, instead of one. The support structure that holds the copper elements in place is CNC milled from PMMA. PMMA is used due to its transparency. The lateral

dimensions of the copper elements are also CNC milled from a copper sheet. The surfaces are mechanically polished. To measure the temperature of the copper elements a miniature T-type thermocouple with a tip size of 0.4 mm was integrated in a 0.5 mm hole in each copper element. Each copper element has a mass of 0.7 g. Mechanical compliance in the contact of SMA film and the heat sink and source elements is of high importance for the operation and performance of SMA film-based elastocaloric cooling devices (see chapter 4.1.1). However, the cascaded setup does not allow for spring-like structures as in the other cooling devices in this work. Thus, the material compliance of an elastomer is used here rather than the structural compliance of a spring. To do so, the copper elements are not connected in a rigid way with the PMMA support structure, but a compliant “cup” of PDMS has been introduced in between the copper elements and the support structure. The PDMS structures are casted with the help of a custom-made casting mold. Two different superelastic SMA materials are used in this experimental setup, cold rolled NiTiFe films with a thickness of 40  $\mu\text{m}$  and sputtered TiNiCuCo films with a thickness of 30  $\mu\text{m}$ . Detailed information on both SMA materials can be found in chapter 3. The lateral dimensions of the films are 32 x 3  $\text{mm}^2$ .

In a typical operation cycle actuator 2 loads the SMA films and at the same time actuator 1 moves in the direction of  $x_1$  and brings the films in contact with the copper elements B to D (see Figure 58). Subsequently, actuator 2 unloads the SMA films and actuator 1 moves to the opposite direction and brings the films in contact with copper elements A to C. In general, the cyclic loading of the SMA films is done according to the sinusoidal operation cycle described in chapter 4.5. The position of actuator 1, which is responsible for the changing mechanical contacts, is controlled in a similar sinusoidal way with holding times.

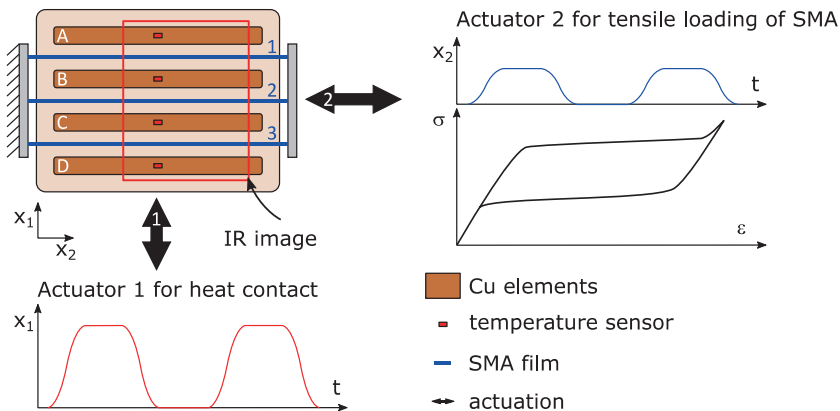


Figure 58 Schematic of the cascaded device with in-plane loading. The cooling device comprises three SMA films and four heat sink / source elements made from copper. Two actuators are needed, one for the cyclic loading of the SMA (actuator 2) and one that changes the contact conditions of the SMA films and the heat sink and source elements (actuator 1). Typical actuation profiles are shown for both of the actuators.

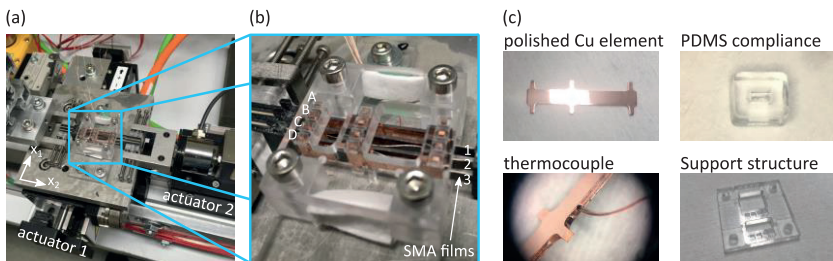


Figure 59 (a) Experimental test setup including the two linear actuators and the cascaded device with in-plane loading. (b) Cascaded SMA film-based elastocaloric cooling device that is operated by in-plane loading. (c) Components of the device.

### 6.2.3 Results

The system architecture of the cascaded device with in-plane loading and two separate linear actuators allows for variation of operation conditions in a wide range. In Figure 60 the influence of the stroke of actuator 1 (a), the delay time between the cycles of the two actuators 1 and 2 (b), the maximum applied strain in case of NiTiFe (c) and TiNiCuCo (d) on the device performance is investigated. In each case, the device temperature span after 20 s  $\Delta T_{device}(20\text{ s})$  and the cooling capacity  $\dot{Q}_0^{cool}$  are determined as a function of the investigated parameter. The used SMA material, the number of SMA films utilized, and the operation frequency are stated in each case in the figures. Small schematics are included to illustrate the investigated parameters.

Actuator 1 changes the mechanical and thermal contact conditions of the SMA films and the sink and source elements. If the stroke of actuator 1,  $\Delta x_1$  is chosen to low, full contact between the films and the sink / source elements cannot be reached, but an air gap persists in between. If  $\Delta x_1$  is too high, the SMA films or the device might be damaged. Both,  $\Delta T_{device}(20\text{ s})$  and  $\dot{Q}_0^{cool}$  increase with  $\Delta x_1$  up to the value of 2.1 mm and saturate afterwards. This shows that it is necessary to achieve full contact, which is reached above 2.1 mm in the present case. A further increase however, does not improve the performance, but only increases the risk of damage. Thus, in following experiments,  $\Delta x_1$  is fixed to 2.2 mm to ensure good contact without applying too much load.

In Figure 60 b) the influence of a delay time  $\Delta t$  between the two oscillatory movements of the two actuators is investigated. The positions of both actuators are controlled to follow a sinusoidal trace with holding times included at the turning points. Holding times and the time for the sinusoidal movement are chosen equal for both actuators. In this investigation, a time delay between the two movements is included. The mechanical loading / unloading of the SMA films and the movement perpendicular to the SMA film do not coincide, but a small delay time is included between the cycles. The perfor-

mance of  $\Delta T_{device}$  (20 s) and  $\dot{Q}_0^{cool}$  show that within a  $\Delta t$  window of -0.05 to 0.05 s no influence can be found. However, if the  $\Delta t$  becomes higher, performance decreases.  $\dot{Q}_0^{cool}$  is more sensible to an increased  $\Delta t$  compared to  $\Delta T_{device}$  (20 s). According to this investigation the delay  $\Delta t$  is chosen to be zero in all other experiments. Nevertheless, the fact that small  $\Delta t$  does not diminish the performance is good for a robust operation of the system.

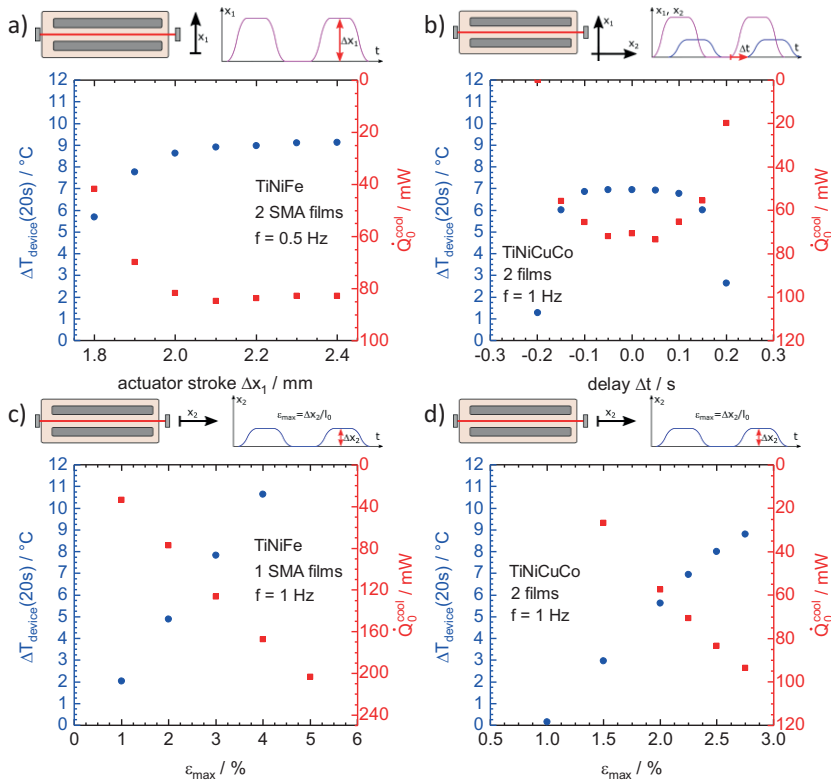


Figure 60 Influence of operation parameters on the performance of the cascaded device with in-plane loading. The device temperature span after 20 s  $\Delta T_{device}$  (20 s) and the cooling capacity  $\dot{Q}_0^{cool}$  are used as performance metrics. The influence of the stroke of actuator 1 (a), the delay time between the operation cycles of the two actuators (b), the maximum strain applied to the SMA material in case of NiTiFe (c) and TiNiCuCo (d) are investigated.

Figure 60 c) and d) illustrate the influence of the maximum strain  $\varepsilon_{max}$  applied to the SMA films within each cycle. The SMA films are cycled between zero strain and  $\varepsilon_{max}$ . The maximum strain is determined by the stroke of actuator 2  $\Delta x_2$  and the initial length of the SMA film  $l_0$  according to  $\varepsilon_{max} = \Delta x_2 / l_0$ . The influence is investigated for NiTiFe (c) and TiNiCuCo (d) films as active material. A clear trend can be found for both SMA materials in the investigated strain range. The  $\Delta T_{device}(20\text{ s})$  and the  $\dot{Q}_0^{cool}$  clearly increase with increasing  $\varepsilon_{max}$ . In case of NiTiFe, a strain range of 1 to 5 % is investigated. An almost linear dependence can be found. TiNiCuCo is investigated in the range from 1 to 2.75 %. TiNiCuCo-3 SMA film material is used. At  $\varepsilon_{max} = 1\%$  almost no cooling performance exists and the SMA is cycled almost completely within the elastic range. For higher strains,  $\Delta T_{device}(20\text{ s})$  and  $\dot{Q}_0^{cool}$  again show an almost linear increase with  $\varepsilon_{max}$ . With the increased strain, the fraction of the SMA undergoing the transformation from austenite to martensite and back increases. Thus, the latent heat of the transformation that is accessed upon load cycling is increased. For higher strains above the transformation strain of the materials a saturation of the device performance is expected. If the SMA already transforms completely, a further increase of  $\varepsilon_{max}$  has only minor influence on the released latent heat. However, this regime is not reached in the present investigation. High strains also increase the risk of material failure [140;226]. Hence, strains are limited to 5 % for NiTiFe and 2.75 % for TiNiCuCo to avoid a high risk of specimen failure.  $\varepsilon_{max}$  has to be determined according to a compromise between high cooling performance and reliability. For further experiments  $\varepsilon_{max}$  has been chosen to be 4.5 % in case of NiTiFe and 2.6 % in case of TiNiCuCo to pay credit to the two opposing trends.

With the pre-tests to determine optimum operation parameters the full potential of the cascaded device with in-plane loading can be revealed. The temperature evolution of the copper elements of the cooling device in the tests that reached the highest temperature spans with NiTiFe and TiNiCuCo as active material are presented in Figure 61 a) and Figure 62 a). The temperatures are plotted as temperature difference between the absolute temperature and the initial starting temperature. As for other SMA film-based elastocaloric

cooling devices, the temperatures change in a stepwise manner representing the discontinuous contacts and heating and cooling within each operation cycle. After operation start, temperatures of the copper elements change fast and then temperatures stabilize and oscillate around a fixed value in each cycle. The first and last elements in the cascade are subjected to the highest temperature changes, whereas intermediate elements follow intermediate temperature trends. The three SMA films of the cascade operate at different temperature levels and transfer heat from element D over C and B to element A.

With the combined cooling effect of the three NiTiFe films the device reaches a temperature span  $\Delta T_{device}$  of 27.3 °C at 1 Hz. The combined temperature span is the sum of the temperature differences between the neighboring copper elements. Here, a temperature difference of roughly 9 °C can be measured between elements A and B, B and C, C and D. A cooling capacity of 190 mW or 3.4 W/g is reached in the experiment. Figure 61 b) reveals the surface temperature distribution of the device in the very same experiment measured by IR thermography before operation start, after 20 s, and after 80 s of operation.

The two TiNiCuCo films operated at 2 Hz reach a combined  $\Delta T_{device}$  of 17.9 °C (Figure 62, a). A TiNiCuCo-1 film is utilized in between the copper elements A and B, whereas TiNiCuCo-3 is used in between B and C (compare chapter 3.3). Temperature differences between element A and B, and B and C are both roughly 9 °C. This specific experiment reaches a cooling capacity of 181 mW or 4.82 W/g.

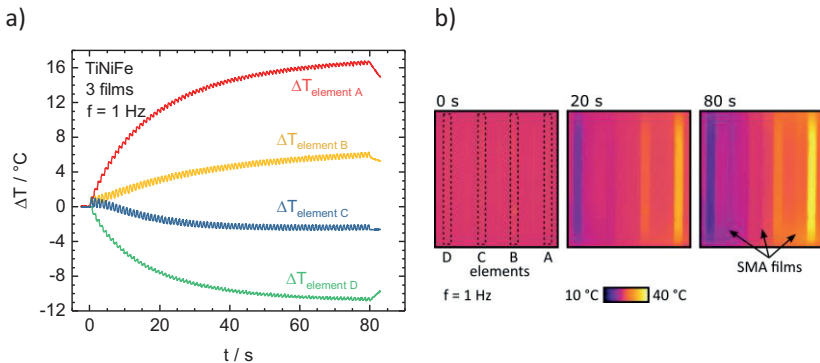


Figure 61 (a) Temperatur evolution of the copper elements A to D of the cascaded elastocaloric cooling device with in-plane loading. Operation takes place with three NiTiFe films at 1 Hz. (b) IR thermographs of the cooling device during operation in the experiment displayed in a). Thermographs are taken before, after 20 s, and after 80 s of operation

The influence of the operation frequency  $f$  on the  $\Delta T_{\text{device}}$  and  $\dot{Q}_0^{\text{cool}}$  of the elastocaloric cooling device is investigated in a series of experiments displayed in Figure 62. Results are given for operation with one and two TiNi-CuCo films.  $\Delta T_{\text{device}}$  increases with  $f$  until 2 Hz, where  $\Delta T_{\text{device}}$  reaches a maximum for operation with one and two SMA films. Especially when operated with one SMA film,  $\Delta T_{\text{device}}$  decreases considerably when  $f$  is further increased to 3 Hz. The usage of two SMA films compared to one SMA film increases  $\Delta T_{\text{device}}$  at 2 Hz by about 58 % from 10.6 to 16.7 °C in this series of experiments. The cooling capacity  $\dot{Q}_0^{\text{cool}}$  increases with  $f$  as well, and saturates at 2 Hz.  $\dot{Q}_0^{\text{cool}}$  is hardly influenced by the number of SMA films. The highest value of  $\dot{Q}_0^{\text{cool}}$  is reached at 2 Hz and 3 Hz with about 180 mW. When the specific cooling capacity is considered instead of absolute values, the number of SMA films however has a significant influence. The absolute values of 180 mW for one and two films relate to specific values of 9.6 and 4.8 W/g, respectively.

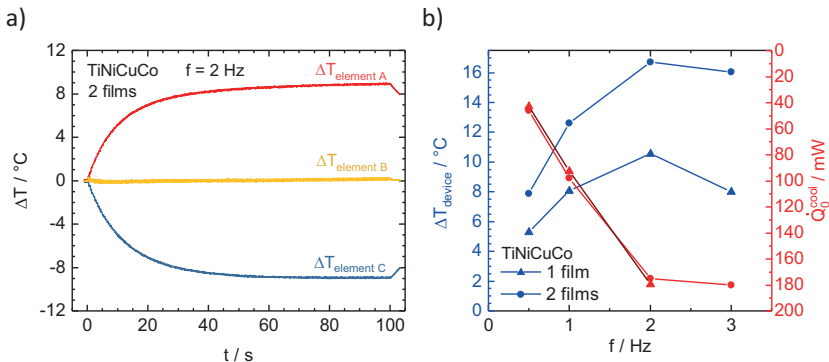


Figure 62 (a) Temperatur evolution of the copper elements A to C of the cascaded elastocaloric device, operated with two TiNiCuCo films at 2 Hz. (b) Influence of the operation frequency  $f$  on the device temperature span  $\Delta T_{\text{device}}$  and the cooling capacity  $\dot{Q}_0^{\text{cool}}$ . Results are given for operation with one and with two TiNiCuCo films.

### 6.2.4 Discussion

The cascaded device with in-plane loading applies the concept of cascading to SMA film-based elastocaloric cooling devices. The cascaded device architecture allows for high device temperature spans, possibly higher than the adiabatic temperature span of the used SMA material.

In addition, the cascaded device with in-plane loading deviates from the other devices in this work by the load application. Here, load is applied in-plane. This rises the need for an additional actuator to change the mechanical contacts, and thereby direct and separate the hot and cold heat flow in the cooling device. The device becomes more complex, but also allows to investigate the influence of parameters that are fixed in devices based on out-of-plane loading.

Different operation parameters are investigated. For a good cooling performance, the stroke of the actuator that changes the mechanical contacts, actuator 1, needs to be above 2.1 mm. A further increase is not beneficial to the

device performance but might apply unnecessary loads to the device. Thus,  $\Delta x_1$  is chosen to be 2.2 mm. The investigation of the influence of a short delay time  $\Delta t$  between the operation cycles of the two actuators reveals that synchronous operation is desirable. This result is also interesting to the devices loaded out-of-plane. In case of out-of-plane loading, the change of contacts and the mechanical loading coincident naturally and cannot be changed. However, the investigation of the delay time  $\Delta t$  in this chapter reveals that this is no disadvantage. Increased maximum strain leads to improved device performance in the investigated strain range for both investigated SMA film materials, NiTiFe and TiNiCuCo. Higher maximum strains force an increased fraction of the SMA material to undergo the stress-induced phase transformation. The amount of latent heat of transformation released and absorbed during load cycling increases and the elastocaloric effect increases as well. Yet, increased maximum strain also increases the risk to damage the SMA film. A compromise is needed. As a good compromise, the maximum strain has been fixed to 4.5 % in case of NiTiFe and 2.6 % in case of TiNiCuCo.

In general, the device would also allow for more complex loading profiles, like e.g. a combined adiabatic isothermal operation cycle or a non-adiabatic adiabatic cycle, which both have been found beneficial for elastocaloric cooling [39]. However, the control of the given experimental test setup is not fast enough to apply the improved cycles in a reliable way, especially under high operation frequencies. So, the investigation of complex loading profiles and operation cycles stays an open task for future work.

The cascaded device with in-plane loading clearly allows increased device temperature spans  $\Delta T_{device}$ . With the combined effect of three NiTiFe films as active material the device reaches a maximum  $\Delta T_{device}$  of 27.3 °C. This compares to the adiabatic temperature span of the SMA material for heating and cooling of 20 and -16 °C. The combined effect of two TiNiCuCo films give rise to a  $\Delta T_{device}$  of 17.9 °C. This compares to a maximum adiabatic temperature span of 12.2 °C and -14.5 C. The cascaded device reaches a  $\Delta T_{device}$  that exceeds the materials  $\Delta T_{ad}$  for both materials. However, the combined

adiabatic temperature span for heating and cooling could not be surpassed in the performed experiments. Nevertheless, compared to the single film device maximum  $\Delta T_{device}$  is increased by 95 % in case of three NiTiFe films, and by 28 % in case of two TiNiCuCo films. Therefore, the potential of the cascaded device architecture is proven. In experiment with TiNiCuCo films the  $\Delta T_{device}$  is increased by 58 % by using two instead of one SMA film. Two different TiNi-CuCo alloys are used in the present investigation with a shift in  $A_f$  according to the altered temperature range of operation in the cascade. The use of different SMA materials with tailored  $A_f$  will become increasingly important in future, as  $\Delta T_{device}$  in elastocaloric cooling devices is expected to increase further.

As known from the other SMA film-based elastocaloric cooling devices, the operation frequency has a tremendous influence on the device performance of the cascaded setup.  $\Delta T_{device}$  and  $\dot{Q}_0^{cool}$  clearly increase with  $f$  for frequencies up to 2 Hz. Other than known from the devices with out-of-plane loading,  $\Delta T_{device}$  even decreases again for the higher frequency of 3 Hz. Saturation of  $\Delta T_{device}$  with increasing  $f$  in SMA film-based elastocaloric cooling devices has been found due to limited heat transfer and decreasing temperature difference between the SMA film and the heat sink and source elements. Since heat transfer mechanisms in the in-plane loaded device are similar, both effects are likely to play a role here. Nevertheless, both effects would not lead to a decrease of  $\Delta T_{device}$  for higher frequencies, but to saturation. The decrease is attributed to insufficient control of the two actuators. As found in the investigation of the influence of a delay between the two actuator cycles, an unfavorable timing of the two cycles can lead to a complete breakdown of the device performance. At 3 Hz, the control of the two actuators is not fast and precise enough to ensure a completely synchronous movement. Consequently, the performance declines.

The cooling capacity  $\dot{Q}_0^{cool}$  and specific cooling capacity  $\dot{q}_0^{cool}$  of the cascaded device are in the range known from other SMA film-based cooling devices developed in this work. It is important to highlight that the absolute cooling

capacity  $\dot{Q}_0^{cool}$  is not influenced by the number of cascaded SMA films. The same absolute cooling capacity is achieved, regardless of the number of cascaded SMA films. Thus, the specific cooling capacity  $\dot{q}_0^{cool}$  is influenced highly, and decreases with the number of SMA films. A single TiNiCuCo film incorporated in the device and operated at 2 Hz gives rise to a cooling capacity of 180 mW or 9.6 W/g. Two TiNiCuCo films at 2 Hz achieve 180 mW or 4.8 W/g. Three NiTiFe films lead to a cooling capacity of 193 mW and 3.4 W/g at 1 Hz.

Although the loading concept of the present device differs from the other cooling devices developed in this work, the basic concept of heat transfer and the mechanism to separate the cold from the hot heat flow are similar. In consequence, the achieved cooling capacity is in a similar range also. This is not the case for the device temperature span. The results prove that cascading of the elastocaloric effect of several SMA films in one device is an effective strategy to increase the device temperature span. The limitations of the device temperature span of single SMA film-based elastocaloric devices do not apply to cascaded devices. This allows SMA film-based elastocaloric cooling devices to address new applications that require high temperature differences.

## 6.3 Cascaded Device with Out-of-plane Loading

### 6.3.1 Concept

The cascaded device with out-of-plane loading combines the potential of the cascaded system architecture with out-of-plane loading. This allows for a comparably simple device setup. As in the single film device only one actuator is needed for operation. The aim is to transfer the insights gained with the single film device and the cascaded device with in-plane loading to a single cascaded cooling device. In this way the device temperature span of the

cascaded device can be increased, while the device complexity is kept as low as possible.<sup>b</sup>

### 6.3.2 Experimental Device and Operation

The cascaded device with out-of-plane loading combines the elastocaloric cooling performance of three SMA films in a serial way. A schematic of the device is illustrated in Figure 63. The device consists of four copper elements and the three TiNiCuCo films in between them. The copper elements have each a flat and a triangular shaped surface at opposite sites. The SMA film can absorb heat from the flat surface and release heat to the triangular shaped surface, which loads the SMA film by out-of-plane deflection. Thus, the two sides of one single copper element are heat sink and source. The middle elements C and B function as heat sink for the SMA film above and as heat source for the film below and combine the single units into a cascaded device. Element A is purely heated, and element D purely cooled.

The SMA films have a thickness of 30 µm and length and width of 20 mm and 2 mm. The SMA films are fixed to a steel frame for better handling. Fabrication and properties of the TiNiCuCo films are addressed in chapter 3.3. The TiNiCuCo alloy used in this device shows a similar mechanical performance as TiNiCuCo-2. However, the alloy has a slightly altered composition with an increased copper content ( $Ti_{53}Ni_{24}Cu_{20.9}Co_{2.1}$ ). The adiabatic temperature span of the specific SMA is 10 °C upon loading and -13 °C upon unloading.

The copper elements are fabricated by wire-electro discharge machining and subsequent mechanical polishing of the shaped surfaces, the elements have a uniform height of 4 mm and a mass of 0.8 g. The copper elements are suspended by a polymer structure fabricated by stereolithographic 3D printing (compare chapter 4.3). The suspension includes spring-like structures that result in a mechanical compliance in the actuation direction. In Figure 64 an

---

<sup>b</sup> The content of chapter 6.3 was previously published by the author in [217;218].

image of the experimental setup is presented. The base area of the structure is 36.50 mm x 20 mm, the height is 22 mm.

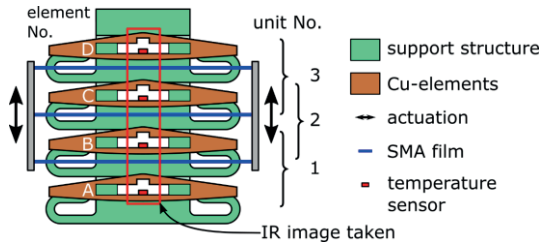


Figure 63 Schematic of the cascaded elastocaloric cooling device loaded in out-of-plane. The device is composed of three single units 1 to 3, each with a SMA film. The three SMA films are mechanically connected at their ends and are actuated by a single actuator as indicated by the arrows. Copper elements A to D function as heat sink and source. A polymer support structure is used to suspend the copper elements. ©2019 IEEE, figure reprinted from [218] with permission.

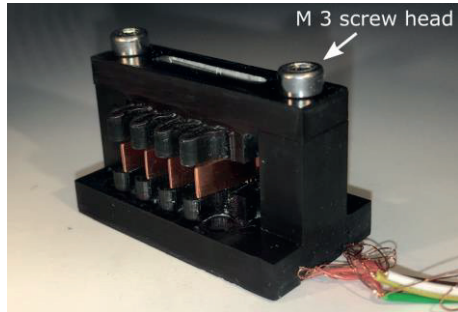


Figure 64 Experimental setup of the cascaded cooling device with out-of-plane loading. The four copper elements A to D can be seen along with their polymer support structure. The actuator unit and SMA films are not included for the sake of clarity. ©2019 IEEE, figure reprinted from [218] with permission.

The device is operated by a single actuator of the experimental test setup described in chapter 4.4. The actuator moves the ends of the SMA film cyclically back and forth. In this way they are first pressed onto the triangular shaped surface of the copper elements and thereby loaded out-of-plane. The mechanical loading induces the phase transformation in the SMA and the released heat is directly transferred to the triangular shaped copper surface, where the SMA film is kept in contact for a defined holding time. Subsequently, the SMA films are moved to the opposite direction. The load is released and the films transform back and absorb heat from their surroundings, in particular from the flat copper surface the SMA film is brought in contact with. The actuator moves the SMA film ends on a sinusoidal trajectory with additional holding times as explained in chapter 4.5. The device is operated under operation frequency of 1, 2 and 4 Hz. The device can also be operated with less than three SMA films. In this way the influence of the number of cascaded SMA films on the cooling performance can be investigated. Experimental results are supported by device simulation. A lumped element simulation model is set up in accordance to chapter 4.2.

### 6.3.3 Results

Operating the complete cascaded elastocaloric cooling device as described above results in a stepwise heat transfer from Cu-element D over C and B to A. Figure 65 shows the temperature evolution of all four Cu-elements during 200 s of operation with an operation frequency of 4 Hz. The temperatures are plotted as temperature difference between the absolute temperature and the initial starting temperature. Clearly Cu-element D cools down and A heats up, B and C follow intermediate trends. The temperature evolution saturates after 100 s and reaches a device temperature span  $\Delta T_{device}$  of 15 °C between the elements A and D.

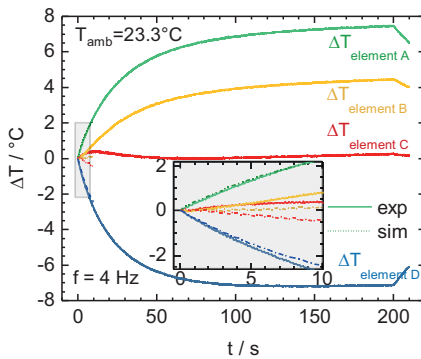


Figure 65 Temperature evolution of the copper elements A to D of the cascaded cooling device during operation. Here an operating frequency of 4 Hz is applied. The excerpt shows simulation results along with the experimental results for the first 10 s of operation (information on simulation in 4.2). ©2019 IEEE, figure reprinted from [218] with permission.

In Figure 66 a) the device temperature span after saturation  $\Delta T_{device}$  is displayed as a function of the operation frequencies for different numbers of cascaded SMA films. Clearly,  $\Delta T_{device}$  rises with the number of cascaded SMA films: at 4 Hz from 7.6 °C (one film) to 15 °C (three film). In addition, the temperature difference increases significantly with the operation frequency: for three cascaded films from 5.4 °C (1 Hz) to 15 °C (4 Hz). The surface temperature profiles of the device section marked in Figure 63 before operation are presented in Figure 66 b). Profiles are shown for one operated SMA film and two and three cascaded SMA films, all operated at 4 Hz.

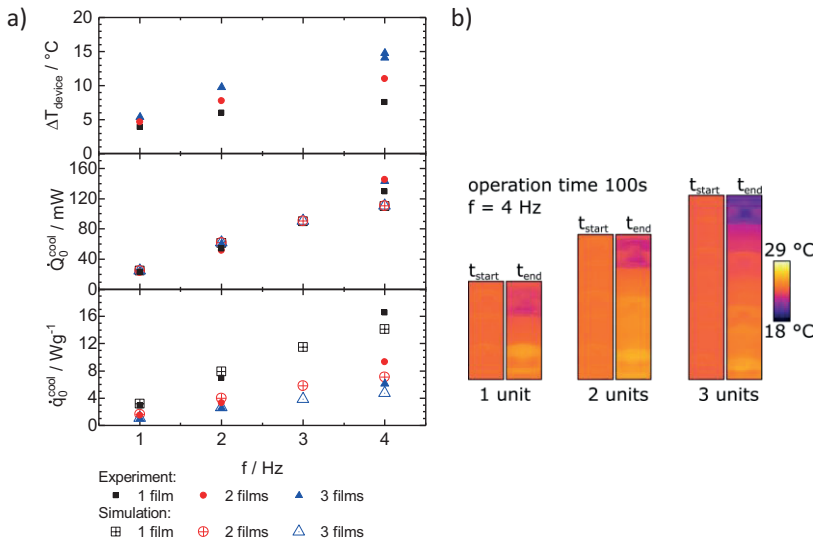


Figure 66 (a) Compilation of results on the device temperature span  $\Delta T_{device}$ , the absolute cooling capacity  $\dot{Q}_0^{cool}$  and the specific cooling capacity  $\dot{q}_0^{cool}$ . All performance metrics are plotted versus the operation frequency. Results are given for operation with a single SMA film as well as for two and three cascaded films to understand the influence of the cascaded system architecture on the device performance. (b) Surface temperature profiles of the cascaded device before and after operation at 4 Hz for 100 s. The profiles are taken by IR thermography. Only a section of the entire device is shown as indicated in Figure 63. ©2019 IEEE, figure reprinted from [218] with permission.

Besides the temperature span, Figure 66 depicts the absolute and specific cooling capacity of the device,  $\dot{Q}_0^{cool}$  and  $\dot{q}_0^{cool}$ . Both, absolute and specific cooling capacities show an almost linear increase with the operation frequency.  $\dot{Q}_0^{cool}$  is not influenced by the number of cascaded SMA films. Thus,  $\dot{q}_0^{cool}$  decreases with the number of cascaded SMA films, as more SMA material is used in the device configuration to achieve the same cooling capacity. The system reaches its highest cooling capacity of 0.145 W at 4 Hz, the maximum specific cooling capacity of 16.7 W/g is reached by the single unit configuration at 4 Hz.

The efficiency of the device, more particular the  $COP_{device}$ , is evaluated for 1 Hz and different numbers of cascaded SMA films. In this device,  $COP_{device}$  follows a similar trend like  $\dot{q}_0^{cool}$ , since the work input scales with the amount of SMA material. For operation of a single SMA film,  $COP_{device}$  reaches 5.7, which compares well to the value found in the single film device presented in chapter 5.1. When the number of cascaded SMA films is increased,  $COP_{device}$  drops to 1.9 for three SMA films.

### 6.3.4 Discussion

The cascaded device with out-of-plane loading combines the concept of cascaded elastocaloric devices that enable high device temperature spans, with a simple system architecture similar to the single film device. Only one actuator is needed for the cyclic loading of all SMA films and the separation of hot and cold heat flows within the system.

Like in the other SMA film-based elastocaloric cooling devices, the operation frequency  $f$  has a high influence on the cooling performance of the cascaded device with out-of-plane loading. Generally, the device temperature span  $\Delta T_{device}$  and the cooling capacity  $\dot{Q}_0^{cool}$ ,  $\dot{q}_0^{cool}$  increase with the operation frequency. Other than in the single film device no clear saturation of the performance with  $f$  can be found for the cascaded device. The number of cascaded films shows a clear influence on  $\Delta T_{device}$ . At 4 Hz,  $\Delta T_{device}$  increases from 7.6 °C to 15 °C when the number of cascaded films is increased from one to three. Therefore,  $\Delta T_{device}$  overcomes the materials  $\Delta T_{ad}$ . However, the combined  $\Delta T_{ad}$  for heating and cooling is not reached. Linear extrapolation suggests that six cascaded films would be necessary to do so. Nevertheless, the improvement in  $\Delta T_{device}$  by cascading comes at cost.  $\dot{Q}_0^{cool}$  is hardly influenced by the number of cascaded films and reaches a maximum of 145 mW at 4 Hz. In turn,  $\dot{q}_0^{cool}$  and  $COP_{device}$  decrease with the number of cascaded SMA films.  $\dot{q}_0^{cool}$  decreases from 16.7 W/g (1 film, 4 Hz) to 6.1 W/g (3 films, 4 Hz) and  $COP_{device}$  from 5.7 (1 film, 1 Hz) to 1.9 (3 film, 1 Hz).

The performance metrics of the cascaded elastocaloric cooling device,  $\Delta T_{device}$ ,  $\dot{Q}_0^{cool}$ ,  $\dot{q}_0^{cool}$ , and  $COP_{device}$  follow different trends with regards to  $f$  and the number of cascade SMA films. Thus, there is no single optimum configuration and operation suitable to all application scenarios. Instead, a compromise has to be found and adapted to each special application. The cascaded device architecture introduces one more parameter, the number of cascaded SMA films, that allows to fit device performance better to specific demands. Even more important, cascading enables operation at higher temperature spans. Consequently, the cascaded device allows to address completely new applications that require higher temperature spans.

## 7 Discussion of Elastocaloric Cooling Devices

Elastocaloric cooling devices need to cyclically apply a uniaxial stress to the elastocaloric material in order to repeatedly trigger the elastocaloric effect. In addition, the hot and cold heat flows, which are generated by the elastocaloric heating and cooling of the active material, have to be separated from each other. As in all cooling devices, the hot heat flow is considered waste heat and has to be released to the environment, whereas the desired cold heat flow is ready to provide cooling. The device must guarantee the function over a long period of time and many load cycles, which places high demands on the device itself and especially on the elastocaloric material. An ideal elastocaloric cooling device should provide the needed cooling capacity over a wide range of temperatures and also large temperature spans. Furthermore, the mechanical power input should be low for efficient operation and thus high coefficient of performance  $COP_{mat}$ .

The elastocaloric cooling devices that are developed and characterized in this work share basic concepts of operation. In Table 8 the devices are categorized according the classification approach for elastocaloric cooling devices developed in chapter 2.4.1. SMA films, mostly with a thickness of 30 µm, are used as active material in all devices (i: 1). Two types of SMA films are used, cold rolled NiTiFe and sputtered TiNiCuCo films (h: 1). Film geometries have a high surface-to-volume ratio and therefore enable efficient and fast heat transfer within the elastocaloric device. All devices are based on heat transfer between solid elements in mechanical contact (b: 1). The hot heat flow is separated from the cold by changing contact conditions (c: 1). The heat transfer concept enables good heat transfer and a simple system architecture. No additional fluidic circuits and pumps are needed. The SMA films are loaded in tension, either in out-of-plane deflection (f: 2) or in pure tension (f: 1). In case of out-of-plane deflection, only a single linear actuator is needed for the

device operation and maximum forces in the device are reduced compared to in-plane loading. The single film devices do not include a concept for caloric amplification (a: 1), and thus their temperature span is limited by the active material's adiabatic temperature span. However, the concept of cascaded elastocaloric cooling devices is developed in this work to reach device temperature spans that are not limited by the available active material (a: 3). In addition, a parallelized device is developed to increase the absolute cooling capacity of SMA film-based cooling devices. The coupled and the parallelized device demonstrate how to include work recovery (WR) in SMA film-based elastocaloric cooling (g: 2).

SMA film-based elastocaloric cooling benefits from its simple device architecture that not only allows to build miniature scale elastocaloric cooling devices, but also to extend the device architecture into parallelized and cascaded systems based on the same basic principle.

The fabrication of the experimental devices presented in this work is similar in most cases. Stereolithographic 3D printing is used for the fabrication of the polymer support structure. The copper heat sink and source elements are precision-machined and mechanically polished (see chapter 4.3).

Operation and monitoring of the device performance are carried out with a test setup that is developed within this work for this specific task (see chapter 4.4).

Table 8 Classification of SMA film-based elastocaloric cooling devices presented in this work. Each device is classified according to the approach introduced in chapter 2.4.1. The single characteristics are coded by numbers according to Figure 13. The overview allows to quickly identify similarities and key differences between the devices. eCM denotes elastocaloric material.

SMA film-based elastocaloric cool- ing device	Chapter No.	classification categories according to chapter 2.4.1								
		a	b	c	d	e	f	g	h	i
caloric amplification	heat transfer	separation of hot and cold heat flow	relative motion	type of actuator move- ment	loading stress state of eCM	work recovery	type of eCM	eCM geometry		
Single film devices	5.1 - 5.3	1	1	1	2	1	2	1	1	1
Coupled device	5.4	1	1	1	2	1	2	2	1	1
Parallelized device	6.1	1	1	1	2	1	2	2	1	1
Cascaded device in- plane loading	6.2	3	1	1	2	1	1	1	1	1
Cascaded device out-of-plane load- ing	6.3	3	1	1	3	1	2	1	1	1

Legend (only characteristics that are applied in this table are listed):

- a) caloric amplification: 1 none; 3 cascaded;
- b) heat transfer: 1 solid-to-solid;
- c) separation of hot and cold heat flow: 1 changing thermal contact conditions;
- d) relative motion: 2 moving eCM, static heat sink and source; 3 static eCM, moving heat sink and source;
- e) type of actuator movement: 1 linear oscillatory;
- f) loading stress state of eCM: 1 pure tension; 2 tension, out-of-plane deflection;
- g) work recovery: 1 none; 2 antagonistic coupling;
- h) type of elastocaloric material: NiTi-based SMA;
- i) geometry of elastocaloric material: 1 film / foil-based;

Table 9 Overview of cooling performance of the SMA film-based devices developed within this work. In addition, selected results of previous work and literature are given as a benchmark. Operation frequency  $f$ , device temperature span  $\Delta T_{device}$ , cooling device temperature span  $\Delta T_{device}^{cool}$ , absolute cooling capacity  $\dot{Q}_0^{cool}$ , specific cooling capacity  $\dot{q}_0^{cool}$  and  $COP_{device}$  are given if possible.

Device	$f / \text{Hz}$	$\Delta T_{device} / ^\circ\text{C}$	$\Delta T_{device}^{cool} / ^\circ\text{C}$	$\dot{Q}_0^{cool} / \text{mW}$	$\dot{q}_0^{cool} / \text{Wg}^{-1}$	$COP_{device} / -$
<b>Single film device (ch. 5.1)</b>	0.5	6.3	2.9	20	1.7	<b>6.7</b>
	1	9.7	4.6	50	4.2	5.8
	2	12.6	5.6	121	10.3	4.3
	4	<b>14</b>	5.9	<b>220</b>	<b>19</b>	2.4
<b>Single film device with thermal load (ch. 5.2)</b>	1	7.3	5.9	68	5.9	
	2	10.5	8.5	107	9.2	
<b>Miniature single film device (ch. 5.3)</b>	4	3.5	1.5	4	10	
<b>Coupled device (ch. 5.4)</b>	1	10.3	5.8	64	4.1	3.2
	2	<b>12.6</b>	6.8	120	<b>7.7</b>	3
	4	12.5	6.3	106	6.8	1.3
<b>Parallelized device (ch. 6.1)</b>	0.25	1.1	0.5	229	1.2	4.5
	0.5	2.3	1.1	436	2.3	3.7
	1	4.4	2.3	<b>902</b>	4.7	3.2
<b>Cascaded device in-plane loading (ch. 6.2)</b>						
1 film, TiNiCuCo	1	8.1	3.9	93	4.9	
	2	10.6	5	180	9.6	
2 films, TiNiCuCo	1	13.1	6.7	96	2.6	
	2	17.9	8.9	181	4.8	
1 film, NiTiFe	1	10.6	5	168	9	
2 films, NiTiFe	1	21	9.2	189	5	
3 films, NiTiFe	1	<b>27.3</b>	<b>10.6</b>	193	3.4	
<b>Cascaded device out-of-plane loading (ch. 6.3)</b>						
1 film	1	3.9	1.7	23	2.9	5.7
	4	7.6	3.3	129	16.7	
2 films	1	4.7	2.2	23	1.5	
	4	11	5.7	145	9.3	
3 films	1	5.4	2.7	24	1	1.9
	4	<b>15</b>	<b>7.2</b>	143	6.1	

Benchmark						
Previous work on SMA Film-Based Elastocaloric Cooling Devices (ch. 2.4.3)						
Single film device, 3 <sup>rd</sup> generation, [169]	0.75	7.9	3.1	24	3.1	2.9
Single film device, 4 <sup>th</sup> generation, [32,p. 168]	0.68	8.2	3.3	12	3.1	1.3
Coupled film device, 3 <sup>rd</sup> generation, [169]	0.76	5.5	5	51	3.3	3.2
Coupled film device, 4 <sup>th</sup> generation, [169]	0.71	9.4	4.4	45	2.9	3.1
<b>Tušek</b> [172;193], $\varepsilon_{max} = 3.4\%$	0.25	15.3		4536*	0.78*	3.5*
$\varepsilon_{max} = 1.7\%$	0.25	6.5		2059*	0.36*	<b>5.5*</b>
$\varepsilon_{max} = 3.5\%$	< 0.33	<b>19.9</b>				
<b>Snodgras</b> [31], highest $\Delta T_{device}$ , 3 stages	0.063	<b>28.3</b>	<b>11.4</b>	228	0.04	0.5
highest $COP_{device}$ , one stage	0.125	5.2	2.3	713	0.65	6
highest $\dot{q}_0^{cool}$ , one stage	0.125	6.9	2.8	847	0.78	4.9
highest $\dot{Q}_0^{cool}$ , two stages	0.91	15.3	6.4	1323	0.24	2

\*value given for heating, not cooling;  
Highlights are marked in bold

## Single SMA film devices

A comprehensive overview of the cooling performance of the SMA-film-based elastocaloric cooling devices of this work is given in Table 9. The design of the single film device is based on previous work [32,p. 168]. It has been reengineered and characterized under improved operation conditions. Maximum values for the device temperature span  $\Delta T_{device}$  of 14 K and for the specific cooling capacity  $\dot{q}_0^{cool}$  of 19 W/g are reached at an operation frequency  $f$  of 4 Hz. The maximum  $COP_{device}$  of 6.7 is reached at the lowest  $f$  of 0.5 Hz. Compared to previous experiments with a similar design, the performance is considerably increased, in case of  $\Delta T_{device}$  by 70 %. The improvement is mainly attributed to enhanced operation with higher  $f$ . The single film device

is considered a benchmark and basis for the other devices developed in this work. Two devices with very similar single film designs are developed in this work to investigate further miniaturization and the cooling performance of SMA film-based elastocaloric cooling devices under thermal load.

The coupled device successfully introduces the concept of WR by antagonistic coupling and pre-straining of films to SMA film-based elastocaloric cooling devices. Similar to the single film device, the coupled device is based on a previous design, but performance is largely increased. The coupled device reaches its best performance at 2 Hz. A maximum  $\Delta T_{device}$  of 12.6 °C,  $\dot{q}_0^{cool}$  of 7.7 W/g and a  $COP_{device}$  of 3 is achieved.

The investigation of the single and coupled film devices already reveals some general trends in SMA film-based elastocaloric cooling devices and allows first conclusions:

- The chosen device fabrication technologies are suitable for the given size range of the devices. The surface quality of the copper heat sink and source surface that is repeatedly brought in contact with the SMA film is highly important.
- Compliant spring-like support structures are found to be beneficial to SMA film-based elastocaloric cooling devices (compare chapter 4.1.1). Compliant structures ensure good and reproducible thermal contact between SMA film and heat sink and source elements. In addition, they reduce the demands on fabrication and operation precision. In addition, risk to damage the device or the SMA film upon operation is reduced. The compliance can also help reduce the relative motion between the SMA film and the copper elements and consequently reduces frictional losses.
- In general, the shared basic operation principle leads to common trends regarding temperature evolution. When the operation of the device is started, the temperatures of the heat sink element(s) and source element(s) increase and decrease in a stepwise manner

each cycle of operation. In the beginning, temperature changes quickly and as the temperature span develops, the temperature change rate decreases and saturates. In saturated state, the temperature change of the heat sink / source in contact with the elastocaloric film and the temperature change due to parasitic heat losses of the sink /source elements reach a stationary equilibrium. The higher the operation frequency, the faster the temperature changes and the faster equilibrium is reached.

- In most cases heating and cooling contribute approximately equally to the  $\Delta T_{device}$ , but heating is slightly higher. Irreversible frictional processes diminish the cooling effect and contribute to heating. In addition, contact forces are higher at the heat sink than at the heat source and thus heat transfer is improved at the sink. A temperature drift to higher temperatures occurs above 2 Hz. At high  $f$ , dissipation losses increase.
- The thermal mass of the heat sink and source elements change the temperature evolution of the sink and source elements. If the thermal mass is low, the device responds fast to the operation, reaches saturation fast and reaches high  $\Delta T_{device}$ . The stepwise temperature changes in each cycle are high, e.g., in the single film device in the order of 0.5 °C. High thermal masses lead to more steady and slower temperature changes. According to the results in this work  $\Delta T_{device}$  decreases for increasing mass of the sink and source.
- Device temperature span and cooling capacity increase with the operation frequency  $f$ . The efficiency  $COP_{device}$  tends to decrease with the operation frequency. At high operation frequencies above 2 Hz  $\Delta T_{device}$  reaches a limit and does not increase further, although the cooling capacity still increases. The reason for this effect is found to be insufficient heat transfer. At high frequencies, heat cannot be transferred efficiently anymore between the SMA film and the heat source and sink elements due to two reasons. First of all, the contact time shortens with increasing  $f$ , and therefore becomes increasingly too short to transfer a significant fraction of

the latent heat released / absorbed in the SMA. Secondly, the highest  $\Delta T_{device}$  is reached at high frequencies, and thus, the temperature gradient between the SMA film and the sink and source elements decreases. An increased heat transfer coefficient of the contact would be desirable, or materials with higher  $\Delta T_{ad}$  would be needed to preserve a high temperature gradient at high operation frequencies.

- Lumped element simulation of the coupled device reproduces the temperature trends found in the experimental results. The simulation confirms hindered heat transfer as the reason for the saturation of  $\Delta T_{device}$  at high  $f$ . The simulation of the device performance at higher operation frequencies up to 6 Hz shows no change of  $\Delta T_{device}$ . In addition, the simulation reveals conduction as the main parasitic heat loss, convection is found to play a minor role.
- The simple device architecture of a single film device is suited well for further miniaturization. The miniature single film device with a footprint of only 6.5 mm x 6 mm shows cooling performance comparable to its larger version.  $\dot{q}_0^{cool}$  reaches 10 W/g, which is in the same range as larger devices. However, effective insulation and separation of cold and hot heat flow becomes increasingly challenging upon downscaling due to the increased influence of parasitic heat flows. Consequently, the maximum  $\Delta T_{device}$  is reduced to 3.5 K in the miniature single film device.

### Cooling performance of SMA film-based cooling devices under thermal load

The cooling performance of the single film device with thermal load reveals, how such a device reacts to the application of a thermal load, as it would be the case in an application. A linear decrease of the device temperature span for increasing thermal load on the device is found. Based on this finding, an approach is developed to approximate the cooling performance of the other SMA film-based elastocaloric cooling devices under an external load (see for

details chapter 5.2.4). In this way a complete device performance characteristic for all possible points of operation is extrapolated from the figures of merit  $\Delta T_{device}^{cool}$ ,  $\dot{Q}_0^{cool}$  and  $COP_{device}$ . In Figure 67 the approach is applied to the single film device. In a) a cooling temperature span  $\Delta T^{cool}$  - cooling capacity  $\dot{Q}^{cool}$  - operation frequency  $f$  space is established that illustrates, which points of operations the device can reach (green) and which not (red). In b) same is done with the  $COP_{device}$  on the y-axis. This approximate model for the device operation under thermal load might be used to estimate the  $\dot{Q}^{cool}$  of the device under a given  $\Delta T^{cool}$  and the  $COP_{device}$  at this point of operation. Similar, if a certain  $\dot{Q}^{cool}$  is needed, the model approximates the  $\Delta T^{cool}$  the device can provide and suggests a  $f$  for the most efficient operation.

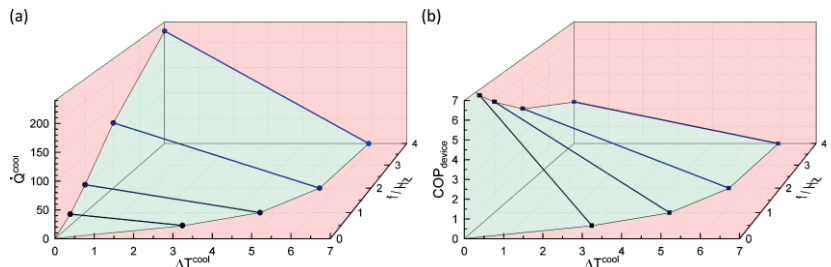


Figure 67 Performance space of the single film device extrapolated by its experimentally determined figures of merit. Operation points within the green volume can be met by the device, points outside (red) the device cannot achieve. The approach illustrates the approximate device performance under a given thermal load in an application.

The approach helps to approximate the device performance under applied thermal load in an application. Figure 67 once more underlines that  $\Delta T_{device}$ ,  $\dot{Q}_0^{cool}$ , and  $COP_{device}$  cannot be optimized all at the same time, since they follow opposing trends. At least for operation frequencies below 2 Hz,  $\Delta T_{device}$  and  $\dot{Q}_0^{cool}$  both increase with  $f$ . However,  $COP_{device}$  follows an opposing trend. Thus, a compromise has to be found according to the needs of a specific application. Nevertheless, the approach also points out the im-

portance of high  $\Delta T_{device}$ ,  $\dot{Q}_0^{cool}$ , and  $COP_{device}$ , to reach a good and efficient cooling performance even at temperature spans and cooling capacities below the maximum values. Since the basic concept and performance trend of the cooling devices in this work are similar, the approach can also easily be applied to the SMA film-based elastocaloric cooling devices.

### Advanced SMA film devices

Although specific cooling capacity  $\dot{q}_0^{cool}$  reaches high values up to 19 W/g in the single film devices, the absolute cooling capacity  $\dot{Q}_0^{cool}$  is limited to 220 mW. The investigation of the scaling laws of elastocaloric refrigerators in chapter 4.1.2 reveals that simply increasing the device size is not an option, since the surface-to-volume ratio of the active material would diminish. At the same time,  $\Delta T_{device}$  approaches its limits as well, as indicated above. Further increase of  $f$  has no, or almost no, beneficial influence on  $\Delta T_{device}$  anymore above 2 Hz for the device geometries and heat transfer mode investigated herein. New concepts are needed to further improve  $\dot{Q}_0^{cool}$  and  $\Delta T_{device}$  in SMA film-based elastocaloric cooling devices while maintaining the good performance and high values of the specific cooling capacity found in single film devices. In this work, parallelization and cascading is proposed to overcome the limitations. Advanced SMA film-based elastocaloric cooling devices are engineered and investigated to examine the effectiveness of the two concepts.

A **parallelized device** is designed and engineered to combine the elastocaloric effect of five SMA films. The SMA films are coupled to include WR. All SMA films cool and heat one single heat sink and source. Thereby, the elastocaloric effects of the films are interconnected in parallel and add up. The parallelized device preserves the high specific cooling capacity  $\dot{q}_0^{cool}$ , 4.7 W/g is reached, and increases the absolute cooling capacity  $\dot{Q}_0^{cool}$  to 0.9 W at 1 Hz. If the cooling capacity is compared to the single film device at the same operation frequency, specific cooling capacities almost equal each other. Absolute cooling capacity is increased largely by a factor of 18. This proves the function of the

parallelized device architecture. However,  $\Delta T_{device}$  is limited to 4.4 °C in the parallelized device due to the high mass of the sink and source elements in this specific device. No influence of parallelization on the device efficiency  $COP_{device}$  can be found, as the values of the parallelized device are comparable to the single film device. The results prove the effectiveness of the parallelized device architecture to increase the absolute cooling capacity, while maintaining the high specific cooling capacity characteristic of SMA film-based elastocaloric cooling devices. No general objections are found that oppose a further upscaling of parallelized devices based on SMA films.

A **cascaded device architecture** is proposed to overcome the limitations of  $\Delta T_{device}$  in single SMA film-based elastocaloric cooling devices (see chapter 4.1.3). The concept is investigated in two different devices that both combine the effect of three SMA films. The main difference between the two devices is the concept of load application. The cascaded device with in-plane loading is the only device in this work that deviates from the out-of-plane loading concept. This is unique to so-far published SMA film-based elastocaloric cooling devices. In-plane loading rises the need for an additional actuator that changes the contact conditions of the SMA film and the heat sink and source elements. The advantage of in-plane loading is possibility to choose the operation parameters more freely. On the other hand, the cascaded device with out-of-plane loading is more similar to the single film device. The basic idea of both cascaded devices is comparable. Heat is transferred between the SMA films and copper elements that function as heat sink and source. The key is that in the configuration of “copper element - SMA film - copper element” is stacked three times. The intermediate copper element functions as heat sink for one neighboring SMA film and as heat source for the other neighboring SMA film. In this way, the cooling capacity of the first film is used to precool the next “copper element - SMA film - copper element” unit. The single SMA films thus operate at different temperature levels and the cascaded device architecture shifts the limit of the device temperature span to higher values with each cascaded film. The cascaded device with in-plane loading reaches a maximum  $\Delta T_{device}$  of 27.3 °C with the combined effect of three NiTiFe films.

This compares to the adiabatic temperature span of the SMA material for heating and cooling of 20 and -16 °C. The combined effect of two TiNiCuCo films give rise to a  $\Delta T_{device}$  of 17.9 °C. This compares to a maximum adiabatic temperature span of 12.2 °C and -14.5 °C. For both materials,  $\Delta T_{device}$  of the cascaded device exceeds the  $\Delta T_{ad}$  of a single element for heating and cooling, but not the combined  $\Delta T_{ad}$  for heating and cooling together. Nevertheless, compared to the single film device maximum  $\Delta T_{device}$  is increased by 95 % in case of three NiTiFe films, and by 28 % in case of two TiNiCuCo films. Thus, the potential of the cascaded device architecture to increase  $\Delta T_{device}$  is proven. In experiments with TiNiCuCo films, the  $\Delta T_{device}$  is increased by 58 % by using two SMA films instead of one within the same device. In the cascaded device with in-plane loading, two different TiNiCuCo alloys are used with a shift in  $A_f$  according to the altered temperature range of operation in the cascade. The use of different SMA materials with tailored  $A_f$  will become increasingly important in future, as  $\Delta T_{device}$  in elastocaloric cooling devices is expected to increase further and might exceed the operation range of a single material.

The cascaded device with out-of-plane loading increases its  $\Delta T_{device}$  from 7.6 °C to 15 °C when the number of cascaded films is increased from one to three at 4 Hz. Therefore, also in the cascaded device with out-of-plane loading,  $\Delta T_{device}$  overcomes the materials  $\Delta T_{ad}$  for heating and cooling, but not the combined  $\Delta T_{ad}$  for heating and cooling together. Like in the other SMA film-based elastocaloric cooling devices, the operation frequency  $f$  has a large influence on the cooling performance of the cascaded device. Generally, the device temperature span  $\Delta T_{device}$  and the cooling capacity  $\dot{Q}_0^{cool}$ ,  $\dot{q}_0^{cool}$  increase with the operation frequency. Other than in the single film devices, no clear saturation of the performance with  $f$  can be found for the cascaded device with out-of-plane loading within the frequency range accessible with the electromechanical actuator used to drive the device. The number of cascaded films shows clearly a beneficial influence on  $\Delta T_{device}$ . In the cascaded device with in-plane loading, the device performance increases with  $f$  until 2 Hz and even decreases afterwards. However, this decrease is found

to originate from insufficient timing of the two actuators and is not related to limited heat transfer, which is the reason for similar effects in the single film devices.

The improvement in  $\Delta T_{device}$  by cascading comes at cost. The absolute cooling capacity  $\dot{Q}_0^{cool}$  is in the same range as in the single film device, but stays the same in cascaded devices, regardless of the number of cascaded SMA films. It reaches a maximum of 145 mW in the cascaded device with out-of-plane loading and 180 mW in the cascaded device with in-plane loading. In turn,  $\dot{q}_0^{cool}$  and  $COP_{device}$  decrease with the number of cascaded SMA films. In the cascaded device with out-of-plane loading  $\dot{q}_0^{cool}$  decreases from 16.7 W/g (1 film, 4 Hz) to 6.1 W/g (3 films, 4 Hz), and  $COP_{device}$  from 5.7 (1 film, 1 Hz) to 1.9 (3 films, 1 Hz). In the cascaded device with in-plane loading  $\dot{q}_0^{cool}$  decreases from 9.6 W/g (1 TiNiCuCo film, 2 Hz) to 4.8 W/g (2 TiNi-CuCo films, 2 Hz), and finally to 3.4 W/g (3 NiTiFe films, 1 Hz).

The performance metrics of the cascaded elastocaloric cooling devices ( $\Delta T_{device}$ ,  $\dot{Q}_0^{cool}$ ,  $\dot{q}_0^{cool}$  and  $COP_{device}$ ) follow different trends with regard to  $f$  and the number of cascaded SMA films. So, no single optimum device configuration is able to fit all application scenarios. Nevertheless, the number of cascaded films in cascaded devices is an additional parameter that helps fitting the device performance to the demands of an application. More importantly, the experimental results of the cascaded devices prove that cascading enables high  $\Delta T_{device}$ , higher than the SMA materials  $\Delta T_{ad}$ , needed for many industrial applications. The use of TiNiCuCo films with tailored transition temperature is especially promising, as it allows the device temperature span to exceed the superelastic operation range of a single SMA material.

### Challenges and critical points

Besides the promising experimental results of single and advanced SMA film-based elastocaloric cooling devices, also some issues and critical points of the technology are revealed in this work:

- Although **heat transfer** of SMA film geometries is highly efficient compared to bulk geometries, it is still a limiting factor in the cooling devices. Increasing the heat transfer coefficient between the SMA film and the solid heat sink and source elements would allow to efficiently apply higher operation frequencies and improve device performance. Possible ways to improve the heat transfer coefficient of the mechanical contact are improved surface quality, additional highly conductive layers or even the use of conductive flexible surfaces for increased effective contact area between SMA film and heat sink and source.
- Efficiency and maximum temperature spans in elastocaloric cooling devices could be improved if parasitic heat losses are reduced. Therefore, improved **insulation** is highly recommended for future elastocaloric devices. LEM simulation reveals conduction as the dominant loss mechanism. Thus, additional insulation layers between the heat sink and source elements and the support structures are expected to reduce the parasitic heat losses considerably.
- One key issue is the reliability of the SMA films in the elastocaloric cooling devices. The lifetime of the devices is clearly limited by fatigue in the active material. The promising ultra-low fatigue properties of TiNiCuCo films so far could not be reproduced on the device level. The maximum number of life cycles reached in this work is about 10000 cycles (TiNiCuCo film in the miniature single film device), however it is often considerably lower. This is sufficient for the characterization of devices, but has to be increased largely for reliable operation in an industrial application. A detailed investigation of fatigue life and failure modes of SMA films in elastocaloric cooling devices is out of scope of this work, but is strongly recommended for future work. Preliminary results underline how important it is to ensure smooth surfaces and edges and to avoid overloading the SMA films.
- Especially in advanced SMA film devices, precision of fabrication and alignment becomes increasingly challenging. This is important

to avoid overloads to the SMA films (see point above). Manual alignment and compliant spring-like structures, which allow sufficiently reliable and precise operation of single film devices, are increasingly hard to apply to the more complex advanced devices. The recurring arrangement of the SMA films restrict the available construction space. In addition, each additional SMA film that has to be aligned with respect to the other films increases the demand on the alignment considerably. The limited construction space restricts the implementation of compliant structures. A promising solution for this is found in the cascaded device with in-plane loading, where the compliance of a soft material (PDMS) is used, instead of a space consuming spring-structure. As a consequence, increased complexity of advanced devices increases the demands on the precision of fabrication, alignment and operation. Modular device architecture might be a second promising approach to reduce the complexity of advanced devices and increase the precision.

- In order to approach the use of SMA film-based elastocaloric cooling devices in an application and to approach commercialization further device integration is needed. At the current state, the function needed for operation of an elastocaloric refrigerator are split between the elastocaloric cooling device and the test platform that takes care of actuation, control and monitoring. In future, all these functions have to be integrated into one single device. Especially the integration of a suitable actuator is needed. This is challenging for small-scale devices. Piezoelectric actuation in combination with auxetic lattices is a promising actuation technology that could be suitable for future small-scale elastocaloric cooling devices [227;228]

## Benchmark

The performance of single film devices and advanced devices with parallelized and cascaded device architecture are discussed above in detail, but how does this performance compare to other elastocaloric cooling prototypes found in literature? A literature review of elastocaloric cooling prototypes is given in chapter 2.4.2. The demonstrators that reach the highest  $\Delta T_{device}^{cool}$  and  $\dot{q}_0^{cool}$  are also included in Table 9 for comparison. One main difference of the SMA film-based elastocaloric devices to elastocaloric cooling prototypes reported in literature is the size. The elastocaloric cooling prototypes found in literature range from the size of decimeter to meters and therefore are considerably larger compared to the devices in this work [15;16;30]. Thus, the absolute cooling capacity of SMA film-based elastocaloric cooling devices is low compared to the highest value of 65 W found in literature [185]. However, the parallelized device highlights the way how to increase the cooling capacity of SMA film-based elastocaloric cooling devices. The 900 mW of the parallelized device already approaches the range of maximum  $\dot{Q}_0^{cool}$  reported in regeneration and cascade-based elastocaloric cooling demonstrators reaching 4536 mW and 1323 mW, respectively [31;172]. In terms of  $\Delta T_{device}$ , values of SMA film-based elastocaloric cooling devices can compete with larger devices reported in literature. Today, the highest literature value of  $\Delta T_{device}$  is reported for a cascaded device that reaches 28.3 °C [31]. The maximum  $\Delta T_{device}$  reached in this work with the cascaded device with in-plane loading is with 27.3 °C only slightly lower. Also the single film device with a maximum  $\Delta T_{device}$  of 14 °C reaches similar values as larger demonstrators found in literature. A focus on the specific cooling capacity  $\dot{q}_0^{cool}$  demonstrates the full potential of SMA film-based elastocaloric cooling devices. Values up to 19 W/g are reached. This is one order of magnitude higher compared to the highest values of about 0.8 W/g found in literature for large-scale devices [31;172]. This is in line with the scaling laws of elastocaloric refrigerators derived in chapter 4.1.2.

To sum up, the absolute cooling capacity  $\dot{Q}_0^{cool}$  of SMA film-based cooling devices lags behind the best values found in literature. However, the parallelized device suggests how to change this in future. The device temperature span  $\Delta T_{device}$  is in a similar range, the best value of  $\Delta T_{device} = 27.3$  °C reached in this work is only slightly lower compared to the highest value of 28.3 °C reported in literature. In terms of specific cooling capacity  $\dot{q}_0^{cool}$ , SMA film-based cooling devices outperform large-scale devices by far. The high performance is related to the efficient heat transfer of high surface-to-volume film geometries enabling high operation frequencies. So far, all large-scale elastocaloric cooling demonstrators have been limited to operation frequencies below 1 Hz.

The different SMA film-based elastocaloric cooling devices developed in this work demonstrate the potential of elastocaloric cooling. They can compete, or even outperform larger scale elastocaloric demonstration devices found in literature. Parallelized and cascaded device architectures have proven to increase the absolute cooling capacity and the device temperature span in elastocaloric cooling devices. They pave the way to adapt the cooling characteristic of future SMA film-based cooling devices to specific applications by shifting the limits regarding  $\dot{Q}_0^{cool}$  and  $\Delta T_{device}$ .



# **8 Conclusion and Outlook**

## **8.1 Conclusion**

The need for new innovative cooling technologies that avoid critical substances and provide efficient cooling is high already and will even increase in the future. Entire industries like the medical sector or the food industry depend on reliable large-scale cooling. Today, this cooling is largely provided by vapor-compression technology that has been used for a century and depends on potentially harmful refrigerants. On the other hand, ongoing miniaturization and thus increased heat flux densities in electronics that are the base for today's technological trends and raise the demand for new efficient cooling and temperature control technologies on the small-scale. Elastocaloric cooling is a new, completely solid-state based technology. It has the potential to provide efficient and environmentally friendly cooling on both small- and large-scale.

The elastocaloric effect describes the reversible heat release and absorption in certain materials due to the application and release of a uniaxial stress field. Today, superelastic SMAs are the most promising elastocaloric materials. In SMAs the latent heat of the solid-state phase transformation between parent austenite phase and a stress-induced martensite phase is utilized for cooling. Upon loading and stress-induced forward transformation, the latent heat of transformation is released resulting in a temperature increase of the SMA under adiabatic conditions. The reverse transformation is related to the absorption of the latent heat that results in the temperature decrease of the SMA specimen under adiabatic conditions. Elastocaloric cooling does not depend on environmentally or climatically harmful refrigerants, and in addition, high efficiencies are possible. However, the elastocaloric cooling technology is still in an early stage and many issues remain unsolved today.

Among first elastocaloric cooling demonstrators, small-scale SMA film-based elastocaloric cooling devices have shown promising results in previous work, with device temperature spans up to 9.4 °C and specific cooling capacities up to 6.4 W/g. The use of film geometries is especially promising to elastocaloric cooling, since the high surface-to-volume ratio allows for efficient and fast heat transfer. The aim of this work is to further investigate SMA film-based elastocaloric cooling and to develop concepts to further improve their cooling performance, especially with respect to absolute cooling capacity and device temperature span.

The ideal elastocaloric material combines a large elastocaloric effect size (latent heat of the transformation  $Q_{lat}$ , isothermal entropy change  $\Delta S_{iso}$ , adiabatic temperature change  $\Delta T_{ad}$ ) with a low work input and therefore high efficiency  $COP_{mat}$  and a high fatigue resistance. Two different sorts of SMA films are used in this work, cold-rolled NiTiFe foils and sputtered TiNiCuCo films. The TiNiCuCo films are especially promising for elastocaloric cooling due to their ultra-low fatigue properties. A combination of a tailored microstructure with small grain size and coherent fine precipitates as well as supercompatibility between the austenite and martensite lattice allow TiNiCuCo tensile samples to withstand more than  $10^7$  load cycles without signs of fatigue. Three alloy compositions of TiNiCuCo films are used with slightly altered cobalt-content. Thus, austenite finish temperatures of the three alloys are shifted between 1.7 °C and 13.3 °C. The TiNiCuCo films reach a maximum  $\Delta T_{ad}$  of 12.2 °C upon loading and -14.5 °C upon unloading. The adiabatic cycle related  $COP_{mat}$  of the TiNiCuCo films reaches high maximum values of 12. However, if quasi-directly measured  $Q_{lat}^{quasi}$  from differential scanning calorimetry (DSC) measurements and the isothermal work input are used as basis for the  $COP_{mat}$  calculation, extraordinarily high values up to 72 are obtained. Nevertheless, this value represents rather a theoretical limit, and will not be reached in a real thermodynamic cycle.

The NiTiFe foils used in this work reach  $\Delta T_{ad}$  of 20 °C for loading and -16 °C for unloading. The materials coefficient of performance  $COP_{mat}$  reaches

values up to 13, based on values gained from quasi-direct measurements and the isothermal work input. The adiabatic loading cycle in contrast leads to a  $COP_{mat}$  of 3.6. The NiTiFe foils reach higher effect sizes compared to the TiNi-CuCo films, but the TiNiCuCo films have a higher elastocaloric efficiency and benefit from their superior fatigue properties. Additionally, the transformation temperatures can easily be tailored in TiNiCuCo by slight changes in the cobalt content. This is especially important for the use in advanced cascaded elastocaloric cooling devices.

An elastocaloric cooling device has to fulfill several tasks in parallel to provide useful cooling and to utilize the promising elastocaloric effect found in SMA films. First of all, the elastocaloric device has to apply a cyclic load to the SMA to trigger the phase transformation and the related elastocaloric effect. In addition, the heat released in the elastocaloric material during loading has to be transferred out of the element (hot heat flow) and the heat absorbed during unloading has to be transferred back into the element (cold heat flow). Furthermore, the resulting hot and cold heat flows have to be separated. This is very important to beneficially use elastocaloric cooling and to avoid that the elastocaloric heating equalizes the cooling. In the SMA film-based elastocaloric cooling devices developed herein these tasks are achieved by an oscillating linear motion and changing heat contact conditions of the SMA film and solid heat sink and source elements. The SMA film is brought in contact with a solid heat sink when heating occurs and with a heat source during cooling. The film geometry allows loading the SMA in out-of-plane direction. Accordingly, a single actuator can load the SMA and change the mechanical and thermal contacts. In this way, the heat sink is heated and the heat source is cooled stepwise by the elastocaloric effect of the SMA film. This results in a temperature difference between the heat sink and source.

A new experimental test setup is developed in the present work in order to characterize SMA film-based elastocaloric cooling devices. It allows the detailed investigation of operation parameters. Especially important, the operation frequencies can be varied in a wide range up to 4 Hz, being unique to

elastocaloric cooling up to now. Operation frequencies of devices reported in literature are limited to frequencies below 1 Hz.

With the new experimental test setup, two elastocaloric cooling devices are characterized that are based on previous designs. In both devices, performance is improved considerably, primarily due to higher operation frequencies. In the single film device, maximum values for the device temperature span  $\Delta T_{device}$  of 14 °C, absolute cooling capacity  $\dot{Q}_0^{cool}$  of 220 mW, and specific cooling capacity  $\dot{q}_0^{cool}$  of 19 W/g are reached at an operation frequency  $f$  of 4 Hz. The maximum  $COP_{device}$  of 6.7 is found at  $f = 0.5$  Hz (for the calculation, work recovery is assumed). The single film device is considered a benchmark and basis for the other devices developed in this work. The coupled device extends the concept of the single film device to include work recovery. Two SMA films are pre-strained with respect to each other and coupled to form an antagonistic pair. In this way, the mechanical power input of the device is decreased and thus efficiency is increased. The coupled device reaches its best performance at 2 Hz. A maximum  $\Delta T_{device}$  of 12.6 °C,  $\dot{q}_0^{cool}$  of 9.9 W/g, and  $COP_{device}$  of 3 is achieved. The detailed characterization of the single film devices, that include besides the single film device and coupled device also the single film device with thermal load and the miniature single film device, reveal general trends in SMA film-based elastocaloric cooling devices. First conclusions can be drawn:

- The shared basic concept of device operation leads to common performance trends. The frequency is a key operation parameter. In general, cooling capacity and device temperature span increase with increased frequency, whereas the efficiency  $COP_{device}$  decreases. The heat transfer mechanism between the elastocaloric element and the heat sink and source limits the improvements of cooling capacity and especially device temperature span with increasing frequency. For the solid-to-solid heat transfer mechanism in this work, the limit is reached at about 2 Hz. Decreasing temperature gradient and contact time and between the SMA film and

the heat sink and source elements hinder efficient heat transfer at high  $f$ . These findings are supported by lumped element model (LEM) based device simulation that predicts almost constant  $\Delta T_{device}$  for  $f$  up to 6 Hz. The saturation of  $\Delta T_{device}$  besides the increasing mechanical input power for increasing  $f$  clearly indicates the limit of the single film device approach.

- The single film devices reach very promising specific cooling capacity  $\dot{q}_0^{cool}$  of up to 19 W/g. This value outperforms other elastocaloric devices reported in literature by far. The maximum literature value is about 0.8 W/g. The high  $\dot{q}_0^{cool}$  in SMA film-based elastocaloric cooling devices is closely related to the high surface-to-volume ratio of the film geometry. Nevertheless, the absolute cooling capacity  $\dot{Q}_0^{cool}$  with a maximum value of 220 mW is found to be limited in single film devices.
- Compliant suspension of the sink and source elements is beneficial for SMA film-based cooling devices. The demands on the accuracy of fabrication and alignment are reduced and the thermal contacts are improved.
- Further miniaturization of single film devices is possible. The keys for further miniaturization are the favorable scaling behavior of elastocaloric devices and the simple device architecture of single film devices with out-of-plane loading of the SMA film.
- Cooling capacity, temperature span and efficiency (COP) of a device are not constant values, but depend on each other and the operating conditions. For SMA film-based elastocaloric cooling devices, a linear relation between temperature span and cooling capacity is found. Therefore, cooling performance under load of SMA film-based cooling devices can be extrapolated by the figures of merit  $\Delta T_{device}$ ,  $\dot{Q}_0^{cool}$  and  $COP_{device}$  that represent limit values.

The findings reveal the potential of SMA film-based elastocaloric cooling, however also the limitations in  $\Delta T_{device}$  and  $\dot{Q}_0^{cool}$  single film devices are subjected to. New approaches are needed to combine the high  $\dot{q}_0^{cool}$

characteristic to SMA film-based cooling devices with increased  $\Delta T_{device}$  and  $\dot{Q}_0^{cool}$ . Hence, advanced elastocaloric cooling devices are developed in this work based on parallelization and cascading.

A parallelized device is developed to combine the elastocaloric effect of five SMA films and increase the absolute cooling capacity of the device without increasing SMA film thickness, to preserve the high surface-to-volume ratio of the films. The SMA films in the device are coupled and thereby work recovery is included. All SMA films heat a single heat sink and cool a single source. Thus, the elastocaloric effects of the films are interconnected in parallel and add up. The parallelized device reaches an absolute cooling capacity  $\dot{Q}_0^{cool}$  of up to 0.9 W at 1 Hz, which increases the maximum achieved  $\dot{Q}_0^{cool}$  in SMA film-based cooling devices largely by a factor of 4. At the same time, the high specific cooling capacity  $\dot{q}_0^{cool}$  of SMA film-based devices is found in the parallelized device: 4.7 W/g is reached at 1 Hz. However,  $\Delta T_{device}$  is limited to 4.4 °C in the parallelized device due to the high thermal mass of the heat sink and source. No influence of parallelization on the device efficiency  $COP_{device}$  can be found. The results prove the effectiveness of the parallelized device architecture to increase the absolute cooling capacity while maintaining the high specific cooling capacity of small-scale SMA film-based elastocaloric cooling devices. No general objections are found that oppose a further upscaling of parallelized devices based on SMA films. The parallelized device reaches cooling capacities in a similar range compared to other elastocaloric cooling demonstrators found in literature. With one exception, they reach maximum values limited to a few W. In the future, massive parallelization based on the introduced concept might pave the way for planar cooling panels that allow for easy integration in the built environment. In this way, innovative environmentally friendly elastocaloric cooling could be integrated into standardized building components and thus a completely new field of application can be addressed.

To overcome the limitation of the device temperature span  $\Delta T_{device}$  in single film devices, a cascaded device architecture is developed. Three SMA films

are cascaded. The first two films of the cascade each pre-cool the next film. Only the third film directly absorbs heat from the heat source. In this way, all three films operate at different temperature levels, and the overall device temperature span of the cascaded device with in-plane loading is increased to a maximum  $\Delta T_{device}$  of 27.3 °C. This compares to the adiabatic temperature span of the NiTiFe films for heating and cooling of 20 and -16 °C, respectively. Therefore,  $\Delta T_{device}$  clearly exceeds the material's  $\Delta T_{ad}$ , but not the combined  $\Delta T_{ad}$  for heating and cooling. Two different TiNiCuCo-films with tailored  $A_f$  are also successfully implemented in the cascaded device with in-plane loading and reach a  $\Delta T_{device}$  of 17.9 °C. The use of different SMA materials with tailored  $A_f$  will become increasingly important in the future, as  $\Delta T_{device}$  in elastocaloric cooling devices is expected to increase further and  $\Delta T_{device}$  might exceed the operation range of a single elastocaloric material. The presented numbers clearly show that a cascaded device architecture increases the  $\Delta T_{device}$  as intended. However, it has to be noted that this comes at cost of the cooling capacity. In cascaded devices, the absolute cooling capacity  $\dot{Q}_0^{cool}$  stays the same, regardless of the number of cascaded SMA films. In turn,  $\dot{q}_0^{cool}$  and  $COP_{device}$  decrease with the number of cascaded SMA films. As a result, the device configuration has to be fitted carefully to the application scenario. Nevertheless, the experimental results of the cascaded devices prove that cascading enables high  $\Delta T_{device}$ . High device temperature spans become feasible regardless of the used elastocaloric material and its  $\Delta T_{ad}$ . This allows SMA film-based elastocaloric cooling devices to address applications that require cooling capacity at a considerable temperature difference like e.g. the case in refrigeration and temperature control below ambient temperature. The  $\Delta T_{device}$  reached in the cascaded device with in-plane loading can compete to the highest values found in literature. It is only slightly lower compared to the maximum  $\Delta T_{device}$  of 28.3 °C reported for elastocaloric devices in literature [31]. The highest values are also reported for a cascaded device that however relies on NiTi wires and heat transfer to a fluid. This again underlines the potential of cascaded device architectures for elastocaloric devices.

The advanced SMA film-based elastocaloric cooling devices developed in this work demonstrate the potential of elastocaloric cooling. SMA film-based devices can compete with larger scale elastocaloric demonstration devices found in literature in terms of absolute cooling capacity and device temperature span, and outperform them in terms of specific cooling capacity. The advanced cooling devices overcome the limits in  $\dot{Q}_0^{cool}$  and  $\Delta T_{device}$  to which single film devices are subjected.

## 8.2 Outlook

Besides the promising performance in SMA film-based elastocaloric cooling devices, key issues and challenges are revealed that are closely related to future work. One issue in SMA film-based elastocaloric cooling, but also the field in general, is fatigue in the active material. So far, the ultra-low fatigue properties of TiNiCuCo films could not be transferred to the device level. A maximum of about 10000 cycles of operation until failure was achieved by TiNi-CuCo films on the device level, although cyclical stability was typically lower. This is sufficient for the characterization of devices, however has to be increased largely for application. The importance of reliability even increases in parallelized and cascaded devices that rely on the operation of several films. A detailed investigation of fatigue and failure modes of SMA films in the special case of elastocaloric cooling was out of scope of this work, but is strongly recommended for future work. Preliminary results underline the beneficial influence of smooth surfaces and edges on the reliability of SMA films on the device level.

Moreover, controlling parasitic and intended heat flows in the cooling device becomes increasingly important as the technology progresses towards application. The heat transfer coefficient of the mechanical contact between the SMA film and the heat sink and source should be increased, whereas insulation should be used to reduce parasitic heat losses. The heat transfer coefficient might be increased by improved surface quality, an additional highly

conductive layers or even by the use of flexible surfaces for increased effective contact area between SMA film and heat sink and source.

On the level of advanced elastocaloric cooling devices it is promising to increase the number of parallelized and cascaded SMA films to further increase the cooling capacity and device temperature span, possibly above the combined adiabatic temperature span for heating and cooling of the used SMA. For large-scale applications, the investigation of natural rubber based elastocaloric materials as a low-cost alternative to SMA would be interesting. However, as the system complexity of parallelized and cascaded devices increases, the demands on fabrication, assembly, and alignment precision increase considerably. In addition, the recurring arrangement of the SMA films in advanced devices restricts the available construction space for compliant structures and alignment mechanisms. New fabrication and assembly concepts are needed. A modular device architecture could be a promising strategy to reduce complexity and increase repeatability and precision in parallelized and cascaded devices. In the future, a modular device architecture could also allow to combine the two concepts of parallelization and cascading in one SMA film-based cooling devices. In this way the device performance could easily be customized to specific applications without limitations of the device temperature span or cooling capacity. The modular device architecture would largely decrease the development cost for new device configurations.

So far, the elastocaloric cooling device and the test platform providing actuation are strictly separated. Operation parameters can easily be modified thereby and precise characterization is ensured. This has proven to be a successful strategy at this stage of research, yet an important next step would be the development of a stand-alone elastocaloric refrigeration device. Actuation and control would have to be integrated into the elastocaloric cooling device. This would be an important future step to demonstrate not only the theoretical potential of the technology but also to demonstrate and increase the readiness for application of SMA film-based elastocaloric cooling.

This work lays the basis for SMA film-based elastocaloric cooling with large cooling capacity and also large temperature span. It has been shown that SMA film-based elastocaloric cooling can compete with other elastocaloric cooling concepts in terms of absolute cooling capacity and temperature span, and reaches the highest specific cooling capacities. Nevertheless, SMA film-based elastocaloric cooling and elastocaloric cooling in general are still in a rather early development state. There is still a lot of research and development work needed to make elastocaloric cooling a commercially successful product. The potential however is high. Compared to other caloric effects, elastocaloric cooling has the advantage of a high effect size and a simple operation principle. The main advantage with reference to conventional technologies is the combination of environmental compatibility and high efficiency. This makes elastocaloric cooling interesting for large-scale applications where it could help avoiding harmful refrigerants in vapor compression cycle-based systems and also for small-scale applications, where it can help to increase the efficiency compared to Peltier cooling.

# Publications

Parts of this thesis and related work have already been published and presented by the author in scientific journals:

**F. Bruederlin**, H. Ossmer, F. Wendler, S. Miyazaki, M. Kohl, "SMA foil-based elastocaloric cooling: from material behavior to device engineering", *Journal of Physics D: Applied Physics*, 50.42 (2017) 424003

**F. Bruederlin**, L. Bumke, C. Chluba, H. Ossmer, E. Quandt, M. Kohl, "Elastocaloric cooling on the miniature scale: A review on materials and engineering of devices", *Energy Technology*, 6.8 (2018) 1588–1604

G. Ulpiani, G. Ranzi, **F. Bruederlin**, R. Paolini, F. Fiorito, S. Haddad, M. Kohl and M. Santamouris, "Elastocaloric cooling: roadmap towards successful implementation in the built environment", *AIMS Materials Science*, 6.6 (2019) 1135-1152

As conference proceedings:

**F. Bruederlin**, L. Bumke, E. Quandt, and M. Kohl, "Cascaded SMA-Film Based Elastocaloric Cooling" in *20th International Conference on Solid-State Sensors, Actuators and Microsystems Eurosensors XXXIII (TRANSDUCERS EUROSSENSORS XXXIII)*, Berlin, Jun. 2019, pp. 1467–1470, doi: 10.1109/TRANSDUCERS.2019.8808605

**F. Bruederlin**, L. Bumke, E. Quandt, and M. Kohl, "Kaskadiertes Elastokalorisches KühlSystem - Cascaded Elastocaloric Cooling System" in *MikroSystem-Technik Kongress 2019*, Berlin, Oct. 2019, p. 344

As conference contributions:

**F. Brüderlin**, H. Ossmer, C. Chluba, F. Wendler, E. Quandt, M. Kohl, "Mechanics and Reliability of Superelastic SMA Films for Cooling Applications", *18th International Symposium on Applied Electromagnetics and Mechanics (ISEM)*, September 3–6, 2017, Chamonix, France (*oral presentation*)

**F. Brüderlin**, L. Bumke, H. Ossmer, C. Chluba, E. Quandt, M. Kohl, "Advanced SMA Film-Based Elastocaloric Cooling Systems", *European Symposium on Martensitic Transformations (esomat)*, August 27-31, 2018, Metz, France (*poster presentation*)

**F. Brüderlin**, L. Bumke, H. Ossmer, E. Quandt, M. Kohl, "A Cascaded System of Elastocaloric Film Cooling Devices", *Thermag VIII - International Conference on Caloric Cooling*, September 16-20, 2018, Darmstadt, Germany (*oral presentation*)

**F. Brüderlin**, L. Bumke, E. Quandt, M. Kohl, "SMA-Film Based Elastocaloric Cooling for Small Scale Applications", *4<sup>th</sup> Euro Intelligent Materials*, June 17-19, 2019, Kiel, Germany (*oral presentation*)

**F. Brüderlin**, L. Bumke, E. Quandt, and M. Kohl, "Cascaded SMA-Film Based Elastocaloric Cooling", *20th International Conference on Solid-State Sensors, Actuators and Microsystems Eurosensors XXXIII (TRANSDUCERS EUROSSENSORS XXXIII)*, June 23-27, 2019, Berlin, Germany (*poster presentation*)

**F. Brüderlin**, L. Bumke, E. Quandt, and M. Kohl, "Kaskadiertes Elastokalorisches KühlSystem - Cascaded Elastocaloric Cooling System", *MikroSystem-Technik Kongress*, October 28-30, 2019, Berlin, Germany (*oral presentation*)

# Figures

- Figure 1 General schematic elastocaloric cooling cycle with four steps: mechanical loading of the elastocaloric element (0-1) that responds to application of the stress field with a rise in temperature; heat release to the environment (1-2); release of the mechanical load and temperature drop of the element (2-3); heat absorption from the environment (3-0). The absorbed heat in (3-0) can be used for cooling..... 3
- Figure 2 (a) Generalized caloric cooling cycle. A caloric cooling cycle can be subdivided into four process steps: field application and heating (0-1), heat release to a heat sink (1-2), field release and cooling (2-3) and heat absorption from a heat source (3-0). (b) Temperature-entropy diagram of the reverse Brayton cycle that is used as reference for the caloric process. Magnet-, electro-, elasto- and barocaloric cooling cycles are illustrated in c), d), e) and f), respectively..... 9
- Figure 3 Unit cell of the crystal structure and according schematic microstructure of the high temperature austenite phase, the intermediate R-phase and the low temperature martensite phase. Martensite and R-phase can both be present in self accommodated twinned state or oriented detwinned state. © 2008, Society for Experimental Mechanics, reprinted from [118] with permission. .... 18
- Figure 4 (a) Schematic differential scanning calorimetry (DSC) measurement of a SMA. The temperature induced phase transition is indicated by the peaks in the DSC curve. DSC measurements are often used to determine the transformation temperatures  $M_s$ ,  $M_f$ ,  $A_s$ , and  $A_f$  of the

- martensitic transformation. (b) Gibbs free energy of the austenite and martensite phase. The phase with the lower free energy is stable. To start the phase transformation, a driving potential  $\Delta G$  is needed. For b) compare [120,p. 23] ..... 20
- Figure 5 Effects in SMAs at different temperature regimes. (a) Superelasticity and the shape memory effect in a stress-strain-temperature space. (b) Thermally induced transformation is illustrated as DSC-curve and indicates the transformation temperatures in stress free state. Lattice structure and simplified microstructure are indicated. Figure adapted from [32,p. 18], © Ossmer, used under Creative Commons License (CC BY-SA 3.0 DE), legend modified. ..... 21
- Figure 6 (a) Simplified schematic model of the shape memory effect (SME) in a single crystal SMA. Austenite is indicated in red, martensite in blue. (b) Regions of the SME and superelasticity in stress-temperature space. For a) compare [120,p. 37], for b) compare [46]. ..... 22
- Figure 7 (a) Simplified schematic model of superelasticity in a single crystal SMAs. Austenite is indicated in red, martensite in blue. (b) Schematic superelastic stress-strain curve with the most important superelastic material parameters indicated. For (a) compare [120,p. 17]. ..... 23
- Figure 8 Implications of the cofactor conditions. If the cofactor conditions are met, an infinite number of combinations between the austenite lattice (red) and the two martensite variants (green and blue) exists that have vanishingly small mismatch stress. Figure reprinted from [136], © 2017 Elsevier, use permitted under Creative Commons License (CC BY NC ND). ..... 27
- Figure 9 The force-displacement characteristic of a SMA originates from its stress-strain characteristic, its geometry and also

- the mode of load application. Here, a schematic stress-strain characteristic is shown in combination with the resulting force-displacement characteristics for loading in-plane and out-of-plane ..... 37
- Figure 10 Force-displacement characteristics of a single SMA element (a,b) and antagonistic coupled SMA elements (c-f). Antagonistic coupling is used for work recovery (WR). Each characteristic (c) - (f) represents a different WR case. The force-displacement characteristic of each single SMA element (blue, red) is given in combination with the coupled characteristic (black). The in-plane and out-of-plane loading conditions are indicated by schematics. Strains in the two coupled elements that are matched by pre-straining are indicated by circles and stars. For each characteristic, loading work  $W_{\text{load}}$ , hysteresis work  $\Delta W_{\text{mat}}$  and elastically stored work  $W_{\text{el}}$  are indicated. ..... 44
- Figure 11 The concept of heat recovery (HR) uses a portion of the heat that is released and absorbed due to the elastocaloric effect internally to pre-heat and pre-cool the caloric element. (a) In the reverse Brayton cycle of a system without HR, not all the heat released during the field application (0-1) can be released to the heat sink, but only the heat represented by the red area. The heat marked as grey area cannot be transferred, since the temperature of the element is lower than the temperature of the heat sink. HR uses a portion of the otherwise unused heat (grey) to pre-heat the caloric element before the next field application occurs (0-1). In case of heat absorption from the heat source (3-0), the concept works similar and the caloric element is pre-cooled before field removal (2-3). (b) Temperature evolution of the caloric element without HR, and with HR (c). ..... 49

- Figure 12 General elastocaloric cooling cycle with four steps (a) and implementation of the steps in the particular case of a SMA film-based elastocaloric cooling device (b). ..... 50
- Figure 13 Classification of elastocaloric cooling devices. Devices are classified based on their most important engineering properties (a to i). Possible characteristic values of the properties are included (1 to 5). eCM denotes elastocaloric material element. ..... 57
- Figure 14 CAD visualization of the complete scientific test setup for SMA-based elastocaloric cooling developed by Schmidt et al., including a section of the heat sink and source unit.  
© 2016 Taylor & Francis, figure reprinted from [39]. ..... 61
- Figure 15 (a) Schematic setup of the compression-based elastocaloric refrigerator including the two SMA beds and the fluidic system with the heat recovery cycle. © 2015 Elsevier Ltd and IIR, reprinted with permission from [192].  
(b) Experimental setup. The image was kindly provided by Suxin Qian, © Suxin Qian..... 62
- Figure 16 (a) Schematic of the elastocaloric heat pump based on active regeneration developed by Tušek et al. (b) Core of the experimental setup including the regenerator with fluidic connections. (c) IR thermograph of the regenerator and the fluidic connection under steady state operation.  
© 2016 Macmillan Publishers Limited, part of Springer Nature, figure reprinted with permission from [172]. ..... 63
- Figure 17 (a) Schematic operation principle of the elastocaloric refrigerator developed at Fraunhofer IPM based on latent heat transfer. In 1) the SMA rods are loaded under compression, heat up, and evaporate HTF. 2) Heat is transferred to the next chamber by the mass flow of gas phase HTF. 3) SMA rods are released and cool down, HTF condensates on the cold rods. 4) Heat is absorbed from the

---

previous chamber by a mass flow of gas phase HTF. (b) Experimental setup of the refrigerator. ©2019 Fraunhofer IPM, reprinted from [186] with permission.....	64
Figure 18 Elastocaloric refrigerator using a NiTi wire loop that is loaded in bending-mode by a continuous rotational actuation. Heat transfer is accomplished through mechanical contacts of the wire with a copper tube functioning as heat sink and a separate copper element that is cooled and utilized as heat source. © 2018 IEEE, figure reprinted from [188] with permission.....	66
Figure 19 (a) Schematic of the operating principle of the elastocaloric air cooler developed by Kirsch et. al. (b) CAD visualization of the device, including the SMA wire bundles illustrated in blue and the flow duct. © 2018 Wiley-VCH Verlag GmbH & Co. KGaA, figure reprinted from [15] with permission.....	66
Figure 20 (a) Schematic setup of the cascaded elastocaloric refrigerator developed by Snodgras and Erickson. (b) Experimental setup comprising the three linear actuators that load a SMA wire based elastocaloric cooling stage each. The stages are connected by a fluidic system. Figure reprinted from [31], © Snodgrass & Erickson, use permitted under Creative Commons License (CC BY). .....	68
Figure 21 (a) Schematic of the active regeneration based elastocaloric cooling device developed by Sebald et al. The device uses the elastocaloric effect of a rubber tube. (b) Experimental implementation of the device. © 2020 Sebald, reprinted with permission from [166]. .....	70
Figure 22 Schematics of miniature elastocaloric cooling demonstrators developed in previous work at KIT. Four device generations are presented for single SMA film devices and coupled double SMA film devices. Figure adapted from [32,pp. 164, 173, 176], © Ossmer, used	

	under Creative Commons License (CC BY-SA 3.0 DE), figure reorganized.....	73
Figure 23	Temperature evolution of the sink and source elements in SMA film-based cooling devices for different operation frequencies. (a) Characteristic of the single film 4 <sup>th</sup> generation device. (b) Results from the coupled 4 <sup>th</sup> generation device. Figure adapted and from [32,pp. 167, 177], © Ossmer, used under Creative Commons License (CC BY-SA 3.0 DE), figure reorganized. .....	75
Figure 24	Schematic illustration of a tensile testing test setup. The tensile testing machine is combined with an IR-camera and a CCD-camera. ....	84
Figure 25	DSC measurement of the NiTiFe SMA foil material. Phase transitions are represented by peaks. The DSC measurement reveals a two-step transformation via an intermediate R-phase for both, the endothermic heating curve (red) and the exothermic cooling curve (blue). © 2017 IOP Publishing Ltd, figure reprinted from [210] with permission. ....	88
Figure 26	(a) Stress-strain curve of the superelastic NiTiFe SMA foil at three different strain rates. With increasing strain rate, the stress plateaus tilt due to self-heating and self-cooling. (b) Local strain and surface temperature profiles of the NiTiFe foil during unloading at a strain rate of 0.01 s-1. Strain and temperature changes occur localized at propagating strain bands. Strain and temperature evolution are correlated. © 2017 IOP Publishing Ltd, figure reprinted from [210] with permission. ....	89
Figure 27	Stress-strain curve of the initial training of the NiTiFe foil. Especially during the first load cycles the material behavior is subjected to changes. Critical stresses decrease and	

- remanent strain accumulates. The material behavior stabilizes after about 20 load cycles. .... 90
- Figure 28 Local surface temperature profiles of the NiTiFe foil during load cycling at four different strain rates between 0.001 s<sup>-1</sup> and 1 s<sup>-1</sup>. In each case, one image depicts the temperature profile before the transformation occurs (1, 5), after the transformation (4, 8) and two images taken during the transformation. With increasing strain rate, the number of temperature bands increases and temperature profiles become increasingly homogenous. .... 92
- Figure 29 (a) Time-dependent temperature evolution of a NiTiFe foil specimen during mechanical loading and unloading at three different strain rates. (b) Temperature changes of a NiTiFe foil specimen upon load cycling as a function of the applied strain rate. At low strain rates, the isothermal case is approached. Released and absorbed heat is directly transferred to the surrounding and does hardly change the specimen temperature. At high strain rates, the adiabatic limit is approached. Heat transfer to the surrounding is hindered. Under quasi adiabatic conditions, the adiabatic temperature change  $\Delta T_{ad}$  of the material is defined to be 20 °C during loading and -16 °C during unloading. © 2017 IOP Publishing Ltd, figure reprinted from [210] with permission. .... 93
- Figure 30 DSC measurement of three TiNiCuCo based alloy compositions with increasing Co-content from TiNiCuCo-1 to TiNiCuCo-3. The increase of the Co-content reduces  $A_f$ . In the TiNiCuCo SMAs the forward and reverse phase transformation occurs in one-step indicated by a single sharp peak in the DSC curve. .... 95
- Figure 31 Stress-strain curves of TiNiCuCo-1, -2 and -3 specimen under isothermal loading conditions at a strain rate of

0.001 s <sup>-1</sup> (a) and under adiabatic loading conditions at 1 s <sup>-1</sup> (b). .....	96
Figure 32 (a) Stress-strain curves of selected load cycles from the second to 1000 <sup>th</sup> load cycles. The SMA shows very stable mechanical properties without degradation. (b) Temperature changes of TiNiCuCo-1, -2, -3 specimen upon load cycling as a function of the applied strain rate. Loading conditions range from quasi-isothermal conditions (0.001 s <sup>-1</sup> ) to quasi-adiabatic conditions (>0.1 s <sup>-1</sup> ). ....	98
Figure 33 Surface temperature profiles before (1), during (2, 3), and after (4) mechanical loading and unloading (5-8) at different strain rates. Images are taken from IR-measurements with TiNiCuCo-1. Temperature changes occur where strain bands nucleate or propagate. The higher the strain rate, the more bands form and the more uniform the temperature profiles occurs. ....	100
Figure 34 (a) Influence of an angular misalignment $\alpha$ on the surface contact in devices with rigid (left) and compliant (right) suspension of the solid heat source. The compliant suspension compensates for the misalignment and thus ensures a flat contact over the whole surface. (b) The required contact force $F_{req}$ needs to be high enough to ensure efficient heat transfer, and at the same time must be limited to avoid damage to the setup. In case of a compliant suspension this requirement can be easily met, since the required accuracy of the position $x_{req}$ is poor. ....	102
Figure 35 Graphical illustration of thermal equivalent circuits used in the simplified analytical model (a,i), and the 1D discretized lumped element model (LEM) (a,ii). Both models represent a SMA film or plate in contact to a copper heat sink that is coupled to ambient. The models are used to estimate the influence of the SMA thickness on the operation frequency	

---

and the cooling capacity of an elastocaloric cooling device (b). © 2018 Wiley-VCHVerlag GmbH&Co. KGaA , figure reprinted from [16] with permission. ....	107
Figure 36 Schematic temperature-entropy diagram of a reverse Brayton cycle. (a) Cycle of a single unit is shown. (b) Cycles of three cascaded units. The cascaded architecture enables increased device temperature spans. Figure adapted from [217] with permission from VDE VERLAG GMBH. ....	110
Figure 37 Schematic of a single cooling unit (a) and a parallelized system (b) in which the cooling capacities of the single units add up to the system cooling capacity. ....	111
Figure 38 Lumped element model (LEM) thermal equivalent circuit representing the coupled device discussed in chapter 5.4. The model of the cooling device is based on three interconnected concentrated thermal masses representing the SMA film and the heat source and sink. The elastocaloric effect is modelled by the source term $Q_l$ . © 2017 IOP Publishing Ltd, figure reprinted from [210] with permission. ....	114
Figure 39 (a) Copper elements that function as combined heat sink and source in the cascaded device with out-of-plane loading after structuring by EDM (i) and after mechanical polishing (ii). (b) 3D printed support structure used in the coupled device. The part is fabricated by stereolithographic 3D printing. All parts are placed on a one euro-cent coin to illustrate the size.....	117
Figure 40 Schematic illustrations of the structure and main components of a fused deposition modeling (FDM) (a) and a stereolithography (SL) (b) based additive manufacturing system. The schematic representations are oriented to the systems used in this work. a) adapted from [46, S. 150], b) adapted from [222,p. 65]). ....	119

Figure 41	Schematic of the main components of an elastocaloric refrigerator and interconnecting flows of energy and information between the components. In this work the functions and components needed in the complete elastocaloric refrigerator are split between an experimental test setup and the elastocaloric cooling devices.....	122
Figure 42	Detailed visualization of the components of the experimental test setup and the integration of the components.....	124
Figure 43	General operating cycle used in this work. The displacement induced by the actuator $\Delta l$ follows a sinusoidal movement, holding times are inserted at the turning points. The time for movement equals the holding time in each cycle. ....	126
Figure 44	(a) Schematic setup of the single film device. Main components are the TiNiCuCo SMA film, the copper heat sink and source elements and the polymer support structure that includes spring-like elements. Actuation is indicated by arrows. (b) Experimental setup. © 2018 Wiley-VCHVerlag GmbH&Co. KGaA , figure adapted and reprinted from [16] with permission.....	128
Figure 45	(a) Temperature evolution of heat sink and source elements of the single SMA film elastocaloric cooling device. A series of experiments with operations frequencies from 0.5 to 4 Hz is depicted. (b) Surface temperature profiles of the device at different indicated times during operation at 4 Hz. (c) Frequency dependence of device temperature span $\Delta T_{device}$ , specific cooling capacity $\dot{q}_0^{cool}$ and COP <sub>device</sub> . Figure a) and b) are adapted from [16], © 2018 Wiley-VCHVerlag GmbH&Co. KGaA , figure reprinted with permission.....	130

---

Figure 46	(a) Schematic device setup of the single film device with thermal load. Besides the large heat source and the resistance heater, the device is comparable to the single film device presented in previous chapter 5.1. (b) Experimental device.	134
Figure 47	Temperature evolution of heat sink and source elements at the operations frequencies of 1 Hz (a), and 2 Hz (b). Temperature curves are presented for different thermal loads applied to the heat source of the cooling device.	135
Figure 48	Device temperature span available for cooling $\Delta T_{\text{device}}^{\text{cool}}$ as a function of the applied thermal load $P_{\text{load}}$ for operation frequencies of 1 and 2 Hz. The device shows a linear decrease of $\Delta T_{\text{device}}^{\text{cool}}$ with the applied thermal load. The absolute cooling capacity $\dot{Q}_0^{\text{cool}}$ is indicated as dots on the x-axis.	136
Figure 49	Schematic characteristic of $\dot{Q}^{\text{cool}}$ and $\text{COP}_{\text{device}}$ as a function of $\Delta T_{\text{cool}}$ . The dependencies are approximated by a simplified model to include the cross dependencies of the device temperature span, cooling capacity and the $\text{COP}_{\text{device}}$ under different points of operation. A complete cooling device characteristic can be interpolated from the figures of merit introduced in chapter 2.3.6. Linear relations are chosen according to the findings on the device performance under thermal load presented in this chapter.	138
Figure 50	(a) Experimental setup of the miniature single film device with a 1 cent coin for scale. Like a larger setup the device consists of a 3D printed support structure, heat sink and source element from copper and the SMA film. Temperature is investigated via miniature scale thermocouples. (b) The core cooling device. (c) Dog-bone	

shaped TiNiCuCo SMA sample geometry used as active material. ....	141
Figure 51 (a) Evolution of the temperature difference of the sink and source elements and the initial temperature during operation at a frequency of 4 Hz. Operation is maintained over a time period of 1000 s or 4000 load cycles. (b) Device temperature span, cooling device temperature span, and specific cooling capacity versus the operation frequency of the miniaturized elastocaloric cooling device. Average values in combination with the standard deviation are given for results gained in a series of experiments. ....	142
Figure 52 (a) Schematic of the coupled device. The actuation is indicated by arrows, the components of the setup by color. (b) Image of the experimental device without SMA films. Figure adapted from [16], © 2018 Wiley-VCHVerlag GmbH&Co. KGaA , figure reprinted with permission. ....	146
Figure 53 Displacement $\Delta l$ induced to the elastocaloric cooling device for operation (a), and the evolution of the temperature differences $\Delta T_1$ to $\Delta T_4$ (b) with time in the first two cycles of operation. Holding time periods with full contact between the SMA and the sink and source elements are highlighted. The operation frequency is 0.5 Hz. Clearly the stepwise evolution of temperatures in the elastocaloric cooling device can be understood. © 2017 IOP Publishing Ltd, figure reprinted from [210] with permission. ....	148
Figure 54 Temperature difference of heat sink and source elements as a function of time during operation at different frequencies. Temperature differences are displayed for 100 s of operation (a) and the first 10 s (b). Experimental and simulated results are given. © 2017 IOP Publishing Ltd, figure reprinted from [210] with permission.....	149

---

Figure 55 Experimental and simulated device temperature span $\Delta T_{device}$ (a) and COP <sub>device</sub> (b) as a function of operation frequency. $\Delta T_{device}$ saturates above 2 Hz, the maximum experimental value of 13 °C is reached at 3 Hz. The maximum COP <sub>device</sub> of 3.2 is reached at 1 Hz. (c) IR image showing the surface temperature profile of the cooling device before and after operation at 2 Hz for 100 s. © 2017 IOP Publishing Ltd, figure reprinted from [210] with permission.	150
Figure 56 (a) Schematic setup of the parallelized elastocaloric cooling device. Two sectional views are presented for better understanding. The SMA films 1 to 5 are loaded by the triangular surfaces of extrusions A, C, E in out-of-plane deflection and are brought in contact with the surfaces of extrusions B, D, F in the unloaded state. Cyclic operation generates a heat flow from the cooled heat source to the heated heat sink. (b) The experimental device with the five SMA films, the frame they are fixed to, and the heat sink. The heat source is not included to enable the view of the SMA films.	156
Figure 57 (a) Temperature evolution of heat sink and source elements as a function of time during operation at 0.1, 0.5 and 1 Hz. The parallelized device is operated for 100 s. (b) Force-displacement characteristic of the five coupled SMA films incorporated in the parallelized device at operation frequencies of 0.05, 0.25 and 1 Hz. (c) Device temperature span $\Delta T_{device}$ , specific cooling capacity $\dot{q}_0^{cool}$ and COP <sub>device</sub> as a function of operation frequency f. $\Delta T_{device}$ and $\dot{q}_0^{cool}$ increase linearly with f. The maximum $\dot{q}_0^{cool}$ is 4.67 W/g and corresponds to an absolute cooling capacity $\dot{Q}_0^{cool}$ of 0.9 W.	158

- Figure 58 Schematic of the cascaded device with in-plane loading. The cooling device comprises three SMA films and four heat sink / source elements made from copper. Two actuators are needed, one for the cyclic loading of the SMA (actuator 2) and one that changes the contact conditions of the SMA films and the heat sink and source elements (actuator 1). Typical actuation profiles are shown for both of the actuators. ..... 164
- Figure 59 (a) Experimental test setup including the two linear actuators and the cascaded device with in-plane loading. (b) Cascaded SMA film-based elastocaloric cooling device that is operated by in-plane loading. (c) Components of the device. ..... 164
- Figure 60 Influence of operation parameters on the performance of the cascaded device with in-plane loading. The device temperature span after 20 s  $\Delta T_{device}$  (20 s) and the cooling capacity  $\dot{Q}_0^{cool}$  are used as performance metrics. The influence of the stroke of actuator 1 (a), the delay time between the operation cycles of the two actuators (b), the maximum strain applied to the SMA material in case of NiTiFe (c) and TiNiCuCo (d) are investigated. ..... 166
- Figure 61 (a) Temperatur evolution of the copper elements A to D of the cascaded elastocaloric cooling device with in-plane loading. Operation takes place with three NiTiFe films at 1 Hz. (b) IR thermographs of the cooling device during operation in the experiment displayed in a). Thermographs are taken before, after 20 s, and after 80 s of operation ..... 169
- Figure 62 (a) Temperatur evolution of the copper elements A to C of the cascaded elastocaloric cooling device, operated with two TiNiCuCo films at 2 Hz. (b) Influence of the operation frequency f on the device temperature span  $\Delta T_{device}$  and

---

the cooling capacity $\dot{Q}_0^{\text{cool}}$ . Results are given for operation with one and with two TiNiCuCo films. ....	170
Figure 63 Schematic of the cascaded elastocaloric cooling device loaded in out-of-plane. The device is composed of three single units 1 to 3, each with a SMA film. The three SMA films are mechanically connected at their ends and are actuated by a single actuator as indicated by the arrows. Copper elements A to D function as heat sink and source. A polymer support structure is used to suspend the copper elements. ©2019 IEEE, figure reprinted from [218] with permission. ....	175
Figure 64 Experimental setup of the cascaded cooling device with out-of-plane loading. The four copper elements A to D can be seen along with their polymer support structure. The actuator unit and SMA films are not included for the sake of clarity. ©2019 IEEE, figure reprinted from [218] with permission. ....	175
Figure 65 Temperature evolution of the copper elements A to D of the cascaded cooling device during operation. Here an operating frequency of 4 Hz is applied. The excerpt shows simulation results along with the experimental results for the first 10 s of operation (information on simulation in 4.2). ©2019 IEEE, figure reprinted from [218] with permission. ....	177
Figure 66 (a) Compilation of results on the device temperature span $\Delta T_{\text{device}}$ , the absolute cooling capacity $\dot{Q}_0^{\text{cool}}$ and the specific cooling capacity $\dot{q}_0^{\text{cool}}$ . All performance metrics are plotted versus the operation frequency. Results are given for operation with a single SMA film as well as for two and three cascaded films to understand the influence of the cascaded system architecture on the device performance. (b) Surface temperature profiles of the cascaded device	

before and after operation at 4 Hz for 100 s. The profiles are taken by IR thermography. Only a section of the entire device is shown as indicated in Figure 63. ©2019 IEEE, figure reprinted from [218] with permission..... 178

- Figure 67 Performance space of the single film device extrapolated by its experimentally determined figures of merit. Operation points within the green volume can be met by the device, points outside (red) the device cannot achieve. The approach illustrates the approximate device performance under a given thermal load in an application. ... 189

# Tables

Table 1	Elastocaloric properties of selected materials suitable for elastocaloric cooling near room temperature. Only polycrystalline materials have been considered. The measurement technique the values are based on is indicated. Numbers in brackets have not been stated in the original work, but have been approximated with the help of equation (IV). Temperature of the investigation T; adiabatic temperature span $\Delta T_{ad}$ ; isothermal entropy change $\Delta S_{iso}$ ; latent heat of transformation $Q_{lat}$ .....	32
Table 2	Categorization of possible modes of heat transfer and separation of hot and cold heat flows in a caloric refrigeration device with associated illustration. Five schematic concepts to achieve the separation of heat flows in caloric devices that have been demonstrated or proposed in literature are presented. HTF denotes heat transfer fluid. Naming b1 to b4 and c1 to c3 is chosen with reference to Figure 13. ....	41
Table 3	Overview on the work needed to load two SMA elements ( $W_{load}$ ) in the loading cases (a) to (f). In addition, hysteresis work ( $\Delta W_{mat}$ ) and the elastically stored work $W_{el}$ are given. $f_{load}$ states the fraction of $W_{load}$ that is recovered by WR. The fraction $f_{el}$ shows, how much of $W_{el}$ is recovered for the different WR cases. The cases (a) to (f) are illustrated in Figure 10.....	46
Table 4	Classification of elastocaloric refrigerators found in literature. Each elastocaloric cooling device is classified according to the approach introduced in chapter 2.4.1. The single characteristics are coded by numbers according to	

	Figure 13. The overview allows to quickly identify similarities and key differences between elastocaloric cooling devices. If no information is available on a specific detail, the corresponding entry is left empty.....	60
Table 5	Key experimental results of the elastocaloric cooling devices presented in this chapter. If known, the following parameters are given: operation frequency $f$ , device temperature span $\Delta T_{\text{device}}$ , cooling temperature span $\Delta T_{\text{device}}^{\text{cool}}$ , absolute cooling capacity $\dot{Q}_0^{\text{cool}}$ , specific cooling capacity $\dot{q}_0^{\text{cool}}$ , efficiency of the device expressed as $\text{COP}_{\text{device}}$ .....	71
Table 6	Key results and performances of the previous SMA film bases elastocaloric cooling devices. For each device the best performance is reported. For detailed information references are given.....	76
Table 7	Fabrication parameters of the three TiNiCuCo SMA films used in this work. ....	81
Table 8	Classification of SMA film-based elastocaloric cooling devices presented in this work. Each device is classified according to the approach introduced in chapter 2.4.1. The single characteristics are coded by numbers according to Figure 13. The overview allows to quickly identify similarities and key differences between the devices. eCM denotes elastocaloric material. ....	183
Table 9	Overview of cooling performance of the SMA film-based devices developed within this work. In addition, selected results of previous work and literature are given as a benchmark. Operation frequency $f$ , device temperature span $\Delta T_{\text{device}}$ , cooling device temperature span $\Delta T_{\text{device}}^{\text{cool}}$ , absolute cooling capacity $\dot{Q}_0^{\text{cool}}$ , specific cooling capacity $\dot{q}_0^{\text{cool}}$ and $\text{COP}_{\text{device}}$ are given if possible.....	184

# References

- [1] A. Friedrich, “The Rise of Cryopower: Biopolitics in the Age of Cryogenic Life,” in *Cryopolitics: Frozen Life in a Melting World*, J. Radin and E. Kowal, Eds. Cambridge: MIT Press, 2017, pp. 59–69.
- [2] International Energy Agency (IEA), “The Future of Cooling - Analysis and key findings. A report by the International Energy Agency,” May 2018. <https://www.iea.org/reports/the-future-of-cooling> (accessed Mar. 09, 2020).
- [3] M. Santamouris, “Cooling the buildings – past, present and future,” *Energy and Buildings*, vol. 128, pp. 617–638, Sep. 2016, doi: 10.1016/j.enbuild.2016.07.034.
- [4] M. Sivak, “Potential energy demand for cooling in the 50 largest metropolitan areas of the world: Implications for developing countries,” *Energy Policy*, vol. 37, no. 4, pp. 1382–1384, Apr. 2009, doi: 10.1016/j.enpol.2008.11.031.
- [5] UN Environment, “About Montreal Protocol - Ozonaction.” <https://www.unenvironment.org/ozonaction/who-we-are/about-montreal-protocol> (accessed Mar. 10, 2020).
- [6] S. M. Sohel Murshed and C. A. Nieto de Castro, “A critical review of traditional and emerging techniques and fluids for electronics cooling,” *Renewable and Sustainable Energy Reviews*, vol. 78, pp. 821–833, Oct. 2017, doi: 10.1016/j.rser.2017.04.112.
- [7] G. Keramidas, N. Voros, and M. Hübner, Eds., *Components and Services for IoT Platforms*. Cham: Springer International Publishing, 2017.
- [8] P. C. H. Li, *Fundamentals of Microfluidics and Lab on a Chip for Biological Analysis and Discovery*. Boca Raton, FL: CRC Press, 2010.
- [9] C. B. Vining, “An inconvenient truth about thermoelectrics,” *Nature Materials*, vol. 8, no. 2, pp. 83–85, Feb. 2009, doi: 10.1038/nmat2361.
- [10] W. Goetzler, R. Zogg, J. Young, and C. Johnson, “Energy Savings Potential and RD&D Opportunities for Non-Vapor-Compression HVAC

- Technologies," Report for the U.S. Department of Energy, DOE/EE--1021, 1220817, Mar. 2014. doi: 10.2172/1220817.
- [11] E. A. Pieczyska, S. P. Gadaj, W. K. Nowacki, and H. Tobushi, "Phase-Transformation Fronts Evolution for Stress- and Strain-Controlled Tension Tests in TiNi Shape Memory Alloy," *Experimental Mechanics*, vol. 46, no. 4, pp. 531–542, Aug. 2006, doi: 10.1007/s11340-006-8351-y.
- [12] J. Frenzel, A. Wieczorek, I. Opahle, B. Maaß, R. Drautz, and G. Eggeler, "On the effect of alloy composition on martensite start temperatures and latent heats in NiTi-based shape memory alloys," *Acta Materialia*, vol. 90, pp. 213–231, May 2015, doi: 10.1016/j.actamat.2015.02.029.
- [13] C. Chluba *et al.*, "Ultralow-fatigue shape memory alloy films," *Science*, vol. 348, no. 6238, pp. 1004–1007, May 2015, doi: 10.1126/science.1261164.
- [14] H. Ossmer, S. Miyazaki, and M. Kohl, "Elastocaloric heat pumping using a shape memory alloy foil device," in *18th International Conference on Solid-State Sensors, Actuators and Microsystems (TRANSDUCERS)*, Anchorage, Jun. 2015, pp. 726–729, doi: 10.1109/TRANSDUCERS.2015.7181026.
- [15] S.-M. Kirsch *et al.*, "NiTi-Based Elastocaloric Cooling on the Macroscale: From Basic Concepts to Realization," *Energy Technology*, vol. 6, no. 8, pp. 1567–1587, 2018, doi: 10.1002/ente.201800152.
- [16] F. Brüderlin, L. Bumke, C. Chluba, H. Ossmer, E. Quandt, and M. Kohl, "Elastocaloric Cooling on the Miniature Scale: A Review on Materials and Device Engineering," *Energy Technology*, vol. 6, no. 8, pp. 1588–1604, Aug. 2018, doi: 10.1002/ente.201800137.
- [17] J. Gough, "A description of a property of caoutchouc, or indian rubber; with some reflections on the cause of the elasticity of this substance. In a letter to Dr. Holme," *The Philosophical Magazine*, vol. 24, no. 93, pp. 39–43, Feb. 1806, doi: 10.1080/14786440608563329.
- [18] J. P. Joule, "V. On some thermo-dynamic properties of solids," *Philosophical Transactions of the Royal Society of London*, vol. 149, pp. 91–131, Jan. 1859, doi: 10.1098/rstl.1859.0005.

- [19] C. Rodriguez and L. C. Brown, "The thermal effect due to stress-induced martensite formation in B-CuAlNi single crystals," *Metall and Mat Trans A*, vol. 11, no. 1, pp. 147–150, Dec. 1980, doi: 10.1007/BF02700450.
- [20] L. C. Brown, "The Thermal Effect in Pseudoelastic Single Crystals of  $\beta$ -CuZnSn," *MTA*, vol. 12, no. 8, pp. 1491–1494, Aug. 1981, doi: 10.1007/BF02643695.
- [21] K. Mukherjee, S. Sircar, and N. B. Dahotre, "Thermal effects associated with stress-induced martensitic transformation in a TiNi alloy," *Materials Science and Engineering*, vol. 74, no. 1, pp. 75–84, Sep. 1985, doi: 10.1016/0025-5416(85)90111-9.
- [22] S. A. Nikitin, G. Myalikgulyev, M. P. Annaorazov, A. L. Tyurin, R. W. Myndyev, and S. A. Akopyan, "Giant elastocaloric effect in FeRh alloy," *Physics Letters A*, vol. 171, no. 3, pp. 234–236, Dec. 1992, doi: 10.1016/0375-9601(92)90432-L.
- [23] M. P. Annaorazov, S. A. Nikitin, A. L. Tyurin, K. A. Asatryan, and A. Kh. Dovletov, "Anomalously high entropy change in FeRh alloy," *Journal of Applied Physics*, vol. 79, no. 3, pp. 1689–1695, Feb. 1996, doi: 10.1063/1.360955.
- [24] M. P. Annaorazov, S. A. Nikitin, A. L. Tyurin, S. A. Akopyan, and R. W. Myndyev, "Heat pump cycles based on the AF–F transition in Fe–Rh alloys induced by tensile stress," *International Journal of Refrigeration*, vol. 25, no. 8, pp. 1034–1042, Dec. 2002, doi: 10.1016/S0140-7007(02)00028-2.
- [25] P. G. McCormick, Y. Liu, and S. Miyazaki, "Intrinsic thermal-mechanical behaviour associated with the stress-induced martensitic transformation in NiTi," *Materials Science and Engineering: A*, vol. 167, no. 1, pp. 51–56, Aug. 1993, doi: 10.1016/0921-5093(93)90336-D.
- [26] E. Bonnot, R. Romero, L. Mañosa, E. Vives, and A. Planes, "Elastocaloric Effect Associated with the Martensitic Transition in Shape-Memory Alloys," *Physical Review Letters*, vol. 100, no. 12, p. 125901, Mar. 2008, doi: 10.1103/PhysRevLett.100.125901.
- [27] L. Mañosa, A. Planes, E. Vives, E. Bonnot, and R. Romero, "The use of shape-memory alloys for mechanical refrigeration," *Funct. Mater. Lett.*,

- vol. 02, no. 02, pp. 73–78, Jun. 2009, doi: 10.1142/S1793604709000594.
- [28] J. Quarini and A. Prince, “Solid state refrigeration: Cooling and refrigeration using crystalline phase changes in metal alloys,” *Proceedings of the Institution of Mechanical Engineers, Part C: Journal of Mechanical Engineering Science*, vol. 218, no. 10, pp. 1175–1179, Oct. 2004, doi: 10.1243/0954406042369062.
- [29] Elsevier B.V., “Scopus - Document search.” <https://www.scopus.com> (accessed Mar. 10, 2020).
- [30] S. Qian *et al.*, “A review of elastocaloric cooling: Materials, cycles and system integrations,” *International Journal of Refrigeration*, vol. 64, pp. 1–19, Apr. 2016, doi: 10.1016/j.ijrefrig.2015.12.001.
- [31] R. Snodgrass and D. Erickson, “A multistage elastocaloric refrigerator and heat pump with 28 K temperature span,” *Sci Rep*, vol. 9, no. 1, p. 18532, Dec. 2019, doi: 10.1038/s41598-019-54411-8.
- [32] H. Ossmer, “Elastocaloric Microcooling,” PhD Thesis, Karlsruhe Institut of Technology (KIT), 2017, doi: 10.5445/IR/1000065209
- [33] W. Goetzler, R. Shandross, J. Young, O. Petritchenco, D. Ringo, and S. McClive, “Energy Savings Potential and RD&D Opportunities for Commercial Building HVAC Systems,” Navigant Consulting, Burlington, MA (United States), Report for the U.S. Department of Energy, DOE/EE-1703 7849, Dec. 2017. doi: 10.2172/1419622.
- [34] S. Qian *et al.*, “Not-in-kind cooling technologies: A quantitative comparison of refrigerants and system performance,” *International Journal of Refrigeration*, vol. 62, pp. 177–192, Feb. 2016, doi: 10.1016/j.ijrefrig.2015.10.019.
- [35] X. Moya, S. Kar-Narayan, and N. D. Mathur, “Caloric materials near ferroic phase transitions,” *Nature Materials*, vol. 13, no. 5, pp. 439–450, Apr. 2014, doi: 10.1038/NMAT3951.
- [36] S. Fähler *et al.*, “Caloric Effects in Ferroic Materials: New Concepts for Cooling,” *Advanced Engineering Materials*, vol. 14, no. 1–2, pp. 10–19, Feb. 2012, doi: 10.1002/adem.201100178.

- 
- [37] H. Struchtrup, *Thermodynamics and Energy Conversion*. Berlin, Heidelberg: Springer, 2014.
  - [38] J. Romero Gómez, R. Ferreiro Garcia, A. De Miguel Catoira, and M. Romero Gómez, "Magnetocaloric effect: A review of the thermodynamic cycles in magnetic refrigeration," *Renewable and Sustainable Energy Reviews*, vol. 17, pp. 74–82, Jan. 2013, doi: 10.1016/j.rser.2012.09.027.
  - [39] M. Schmidt, S.-M. Kirsch, S. Seelecke, and A. Schütze, "Elastocaloric cooling: From fundamental thermodynamics to solid state air conditioning," *Science and Technology for the Built Environment*, vol. 22, no. 5, pp. 475–488, Jul. 2016, doi: 10.1080/23744731.2016.1186423.
  - [40] V. K. Pecharsky and K. A. Gschneidner, "Giant Magnetocaloric Effect in  $\text{Gd}_5(\text{Si}_2\text{Ge}_2)$ ," *Physical Review Letters*, vol. 78, no. 23, pp. 4494–4497, Jun. 1997, doi: 10.1103/PhysRevLett.78.4494.
  - [41] A. S. Mischenko, Q. Zhang, J. F. Scott, R. W. Whatmore, and N. D. Mathur, "Giant Electrocaloric Effect in Thin-Film  $\text{PbZr}_{0.95}\text{Ti}_{0.05}\text{O}_3$ ," *Science*, vol. 311, no. 5765, pp. 1270–1271, Mar. 2006, doi: 10.1126/science.1123811.
  - [42] T. Strässle, A. Furrer, P. Lacorre, and K. A. Müller, "A novel principle for cooling by adiabatic pressure application in rare-earth compounds," *Journal of Alloys and Compounds*, vol. 303–304, pp. 228–231, May 2000, doi: 10.1016/S0925-8388(00)00662-9.
  - [43] L. Mañosa and A. Planes, "Materials with Giant Mechanocaloric Effects: Cooling by Strength," *Advanced Materials*, vol. 29, no. 11, p. 1603607, Mar. 2017, doi: 10.1002/adma.201603607.
  - [44] S. Fähler and V. K. Pecharsky, "Caloric effects in ferroic materials," *MRS Bull.*, vol. 43, no. 4, pp. 264–268, Apr. 2018, doi: 10.1557/mrs.2018.66.
  - [45] A. Kitanovski, J. Tušek, U. Tomc, U. Plaznik, M. Ožbolt, and A. Poredoš, *Magnetocaloric Energy Conversion*. Cham: Springer International Publishing, 2015.

- [46] S. Miyazaki and K. Otsuka, "Development of Shape Memory Alloys," *ISIJ International*, vol. 29, no. 5, pp. 353–377, 1989, doi: 10.2355/isijinternational.29.353.
- [47] T. Krenke *et al.*, "Inverse magnetocaloric effect in ferromagnetic Ni–Mn–Sn alloys," *Nature Mater.*, vol. 4, no. 6, pp. 450–454, Jun. 2005, doi: 10.1038/nmat1395.
- [48] M. M. Vopson, "The multicaloric effect in multiferroic materials," *Solid State Communications*, vol. 152, no. 23, pp. 2067–2070, Dec. 2012, doi: 10.1016/j.ssc.2012.08.016.
- [49] A. Kitanovski, U. Plaznik, U. Tomc, and A. Poredoš, "Present and future caloric refrigeration and heat-pump technologies," *International Journal of Refrigeration*, vol. 57, pp. 288–298, Sep. 2015, doi: 10.1016/j.ijrefrig.2015.06.008.
- [50] L. Mañosa, A. Planes, and M. Acet, "Advanced materials for solid-state refrigeration," *Journal of Materials Chemistry A*, vol. 1, no. 16, p. 4925, 2013, doi: 10.1039/c3ta01289a.
- [51] S. Crossley, N. D. Mathur, and X. Moya, "New developments in caloric materials for cooling applications," *AIP Advances*, vol. 5, no. 6, p. 067153, Jun. 2015, doi: 10.1063/1.4922871.
- [52] A. Smith, C. R. H. Bahl, R. Bjørk, K. Engelbrecht, K. K. Nielsen, and N. Pryds, "Materials Challenges for High Performance Magnetocaloric Refrigeration Devices," *Advanced Energy Materials*, vol. 2, no. 11, pp. 1288–1318, 2012, doi: 10.1002/aenm.201200167.
- [53] T. Gottschall *et al.*, "Making a Cool Choice: The Materials Library of Magnetic Refrigeration," *Advanced Energy Materials*, vol. 9, no. 34, p. 1901322, 2019, doi: 10.1002/aenm.201901322.
- [54] S. Yu. Dan'kov, A. M. Tishin, V. K. Pecharsky, and K. A. Gschneidner, "Magnetic phase transitions and the magnetothermal properties of gadolinium," *Phys. Rev. B*, vol. 57, no. 6, pp. 3478–3490, Feb. 1998, doi: 10.1103/PhysRevB.57.3478.
- [55] A. Fujita, S. Fujieda, Y. Hasegawa, and K. Fukamichi, "Itinerant-electron metamagnetic transition and large magnetocaloric effects in LaFeSi13

- compounds and their hydrides," *Phys. Rev. B*, vol. 67, no. 10, p. 104416, Mar. 2003, doi: 10.1103/PhysRevB.67.104416.
- [56] S. A. Nikitin, G. Myalikgulyev, A. M. Tishin, M. P. Annaorazov, K. A. Asatryan, and A. L. Tyurin, "The magnetocaloric effect in Fe49Rh51 compound," *Physics Letters A*, vol. 148, no. 6, pp. 363–366, Aug. 1990, doi: 10.1016/0375-9601(90)90819-A.
- [57] N. H. Dung *et al.*, "Mixed Magnetism for Refrigeration and Energy Conversion," *Advanced Energy Materials*, vol. 1, no. 6, pp. 1215–1219, 2011, doi: 10.1002/aenm.201100252.
- [58] X. Moya, L. Mañosa, A. Planes, T. Krenke, M. Acet, and E. F. Wassermann, "Martensitic transition and magnetic properties in Ni–Mn–X alloys," *Materials Science and Engineering: A*, vol. 438–440, pp. 911–915, Nov. 2006, doi: 10.1016/j.msea.2006.02.053.
- [59] V. Franco, J. S. Blázquez, J. J. Ipus, J. Y. Law, L. M. Moreno-Ramírez, and A. Conde, "Magnetocaloric effect: From materials research to refrigeration devices," *Progress in Materials Science*, vol. 93, pp. 112–232, Apr. 2018, doi: 10.1016/j.pmatsci.2017.10.005.
- [60] N. R. Ram *et al.*, "Review on Magnetocaloric Effect and Materials," *J Supercond Nov Magn*, vol. 31, no. 7, pp. 1971–1979, Jul. 2018, doi: 10.1007/s10948-018-4666-z.
- [61] J. Lyubina, "Magnetocaloric materials for energy efficient cooling," *J. Phys. D: Appl. Phys.*, vol. 50, no. 5, p. 053002, Feb. 2017, doi: 10.1088/1361-6463/50/5/053002.
- [62] M. Balli, S. Jandl, P. Fournier, and A. Kedous-Lebouc, "Advanced materials for magnetic cooling: Fundamentals and practical aspects," *Applied Physics Reviews*, vol. 4, no. 2, p. 021305, May 2017, doi: 10.1063/1.4983612.
- [63] R. Bjørk, A. Smith, C. R. H. Bahl, and N. Pryds, "Determining the minimum mass and cost of a magnetic refrigerator," *International Journal of Refrigeration*, vol. 34, no. 8, pp. 1805–1816, Dec. 2011, doi: 10.1016/j.ijrefrig.2011.05.021.
- [64] F. Scarpa, G. Tagliafico, and L. A. Tagliafico, "Classification proposal for room temperature magnetic refrigerators," *International Journal of*

- Refrigeration*, vol. 35, no. 2, pp. 453–458, Mar. 2012, doi: 10.1016/j.ijrefrig.2011.09.010.
- [65] A. Kitanovski, “Energy Applications of Magnetocaloric Materials,” *Advanced Energy Materials*, vol. 10, p. 1903741, Feb. 2020, doi: 10.1002/aenm.201903741.
- [66] C. Zimm, A. Boeder, B. Mueller, K. Rule, and S. L. Russek, “The evolution of magnetocaloric heat-pump devices,” *MRS Bulletin*, vol. 43, no. 4, pp. 274–279, Apr. 2018, doi: 10.1557/mrs.2018.71.
- [67] A. Greco, C. Aprea, A. Maiorino, and C. Masselli, “A review of the state of the art of solid-state calorific cooling processes at room-temperature before 2019,” *International Journal of Refrigeration*, vol. 106, pp. 66–88, Oct. 2019, doi: 10.1016/j.ijrefrig.2019.06.034.
- [68] R. Gimaev, Y. Spichkin, B. Kovalev, K. Kamilov, V. Zverev, and A. Tishin, “Review on magnetic refrigeration devices based on HTSC materials,” *International Journal of Refrigeration*, vol. 100, pp. 1–12, Apr. 2019, doi: 10.1016/j.ijrefrig.2019.01.024.
- [69] B. Yu, M. Liu, P. W. Egolf, and A. Kitanovski, “A review of magnetic refrigerator and heat pump prototypes built before the year 2010,” *International Journal of Refrigeration*, vol. 33, no. 6, pp. 1029–1060, Sep. 2010, doi: 10.1016/j.ijrefrig.2010.04.002.
- [70] F. Scarpa, G. Tagliafico, and L. A. Tagliafico, “A classification methodology applied to existing room temperature magnetic refrigerators up to the year 2014,” *Renewable and Sustainable Energy Reviews*, vol. 50, pp. 497–503, Oct. 2015, doi: 10.1016/j.rser.2015.05.029.
- [71] S. Jacobs *et al.*, “The performance of a large-scale rotary magnetic refrigerator,” *International Journal of Refrigeration*, vol. 37, pp. 84–91, Jan. 2014, doi: 10.1016/j.ijrefrig.2013.09.025.
- [72] K. Engelbrecht *et al.*, “Experimental results for a novel rotary active magnetic regenerator,” *International Journal of Refrigeration*, vol. 35, no. 6, pp. 1498–1505, Sep. 2012, doi: 10.1016/j.ijrefrig.2012.05.003.

- 
- [73] H. Johra *et al.*, “Integration of a magnetocaloric heat pump in an energy flexible residential building,” *Renewable Energy*, vol. 136, pp. 115–126, Jun. 2019, doi: 10.1016/j.renene.2018.12.102.
  - [74] “Ubiblue – Pioneer in magnetic refrigeration system.” <https://ubiblue.com/> (accessed Mar. 27, 2020).
  - [75] “magnotherm-solutions,” *Magnotherm Solutions*. <https://www.magnotherm-solutions.com/> (accessed Mar. 27, 2020).
  - [76] “BASF - Magnetic cooling.” <https://www.bASF.com/be/en/media/Magazine/resources-environment-and-climate/magnetic-cooling.html> (accessed Mar. 27, 2020).
  - [77] J. F. Scott, “Electrocaloric Materials,” *Annual Review of Materials Research*, vol. 41, no. 1, pp. 229–240, 2011, doi: 10.1146/annurev-matsci-062910-100341.
  - [78] G. G. Wiseman and J. K. Kuebler, “Electrocaloric Effect in Ferroelectric Rochelle Salt,” *Phys. Rev.*, vol. 131, no. 5, pp. 2023–2027, Sep. 1963, doi: 10.1103/PhysRev.131.2023.
  - [79] M. Ožbolt, A. Kitanovski, J. Tušek, and A. Poredoš, “Electrocaloric refrigeration: Thermodynamics, state of the art and future perspectives,” *International Journal of Refrigeration*, vol. 40, pp. 174–188, Apr. 2014, doi: 10.1016/j.ijrefrig.2013.11.007.
  - [80] J. Shi *et al.*, “Electrocaloric Cooling Materials and Devices for Zero-Global-Warming-Potential, High-Efficiency Refrigeration,” *Joule*, vol. 3, no. 5, pp. 1200–1225, May 2019, doi: 10.1016/j.joule.2019.03.021.
  - [81] A. Barman, S. Kar-Narayan, and D. Mukherjee, “Caloric Effects in Perovskite Oxides,” *Advanced Materials Interfaces*, vol. 6, no. 15, p. 1900291, 2019, doi: 10.1002/admi.201900291.
  - [82] X. Li, S.-G. Lu, X.-Z. Chen, H. Gu, X. Qian, and Q. M. Zhang, “Pyroelectric and electrocaloric materials,” *J. Mater. Chem. C*, vol. 1, no. 1, pp. 23–37, 2013, doi: 10.1039/C2TC00283C.
  - [83] S. G. Lu *et al.*, “Organic and inorganic relaxor ferroelectrics with giant electrocaloric effect,” *Appl. Phys. Lett.*, vol. 97, no. 16, p. 162904, Oct. 2010, doi: 10.1063/1.3501975.

- [84] M. Valant, "Electrocaloric materials for future solid-state refrigeration technologies," *Progress in Materials Science*, vol. 57, no. 6, pp. 980–1009, Jul. 2012, doi: 10.1016/j.pmatsci.2012.02.001.
- [85] J. Qian *et al.*, "High electrocaloric cooling power of relaxor ferroelectric BaZrxTi1-xO3 ceramics within broad temperature range," *Science Bulletin*, vol. 63, no. 6, pp. 356–361, Mar. 2018, doi: 10.1016/j.scib.2018.02.016.
- [86] X. Li *et al.*, "Giant electrocaloric effect in ferroelectric poly(vinylidenefluoride-trifluoroethylene) copolymers near a first-order ferroelectric transition," *Appl. Phys. Lett.*, vol. 101, no. 13, p. 132903, Sep. 2012, doi: 10.1063/1.4756697.
- [87] U. Plaznik *et al.*, "Numerical modelling and experimental validation of a regenerative electrocaloric cooler," *International Journal of Refrigeration*, vol. 98, pp. 139–149, Feb. 2019, doi: 10.1016/j.ijrefrig.2018.10.029.
- [88] P. Blumenthal and A. Raatz, "Classification of electrocaloric cooling device types," *EPL (Europhysics Letters)*, vol. 115, no. 1, p. 17004, Jul. 2016, doi: 10.1209/0295-5075/115/17004.
- [89] R. Ma *et al.*, "Highly efficient electrocaloric cooling with electrostatic actuation," *Science*, vol. 357, no. 6356, pp. 1130–1134, Sep. 2017, doi: 10.1126/science.aan5980.
- [90] G. Suchaneck, O. Pakhomov, and G. Gerlach, "Electrocaloric Cooling," in *Refrigeration*, O. Ekren, Ed. London: IntechOpen, 2017.
- [91] I. A. Stepanov, "Entropy change in materials under compression and expansion," *Materials Letters*, vol. 234, pp. 38–39, Jan. 2019, doi: 10.1016/j.matlet.2018.09.052.
- [92] S. Yuce *et al.*, "Barocaloric effect in the magnetocaloric prototype Gd5Si2Ge2," *Appl. Phys. Lett.*, vol. 101, no. 7, p. 071906, Aug. 2012, doi: 10.1063/1.4745920.
- [93] A. Aznar *et al.*, "Giant barocaloric effect in all-d-metal Heusler shape memory alloys," *Phys. Rev. Materials*, vol. 3, no. 4, p. 044406, Apr. 2019, doi: 10.1103/PhysRevMaterials.3.044406.

- [94] L. Mañosa *et al.*, “Inverse barocaloric effect in the giant magnetocaloric La–Fe–Si–Co compound,” *Nat Commun*, vol. 2, no. 1, pp. 1–5, Dec. 2011, doi: 10.1038/ncomms1606.
- [95] E. Stern-Taulats *et al.*, “Reversible adiabatic temperature changes at the magnetocaloric and barocaloric effects in Fe<sub>49</sub>Rh<sub>51</sub>,” *Appl. Phys. Lett.*, vol. 107, no. 15, p. 152409, Oct. 2015, doi: 10.1063/1.4933409.
- [96] E. Stern-Taulats *et al.*, “Inverse barocaloric effects in ferroelectric BaTiO<sub>3</sub> ceramics,” *APL Materials*, vol. 4, no. 9, p. 091102, Sep. 2016, doi: 10.1063/1.4961598.
- [97] P. Lloveras *et al.*, “Giant barocaloric effects at low pressure in ferrielectric ammonium sulphate,” *Nat Commun*, vol. 6, no. 1, pp. 1–6, Nov. 2015, doi: 10.1038/ncomms9801.
- [98] M. Gorev, E. Bogdanov, I. Flerov, and N. Laptash, “Thermal expansion, phase diagrams and barocaloric effects in (NH<sub>4</sub>)<sub>2</sub>NbOF<sub>5</sub>,” *J. Phys.: Condens. Matter*, vol. 22, no. 18, p. 185901, Apr. 2010, doi: 10.1088/0953-8984/22/18/185901.
- [99] A. Aznar *et al.*, “Giant barocaloric effects over a wide temperature range in superionic conductor AgI,” *Nat Commun*, vol. 8, no. 1, pp. 1–6, Nov. 2017, doi: 10.1038/s41467-017-01898-2.
- [100] A. M. G. Carvalho, W. Imamura, E. O. Usuda, and N. M. Bom, “Giant room-temperature barocaloric effects in PDMS rubber at low pressures,” *European Polymer Journal*, vol. 99, pp. 212–221, Feb. 2018, doi: 10.1016/j.eurpolymj.2017.12.007.
- [101] E. O. Usuda, W. Imamura, N. M. Bom, L. S. Paixão, and A. M. G. Carvalho, “Giant Reversible Barocaloric Effects in Nitrile Butadiene Rubber around Room Temperature,” *ACS Applied Polymer Materials*, vol. 1, pp. 1991–1997, Jul. 2019, doi: 10.1021/acsapm.9b00235.
- [102] N. M. Bom, W. Imamura, E. O. Usuda, L. S. Paixão, and A. M. G. Carvalho, “Giant Barocaloric Effects in Natural Rubber: A Relevant Step toward Solid-State Cooling,” *ACS Macro Letters*, vol. 7, no. 1, pp. 31–36, Jan. 2018, doi: 10.1021/acsmacrolett.7b00744.

- [103] A. Aznar *et al.*, “Reversible and irreversible colossal barocaloric effects in plastic crystals,” *J. Mater. Chem. A*, vol. 8, no. 2, pp. 639–647, 2020, doi: 10.1039/C9TA10947A.
- [104] B. Li *et al.*, “Colossal barocaloric effects in plastic crystals,” *Nature*, vol. 567, no. 7749, pp. 506–510, Mar. 2019, doi: 10.1038/s41586-019-1042-5.
- [105] C. Cazorla, “Novel mechanocaloric materials for solid-state cooling applications,” *Applied Physics Reviews*, vol. 6, no. 4, p. 041316, Dec. 2019, doi: 10.1063/1.5113620.
- [106] Z. Xie, G. Sebald, and D. Guyomar, “Comparison of elastocaloric effect of natural rubber with other caloric effects on different-scale cooling application cases,” *Applied Thermal Engineering*, vol. 111, pp. 914–926, Jan. 2017, doi: 10.1016/j.applthermaleng.2016.09.164.
- [107] W. Gao *et al.*, “Energy transduction ferroic materials,” *Materials Today*, vol. 21, no. 7, pp. 771–784, Sep. 2018, doi: 10.1016/j.mattod.2018.01.032.
- [108] Y. Liu, L. C. Phillips, R. Mattana, M. Bibes, A. Barthélémy, and B. Dkhil, “Large reversible caloric effect in FeRh thin films via a dual-stimulus multicaloric cycle,” *Nat Commun*, vol. 7, no. 1, pp. 1–6, May 2016, doi: 10.1038/ncomms11614.
- [109] E. Stern-Taulats, T. Castán, L. Mañosa, A. Planes, N. D. Mathur, and X. Moya, “Multicaloric materials and effects,” *MRS Bulletin*, vol. 43, no. 4, pp. 295–299, Apr. 2018, doi: 10.1557/mrs.2018.72.
- [110] T. Gottschall *et al.*, “A multicaloric cooling cycle that exploits thermal hysteresis,” *Nature Mater.*, vol. 17, no. 10, pp. 929–934, Oct. 2018, doi: 10.1038/s41563-018-0166-6.
- [111] A. S. Starkov, O. V. Pakhomov, V. V. Rodionov, A. A. Amirov, and I. A. Starkov, “Estimation of the Thermodynamic Efficiency of a Solid-State Cooler Based on the Multicaloric Effect,” *Tech. Phys. Lett.*, vol. 44, no. 3, pp. 243–246, Mar. 2018, doi: 10.1134/S1063785018030276.
- [112] A. Planes, E. Stern-Taulats, T. Castán, E. Vives, L. Mañosa, and A. Saxena, “Caloric and Multicaloric Effects in Shape Memory Alloys,”

- Materials Today: Proceedings*, vol. 2, pp. S477–S484, Jan. 2015, doi: 10.1016/j.matpr.2015.07.332.
- [113] A. Czernuszewicz, J. Kaleta, and D. Lewandowski, “Multicaloric effect: Toward a breakthrough in cooling technology,” *Energy Conversion and Management*, vol. 178, pp. 335–342, Dec. 2018, doi: 10.1016/j.enconman.2018.10.025.
- [114] Y. Liu *et al.*, “Towards multicaloric effect with ferroelectrics,” *Phys. Rev. B*, vol. 94, no. 21, p. 214113, Dec. 2016, doi: 10.1103/PhysRevB.94.214113.
- [115] I. N. Flerov, E. A. Mikhaleva, M. V. Gorev, and A. V. Kartashev, “Caloric and multicaloric effects in oxygen ferroics and multiferroics,” *Phys. Solid State*, vol. 57, no. 3, pp. 429–441, Mar. 2015, doi: 10.1134/S1063783415030075.
- [116] J. F. Scott, “Multiferroic memories,” *Nature Mater.*, vol. 6, no. 4, pp. 256–257, Apr. 2007, doi: 10.1038/nmat1868.
- [117] M. Liu and N. X. Sun, “Voltage control of magnetism in multiferroic heterostructures,” *Philosophical Transactions of the Royal Society A: Mathematical, Physical and Engineering Sciences*, vol. 372, no. 2009, p. 20120439, Feb. 2014, doi: 10.1098/rsta.2012.0439.
- [118] J. A. Shaw, C. B. Churchill, and M. A. Iadicola, “Tips and Tricks for Characterizing Shape Memory Alloy Wire: Part 1 - Differential Scanning Calorimetry and Basic Phenomena,” *Experimental Techniques*, vol. 32, no. 5, pp. 55–62, 2008, doi: 10.1111/j.1747-1567.2008.00410.x.
- [119] S. Miyazaki and K. Otsuka, “Mechanical behaviour associated with the premartensitic rhombohedral-phase transition in a Ti50Ni47Fe3 alloy,” *Philosophical Magazine A*, vol. 50, no. 3, pp. 393–408, Mar. 1985, doi: 10.1080/01418618408244235.
- [120] K. Otsuka and C. M. Wayman, *Shape memory materials*, 1st paperback edition. Cambridge: Cambridge university press, 1998.
- [121] H. Tobushi, S. Yamada, T. Hachisuka, A. Ikai, and K. Tanaka, “Thermomechanical properties due to martensitic and R-phase transformations of TiNi shape memory alloy subjected to cyclic

- loadings," *Smart Mater. Struct.*, vol. 5, no. 6, pp. 788–795, Dec. 1996, doi: 10.1088/0964-1726/5/6/008.
- [122] M. Kohl, *Shape Memory Microactuators*. Berlin Heidelberg: Springer-Verlag, 2004.
- [123] J. Mohd Jani, M. Leary, A. Subic, and M. A. Gibson, "A review of shape memory alloy research, applications and opportunities," *Materials & Design (1980-2015)*, vol. 56, pp. 1078–1113, Apr. 2014, doi: 10.1016/j.matdes.2013.11.084.
- [124] M. Kohl, B. Krevet, and E. Just, "SMA microgripper system," *Sensors and Actuators A: Physical*, vol. 97–98, pp. 646–652, Apr. 2002, doi: 10.1016/S0924-4247(01)00803-2.
- [125] C. Megnin and M. Kohl, "Shape memory alloy microvalves for a fluidic control system," *J. Micromech. Microeng.*, vol. 24, no. 2, p. 025001, Dec. 2013, doi: 10.1088/0960-1317/24/2/025001.
- [126] K. Jacob, S. Ahmadi, F. Wendler, S. Miyazaki, M. Gueltig, and M. Kohl, "Shape Memory Foil-Based Active Micro Damping for Portable Applications," in *2019 20th International Conference on Solid-State Sensors, Actuators and Microsystems Eurosensors XXXIII (TRANSDUCERS EUROSENSORS XXXIII)*, Berlin, Jun. 2019, pp. 590–593, doi: 10.1109/TRANSDUCERS.2019.8808494.
- [127] K. Kitamura, S. Miyazaki, H. Iwai, and M. Kohl, "Effect of rolling reduction on the deformation texture and anisotropy of transformation strain in Ti–50.2at.%Ni thin plates," *Materials Science and Engineering: A*, vol. 273–275, pp. 758–762, Dec. 1999, doi: 10.1016/S0921-5093(99)00411-6.
- [128] G. Eggeler, E. Hornbogen, A. Yawny, A. Heckmann, and M. Wagner, "Structural and functional fatigue of NiTi shape memory alloys," *Materials Science and Engineering: A*, vol. 378, no. 1, pp. 24–33, Jul. 2004, doi: 10.1016/j.msea.2003.10.327.
- [129] K. Engelbrecht *et al.*, "Effects of surface finish and mechanical training on Ni-Ti sheets for elastocaloric cooling," *APL Materials*, vol. 4, no. 6, p. 064110, Jun. 2016, doi: 10.1063/1.4955131.

- 
- [130] J. Frenzel, “On the Importance of Structural and Functional Fatigue in Shape Memory Technology,” *Shap. Mem. Superelasticity*, vol. 6, pp. 213–222, May 2020, doi: 10.1007/s40830-020-00281-3.
  - [131] C. Bechtold, C. Chluba, R. Lima de Miranda, and E. Quandt, “High cyclic stability of the elastocaloric effect in sputtered TiNiCu shape memory films,” *Appl. Phys. Lett.*, vol. 101, no. 9, p. 091903, Aug. 2012, doi: 10.1063/1.4748307.
  - [132] K. Gall and H. J. Maier, “Cyclic deformation mechanisms in precipitated NiTi shape memory alloys,” *Acta Materialia*, vol. 50, no. 18, pp. 4643–4657, Oct. 2002, doi: 10.1016/S1359-6454(02)00315-4.
  - [133] E. Hornbogen, “Review Thermo-mechanical fatigue of shape memory alloys,” *Journal of Materials Science*, vol. 39, no. 2, pp. 385–399, Jan. 2004, doi: 10.1023/B:JMSC.0000011492.88523.d3.
  - [134] R. Delville, B. Malard, J. Pilch, P. Sittner, and D. Schryvers, “Microstructure changes during non-conventional heat treatment of thin Ni–Ti wires by pulsed electric current studied by transmission electron microscopy,” *Acta Materialia*, vol. 58, no. 13, pp. 4503–4515, Aug. 2010, doi: 10.1016/j.actamat.2010.04.046.
  - [135] X. Chen, V. Srivastava, V. Dabade, and R. D. James, “Study of the cofactor conditions: Conditions of supercompatibility between phases,” *Journal of the Mechanics and Physics of Solids*, vol. 61, no. 12, pp. 2566–2587, Dec. 2013, doi: 10.1016/j.jmps.2013.08.004.
  - [136] H. Gu, L. Bumke, C. Chluba, E. Quandt, and R. D. James, “Phase engineering and supercompatibility of shape memory alloys,” *Materials Today*, vol. 21, no. 3, pp. 265–277, Apr. 2018, doi: 10.1016/j.mattod.2017.10.002.
  - [137] Y. Song, X. Chen, V. Dabade, T. W. Shield, and R. D. James, “Enhanced reversibility and unusual microstructure of a phase-transforming material,” *Nature*, vol. 502, no. 7469, pp. 85–88, Oct. 2013, doi: 10.1038/nature12532.
  - [138] C. Chluba *et al.*, “Effect of crystallographic compatibility and grain size on the functional fatigue of sputtered TiNiCuCo thin films,” *Philosophical Transactions of the Royal Society A: Mathematical,*

- Physical and Engineering Sciences*, vol. 374, no. 2074, p. 20150311, Aug. 2016, doi: 10.1098/rsta.2015.0311.
- [139] T. Dankwort *et al.*, “Martensite adaption through epitaxial nano transition layers in TiNiCu shape memory alloys,” *Journal of Applied Crystallography*, vol. 49, no. 3, pp. 1009–1015, Jun. 2016, doi: 10.1107/S160057671600710X.
  - [140] J. Tušek *et al.*, “Elastocaloric effect vs fatigue life: Exploring the durability limits of Ni-Ti plates under pre-strain conditions for elastocaloric cooling,” *Acta Materialia*, vol. 150, pp. 295–307, May 2018, doi: 10.1016/j.actamat.2018.03.032.
  - [141] H. Hou *et al.*, “Overcoming fatigue through compression for advanced elastocaloric cooling,” *MRS Bull.*, vol. 43, no. 4, pp. 285–290, Apr. 2018, doi: 10.1557/mrs.2018.70.
  - [142] J. Chen, K. Zhang, Q. Kan, H. Yin, and Q. Sun, “Ultra-high fatigue life of NiTi cylinders for compression-based elastocaloric cooling,” *Appl. Phys. Lett.*, vol. 115, no. 9, p. 093902, Aug. 2019, doi: 10.1063/1.5115793.
  - [143] H. Hou *et al.*, “Fatigue-resistant high-performance elastocaloric materials made by additive manufacturing,” *Science*, vol. 366, no. 6469, pp. 1116–1121, Nov. 2019, doi: 10.1126/science.aax7616.
  - [144] S. Qian, L. Yuan, J. Yu, and G. Yan, “The mechanism of  $\Delta T$  variation in coupled heat transfer and phase transformation for elastocaloric materials and its application in materials characterization,” *Applied Physics Letters*, vol. 111, no. 22, p. 223902, Nov. 2017, doi: 10.1063/1.5001971.
  - [145] E. Polatidis, N. Zotov, and E. J. Mittemeijer, “Stress-induced phase transformations in thermally cycled superelastic NiTi alloys: in situ X-ray diffraction studies,” *Powder Diffraction*, vol. 30, no. S1, pp. S76–S82, Jun. 2015, doi: 10.1017/S0885715614001456.
  - [146] F. Wendler, H. Ossmer, C. Chluba, E. Quandt, and M. Kohl, “Mesoscale simulation of elastocaloric cooling in SMA films,” *Acta Materialia*, vol. 136, pp. 105–117, Sep. 2017, doi: 10.1016/j.actamat.2017.06.044.

- [147] N. Michaelis, A. Schütze, F. Welsch, S.-M. Kirsch, and S. Seelecke, “Novel Experimental Approach to Determine Elastocaloric Latent Heat,” *Shap. Mem. Superelasticity*, vol. 5, pp. 352–361, Dec. 2019, doi: 10.1007/s40830-019-00249-y.
- [148] S. Qian, J. Ling, Y. Hwang, R. Radermacher, and I. Takeuchi, “Thermodynamics cycle analysis and numerical modeling of thermoelastic cooling systems,” *International Journal of Refrigeration*, vol. 56, pp. 65–80, Aug. 2015, doi: 10.1016/j.ijrefrig.2015.04.001.
- [149] W. J. Buehler, J. V. Gilfrich, and R. C. Wiley, “Effect of Low-Temperature Phase Changes on the Mechanical Properties of Alloys near Composition TiNi,” *Journal of Applied Physics*, vol. 34, no. 5, pp. 1475–1477, May 1963, doi: 10.1063/1.1729603.
- [150] Y. Wu, E. Ertekin, and H. Sehitoglu, “Elastocaloric cooling capacity of shape memory alloys – Role of deformation temperatures, mechanical cycling, stress hysteresis and inhomogeneity of transformation,” *Acta Materialia*, vol. 135, pp. 158–176, Aug. 2017, doi: 10.1016/j.actamat.2017.06.012.
- [151] L. Mañosa, S. Jarque-Farnos, E. Vives, and A. Planes, “Large temperature span and giant refrigerant capacity in elastocaloric Cu-Zn-Al shape memory alloys,” *Applied Physics Letters*, vol. 103, no. 21, p. 211904, Nov. 2013, doi: 10.1063/1.4832339.
- [152] J. Cui *et al.*, “Demonstration of high efficiency elastocaloric cooling with large  $\Delta T$  using NiTi wires,” *Applied Physics Letters*, vol. 101, no. 7, p. 073904, Aug. 2012, doi: 10.1063/1.4746257.
- [153] H. Ossmer, F. Lambrecht, M. Gültig, C. Chluba, E. Quandt, and M. Kohl, “Evolution of temperature profiles in TiNi films for elastocaloric cooling,” *Acta Materialia*, vol. 81, pp. 9–20, Dec. 2014, doi: 10.1016/j.actamat.2014.08.006.
- [154] A. Wieczorek *et al.*, “Optimizing Ni–Ti-based shape memory alloys for ferroic cooling,” *Funct. Mater. Lett.*, vol. 10, no. 01, p. 1740001, 2017, doi: 10.1142/S179360471740001X.
- [155] C. Chluba, H. Ossmer, C. Zamponi, M. Kohl, and E. Quandt, “Ultra-Low Fatigue Quaternary TiNi-Based Films for Elastocaloric Cooling,” *Shape*

- Memory and Superelasticity*, vol. 2, no. 1, pp. 95–103, Mar. 2016, doi: 10.1007/s40830-016-0054-3.
- [156] W. Sun, J. Liu, B. Lu, Y. Li, and A. Yan, “Large elastocaloric effect at small transformation strain in Ni45Mn44Sn11 metamagnetic shape memory alloys,” *Scripta Materialia*, vol. 114, pp. 1–4, Mar. 2016, doi: 10.1016/j.scriptamat.2015.11.021.
- [157] D. Cong *et al.*, “Colossal Elastocaloric Effect in Ferroelastic Ni-Mn-Ti Alloys,” *Phys. Rev. Lett.*, vol. 122, no. 25, p. 255703, Jun. 2019, doi: 10.1103/PhysRevLett.122.255703.
- [158] Z. Xie, G. Sebald, and D. Guyomar, “Temperature dependence of the elastocaloric effect in natural rubber,” *Physics Letters A*, vol. 381, no. 25–26, pp. 2112–2116, Jul. 2017, doi: 10.1016/j.physleta.2017.02.014.
- [159] L. Bumke, C. Chluba, H. Ossmer, C. Zamponi, M. Kohl, and E. Quandt, “Cobalt Gradient Evolution in Sputtered TiNiCuCo Films for Elastocaloric Cooling,” *physica status solidi (b)*, p. 1700299, Nov. 2017, doi: 10.1002/pssb.201700299.
- [160] M. Elahinia, N. Shayesteh Moghaddam, M. Taheri Andani, A. Amerinatanzi, B. A. Bimber, and R. F. Hamilton, “Fabrication of NiTi through additive manufacturing: A review,” *Progress in Materials Science*, vol. 83, pp. 630–663, Oct. 2016, doi: 10.1016/j.pmatsci.2016.08.001.
- [161] H. Hou *et al.*, “Elastocaloric cooling of additive manufactured shape memory alloys with large latent heat,” *J. Phys. D: Appl. Phys.*, vol. 50, no. 40, p. 404001, Sep. 2017, doi: 10.1088/1361-6463/aa85bf.
- [162] A. Chauhan, S. Patel, and R. Vaish, “Elastocaloric effect in ferroelectric ceramics,” *Appl. Phys. Lett.*, vol. 106, no. 17, p. 172901, Apr. 2015, doi: 10.1063/1.4919453.
- [163] M. Li, Z. Guo, and T. Chang, “Adhesion and stress-enhanced elastocaloric effect in graphene,” *Sci. China Technol. Sci.*, vol. 63, no. 2, pp. 297–302, Feb. 2020, doi: 10.1007/s11431-018-9395-6.
- [164] S. Lisenkov, R. Herchig, S. Patel, R. Vaish, J. Cuozzo, and I. Ponomareva, “Elastocaloric Effect in Carbon Nanotubes and

- Graphene," *Nano Letters*, vol. 16, no. 11, pp. 7008–7012, Nov. 2016, doi: 10.1021/acs.nanolett.6b03155.
- [165] M. Trček *et al.*, "Electrocaloric and elastocaloric effects in soft materials," *Philosophical Transactions of the Royal Society A: Mathematical, Physical and Engineering Sciences*, vol. 374, no. 2074, p. 20150301, Aug. 2016, doi: 10.1098/rsta.2015.0301.
- [166] G. Sebald, A. Komiya, J. Jay, G. Coatavy, and L. Lebrun, "Regenerative cooling using elastocaloric rubber: Analytical model and experiments," *Journal of Applied Physics*, vol. 127, no. 9, p. 094903, Mar. 2020, doi: 10.1063/1.5132361.
- [167] P. Kabirifar, A. Žerovník, Ž. Ahčin, L. Porenta, M. Brojan, and J. Tušek, "Elastocaloric Cooling: State-of-the-art and Future Challenges in Designing Regenerative Elastocaloric Devices," *SV-JME*, vol. 65, no. 11–12, pp. 615–630, Nov. 2019, doi: 10.5545/sv-jme.2019.6369.
- [168] A. Czernuszewicz, L. Griffith, J. Slaughter, and V. Pecharsky, "Low-force compressive and tensile actuation for elastocaloric heat pumps," *Applied Materials Today*, vol. 19, p. 100557, Jun. 2020, doi: 10.1016/j.apmt.2020.100557.
- [169] H. Ossmer, F. Wendler, M. Gueltig, F. Lambrecht, S. Miyazaki, and M. Kohl, "Energy-efficient miniature-scale heat pumping based on shape memory alloys," *Smart Materials and Structures*, vol. 25, no. 8, p. 085037, Aug. 2016, doi: 10.1088/0964-1726/25/8/085037.
- [170] M. Bahrami, M. M. Yovanovich, and J. R. Culham, "Thermal contact resistance at low contact pressure: Effect of elastic deformation," *International Journal of Heat and Mass Transfer*, vol. 48, no. 16, pp. 3284–3293, Jul. 2005, doi: 10.1016/j.ijheatmasstransfer.2005.02.033.
- [171] S.-M. Kirsch, M. Schmidt, F. Welsch, N. Michaelis, A. Schütze, and S. Seelecke, "Development of a shape memory based air conditioning system," in *Engineering for a Changing World: Proceedings; 59th IWK, Ilmenau Scientific Colloquium*, Ilmenau, 2017, vol. 59, Available: [https://www.db-thueringen.de/receive/dbt\\_mods\\_00033169](https://www.db-thueringen.de/receive/dbt_mods_00033169). (accessed May 24, 2020)

- [172] J. Tušek, K. Engelbrecht, D. Eriksen, S. Dall’Olio, J. Tušek, and N. Pryds, “A regenerative elastocaloric heat pump,” *Nature Energy*, vol. 1, no. 10, p. 16134, Sep. 2016, doi: 10.1038/nenergy.2016.134.
- [173] S. Qian *et al.*, “Design of a hydraulically driven compressive elastocaloric cooling system,” *Science and Technology for the Built Environment*, vol. 22, no. 5, pp. 500–506, Jul. 2016, doi: 10.1080/23744731.2016.1171630.
- [174] R. Richter and J. M. Gottschlich, “Thermodynamic aspects of heat pipe operation,” *Journal of Thermophysics and Heat Transfer*, vol. 8, no. 2, pp. 334–340, Apr. 1994, doi: 10.2514/3.543.
- [175] K. Bartholomé, T. Hess, M. Winkler, A. Mahlke, and J. König, “New Concept for High-Efficient Cooling Systems Based on Solid-State Caloric Materials as Refrigerant,” in *Energy and Thermal Management, Air Conditioning, Waste Heat Recovery*, C. Junior, D. Jänsch, and O. Dingel, Eds. Cham: Springer International Publishing, 2017, pp. 178–186.
- [176] H. Gu *et al.*, “A chip scale electrocaloric effect based cooling device,” *Applied Physics Letters*, vol. 102, no. 12, p. 122904, Mar. 2013, doi: 10.1063/1.4799283.
- [177] T. Hess, L. M. Maier, P. Corhan, O. Schäfer-Welsen, J. Wöllenstein, and K. Bartholomé, “Modelling cascaded caloric refrigeration systems that are based on thermal diodes or switches,” *International Journal of Refrigeration*, vol. 103, pp. 215–222, Jul. 2019, doi: 10.1016/j.ijrefrig.2019.04.013.
- [178] G. Wehmeyer, T. Yabuki, C. Monachon, J. Wu, and C. Dames, “Thermal diodes, regulators, and switches: Physical mechanisms and potential applications,” *Applied Physics Reviews*, vol. 4, no. 4, p. 041304, Nov. 2017, doi: 10.1063/1.5001072.
- [179] K. Klinar and A. Kitanovski, “Thermal control elements for caloric energy conversion,” *Renewable and Sustainable Energy Reviews*, vol. 118, p. 109571, Feb. 2020, doi: 10.1016/j.rser.2019.109571.
- [180] K. L. Engelbrecht, G. F. Nellis, S. A. Klein, and C. B. Zimm, “Review Article: Recent Developments in Room Temperature Active Magnetic

- Regenerative Refrigeration," *HVAC&R Research*, vol. 13, no. 4, pp. 525–542, Jul. 2007, doi: 10.1080/10789669.2007.10390970.
- [181] S. Qian, J. Ling, J. Muehlbauer, Y. Hwang, and R. Radermacher, "Study on high efficient heat recovery cycle for solid-state cooling," *International Journal of Refrigeration*, vol. 55, pp. 102–119, Jul. 2015, doi: 10.1016/j.ijrefrig.2015.03.023.
- [182] M. Schmidt, A. Schütze, and S. Seelecke, "Scientific test setup for investigation of shape memory alloy based elastocaloric cooling processes," *International Journal of Refrigeration*, vol. 54, pp. 88–97, Jun. 2015, doi: 10.1016/j.ijrefrig.2015.03.001.
- [183] M. Schmidt *et al.*, "Thermal Stabilization of NiTiCuV Shape Memory Alloys: Observations During Elastocaloric Training," *Shape Memory and Superelasticity*, vol. 1, no. 2, pp. 132–141, Jun. 2015, doi: 10.1007/s40830-015-0021-4.
- [184] M. Schmidt, A. Schütze, and S. Seelecke, "Elastocaloric cooling processes: The influence of material strain and strain rate on efficiency and temperature span," *APL Materials*, vol. 4, no. 6, p. 064107, Jun. 2016, doi: 10.1063/1.4953433.
- [185] S. Qian, Y. Wang, Y. Geng, J. Ling, and J. Muehlbauer, "Experimental Evaluation of Compressive Elastocaloric Cooling System," presented at the International Refrigeration and Air Conditioning, West Lafayette, IN, United States, 2016, Paper No. 1726, doi: <http://docs.lib.psu.edu/iracc/1726>.
- [186] Fraunhofer IPM, "Elastokalorische systemeffiziente Kühlsysteme ohne schädliche Kältemittel," Aug. 2019.  
<https://www.ipm.fraunhofer.de/content/dam/ipm/de/PDFs/produktblaetter/TE/KAS/Elastokalorik-kaeltemittelfreie-kuehlsysteme.pdf> (accessed May 09, 2020).
- [187] Fraunhofer IPM, "Small fridge, big potential: Cooling with elastocaloric materials," 2018.  
<https://www.ipm.fraunhofer.de/content/dam/ipm/en/PDFs/reports/AR-articles-2018-2019/AR-2018-elastocaloric-fridge.pdf> (accessed May 09, 2020).

- [188] D. J. Sharar, J. Radice, R. Warzoha, B. Hanrahan, and B. Chang, "First Demonstration of a Bending-Mode Elastocaloric Cooling 'Loop,'" in *2018 17th IEEE Intersociety Conference on Thermal and Thermomechanical Phenomena in Electronic Systems (ITHERM)*, San Diego, CA, USA, May 2018, pp. 218–226, doi: 10.1109/ITHERM.2018.8419513.
- [189] S.-M. Kirsch *et al.*, "Continuous Operating Elastocaloric Heating and Cooling Device: Air Flow Investigation and Experimental Parameter Study," presented at the ASME 2019 Conference on Smart Materials, Adaptive Structures and Intelligent Systems, Louisville, Ky, Dec. 2019, Paper No. 5636, doi: 10.1115/SMASIS2019-5633.
- [190] H. Ossmer, C. Chluba, S. Kauffmann-Weiss, E. Quandt, and M. Kohl, "TiNi-based films for elastocaloric microcooling - Fatigue life and device performance," *APL Materials*, vol. 4, no. 6, p. 064102, Jun. 2016, doi: 10.1063/1.4948271.
- [191] S. Qian *et al.*, "Design, Development and Testing of a Compressive Thermoelastic Cooling System," presented at the 24<sup>th</sup> International Congress of Refrigeration, Yokohama, Japan, Aug. 2015, Paper No. 0092.
- [192] S. Qian *et al.*, "Performance enhancement of a compressive thermoelastic cooling system using multi-objective optimization and novel designs," *International Journal of Refrigeration*, vol. 57, pp. 62–76, Sep. 2015, doi: 10.1016/j.ijrefrig.2015.04.012.
- [193] K. Engelbrecht *et al.*, "A regenerative elastocaloric device: experimental results," *Journal of Physics D: Applied Physics*, vol. 50, no. 42, p. 424006, Oct. 2017, doi: 10.1088/1361-6463/aa8656.
- [194] N. Michaelis, F. Welsch, S.-M. Kirsch, M. Schmidt, S. Seelecke, and A. Schütze, "Experimental parameter identification for elastocaloric air cooling," *International Journal of Refrigeration*, vol. 100, pp. 167–174, Apr. 2019, doi: 10.1016/j.ijrefrig.2019.01.006.
- [195] N. Michaelis, F. Welsch, S.-M. Kirsch, S. Seelecke, and A. Schütze, "Resistance monitoring of shape memory material stabilization during elastocaloric training," *Smart Mater. Struct.*, vol. 28, no. 10, p. 105046, Oct. 2019, doi: 10.1088/1361-665X/ab3d62.

- [196] F. Welsch, S.-M. Kirsch, N. Michaelis, P. Motzki, A. Schütze, and S. Seelecke, "Continuous Operating Elastocaloric Heating and Cooling Device: Model-Based Parameter Study With Airflow Losses," presented at the ASME 2019 Conference on Smart Materials, Adaptive Structures and Intelligent Systems, Louisville, KY, USA, Dec. 2019, Paper No. 5636, doi: 10.1115/SMASIS2019-5636.
- [197] F. Welsch *et al.*, "Numerical simulation and experimental investigation of the elastocaloric cooling effect in sputter-deposited TiNiCuCo thin films," *Continuum Mech. Thermodyn.*, vol. 30, no. 1, pp. 53–68, Jan. 2018, doi: 10.1007/s00161-017-0582-x.
- [198] C. Haberland and M. H. Elahinia, "Fabricating NiTi SMA Components," in *Shape Memory Alloy Actuators*, M. H. Elahinia, Ed. Chichester, West Sussex, U.K.: John Wiley & Sons, Ltd, 2015, pp. 191–238.
- [199] S. Miyazaki, V. H. No, K. Kitamura, A. Khantachawana, and H. Hosoda, "Texture of Ti–Ni rolled thin plates and sputter-deposited thin films," *International Journal of Plasticity*, vol. 16, no. 10–11, pp. 1135–1154, Jan. 2000, doi: 10.1016/S0749-6419(00)00004-8.
- [200] H. Hosoda *et al.*, "Cold rolling of B2 intermetallics," *Journal of Alloys and Compounds*, vol. 302, no. 1–2, pp. 266–273, Apr. 2000, doi: 10.1016/S0925-8388(00)00583-1.
- [201] R. Lima de Miranda, C. Zamponi, and E. Quandt, "Micropatterned Freestanding Superelastic TiNi Films," *Advanced Engineering Materials*, vol. 15, no. 1–2, pp. 66–69, Feb. 2013, doi: 10.1002/adem.201200197.
- [202] C. Bechtold, R. Lima de Miranda, and E. Quandt, "Capability of Sputtered Micro-patterned NiTi Thick Films," *Shap. Mem. Superelasticity*, vol. 1, no. 3, pp. 286–293, Sep. 2015, doi: 10.1007/s40830-015-0029-9.
- [203] K. Schiebold, *Zerstörende Werkstoffprüfung*. Berlin, Heidelberg: Springer, 2018.
- [204] C. Eberl, "Digital Image Correlation and Tracking," *MATLAB Central File Exchange*.  
<https://de.mathworks.com/matlabcentral/fileexchange/12413> (accessed Apr. 13, 2020).

- [205] W. Minkina and S. Dudzik, *Infrared thermography: errors and uncertainties*. Chichester, West Sussex, U.K. ; Hoboken, NJ: J. Wiley, 2009.
- [206] J. Tušek, K. Engelbrecht, L. Mañosa, E. Vives, and N. Pryds, "Understanding the Thermodynamic Properties of the Elastocaloric Effect Through Experimentation and Modelling," *Shape Memory and Superelasticity*, vol. 2, no. 4, pp. 317–329, Dec. 2016, doi: 10.1007/s40830-016-0094-8.
- [207] A. Frick and C. Stern, *DSC-Prüfung in der Anwendung*. Munich: Carl Hanser Verlag, 2013.
- [208] ASTM International, "F2004-17 Standard Test Method for Transformation Temperature of Nickel-Titanium Alloys by Thermal Analysis," ASTM International, West Conshohocken, PA, USA, 2017. doi: 10.1520/F2004-17.
- [209] K. Otsuka and X. Ren, "Physical metallurgy of Ti–Ni-based shape memory alloys," *Progress in Materials Science*, vol. 50, no. 5, pp. 511–678, Jul. 2005, doi: 10.1016/j.pmatsci.2004.10.001.
- [210] F. Bruederlin, H. Ossmer, F. Wendler, S. Miyazaki, and M. Kohl, "SMA Foil-Based Elastocaloric Cooling – From Material Behavior to Device Engineering," *Journal of Physics D: Applied Physics*, vol. 50, p. 424003, 2017, doi: <https://doi.org/10.1088/1361-6463/aa87a2>.
- [211] S. Miyazaki and K. Otsuka, "Deformation and transition behavior associated with the R-phase in Ti-Ni alloys," *Metallurgical Transactions A*, vol. 17, no. 1, pp. 53–63, Jan. 1986, doi: 10.1007/BF02644442.
- [212] P. Šittner, M. Landa, P. Lukáš, and V. Novák, "R-phase transformation phenomena in thermomechanically loaded NiTi polycrystals," *Mechanics of Materials*, vol. 38, no. 5, pp. 475–492, May 2006, doi: 10.1016/j.mechmat.2005.05.025.
- [213] P. Sittner, Y. Liu, and V. Novak, "On the origin of Lüders-like deformation of NiTi shape memory alloys," *Journal of the Mechanics and Physics of Solids*, vol. 53, no. 8, pp. 1719–1746, Aug. 2005, doi: 10.1016/j.jmps.2005.03.005.

- [214] A. Ishida, M. Sato, and Z. Gao, "Effects of Ti content on microstructure and shape memory behavior of  $TixNi(84.5-x)Cu15.5$  ( $x=44.6\text{--}55.4$ ) thin films," *Acta Materialia*, vol. 69, pp. 292–300, May 2014, doi: 10.1016/j.actamat.2014.02.006.
- [215] H. Rösner, P. Schloßmacher, A. V. Shelyakov, and A. M. Glezer, "The influence of coherent TiCu plate-like precipitates on the thermoelastic martensitic transformation in melt-spun  $Ti50Ni25Cu25$  shape memory alloys," *Acta Materialia*, vol. 49, no. 9, pp. 1541–1548, May 2001, doi: 10.1016/S1359-6454(01)00055-6.
- [216] Y. Frekers, T. Helmig, E. M. Burghold, and R. Kneer, "A numerical approach for investigating thermal contact conductance," *International Journal of Thermal Sciences*, vol. 121, pp. 45–54, Nov. 2017, doi: 10.1016/j.ijthermalsci.2017.06.026.
- [217] F. Bruederlin, L. Bumke, E. Quandt, and M. Kohl, "Kaskadiertes Elastokalorisches KühlSystem - Cascaded Elastocaloric Cooling System," in *MikroSystemTechnik Kongress 2019*, Berlin, Oct. 2019, p. 340.
- [218] F. Bruederlin, L. Bumke, E. Quandt, and M. Kohl, "Cascaded SMA-Film Based Elastocaloric Cooling," in *20th International Conference on Solid-State Sensors, Actuators and Microsystems Eurosensors XXXIII (TRANSDUCERS EUROSENSORS XXXIII)*, Berlin, Jun. 2019, pp. 1467–1470, doi: 10.1109/TRANSDUCERS.2019.8808605.
- [219] F. P. Incropera, Ed., *Fundamentals of heat and mass transfer*, 6th ed. Hoboken, NJ: John Wiley, 2007.
- [220] Uwe Heisel, Johannes Rothmund, Werner Degner, Hans Lutze, and Erhard Smejkal, *Spanende Formung - Hanser Fachbuch*, 18. edition. München: Hanser, 2019.
- [221] G. Kibria, M. P. Jahan, and B. Bhattacharyya, *Micro-electrical Discharge Machining Processes: Technologies and Applications*. Singapore: Springer Singapore, 2019.
- [222] I. Gibson, D. Rosen, and B. Stucker, *Additive Manufacturing Technologies: 3D Printing, Rapid Prototyping, and Direct Digital Manufacturing*, 2nd ed. New York: Springer-Verlag, 2015.

- [223] M. Miwa, S. Juodkazis, T. Kawakami, S. Matsuo, and H. Misawa, "Femtosecond two-photon stereo-lithography," *Appl Phys A*, vol. 73, no. 5, pp. 561–566, Nov. 2001, doi: 10.1007/s003390100934.
- [224] "NextDent Model 2.0," NextDent.  
<https://nextdent.com/products/model-2/> (accessed Feb. 26, 2020).
- [225] G. Ulpiani et al., "Elastocaloric cooling: roadmap towards successful implementation in the built environment," *AIMS Materials Science*, vol. 6, no. 6, p. 1135, Nov. 2019, doi: 10.3934/matersci.2019.6.1135.
- [226] D. Song, G. Kang, Q. Kan, C. Yu, and C. Zhang, "Effects of peak stress and stress amplitude on multiaxial transformation ratchetting and fatigue life of superelastic NiTi SMA micro-tubes: Experiments and life-prediction model," *International Journal of Fatigue*, vol. 96, pp. 252–260, Mar. 2017, doi: 10.1016/j.ijfatigue.2016.12.006.
- [227] J. Ueda, T. W. Secord, and H. H. Asada, "Large Effective-Strain Piezoelectric Actuators Using Nested Cellular Architecture With Exponential Strain Amplification Mechanisms," *IEEE/ASME Transactions on Mechatronics*, vol. 15, no. 5, pp. 770–782, Oct. 2010, doi: 10.1109/TMECH.2009.2034973.
- [228] T. Fey et al., "Mechanical and electrical strain response of a piezoelectric auxetic PZT lattice structure," *Smart Materials and Structures*, vol. 25, no. 1, p. 015017, Jan. 2016, doi: 10.1088/0964-1726/25/1/015017.

### Co-Supervised Bachelor and Master Theses

- [a] R. Buda, Co-Supervisor: F. Brüderlin, Supervisor: M. Kohl, "Entwicklung einer elastokalorischen Miniatur-Kühleinheit mit rotatorischem Antrieb", IMT, Karlsruhe Institute of Technology, Master Thesis, 2019
- [b] A. Ghiami, Co-Supervisor: F. Brüderlin, Supervisor: M. Kohl, "Novel concepts for heat transfer in elastocaloric cooling devices", IMT, Karlsruhe Institute of Technology, Master Thesis, 2017

- [c] D. Schall, Co-Supervisor: F. Brüderlin, Supervisor: M. Kohl, "Der elastokalorische Effekt auf Basis von Elastomerfolien", IMT, Karlsruhe Institute of Technology, Bachelor Thesis, 2019
- [d] R. Weidemann, Co-Supervisor: F. Brüderlin, Supervisor: M. Kohl, "Entwicklung eines parallelisierten elastokalorischen Kühlelements", IMT, Karlsruhe Institute of Technology, Master Thesis, 2019



Schriften des Instituts für Mikrostrukturtechnik  
am Karlsruher Institut für Technologie (KIT)

---

ISSN 1869-5183

---

- Band 1 Georg Obermaier  
Research-to-Business Beziehungen: Technologietransfer  
durch Kommunikation von Werten (Barrieren, Erfolgs-  
faktoren und Strategien).  
ISBN 978-3-86644-448-5
- Band 2 Thomas Grund  
Entwicklung von Kunststoff-Mikroventilen im  
Batch-Verfahren.  
ISBN 978-3-86644-496-6
- Band 3 Sven Schüle  
Modular adaptive mikrooptische Systeme in Kombination  
mit Mikroaktoren.  
ISBN 978-3-86644-529-1
- Band 4 Markus Simon  
Röntgenlinsen mit großer Apertur.  
ISBN 978-3-86644-530-7
- Band 5 K. Phillip Schierjott  
Miniaturlisierte Kapillarelektrophorese zur kontinuierlichen  
Überwachung von Kationen und Anionen in Prozess-  
strömen.  
ISBN 978-3-86644-523-9
- Band 6 Stephanie Kißling  
Chemische und elektrochemische Methoden zur  
Oberflächenbearbeitung von galvanogeformten  
Nickel-Mikrostrukturen.  
ISBN 978-3-86644-548-2

- Band 7 Friederike J. Gruhl**  
Oberflächenmodifikation von Surface Acoustic Wave (SAW)  
Biosensoren für biomedizinische Anwendungen.  
ISBN 978-3-86644-543-7
- Band 8 Laura Zimmermann**  
Dreidimensional nanostrukturierte und superhydrophobe  
mikrofluidische Systeme zur Tröpfchengenerierung und  
-handhabung.  
ISBN 978-3-86644-634-2
- Band 9 Martina Reinhardt**  
Funktionalisierte, polymere Mikrostrukturen für die  
dreidimensionale Zellkultur.  
ISBN 978-3-86644-616-8
- Band 10 Mauno Schelb**  
Integrierte Sensoren mit photonischen Kristallen auf  
Polymerbasis.  
ISBN 978-3-86644-813-1
- Band 11 Daniel Auernhammer**  
Integrierte Lagesensorik für ein adaptives mikrooptisches  
Ablenksystem.  
ISBN 978-3-86644-829-2
- Band 12 Nils Z. Danckwardt**  
Pumpfreier Magnetpartikeltransport in einem  
Mikroreaktionssystem: Konzeption, Simulation  
und Machbarkeitsnachweis.  
ISBN 978-3-86644-846-9
- Band 13 Alexander Kolew**  
Heißprägen von Verbundfolien für mikrofluidische  
Anwendungen.  
ISBN 978-3-86644-888-9

- Band 14** Marko Brammer  
Modulare Optoelektronische Mikrofluidische Backplane.  
ISBN 978-3-86644-920-6
- Band 15** Christiane Neumann  
Entwicklung einer Plattform zur individuellen Ansteuerung von Mikroventilen und Aktoren auf der Grundlage eines Phasenüberganges zum Einsatz in der Mikrofluidik.  
ISBN 978-3-86644-975-6
- Band 16** Julian Hartbaum  
Magnetisches Nanoaktorsystem.  
ISBN 978-3-86644-981-7
- Band 17** Johannes Kenntner  
Herstellung von Gitterstrukturen mit Aspektverhältnis 100 für die Phasenkontrastbildung in einem Talbot-Interferometer.  
ISBN 978-3-7315-0016-2
- Band 18** Kristina Kreppenhofer  
Modular Biomicrofluidics - Mikrofluidikchips im Baukastensystem für Anwendungen aus der Zellbiologie.  
ISBN 978-3-7315-0036-0
- Band 19** Ansgar Waldbaur  
Entwicklung eines maskenlosen Fotolithographiesystems zum Einsatz im Rapid Prototyping in der Mikrofluidik und zur gezielten Oberflächenfunktionalisierung.  
ISBN 978-3-7315-0119-0
- Band 20** Christof Megnин  
Formgedächtnis-Mikroventile für eine fluidische Plattform.  
ISBN 978-3-7315-0121-3
- Band 21** Srinivasa Reddy Yeduru  
Development of Microactuators Based on the Magnetic Shape Memory Effect.  
ISBN 978-3-7315-0125-1

- Band 22** Michael Röhrig  
Fabrication and Analysis of Bio-Inspired Smart Surfaces.  
ISBN 978-3-7315-0163-3
- Band 23** Taleieh Rajabi  
Entwicklung eines mikrofluidischen Zweikammer-Chipsystems mit integrierter Sensorik für die Anwendung in der Tumorforschung.  
ISBN 978-3-7315-0220-3
- Band 24** Frieder Märkle  
Laserbasierte Verfahren zur Herstellung hochdichter Peptidarrays.  
ISBN 978-3-7315-0222-7
- Band 25** Tobias Meier  
Magnetoresistive and Thermoresistive Scanning Probe Microscopy with Applications in Micro- and Nanotechnology.  
ISBN 978-3-7315-0253-1
- Band 26** Felix Marschall  
Entwicklung eines Röntgenmikroskops für Photonenenergien von 15 keV bis 30 keV.  
ISBN 978-3-7315-0263-0
- Band 27** Leonardo Pires Carneiro  
Development of an Electrochemical Biosensor Platform and a Suitable Low-Impedance Surface Modification Strategy.  
ISBN 978-3-7315-0272-2
- Band 28** Sebastian Mathias Schillo  
Prozessentwicklung für die Automatisierung der Herstellung und Anwendung von hochdichten Peptidmicroarrays.  
ISBN 978-3-7315-0274-6

- Band 29** Nicole E. Steidle  
Micro- and Nanostructured Microfluidic Devices  
for Localized Protein Immobilization and Other  
Biomedical Applications.  
ISBN 978-3-7315-0297-5
- Band 30** Jochen Heneka  
Prozessentwicklung eines industrietauglichen Verfahrens  
zur Fertigung von vereinzelten LIGA-Mikrobauteilen.  
ISBN 978-3-7315-0326-2
- Band 31** Seoung-Eun Kim  
Konzeption und prototypische Fertigung einer  
nicht-invasiven mikrofluidischen Plattform für die  
Elektrophysiologie (NIMEP) zur Zellenanalyse.  
ISBN 978-3-7315-0378-1
- Band 32** Elisabeth Wilhelm  
Entwicklung eines mikrofluidischen Brailledisplays.  
ISBN 978-3-7315-0385-9
- Band 33** Viktor Pinnecker  
Entwicklung miniaturisierter Aktorsysteme basierend  
auf magnetischen Formgedächtnislegierungen.  
ISBN 978-3-7315-0500-6
- Band 34** Ali Caglar Özen  
Novel MRI Technologies for Structural and Functional  
Imaging of Tissues with Ultra-short  $T_2$  Values.  
ISBN 978-3-7315-0657-7
- Band 35** Anne Bäcker  
Veränderliche 3D Zellgerüstträger auf Cryogelbasis  
zur Kultivierung von Prostatakarzinomzellen.  
ISBN 978-3-7315-0676-8
- Band 36** Frieder Johannes Koch  
X-ray optics made by X-ray lithography:  
Process optimization and quality control.  
ISBN 978-3-7315-0679-9

- Band 37** Tobias Jörg Schröter  
Vergrößerung des Sehfeldes der Röntgen-Phasenkontrast-Bildgebung für die klinische Anwendung.  
ISBN 978-3-7315-0731-4
- Band 38** Felix Vüllers  
Bioinspired Superhydrophobic Nano- and Microstructured Surfaces for Drag Reduction and Optoelectronics.  
ISBN 978-3-7315-0816-8
- Band 39** Frederik Kotz  
Entwicklung neuer Materialien für die additive Fertigung und das Rapid Prototyping von Glas und Polymethylmethacrylat.  
ISBN 978-3-7315-0835-9
- Band 40** Michael Oldenburg  
Photon upconversion heterostructures made from surface-anchored metal-organic frameworks.  
ISBN 978-3-7315-0863-2
- Band 41** Elisa Kornemann  
Entwicklung einer Röntgenzoomlinse.  
ISBN 978-3-7315-0885-4
- Band 42** Hossein Davoodi  
NMR micro-detectors tailored for multinuclear and electro-chemistry lab-on-a-chip applications.  
ISBN 978-3-7315-1118-2
- Band 43** Florian Brüderlin  
Advanced Elastocaloric Cooling Devices Based on Shape Memory Alloy Films.  
ISBN 978-3-7315-1065-9



FLORIAN BRÜDERLIN

Advanced Elastocaloric Cooling Devices Based on  
Shape Memory Alloy Films

Technological progress and climate warming pose a tremendous need for innovative cooling technologies that are both environmentally friendly and efficient. Elastocaloric cooling is a new emerging solid-state cooling technology with the potential to meet this need. Currently, superelastic shape memory alloys (SMA) are the most promising elastocaloric materials. Superelastic SMA responds with heating and cooling to a stress application and removal due to a reversible solid-to-solid phase transformation. SMA film geometries with high surface-to-volume ratio are especially promising, since they combine a high elastocaloric effect size with highly efficient heat transfer. In previous work, SMA film-based elastocaloric cooling has shown potential for small-scale applications. This work investigates the limits of SMA film-based elastocaloric cooling and develops new concepts to overcome limitations. Cascaded and parallelized devices are introduced to increase device temperature span and cooling capacity. The capability of these advanced devices is shown experimentally. The maximum cooling capacity has been increased by 4.5 to 900 mW by operating 5 SMA films in parallel, while a maximum cooling temperature span of 27.3 C has been achieved by a cascade of 3 SMA films. These results point out a route for the design of next generation SMA film-based elastocaloric cooling devices with enhanced cooling capacity and large device temperature span. They form the basis to address a variety of applications with efficient and environmentally friendly cooling technology.

ISSN 1869-5183

ISBN 978-3-7315-1065-9

Gedruckt auf FSC-zertifiziertem Papier

ISBN 978-3-7315-1065-9



9 783731 510659 >